



Faculteit Wetenschappen  
Departement Fysica

**Shape-function relations in Darwin's finch beaks: finite element modeling, mechanical testing and interferometric deformation measurements**

---

**Het verband tussen vorm en functie in de bekken van Darwinvinken: eindige elementen modellering, mechanische experimenten en interferometrische vervormingsmetingen**

Proefschrift voorgelegd tot het behalen van de graad van  
**doctor in de Wetenschappen: Fysica**  
aan de Universiteit Antwerpen  
te verdedigen door  
**Joris SOONS**

**Promotoren:**

Antwerpen, 2012

Prof. Dr. Joris Dirckx  
Prof. Dr. Peter Aerts

De kandidaat werd financieel gesteund door het Fonds voor Wetenschappelijk  
Onderzoek (FWO) Vlaanderen (aspirant mandaat).

The candidate was financially supported by the Research Foundation Flanders.



---

## Doctoral committee

---

### **Chairman**

Prof. Dr. B. Partoens: *Department of Physics, University of Antwerp*

### **Supervisors**

Prof. Dr. J. Dirckx: *Department of Physics, University of Antwerp*

Prof. Dr. P. Aerts: *Department of Biology, University of Antwerp*

### **Members**

Prof. Dr. D. Lamoen: *Department of Physics, University of Antwerp*

### **External members**

Prof. Dr. M. Fagan: *Department of Engineering, University of Hull (UK)*

Dr. A. Herrel: *Département d'Ecologie et de Gestion de la Biodiversité, Museum national d'histoire naturelle (France)*



One of nature's premier illustrations of adaptive evolution concerns the tight correspondence between beak morphology and feeding habits in birds. In seed-crushing birds, beaks evolve in part to avoid fracture. Before this thesis, little was known about mechanical relationships between beak shape, stress dissipation and fracture avoidance. Here, I will test these relationships for Darwin's finches, a clade of birds renowned for their diversity in beak form and function and a text book example for evolutionary biology. From a single ancestor, fourteen species of Darwin's finches differing in beak size and shape and specializing in different food resources have radiated in the Galápagos archipelago. It has been shown that beak morphology in Darwin's finches evolves via natural selection as a response to variation in food type, food availability, and interspecific competition for food. However, seed cracking ability is principally determined by bite force capacity, which in turn is related to jaw closer muscle cross-sectional area. Thus, beak morphology is expected to evolve in concert with jaw adductor strength in order to avoid structural failure because of increased loading.

*The main goal of this dissertation is to give physics-based evidence for the important role of beak size and shape in fracture avoidance. To do so, finite element modeling and interferometric validation measurements will be used.*

Finite element (FE) modeling is ideally suited for this purpose as it allows us to model the effect of complex shape variation on stress magnitude and distribution. It is a widely used computational technique. Applying this technique to biological samples, however, is not straightforward, especially for the small, complex and multi-layered bird beaks. Developing a method to perform FE calculations on such geometries will be a first practical challenge. Second, dedicated experimental setups need to be introduced to obtain material parameters and to validate my model. Third, the mechanical functioning of the beak is not totally understood, and the role of keratin in this strong, but lightweight composite, should be clarified. Finally, my findings will be

applied on a unique collection of 13 Darwin's finch specimens in order to investigate the main research question of this dissertation.

### **Outline of dissertation**

This dissertation is divided into three parts. The first part is meant to be an introduction, and is as such more or less a literature study. In **chapter 1**, some biological aspects are discussed so that the results, presented later in this dissertation, can be better understood by readers who are not familiar with basic concepts in the biology, morphology and evolution of birds. The importance of the beak is explained, its anatomical setup is briefly discussed and more information is given about the famous Darwin's finches. **Chapter 2** starts with a mechanical introduction. Next, more rigorous (mathematical) definitions are given and it is shown how finite element (FE) modeling can be used to solve non-linear mechanical problems. FE modeling was originally introduced to deal with engineering problems. Applying it in biomechanical problems yields some practical issues, which are discussed at the end of this chapter in 'a practical guideline to build a multi-parts geometry-based finite element model'. In the second part, I present two custom made experimental setups, needed in the remainder of the thesis. A first problem is the material characterization of small and thin biological samples. For such samples, it is hard to meet certain boundary conditions, often required by standard testing setups. Therefore, a novel double indentation technique is presented in **chapter 3**. The outcome is compared with a standard compression test for some well-known materials. Subsequently, results are presented for ossicle bone, beak bone and beak keratin. Secondly in **chapter 4**, a dedicated interferometric setup (digital speckle pattern interferometry, DSPI) is proposed to validate the outcome of my FE models. Some theory, the experimental setup and preliminary results are also presented here.

In the final part, the actual modeling results on beaks are presented. The role of the rhamphotheca (keratin layer) on stress dissipation is shown in **chapter 5**. FE modeling is used to study the influence of the material parameters on beak fracture avoidance and I was able to define a set of mechanically optimal values. Such a modeling approach requires a validation procedure, presented in **chapter 6**. Upper beak bending obtained in the model is compared with experimental results from digital image correlation (DIC) and from the custom made DSPI setup. In **chapter 7**, it is shown that the highly sensitive DSPI results can also be used in an inverse analysis for material identification. As a consequence, the results from the proposed double indentation (chapter 3) can be validated. Finally in **chapter 8**, the insights gained in this thesis will be applied to the Darwin's finches. Models of the beak with realistic boundary conditions are constructed so natural stresses can be studied. Next, all 13 beaks are size-scaled so that only their shapes differ. In total, 40 different FE models will be compared to link the fracture avoidance in tip and base biting with beak shape and size. **Chapter 9** includes the general conclusions.

<b>Doctoral committee</b>	<b>3</b>
<b>Preface</b>	<b>5</b>
<b>Contents</b>	<b>7</b>
<b>I Introduction</b>	<b>11</b>
<b>1 Introduction 1: Biological aspects</b>	<b>13</b>
1.1 Bird beaks . . . . .	13
1.2 Darwin's finches . . . . .	17
<b>2 Introduction 2: Mechanics and finite element modeling</b>	<b>21</b>
2.1 One-dimensional example . . . . .	22
2.2 Infinitesimal kinematics . . . . .	23
2.3 Kinematics . . . . .	25
2.4 Stress . . . . .	27
2.5 Constitutive equation . . . . .	29
2.6 Finite element modeling . . . . .	30
2.7 Practical guideline . . . . .	32
2.7.1 Geometry . . . . .	33
2.7.2 Material properties . . . . .	39
2.7.3 Boundary conditions . . . . .	41
2.7.4 Convergence testing . . . . .	42
2.7.5 Validation . . . . .	42

<b>II</b>	<b>Experimental methods</b>	<b>45</b>
<b>3</b>	<b>Double indentation technique</b>	<b>47</b>
3.1	Introduction . . . . .	48
3.1.1	Middle ear ossicle bone . . . . .	49
3.1.2	Java finch beak . . . . .	50
3.2	Material and methods . . . . .	50
3.2.1	Experimental setup . . . . .	50
3.2.2	Calibration and loading protocol . . . . .	52
3.2.3	FE calculations for correction factor ( $\kappa$ ) . . . . .	55
3.2.4	Validation materials and compression test . . . . .	56
3.2.5	Middle ear ossicles . . . . .	57
3.2.6	Java finch beak . . . . .	58
3.3	Results . . . . .	59
3.3.1	Validation materials . . . . .	59
3.3.2	Middle ear ossicles . . . . .	60
3.3.3	Java finch beak . . . . .	62
3.4	Discussion . . . . .	64
3.4.1	FE corrected double indentation method . . . . .	64
3.4.2	Loading protocol . . . . .	66
3.4.3	Validation . . . . .	66
3.4.4	Biological materials . . . . .	67
3.5	Conclusions . . . . .	69
<b>4</b>	<b>Digital speckle pattern interferometry</b>	<b>71</b>
4.1	Introduction . . . . .	72
4.2	Theory . . . . .	73
4.2.1	Direct correlation method . . . . .	74
4.2.2	Subtraction method . . . . .	76
4.2.3	Phase unwrapping . . . . .	77
4.2.4	Angle corrections . . . . .	77
4.2.5	Shearography . . . . .	78
4.2.6	Speckle effect . . . . .	80
4.3	Experimental setup . . . . .	82
4.3.1	Digital Speckle Pattern Interferometry . . . . .	82
4.3.2	Shearography . . . . .	83
4.3.3	Deflection of a cantilever beam . . . . .	84
4.3.4	Beak deformation . . . . .	84
4.4	Results . . . . .	85
4.4.1	Deflection of a cantilever beam . . . . .	85
4.4.2	Beak deformation . . . . .	87
4.5	Discussion . . . . .	90
4.5.1	Deflection of a cantilever beam . . . . .	90
4.5.2	Beak deformation . . . . .	91

---

4.6	Conclusions . . . . .	92
<b>III</b>	<b>Results</b>	<b>93</b>
<b>5</b>	<b>The role of keratin in stress dissipation</b>	<b>95</b>
5.1	Introduction . . . . .	96
5.2	Material and methods . . . . .	97
5.3	Results . . . . .	101
5.4	Discussion . . . . .	104
5.5	Conclusions . . . . .	106
<b>6</b>	<b>Validation experiments</b>	<b>107</b>
6.1	Introduction . . . . .	108
6.2	Material and methods . . . . .	109
6.2.1	Bending experiment . . . . .	109
6.2.2	Digital speckle pattern interferometry . . . . .	110
6.2.3	Validation finite element model . . . . .	111
6.2.4	Digital image correlation . . . . .	113
6.3	Results . . . . .	114
6.3.1	Digital speckle pattern interferometry . . . . .	114
6.3.2	Digital image correlation . . . . .	115
6.4	Discussion . . . . .	117
6.4.1	Digital Speckle Pattern interferometry . . . . .	117
6.4.2	Digital image correlation . . . . .	118
6.5	Conclusions . . . . .	118
<b>7</b>	<b>Inverse analysis</b>	<b>121</b>
7.1	Introduction . . . . .	122
7.2	Material and methods . . . . .	122
7.3	Results . . . . .	123
7.3.1	Inverse analysis with derivative of displacement . . . . .	123
7.3.2	Inverse analysis with displacement . . . . .	125
7.4	Discussion . . . . .	127
7.5	Conclusions . . . . .	128
<b>8</b>	<b>Darwin's finches</b>	<b>129</b>
8.1	Tuning of beak morphology to loading demands . . . . .	130
8.2	Results and discussion . . . . .	131
8.3	Materials and Methods . . . . .	137
8.3.1	Sample collection and CT scanning . . . . .	137
8.3.2	Muscle data . . . . .	137
8.3.3	FE model . . . . .	138
8.4	Supplementary data . . . . .	139

---

<b>9</b>	<b>General conclusions</b>	<b>151</b>
<b>A</b>	<b>Stereoscopy</b>	<b>153</b>
A.1	Theory . . . . .	154
A.2	Matlab code . . . . .	156
<b>B</b>	<b>Mechanical stress in Darwin's ground finches</b>	<b>161</b>
B.1	Introduction . . . . .	162
B.2	Material and methods . . . . .	162
B.2.1	Finite element modeling . . . . .	162
B.3	Results . . . . .	166
B.4	Discussion . . . . .	168
<b>C</b>	<b>Bull finch</b>	<b>171</b>
	<b>Bibliography</b>	<b>173</b>
	<b>Nomenclature</b>	<b>185</b>
	<b>Samenvatting</b>	<b>187</b>
	<b>Curriculum Vitae</b>	<b>189</b>
	<b>List of publications</b>	<b>191</b>
	<b>Acknowledgements - Dankwoord</b>	<b>195</b>

# **Part I**

## **Introduction**



### 1.1 Bird beaks

A great diversity is found in the size and shapes of vertebrate skulls. It is thought that this diversity can be linked to their diverse functioning, especially due to different feeding strategies. This variety can be clearly observed in birds. Different beak shapes can be linked to the birds respective diet and beak use (figure 1.1). Most birds can fly and as such they need, in contrast with most mammals (except bats), a lightweight skeleton, skull and beak [39]. A good example for this property is the beak of toucans (figure 1.1, fruit eating). It is almost  $1/3$  of the bird's total length, but it only weights  $1/20$  of its total mass, giving this animal a great tool for food gathering, but still enables it to fly. This remarkable light, but strong structure is built up from a sandwich structure of bone and keratin. Such lightweight sandwich is also used in many engineering applications, for instance the wings of aircrafts. Sections of the toucan beak were successfully measured and modeled by Seki and co-authors [110, 111, 112].

Another example of a remarkable adapted beak is found in the hummingbird (figure 1.1, nectar eating). Besides nectar, hummingbirds also need to eat insects because floral nectars are deficient in essential amino acids. Their long, nectar eating beak has an intramandibular flexion to catch insects in the air [143]. A third example is the woodpecker (figure 1.1, chiseling) [140]: special adaptations in macro and micro morphology enable them to withstand deceleration of  $1000g$ . The functioning of its skull during chiseling can be an instructive example to prevent head injury in humans. A last example is the beak of the extinct terror bird. This gigantic predator lived in South America from 62 until 2 millions years ago. Degrange et al. [32] used FE modeling to show that, compared to the eagle (figure 1.1, raptorial), relative high stresses occurs during lateral loading of the beak. They conclude that it was probably to risky for this terror bird to catch large, struggling preys and they suggested that their beak is

probably more adapted to eat smaller preys that could be killed and consumed more safely.

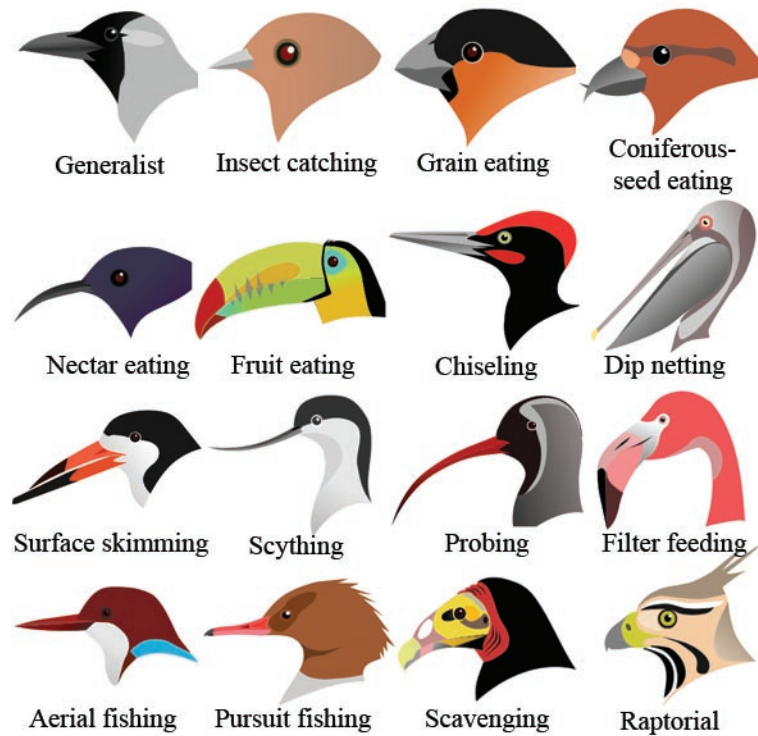


**Figure 1.1:** Schematic representation of the large variety of bird beaks, depending on their respective diet (adapted from <http://en.wikipedia.org/wiki/Beak>).

The briefly discussed examples show a great diversity in beak shape and suggest that these beaks are adapted to their different functioning (feeding, social behavior, etc). Such a variety is also observed for the beak of Darwin's finches, a closely related group of finches. In this dissertation, I will show how the beaks of these Darwin's finches are well adapted to their respective diet. In section 1.2, some more introduction about these renowned finch species is given.

Since Darwin's finches are highly protected, and some are even critical threatened according IUCN standard, a more common model finch for more invasive work, such as mechanical testing is needed. Therefore the Java finch (*Padda oryzivora*), another granivorous bird, is chosen (figure 1.2). Although this finch is not closely related to Darwin's finches, its appearance is more or less the same, suggesting that the same natural challenges converged to the same biological solution [52]. In this thesis, the mechanical behavior of this granivorous beak will be studied. The results of such a study are not only interesting from a biological point of view, but also from a mechanical one. Indeed, the beak of granivorous birds seems to rely on a highly optimized

design: it needs to deal with large forces<sup>1</sup>, but over-engineering will not only impede flying but also increase the beak its moment of inertia, resulting in a longer husking time and a worse song capacity [134]. Van der Meij and Bout [134] also show how bite force is acting on the seed (figure 1.3).

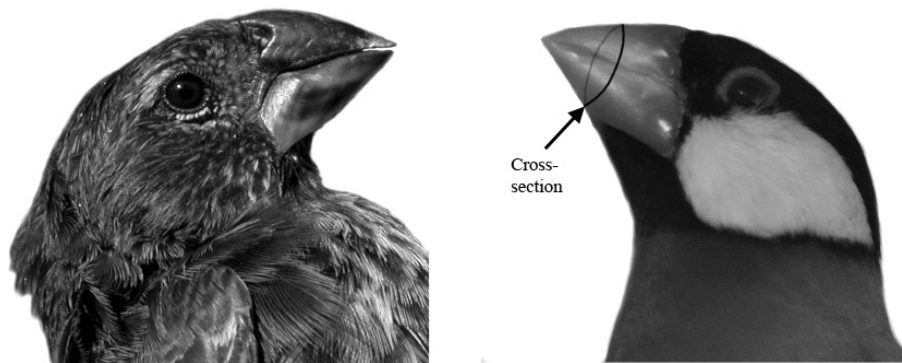


**Figure 1.2:** *G. Fortis* (left) and its model finch used in this dissertation, the Java finch (right). Cross-sectional area for figure 1.3 and 1.4 is indicated.

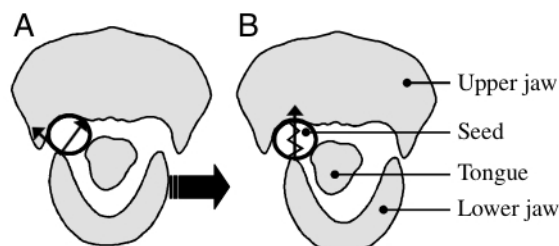


**Figure 1.3:** Schematic representation of a Java finch upper and lower beak cross-section. (A) Resting position (B) Perpendicular bite force is obtained by moving the lower jaw (according large arrow in A) (figure from Van der Meij and Bout [134]).

A histological section of the upper beak is shown in figure 1.4. The upper beak includes a bony core covered with the dermis and epidermis, known as the rhamphotheca or keratin layer. Those different layers are connected to each other with collagen fibers. Bone and keratin have, as many biological materials, outstanding properties which make them interesting materials to study and to (bio-)mimic. Typical for biological materials is the hierarchical build-up. Nano building blocks (basic polymer and minerals) with quite poor mechanical properties, are organized in meso and macro structures, resulting in composite materials with good characteristics. Due

<sup>1</sup>e.g. An eagle weighs approximately 100 times more than *G. magnirostris* (30g), but both have a bite force of 50N [32].

to this hierarchical build-up, inhomogeneity is expected and it is important to use general bulk properties for macroscopic modeling. The most astonishing properties of biological materials are their multi-functionality and self-healing capability. These properties are due to the self-organization character of the constituent molecules [92].

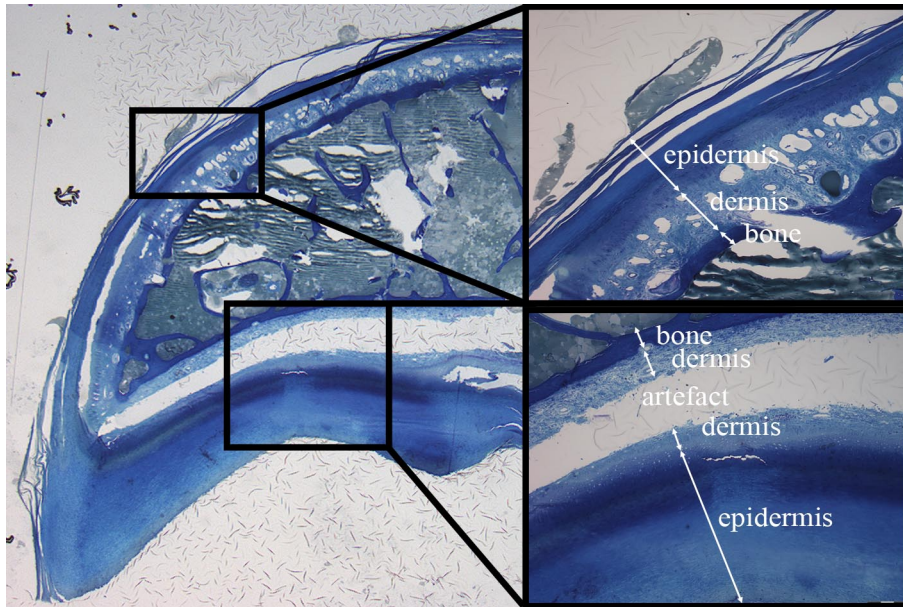


**Figure 1.4:** Histological section of Java finch upper beak (pers. obs. Annelies Genbrugge).

Bone is a ceramic-polymer composite. Two types of bone arrangements are distinguished, cortical (compact) bone and cancellous (trabecular) bone. Bone is inhomogeneous and anisotropic. Consequently, it is stronger for certain loading conditions without a huge increase of density. Nevertheless, homogeneous and isotropic material description [27] (chapter 2) is often successfully used in modeling.

A layer of living cells surrounds the bony core of the beak (figure 1.4). The outer-cells keratinize towards the outer side of the beak, where epidermal cells die and build up a hard, cornified, dead keratin layer at the out surface of the beak [135]. Keratin is a biological fiber-reinforced composite. The fibers with high elasticity modulus make the keratin strong during loading while the matrix prevent crack propagation [47]. Keratin is known to be very tough. As a consequence, it can be found as an external layer in most vertebrates (e.g. skin, hair and nails are built from keratin). Keratin's mechanical properties are known to be highly dependent on its humidity [77].

For both keratin and bone, a wide range of possible mechanical properties are found in literature: bone moduli range from 100 MPa to 35 GPa and its ultimate strength from 0.5 MPa to 250 MPa [27, 49, 92], while keratin moduli range from 0.23 GPa to 3.7 GPa and ultimate strengths from 14 MPa to 221MPa [92, 126]. Consequently, it is important to obtain the actual material parameters on the sample itself.

It is clear that bird beaks are a complex mechanical system. They are, however, an

interesting object to study. Modeling is a very useful tool to investigate such complex systems, but they should be interpreted with care. In this thesis, FE models of the beak will be created, but also dedicated mechanical and optical setups to test them, will be introduced.

## 1.2 Darwin's finches

Darwin's finches live in the Galápagos archipelago. They were first collected by Charles Darwin during the second voyage of HMS Beagle in 1835. They have been the subjects of intense research and nowadays they are considered as a text book example in evolutionary theory, more specific for speciation and adaptive radiation under natural selection. Indeed, this closely related group of birds has been radiated from a shared ancestor over a few millions years into 14 descendent species, each specializing on distinct food resources (figure 1.5 and 1.6) and evolving different shape, size and use of their beak (figure 1.7, 1.8). The ground finches (e.g. *G. magnirostris*) explore the soil for hard seeds, while cactus finches (e.g. *G. scandens*) penetrate cactus flowers and fruits with their pointed beak. The most curious diet is that of the the sharp-beaked ground finch (*G. difficilis*), also known as the vampire finch, who pecks on other birds to drink their blood.

This great variation in beak shape was already noted by Charles Darwin [51]:

*"I have stated that in the thirteen species of ground-finches, a nearly perfect gradation may be traced, from a beak extraordinarily thick, to one so fine, that it may be compared to that of a warbler."*

CHARLES DARWIN

These birds were to play an important part in the inception of Darwin's theory of evolution by natural selection:

*"Seeing this gradation and diversity of structure in one small, intimately related group of birds, one might fancy that, from an original paucity of birds in this archipelago, one species has been taken and modified for different ends."*

CHARLES DARWIN

Many species are being studied, but few have as much historical, symbolic and scientific importance to the evolutionary theory as these finches. They seem to be ideal as example. They all look very similar in plumage and song and live in the same geographical location, where human interference was absent for a long time. A species can for instance become geographically isolated on a different island, has to specialize to a different ecology by adapting their beak size and shape through natural selection and diverges in another species. This natural selection is even amplified by extremely wet (El Niño) and dry seasons on the Galápagos Islands, leaving for instance only harder seeds. Birds with beaks that could handle these seeds have an advantage and



**Figure 1.5:** Some Darwin's finches in natural habitat. Notice the large variety in beak shape and use. First row: Large Ground Finch (*G. magnirostris*), Medium Ground Finch (*G. fortis*), Small Ground Finch (*G. fuliginosa*), Second Row: Vegetarian Finch (*P. crassirostris*), Small Cactus Finch (*G. scandens*), Small Tree Finch (*C. parvulus*), Third Row: Large Tree Finch (*C. psittacula*), Woodpecker Finch (*C. pallida*), Warbler Finch (*C. olivacea*) (Pictures from Anthony Herrel).

can pass their genes [58]. On the other hand, two closely related species can come back together on the same island, but be kept apart due to the nature of the reproductive barrier. It has been shown that the beak shape and size is also important for this sexual selection [57, 70]. As such, these Galapagos finches, and especially their beaks, give us more insight in evolution and questions such as: 'how and why stay species apart?', 'why do species differ?', 'why are there so many species?', etc.

Anyhow, as already stated above, divergent beak sizes and shapes evolved in the Darwin's finches and reflect differences in their respective diet [15, 45, 56, 81]. As such, the beak morphology of all 14 Darwin's finches can be subdivided in four groups. These groups are presented in figure 1.8 [58]: base crushing, probing and crushing, probing and tip biting beaks. Variation in beak shape in the ground finches is situated mainly along two axes: variation in width and depth which covary, and variation in length [15]. Species that crush hard seeds at the base of their beaks, such as *G. fortis* and *G. magnirostris*, tend to have relatively short but wide and deep beaks (Grant 1999). Other species, such as *G. scandens* and *G. difficilis*, tend to have longer yet narrower and shallower beaks, a design that has been suggested to be a compromise between base crushing and probing [15]. Interestingly, the two principal axes of variation observed within the ground finches are also reflected in distinct developmental pathways [2, 1, 23].

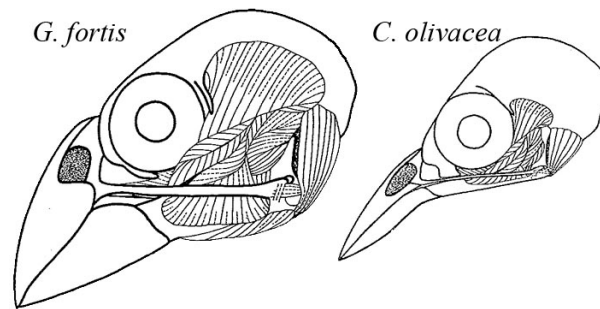


**Figure 1.6:** Schematical representation of *G. fortis* and *C. olivacea* by Bowman (1961) [15].

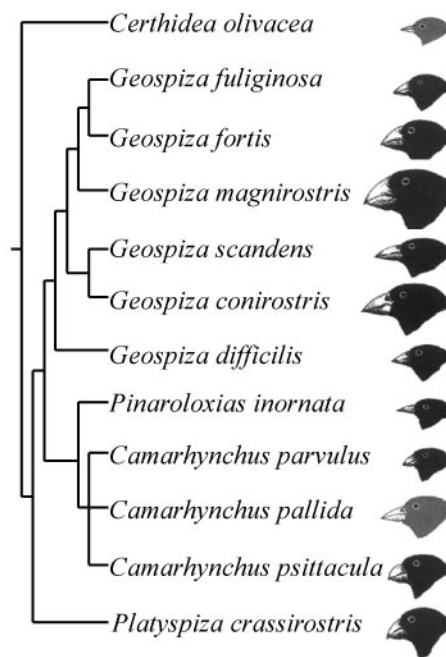


**Figure 1.7:** Phylogenetic relationships of the Darwin's finches [23].

Despite of the importance of beak morphology in Darwin's finches natural selection, up till now no mechanics based evidence was given. It is expected that beak size and shape is strongly correlated to the size and hardness of seeds that can be cracked [15]. This beak shape and size variation is externally clearly visible. Nevertheless, muscle force is more directly correlated to the maximal bite force [63, 64]. The beak can be seen as an instrument, transmitting the muscle forces to the seed. Therefore, the beak has to be strong enough to avoid fracture. Indeed, more than 50 years ago, Bowman [15] suggested that the shape of the beak was adapted to fracture avoidance, with beaks with more or less straightened culmen or gonys (upper and lower beak, respectively) tending to reduce fracture risk. Modifications towards increased beak depth, on the other hand, were interpreted as adaptations towards more powerful crushing bites [15]. The main goal of this dissertation, more than 150 years after the

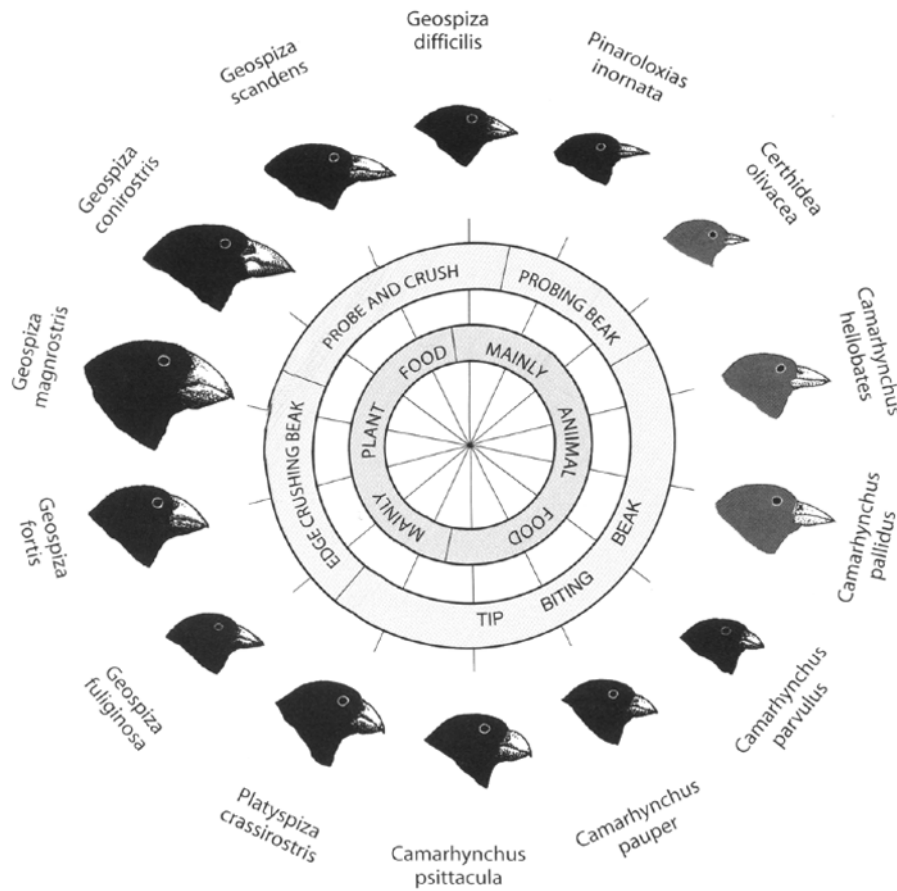


**Figure 1.8:** Schematic representation of the Darwin's finches to emphasize their feeding habits and beak shape (Annelies Genbrugge, adapted from Grant and Grant (2008) [58]).

publication of Darwin's '*on the origin of species*', is to test this important fracture avoidance hypothesis and to provide mechanical evidence. Therefore, some state-of-the-art mechanical tools will be used and developed.

---

### Introduction 2: Mechanics and finite element modeling

---

#### **Abstract**

*This chapter gives an introduction to the mechanics used in this dissertation. First a one-dimensional bar example shows some principles in the mechanics of deformable bodies. Next, these principles are extended to three-dimensional infinitesimal kinematics. A basic knowledge of vector and tensor algebra is supposed. Infinitesimal kinematics, however, do not allow finite rotations and do not include geometrical nonlinearities. Consequently, more rigorous definitions are introduced. Afterwards, material description is included and finite element modeling is introduced. Some practical issues arise when building a finite element model starting from a biological geometry. The beaks of birds, for instance, have a multi-layered design. The challenges regarding the modeling of these complex structures are discussed in a practical guideline.*

This chapter is based on:

Soons Joris and Dirckx Joris. Multi-Parts Geometry-Based Finite Element Modeling in Biomechanics: Elastic Modulus Determination of Bone and Keratin in the Java Finch's Beak by Double Indentation Technique and Inverse Analysis. In *Horizons in World Physics*, Volume 278 and in *Advances in Mathematics Research*, Volume 17, Nova Science Publishers, Inc., 2011

and on standard textbooks [11, 67, 88, 104, 119, 148]

## 2.1 One-dimensional example

This section can be seen as a short introduction to the basic principles of continuum mechanics. Therefore, a one-dimensional example is shown in figure 2.1. A rod with length  $L$  and cross area  $A$  is stretched to a final length  $l$  with a final area  $a$ . We can define the engineering strain as:

$$\epsilon_E = \frac{l - L}{L} \quad (2.1)$$

It is clear that other definitions are possible. One can take  $l$  instead of  $L$  as denominator, yielding the same strains for infinitesimal small deformations. More generalized definitions for strain, which will be significant different for large deformations, are the Green strain  $\epsilon_G$  and the Almansi strain  $\epsilon_A$ :

$$\epsilon_G = \frac{l^2 - L^2}{2L^2} \quad (2.2)$$

$$\epsilon_A = \frac{l^2 - L^2}{2l^2} \quad (2.3)$$

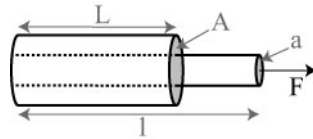


Figure 2.1: One-dimensional example.

The Cauchy stress is defined as the force ( $F$ ) acting on the cross-sectional area ( $a$ ), yielding the next equation for the one-dimensional problem:

$$\sigma = \frac{F}{a} \quad (2.4)$$

One can also define the engineering stress by dividing the force ( $F$ ) by the initial surface ( $A$ ).

For small displacements, one can define the next constitutive equation for this one-dimensional case (Hooke's Law), linking the stress  $\sigma$  and strain  $\epsilon$  with a constant elastic (Young's) modulus  $E$ :

$$\sigma = E\epsilon \quad (2.5)$$

When a material is extended in one direction, it usually tends to contract in the other two directions perpendicular to the direction of extension (as can be seen in figure 2.1). This phenomenon is called the Poisson effect. The Poisson's ratio ( $\nu$ ) is a measure of the Poisson effect and is defined as the ratio of the transversal contraction (as a fraction) divided by the longitudinal extension (as a fraction). The Poisson's ratio of incompressible materials is 0.5, while this ratio becomes 0 if there is no resulting transversal contraction.

The one-dimensional bar model from figure 2.1 is often used for material characterization and tests, such as tensile or compression testing (section 3.2.4). Although eq. 2.5 suggests a linear behavior, it should be noticed that real materials can have a non-linear behavior, especially when the deformations are finite. In addition, identical materials can have a different modulus under various test conditions: one can for instance obtain a different modulus for compression or tensile test. A typical stress-strain curve is shown in figure 2.2. In such curves one often uses the engineering stress instead of the Cauchy stress. The lowest stress at which permanent deformation can be measured is called the yield strength. Beyond this yield point, no linear behavior is found and permanent deformation will occur. The dotted line indicates this permanent plastic deformation. The ultimate strength is the highest possible strength in the material. At the end of the curve, fracture occurs. Toughness is defined as the total energy absorbed per unit volume:

$$Toughness = \int_0^{\epsilon_{fracture}} \sigma d\epsilon \quad (2.6)$$

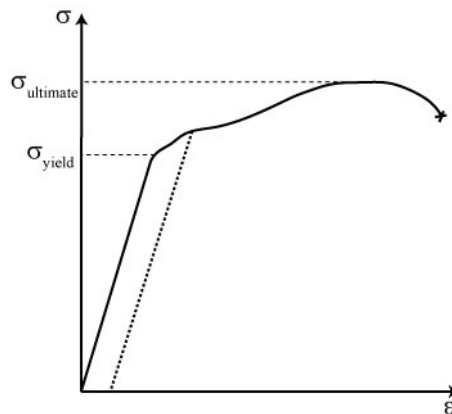


**Figure 2.2:** Typical Stress( $\sigma$ )-Strain( $\epsilon$ ) curve. The dashed lines indicate the yield and ultimate strength, while the end of the curve indicates fracture. The dotted line shows the plastic deformation after yielding.

In real samples, however, the stress and strain descriptions have to be three-dimensional. The next section deals with infinitesimal kinematics (i.e. strains).

## 2.2 Infinitesimal kinematics

Kinematics in mechanics describe the material deformation without reference to the cause. Strains are introduced when the relative displacements between points in the body are changed. In contrast, the distance between points remains the same for

rigid body movements. An example of a deformation is shown in figure 2.3. One can calculate the difference  $\Delta \mathbf{r} = \mathbf{r}' - \mathbf{r}$  as follows:

$$\Delta \mathbf{r} = \mathbf{r}' - \mathbf{r} = \mathbf{r} + \mathbf{u}(\mathbf{X}+\mathbf{r}) - \mathbf{u}(\mathbf{X}) - \mathbf{r} \quad (2.7)$$

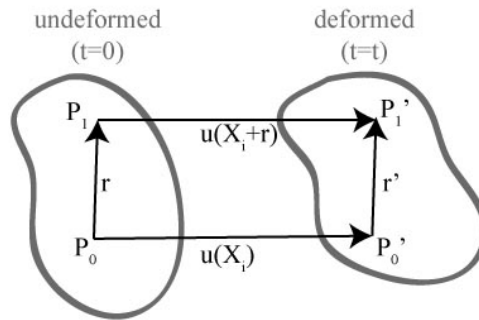


**Figure 2.3:** Undeformed ( $t = 0$ ) and deformed ( $t$ ) state of a body.

If  $P_0$  is close to  $P_1$ , Taylor expansion can be used:

$$u_i(\mathbf{X}+\mathbf{r}) = u_i(\mathbf{X}) + \sum \frac{\partial u_i}{\partial X_j} r_j \quad (2.8)$$

As such one can find:

$$\Delta r_i = \frac{\partial u_i}{\partial X_j} r_j \quad (2.9)$$

A symmetric ( $e_{ij}$ ) and anti-symmetric ( $w_{ij}$ ) tensor can be built as follows:

$$\frac{\partial u_i}{\partial X_j} = e_{ij} + w_{ij} \quad (2.10)$$

$$e_{ij} = \frac{1}{2} \left( \frac{\partial u_i}{\partial X_j} + \frac{\partial u_j}{\partial X_i} \right) \quad (2.11)$$

$$w_{ij} = \frac{1}{2} \left( \frac{\partial u_i}{\partial X_j} - \frac{\partial u_j}{\partial X_i} \right) \quad (2.12)$$

where  $e_{ij}$  is called the strain tensor and  $w_{ij}$  the rotation tensor. The strain tensor  $e_{ij}$  will be independent of (small) rotations. Due to the symmetry of this tensor, one can

define the following strain variables ( $\varepsilon$  are normal strains and  $\gamma$  are shearing strains):

$$\varepsilon_x = \frac{\partial u}{\partial X} \quad (2.13)$$

$$\varepsilon_y = \frac{\partial v}{\partial Y} \quad (2.14)$$

$$\varepsilon_z = \frac{\partial w}{\partial Z} \quad (2.15)$$

$$\gamma_{xy} = \gamma_{yx} = 2 \cdot \varepsilon_{xy} = \frac{\partial u}{\partial Y} + \frac{\partial v}{\partial X} \quad (2.16)$$

$$\gamma_{yz} = \gamma_{zy} = 2 \cdot \varepsilon_{yz} = \frac{\partial v}{\partial Z} + \frac{\partial w}{\partial Y} \quad (2.17)$$

$$\gamma_{xz} = \gamma_{zx} = 2 \cdot \varepsilon_{xz} = \frac{\partial u}{\partial Z} + \frac{\partial w}{\partial X} \quad (2.18)$$

Principal strains can be obtained by calculating the eigenvalues and vectors (principal coordinate system) of  $\varepsilon_{ij}$ . The deformation of a beam orientated along the principal axes will not produce shearing and will preserve the orthogonal shape.

## 2.3 Kinematics

The strain is introduced to describe the deformation of a body, e.g. how the distance between points change. The definitions of equations 2.13-2.18 depend on the assumption of small displacements ( $u_i$ ). If one takes for instance a rotation of  $90^\circ$ , one finds for  $u_x = -X - Y$  and  $u_y = X - Y$  (X and Y are original coordinates):

$$\varepsilon_x = \varepsilon_y = -1 \quad (2.19)$$

$$\varepsilon_{xy} = 0 \quad (2.20)$$

These strains are clearly wrong because no strain is expected for a rigid body movement. Therefore, a more rigorous definition is needed without assumptions for the displacements.

Relevant quantities, such as density ( $\rho$ ), can be described in terms of where the body:

- was before deformation: material or Lagrangian description (X-coordinates for particles in initial state time=0, resulting in  $\rho(X, t)$ ),
- is during deformation: spatial or Eulerian description (x-coordinate for the particles in the deformed state time=t, resulting in  $\rho(x, t)$ )).

Where fluid mechanics mostly work with spatial description, in solid mechanics one chooses for a material description. Indeed, it is more convenient to describe material parameters, such as density, as a function of its original position. A schematical picture of a body under deformation is shown in figure 2.4.

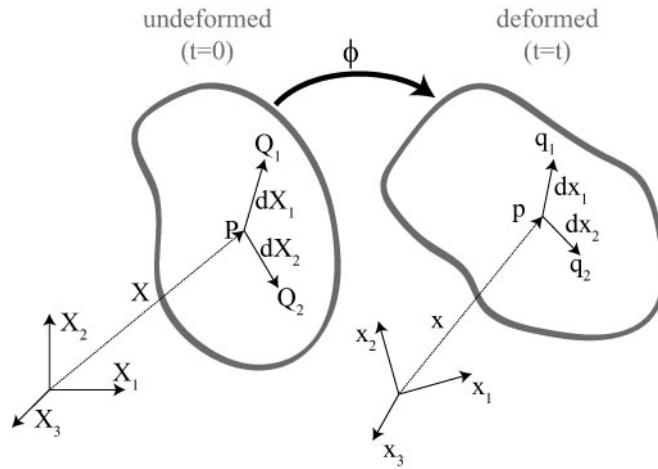


**Figure 2.4:** Undeformed ( $t = 0$ ) and deformed ( $t$ ) state of a body.

Consider two material particles  $Q_1$  and  $Q_2$ , close to  $P$ . The positions of  $Q_i$  relative to  $P$  are given as (figure 2.4):

$$d\mathbf{X}_1 = \mathbf{X}_{Q_1} - \mathbf{X}_P, \quad d\mathbf{X}_2 = \mathbf{X}_{Q_2} - \mathbf{X}_P \quad (2.21)$$

After deformation, at time  $t$ , the material particles have spatial positions:

$$d\mathbf{x}_p = \phi(\mathbf{X}_P, t), \quad d\mathbf{x}_{q_1} = \phi(\mathbf{X}_{Q_1}, t), \quad d\mathbf{x}_{q_2} = \phi(\mathbf{X}_{Q_2}, t) \quad (2.22)$$

with their relative position to  $p$ :

$$d\mathbf{x}_1 = \mathbf{x}_{q_1} - \mathbf{x}_p = \phi(\mathbf{X}_P + d\mathbf{X}_1, t) - \phi(\mathbf{X}_P, t) \quad (2.23)$$

As such one can define the deformation gradient  $F$  as:

$$d\mathbf{x}_1 = F d\mathbf{X}_1 \quad (2.24)$$

with:

$$F_{iI} = \frac{\partial \phi_i}{\partial X_I} \quad (2.25)$$

Similarly, one can obtain  $d\mathbf{X}_1 = F^{-1} d\mathbf{x}_1$ .

From equation 2.24, one can obtain the next equation:

$$\frac{1}{2} (d\mathbf{x}_1 \cdot d\mathbf{x}_2 - d\mathbf{X}_1 \cdot d\mathbf{X}_2) = d\mathbf{X}_1 E d\mathbf{X}_2 \quad (2.26)$$

with  $E$  the Lagrangian or Green tensor:

$$E = \frac{1}{2} (C - I) \quad (2.27)$$

where  $I$  is the identity matrix and  $C$  the right Cauchy-Green deformation tensor:

$$C = F^T F \quad (2.28)$$

One can also work the other way around to obtain the Eulerian or Almansi strain tensor  $e$ . For small displacements, the components of both strain tensors are identical, resulting in the infinitesimal strain tensor (eq. 2.13 - 2.18).

The physical interpretation becomes clear by taking  $d\mathbf{X}_1 = d\mathbf{X}_2 = d\mathbf{X}$  and consequently  $dx_1 = dx_2 = dx$ . As such we can define an initial (material) length  $dS$  as  $dS^2 = d\mathbf{X} \cdot d\mathbf{X}$  and the resulting (spatial) length  $ds$  as  $ds^2 = dx \cdot dx$ . The next equation is obtained (from eq. 2.26):

$$\frac{1}{2} \frac{ds^2 - dS^2}{2dS^2} = \frac{d\mathbf{X}}{dS} E \frac{d\mathbf{X}}{dS} \quad (2.29)$$

Since  $\frac{d\mathbf{X}}{dS}$  is a unit vector to give the direction, one can see the scalar Green's strain (see equation 2.2 for one dimensional example).

The concept of objectivity (frame invariance) in solid mechanics means that qualitative and quantitative descriptions of physical phenomena remain unchanged when the phenomena are observed under a variety of conditions. Their spatial description may change, but their intrinsic nature remains unchanged. The concept can be explored by studying the effect of a rigid body motion superimposed on the deformed configuration ( $\phi^* = Q\phi$ ), resulting in the next deformation gradient:

$$F^* = \frac{\partial \phi^*}{\partial X} = \frac{\partial \phi^*}{\partial \phi} \frac{\partial \phi}{\partial X} = QF \quad (2.30)$$

As a result, we obtain  $E = QE$  (eq. 2.27) and show that the strain is indeed objective.

## 2.4 Stress

External forces applied on a deformable body will result in internal forces and the deformation of the body's shape. The stress is a measure for this internal force (per unit area). In one dimension the description is easy (eq. 2.4). In three dimensions, the Cauchy stress tensor at every point can be described by a symmetric tensor (as described below).

A cross-section through a deformable body is shown in figure 2.5. In a point  $P$ , a traction vector  $\mathbf{t}$  (=force/area) is applied on an infinitesimal surface ( $da$ ) with normal  $\mathbf{n}$ . The force component perpendicular on the surface is the normal force, the component parallel to the surface is the shear force. For every infinitesimal surface in  $P$ , with a different normal  $\mathbf{n}$ , a different traction vector  $\mathbf{t}(\mathbf{n})$  is found. Applying translational equilibrium on an elemental tetrahedron (figure 2.6) results in the following equation, with  $\mathbf{e}_i$  Cartesian directions and an external force  $\mathbf{f}$  working on volume  $dV$ :

$$\mathbf{t}(\mathbf{n})da + \sum t(-\mathbf{e}_i)dA_i + \mathbf{f}dV = 0 \quad (2.31)$$

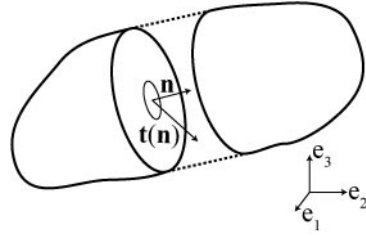


Figure 2.5: Surface with normal  $\mathbf{t}(\mathbf{n})$  and traction vector  $\mathbf{n}$ .

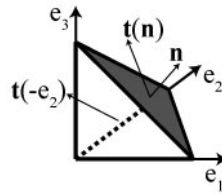


Figure 2.6: Elemental tetrahedron.

Dividing this equation by  $da$ , using Newton's third law ( $t(-\mathbf{e}_i) = -t(\mathbf{e}_i)$ ), using the limit  $dv/da \rightarrow 0$  and the equation  $da_i/da = \mathbf{n} \cdot \mathbf{e}_i$  results in:

$$\mathbf{t}(\mathbf{n}) = \sum t(\mathbf{e}_i)(\mathbf{n} \cdot \mathbf{e}_i) \quad (2.32)$$

The Cauchy stress tensor is now defined as the traction vector associated with the three Cartesian directions:

$$t(\mathbf{e}_j) = \sum \sigma_{ij} \mathbf{e}_i \quad (2.33)$$

As a result, the traction vector on a plane bisecting the body can be calculated. The translational equilibrium yields the spatial equilibrium equation for a deformable body (with  $\sigma$  Cauchy stress and  $\mathbf{f}$  force per unit volume):

$$\nabla_j \cdot \sigma_{ij} + f_i = 0 \quad (2.34)$$

By considering both translational and rotational equilibrium, one can prove the symmetry of the Cauchy stress tensor [11]:

$$\sigma_{ij} = \sigma_{ji} \quad (2.35)$$

One can find three planes ( $da$ ) where  $\mathbf{t}(\mathbf{n})$  is parallel with  $\mathbf{n}$ . As a result, there are no shear stresses in those planes. The three normal stresses are called principal stresses ( $\sigma_1, \sigma_2, \sigma_3$ ) and can be calculated by an Eigen analysis of  $\sigma_{ij}$ .

In practice, these stresses have often to be compared with the yield strength of the material to find when permanent shape changes or structural failure occur. Difficulties on interpretation of the complex three-dimensional stress state, can be overcome by using the von Mises (VM) yield criterium [76]. The criterion suggests that yielding

occurs when the ‘combined stress’ ( $\sigma_{vm}$ ) is larger than the yield strength ( $\sigma_{yield}$ ) of the material:

$$\sigma_{vm} = \sqrt{\frac{(\sigma_1 - \sigma_2)^2 + (\sigma_2 - \sigma_3)^2 + (\sigma_3 - \sigma_1)^2}{2}} > \sigma_{yield} \quad (2.36)$$

The Cauchy tensor is a spatial tensor. It would be convenient to have a stress tensor in material description. Therefore one can define the second Piola-Kirchhoff (2nd PK) stress tensor [11]:

$$S = JF^{-1}\sigma F^{-T} \quad (2.37)$$

With  $J = \det(F)$ .

## 2.5 Constitutive equation

Constitutive equations define the relationship between stresses and strains. The 1D Hooke’s law from eq. 2.5 can be extended to three dimensions. As a result, a fourth-order elasticity tensor  $\zeta$  is introduced:

$$\sigma_{ij} = \zeta_{ijkl}\epsilon_{kl} \quad (2.38)$$

This equation is only valid for infinitesimal displacements. For isotropic materials,  $\zeta$  can be simplified:

$$\zeta_{ijkl} = \lambda\delta_{ij}\delta_{kl} + 2\mu\delta_{ik}\delta_{jl} \quad (2.39)$$

With  $\lambda$ , the first Lamé parameter and  $\mu$  the second Lamé parameter or shear modulus. These mathematical parameters can be written as a function of the Young’s modulus ( $E$ ) and the Poisson’s ratio ( $\nu$ ):

$$\lambda = \frac{E\nu}{(1+\nu)(1-2\nu)} \quad (2.40)$$

$$\mu = \frac{E}{2(1+\nu)} \quad (2.41)$$

The Young’s modulus is a measure of stiffness (see also modulus in 1D problem, section 2.1), while the Poisson’s ratio indicates the resulting transversal strain for an axial strain (as described in section 2.1).

A second order differential equation is obtained by using Newton’s second law

$$\nabla_j \cdot \sigma_{ij} + f_i = \rho \frac{\partial^2 u_i}{\partial t^2} \quad (2.42)$$

and by using equation 2.38 and the definition of  $\epsilon_{kl}$  (equation 2.11). This differential equation and linear elasticity is only valid for infinitesimal displacement.

If the deformation is only dependent on the initial and the final state, the material is called hyper-elastic. Due the path-independency of hyper-elastic materials, a strain

energy function (elastic potential)  $\Psi$  can be defined as the work done by the stress from the initial to the final state. The next equation can be derived and is equivalent to the classic definition of work [11]:

$$S(F(X), X) = \frac{\partial \Psi(F(X), X)}{\partial E} \quad (2.43)$$

where  $S$  is the 2nd PK stress tensor and  $E$  is the green strain tensor. The fourth-order material elasticity tensor is defined as:

$$\zeta = \frac{\partial S}{\partial E} \quad (2.44)$$

A simple hyper-elastic material model is the Saint Venant-Kirchhoff model, which is an extension of the linear elastic model to the non-linear regime. Large rotations in this hyper-elastic material will not result in strains and stresses.

$$\Psi(E_{ij}) = \frac{\lambda}{2}(E_{ij}\delta_{ij})^2 + \mu(E_{ij})^2 \quad (2.45)$$

Notice that this equation results in eq. 2.39 for small displacements when using eq. 2.44.

## 2.6 Finite element modeling

The finite element method is a numerical technique that becomes very useful when exact analytical solutions of a problem cannot be found. The finite element method may be summarized as follows [11] . “It is a procedure whereby the continuum behavior described at an infinity of points is approximated in terms of a finite number of points, called nodes, located at specific points in the continuum. These nodes are used to define regions, called finite elements, over which both the geometry and the primary variables in the governing equations are approximated. For example, in the stress analysis of a solid the finite element could be a tetrahedra defined by four nodes and the primary variables the three displacements in the Cartesian directions. The governing equations describing the nonlinear behavior of the solid (equation 2.42) are usually recast in a so-called weak integral form using, in the case of mechanics, the principle of virtual work. The finite element approximations are then introduced into these integral equations, and a standard textbook manipulation yields a finite set of non-linear algebraic equations in the primary variable. These equations are then usually solved using the Newton-Raphson iterative technique.”

It is difficult to explain the basics of the finite element method in only a few pages. In this thesis, finite element modeling was used as a tool. Nevertheless, a basic knowledge is needed. Therefore some basic concepts and equations are sketched.

In the case of a stationary study, inertial effects are neglected and the static equilibrium is sought. The equilibrium equation is based on the principle of virtual work.

Therefore, we need the weak formulation of the equilibrium equation 2.34.

Consider a closed subdomain with volume  $V$  and surface  $S$  within a body in equilibrium. The region has a general distribution of surface tractions  $t$  and body forces  $f$ . For static equilibrium, the forces acting on the surface are balanced by the body forces:

$$\int_S t_i dS + \int_V f_i dV = 0 \quad (2.46)$$

The virtual displacement ( $\delta u_i$ ) of a material point is now defined as a fictitious displacement such that the forces acting on the point remain unchanged. The work done by these forces during the virtual displacement is called the virtual work:

$$\delta W = \int_S t_i \delta u_i dS + \int_V f_i \delta u_i dV \quad (2.47)$$

Following standard procedures, this surface integral can be changed to a volume integral and combined with the body force term [104]:

$$\delta W = \int_V \sigma_{ij} \delta \epsilon_{ij} dV \quad (2.48)$$

with  $\delta \epsilon_{ij}$  the virtual strains corresponding the virtual displacements<sup>1</sup>. As a function of a strain energy function  $\Psi$  (e.g. equation 2.45). The stresses can be expressed in terms of the strains (analogous to equation 2.43). As a result, equation 2.48 can be written as  $\delta \int_V \Psi dV$  so that:

$$\delta \left( \int_V \Psi dV - \int_S t_i u_i dS - \int_V f_i u_i dV \right) = \delta(\Psi - W) = 0 \quad (2.49)$$

$(\Psi - W)$  represents the potential energy of the volume. The previous equation states that the change of the potential energy during a virtual displacement from a equilibrium is zero.

In order to obtain a numerical solution, a discretization is necessary. Therefore, the geometry and displacement are interpolated with elements; this process is called meshing. The principal of virtual work over one element can be stated as:

$$\int_V \sigma_{ij} \delta \epsilon_{ij} dV = \int_S t_i \delta u_i dS + \int_V f_i \delta u_i dV \quad (2.50)$$

The strain components  $\epsilon_{ij}$  can be written as displacements  $u_i$ . In order to obtain a numerical solution, a discretization is necessary. The basic idea is to approximate the continuous (unknown) variable  $\mathbf{u}$  by a linear combination of  $n$  shape functions  $N$ :

$$\mathbf{u} = \sum_{a=1}^n \mathbf{b}_a N_a(x_1, x_2, x_3) \quad (2.51)$$

---

<sup>1</sup>as an example, the equation are given in terms of the stress and strains for simple linear elasticity

With  $N_a$  a set of basis functions and  $\mathbf{b}_a$  a set of unknown parameters. The number  $n$  depends on the number of nodes in an element and on the type of the element. For example, for a linear element interpolation in a tetrahedral element,  $n$  equals 4 (4 linear basis functions which yield 1 in a vertex and 0 in the three other vertices). It should be noticed that such a linear interpolation for the displacements will result in a constant strain and stress description in an element.

Substituting the approximation of equation 2.51 into equation 2.50 results in a discrete formulation of equilibrium in one element. The overall problem is then modeled by assembling the entire set of elements through a process of invoking equilibrium at each node in the mesh, which is sometimes referred to as system connectivity. This procedure creates a global assembled matrix system equation of the form:

$$K \cdot \mathbf{u} = \mathbf{f} \quad (2.52)$$

with  $K$  the stiffness matrix that is assembled from the known geometry and material properties of each element,  $\mathbf{f}$  the force vector that is assembled from the known applied forces and geometry and  $\mathbf{u}$  the unknown vector of nodal displacements. This equation is in general highly non-linear ( $K$  depends on the displacements), and must be iteratively solved with e.g. the Newton-Raphson method.

The finite element calculations in this thesis were performed in the FEBio software package [88]. FEBio is an open-source, non-linear finite element solver, specially designed for biomechanical applications. In this way, importing a geometry and applying boundary conditions are more convenient.

## 2.7 Practical guideline

When building a mechanical finite element (FE) model, one needs to run through five necessary steps: building up a geometry with FE elements, assigning material properties, applying boundary conditions, conducting a convergence study and a validation test. These steps are quite straightforward in standard FE-packages where a computer-aided design (CAD) is used as starting point. In my research, however, I had to start from a biological object which is obviously not described in CAD drawings. Consequently, the above-mentioned steps are more challenging.

First, constructing the geometry, which will consist of elements and nodes, is a very important part. CAD-models are mostly constructed from basic building blocks like beams, rods, etc. Hence the meshing, creating the elements and nodes, is easier. Here, we have to obtain the geometry first by three-dimensional imaging. Building a good FE mesh means finding a good equilibrium between describing the complex shape accurately and minimizing the calculation efforts.

After establishing the geometry, we will need material properties for the specimen. For a linear elastic FE model the Young's modulus is necessary. Several techniques can be used to determine this essential parameter. Their advantages and drawbacks will be discussed in paragraph 2.7.2. The third step is to assign the boundary conditions in

the FE model. A proper understanding of the actual biomechanics is essential for a realistic outcome.

Finally, a very important part is the testing of the FE model. Two important steps are necessary: convergence testing and validation. In the convergence test, the stability of the solution in function of the number of used elements is examined. More elements typically result in a more accurate solution but also in a higher calculation cost. The FE results are finally compared with experimental results in the validation test.

I will now go into detail and indicate the pitfalls for each of the five steps. I will use a Java Finch (*Padda oryzivora*) during biting as an example.

### 2.7.1 Geometry

Standard FE analyses start from a computer aided design. In order to understand problems in biology, the exact geometry itself is often important [122]. Taking into account the realistic geometry has become feasible since computers can handle larger problems. In order to obtain this geometry several techniques can be used, all with their advantages and drawbacks: physical sectioning (figure 1.4), magnetic resonance imaging (MRI, figure 2.7), orthogonal-plane fluorescence optical sectioning (OPFOS) [20], confocal microscopy, (micro) computer tomography (figure 2.8), etc [20]. All these techniques yield a three-dimensional grid of voxels. They can be presented in two-dimensional cross-sections through the object, either virtual or physical. In this chapter, images which were obtained by synchrotron computer tomography (CT) are used. Those CT images give a very good resolution and identification of the keratin layer. Additional information about the micro make-up of the upper beak is acquired from physical sectioning (previous chapter: figure 1.4).

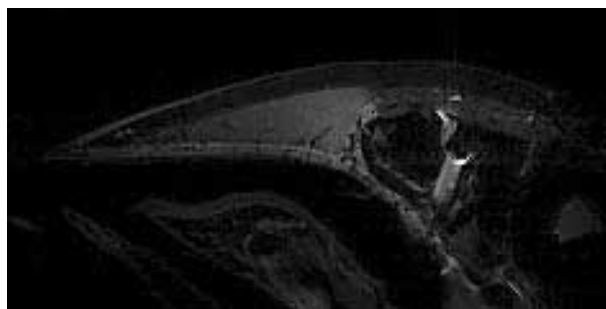


**Figure 2.7:** Magnetic resonance imaging (MRI) of the Java finch upper beak.

Next, regions which represent the same material are identified in the cross-sectional images. In computer image processing, the process of partitioning the image into segments or sets of pixels is called segmentation. The goal of this segmentation is to locate objects and boundary lines. A good segmentation is a first and important step to create a good FE model. The segmentation is done semi-automatically. First,

the volume of interest (VOI) is selected automatically with grayscale thresholding. Afterwards, the outcome is inspected and manually corrected to reduce artifacts. Consequently, the equilibrium between selecting the material without holes and not selecting the noisy parts can be found. In addition one can correct other errors such as separating the upper and lower beak (see figure 2.8). The manual segmentation will be more necessary for softer tissue structures [20]. This manual interception requires experience and prior knowledge of the user.

I perform the segmentation using the software package Amira (Visage Imaging). Figure 2.8 shows a sagittal cross-section of a Java Finch's head. The segmentation on the upper beak is showed on a magnified and grayscale inverted CT slice. The gray area 'A' represents the keratin, the black area 'B' is the connecting tissue and the gray area 'C' represents the bony structures. In the proposed FE model, the connecting tissue will be added to the keratin.

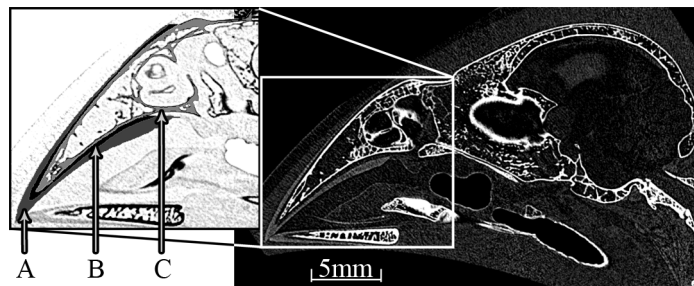


**Figure 2.8:** Sagittal computer tomographical cross-section of a Padda's head. The segmentation is shown on a detail of the upper beak (grayscale inverted and magnified): A. keratin layer; B. connecting tissue; C. bone.

Subsequently, the marching cubes algorithm (in Amira) is used to produce a triangular mesh. This algorithm was first demonstrated by Lorensen and Cline [87] to generate a surface model from a two material segmentation (inside and outside). A grid of cells, where every cell has 8 surrounding voxels which can be 0 (=outside) or 1 (=inside), is established. Next, a lookup table is used to associate each of the 256 ( $= 2^8$ ) possibilities with a corresponding triangular configuration. Afterwards, the method was extended to multi-parts models [145]. The marching cubes algorithm is very robust but it produces a huge stack of nodes and faces. Consequently, the surface model have to be simplified or decimated.

Decimating is the reduction of the total number of triangles by removing vertices in a mesh. The goal is to obtain the original geometry to a good approach [109]. In computer graphics, one wants to reduce the number of triangles to improve the rendering speed. Therefore the new mesh needs to describe the original mesh in the best possible way with a minimum of triangles. For FE modeling, however, the triangles also need to meet the following demands [145, 90]:

### Number of triangles

The marching cubes algorithm yields a very robust, but huge set of triangles. Hence decimating will be necessary. Furthermore, a FE model with a lot of triangles results in a high computation cost (also look at paragraph 2.7.4). On the other hand, relevant geometrical information can be lost.

### Islands and holes

Islands are isolated and detached parts of material which are not loaded in the FE model. They are superfluous and they have to be removed. In contrast, holes are small islands of no material. Small holes result in too much triangles and they have to be removed to reduce computation cost.

### Smoothness

Smoothing will be necessary for multiple reasons. Due to the scanning, one has to deal with noise and partial volume effects. The slice-based segmentation introduces block and staircase artifacts. Besides the visual requirement to smooth, there is also a mechanical need: too sharp and too small structures will result in very high unnatural stresses. Therefore smoothing is applied. Amira uses a Laplace filter iteratively:

$$p_{smoothed} = p + \frac{\lambda}{n} \sum_{i=1}^n (q_i - p) \quad (2.53)$$

Vertex  $p$  is shifted towards the average position of its  $n$  neighbors  $q_i$ . The factor  $\lambda$  regulates the influences of the neighbors. Special care is taken in the case of boundary vertices so that sharp boundaries are preserved. However, just as for decimating, smoothing too much will cause a loss of relevant geometrical information. For instance: when smoothing the upper beak, some small bony structures in the upper beak, called trabeculae, will be removed. On the other hand, if all the trabeculae are kept, the FE model will be too large for calculation [6].

### Aspect ratio

The aspect ratio of a triangle is defined as the ratio of the radii of its circumcircle and its incircle. A triangle with a large aspect ratio results in an ill-conditioned tetrahedron in the final FE mesh. In my models, I try to keep this ratio below 10. This ratio can be improved by flipping edges. With this technique, the common edge of two triangles (four vertices) will be flipped and thus the aspect ratio is changed. Adding or translating vertices can also improve the aspect ratio.

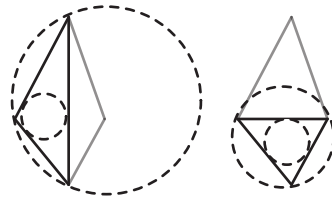


**Figure 2.9:** The aspect ratio of a triangle is defined as the ratio of the radii of its circumcircle and its incircle. It can be improved by flipping edges.

### Maximal and minimal edge length

Smaller and therefore more triangles are obtained by taking a small maximal edge length for the triangles. If this small maximal edge length is combined with a relatively large minimal edge length, it will result in a smaller ratio, which will improve the resulting FE mesh. In the example of the upper beak a ratio from approximately four is taken. Contracting some edges can increase the minimal edge length

### Dihedral angle

The dihedral angle is the angle between two triangles and their common edge. It should be taken not too small. All dihedral angles larger than  $10^\circ$  are taken. Flipping edges can improve this angle, but mostly, one has to translate one or two of the two non common vertices.

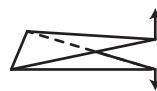


**Figure 2.10:** The dihedral angle can be improved by translating one or two of the non common vertices.

### Closeness and intersections

A surface model obtained by the marching cubes algorithm is robust, which means that one always finds a closed surface without intersections. Closeness implies that there are no gaps in the surface. Intersection refers to an intersection of a triangle with an edge. Both requirements are essential to generate a volume model. However, if one wants to improve the polygonal model, as described in the previous steps, one can accidentally introduce an intersection or annihilate the closeness of the model. Consequently, examination of these two properties is crucial.

### Connecting parts

A polygonal mesh contains vertices and faces. These vertices are presented by three-dimensional coordinates. The triangular faces consist of pointers to three vertices and a material number. For multi-parts models, one has coplanar faces from different materials to define the border between the two materials. It is important that both faces point to the same vertices so a connection is established in the FE model. Coplanar planes from the same material can be removed.

I iteratively perform these steps on the upper beak's polygonal model with the Amira software package [90]. A well-conditioned triangular mesh is important for the creation of a good FE volume grid, which will consist of qualitative tetrahedrons. There are some ill-conditioned tetrahedral shapes, for instance: wedge, needle, cap, sliver (see figure 2.11). The tetrahedrons representation consists of four pointers to the corner points and a material number. Starting from the polygonal surface mesh, two possible strategies can be followed for automatic grid generation: the advancing front approach and the Delaunay tetrahedralization [86].

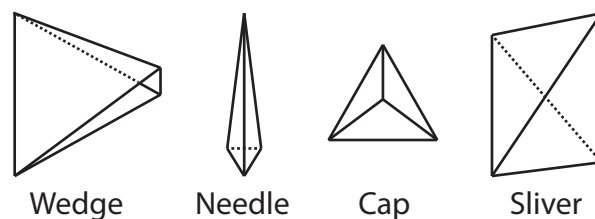


**Figure 2.11:** Four examples of ill-conditioned tetrahedron shapes.

In the advancing front approach, additional vertices are added in the domain and a first layer of tetrahedrons, starting from the initial triangular surface mesh, is generated. New layers are iteratively added forming an advancing front until the domain is filled. A high-quality starting mesh is important and the advancing front needs to have enough space. Especially the last requirement is a problem for thin layers, such as the bony and keratin parts in the upper beak.

For Delaunay tetrahedralization, a Dirichlet tessellation of points in a convex hull is generated. In this way every point is surrounded with a Voronoi cell. A Voronoi cell of a vertex is defined as the positions where the distance to every other vertex is larger than the distance to the vertex itself. Connecting these vertices across the Voronoi cells will result in a Delaunay tetrahedralization of the volume. These tetrahedrons have the interesting property that their circumscribing spheres do not contain any other vertex in the domain. One can now introduce new points in the domain, remove the tetrahedrons whose circumsphere includes the new point and do the tetrahedralization again. In this way, Delaunay tetrahedralization avoids ill-conditioned tetrahedrons, as they have mostly large circumspheres. Compared to two-dimensional Delaunay

triangulation, three-dimensional Delaunay meshing is more complicated and it has no guarantee for the absence of bad tetrahedrons. A major advantage of Delaunay is the easy refinement of the model and so simply enabling convergence testing (see paragraph 2.7.4) [16, 115].

The Delaunay method was chosen due to its easy refinement property and the thin layer issue of the advancing front approach. The Delaunay tetrahedralization was conducted in the ‘TetGen’ software package, which is free for non-commercial use [114]. In this program a quality mesh generation is implemented. The aspect ratio of the maximum side length to the minimum altitude is a good quality measurement and it should be as small as possible. For example, a thin and flat tetrahedron tends to have a large aspect ratio. ‘TetGen’ has several tools to keep this aspect ratio small, but some bad elements, such as slivers, can still occur. The finite element grid is shown in figure 2.12. In figure 2.13, one can see the histogram for the aspect ratio of the final tetrahedral grid [16, 114, 115].

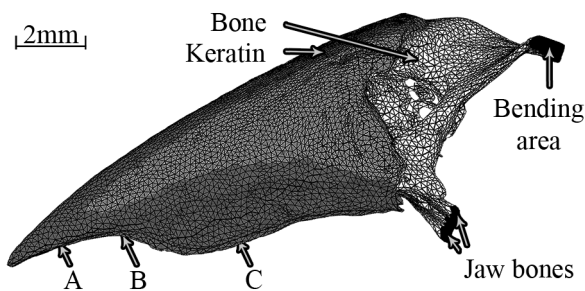


**Figure 2.12:** FE model of the Padda’s upper beak. The white elements indicate the bony part and the grey elements indicate the keratin layer. The black elements are elements with boundary conditions: bending area, jaw bones and 3 different ‘bite spots’ (A. rostral-most part of the keratinous upper beak, B. tip, C. center).

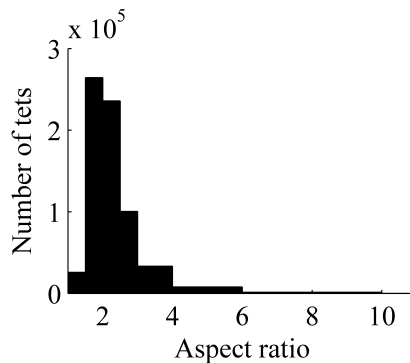


**Figure 2.13:** Mesh quality histogram of the volume grid: the aspect ratio is the ratio of the maximum side length to the minimum altitude.

## 2.7.2 Material properties

After establishing a high quality geometry-based volume grid, a correct material behavior has to be added in the FE model. My upper beak model consists of two materials: bone and keratin (see figure 2.12). I use an isotropic and homogenous linear elastic model for both materials. As such, the resulting strains and stresses are linearly related. Linear elasticity can be a good approximation for most harder materials such as bone and keratin, especially when only small strains are applied. The Young's modulus defines the slope in this linear relation (section 2.5). The exact value of this elastic modulus is an important parameter [122], especially for a multi-parts model. Indeed, making a material stiffer in a multi-parts model can result in higher stresses in this material for the same input force.

Another important mechanical parameter is the material strength (section 2.1). There are different definitions possible: the yield strength for instance, which is the lowest stress that produces a permanent plastic deformation in a material. The material is damaged when measuring this value. Difficulties on interpreting the complex stress field can be overcome by using von Mises yieldings criterium (distortion energy theory) (eq. 2.36). In addition, tensile and compressive testing may result in significant different values. In practice, if one wants to avoid rupture, stresses in a material should be kept below the strength. Actually, one wants to keep the maximal stresses in the material a factor below this strength. This factor is called the safety factor [92].

Obtaining the material parameters from biological samples is usually not straightforward. A first and important issue is the 'natural production' of the samples. Consequently, only a limited amount of samples is available and one cannot choose the sample size or shape. I will now summarize some techniques to obtain the material parameters from biological materials. The first two described techniques, tensile and ultrasound testing, are difficult to apply on the small upper beak, so only literature values are presented. The two following techniques, double indentation and inverse analysis, are better suited for small samples and they will be presented in this dissertation (chapter 3 and 7).

### Tensile testing

Compression and tensile tests are well-known, standardized experiments to obtain the elastic modulus and strength of materials. They are very useful to determine the mechanical parameters for larger samples, but they cannot be applied on smaller and more complex samples. Indeed, a well-known geometry and controlling boundary conditions are two conditions very hard to meet on small samples. As a result, a large error is expected for measurements on the upper beak [118]. However, values measured on larger samples of other bone or keratin specimens can be used. Of course these values may deviate from the values for the real sample. It is preferable, if possible, to do measurements on the sample itself [122]. Evans [43] measured on the unembalmed wet cortical bone of the human femur, and a compressive Young's

modulus of 14 GPa and a compressive strength of 108 MPa were found. In another paper [126] the mechanical properties of dry feather keratin were determined and a tensile modulus of 3.66 GPa and a strength of 221 MPa were found. More details on compression testing can be found in section 3.2.4.

## Ultrasound

The velocity of wave propagation through an object is related to the stiffness of that material. Consequently, the Young's modulus and Poisson's ratio can be calculated in different directions. Dechow and co-workers [29] use this technique to obtain the Young's modulus in the jaw bone (Mandible) of human. He found in the normal, longitudinal and tangential directions the following values:  $E_{normal} = 11 \pm 2$  GPa,  $E_{long} = 14 \pm 3$  GPa,  $E_{tang} = 19 \pm 4$  GPa. As such, a more realistic modeling approach of bone can be established by introducing anisotropy and making the bone stiffer in certain loading directions.

## Indentation techniques

In chapter 3, I introduce a new method to measure the Young's modulus on thin materials, such as the keratin layer and the bony structures of the upper beak. I start from Sneddon's solution for an indentation of a material which is thick as compared to the size of the indentation punch. Scaling the needle to measure on thinner materials is not a good idea. Indeed, micro-structure properties of the biomaterial can be measured instead of the desired bulk-properties. Instead, I used an approach which adds a second indentation punch replacing this sample stage. In this way a virtual mirror plane is created between the two needles and problems at the contact zone between sample and sample stage are avoided. Finally a FE-calculated correction factor  $\kappa$  is introduced to compensate for the thin sample. The technique is tested on well-known samples of a few  $100\mu m$  with a indentation needle with a radius of  $61\mu m$ . Next, it is successfully applied for acquiring the Young's modulus of the middle ear ossicle bone of Rabbit,  $E = 16 \pm 3$  GPa, beak bone  $E = 7.3 \pm 0.6$  GPa and fresh keratin  $E = 1.7 \pm 0.4$  GPa.

## Inverse analysis

The material properties in a model can be found by adapting the model in such a way that a best fit between model and experiment is obtained. Depending on the experimental data, very good results can be acquired. A major advantage of this technique is that material determination can be done *in situ*. The drawbacks of the technique are the time-consuming simulations and the unique experimental design. The best fit is obtained by minimizing the error ( $SS_{err}$ ) for  $N$  points  $q_i$  between the

output of the model ( $FE$ ) and the experiment ( $Exp$ ):

$$SS_{err} = \sum_{i=1}^N (Exp(q_i) - FE(q_i)) \quad (2.54)$$

In order to find this minimal error, a surrogate model is created with the ‘Matlab SUMO toolbox’ [3, 54]. This surrogate model maps the input parameters of the FE model, in this case the Young’s modulus of bone and keratin, to a corresponding error ( $SS_{err}$ ). Once the surrogate model is established in a selected domain, one can obtain the minimal error and thus the optimal material parameters to describe the experiment. The technique has several advantages. First, the calculation cost is reduced due to an intelligent sample selection. Second, if the model is calculated correctly, we are sure to find the absolute minimum in the selected domain. In addition, visual inspection of the surrogate model is possible. Finally, since an error map for the entire domain is obtained, different surrogate models can be combined to obtain the optimal parameters for multiple experiments.

In this dissertation, surrogate modeling will be used to determine the elastic modulus of beak bone and beak keratin. In chapter 7, the seed crushing force is imitated by applying an indentation force at three different points.

**Table 2.1:** Values for the Young’s modulus of bone and keratin with their reference: (a)human femur [43] (b) claw keratin [12] (c) human mandibular bone [29] (d) beak bone and keratin (dry) (chapter 3) (e) ossicle bone (chapter 3) and (f) beak bone and keratin (dry) (chapter 3).

Technique	$E_{bone}$ (GPa)	$E_{keratin}$ (GPa)
Tensile testing	14 (a)	1.8 (b)
Ultrasound	11 ↔ 19 (c)	
Double indentation	7.6 ± 0.7 (d)	2.8 ± 0.4 (d)
	16 ± 3 (e)	
Inverse analysis	7.3 ± 0.6 (f)	3.1 ± 0.4 (f)

### 2.7.3 Boundary conditions

Next, boundary conditions are introduced in the model. For this step, a proper understanding of the biomechanics is essential: ‘which muscles produce forces?’, ‘where can we add a constraint?’, ‘which parts can be left away?’, etc. The standard boundary conditions are: displacement, constraints or forces. Other, more advance boundary conditions, such as sliding contacts are also possible. They make, however, the model much more complicated and harder to compute. As such, they are best avoided if possible, especially in larger models.

In chapter 6, a validation experiment is introduced to imitate the seed reaction force by

indenting the upper beak. In the FE model, this boundary condition can be described as a sliding interface between the needle and the beak. However, the sliding interface will increase the calculation cost drastically. Alternatively, a force can be applied on the elements at the bite spot. The displacement values on top of the beak will be hardly different and the calculation cost is decreased. The fixation of the skull, as described in chapter 6, is simulated by constraining the elements at the bending area and at the jaw bones.

### 2.7.4 Convergence testing

A good FE mesh is important to obtain an accurate solution (paragraph 2.7.1). One needs to know if the amount of tetrahedrons is adequate before one can trust the solution. On the other hand, it is desirable to keep the number of elements low. Indeed, finer meshes come with a calculation cost: more calculation time and large memory requirements. This calculation cost is not an issue if the model has to be calculated only one time (e.g. the Darwin's finch models in chapter 8). It is, however, more important for repetitive calculations, used in inverse analysis (e.g. chapter 7). In general it is difficult to give an answer to this question in advance. Therefore, conducting a convergence test is necessary. The relevant results are compared for different meshes. If the results are nearly similar, for instance if they do not change for more than 5%, a good mesh is obtained. As a final step, a very fine mesh is taken to be sure that a stable result is obtained. Making the mesh denser is simple since the Delaunay meshing strategy, discussed in paragraph 2.7.1, is used. The results of the convergence test of the FE model are shown in table 2.2.

**Table 2.2:** Convergence test: values for the number of tetrahedrons in the FE model, the corresponding Z-displacement at the bite spot and the calculation time (quadratic relationship with number of tetrahedrons). Bold: the model I have chosen for inverse analysis.

Number of Tetrahedrons ( $10^3$ )	235	505	<b>738</b>	959	1405
z-displacement at bite spot ( $\mu m$ )	130	134	<b>137</b>	139	141
calculation cost (s)	65	292	<b>598</b>	976	2066

### 2.7.5 Validation

Even if the previous steps to achieve a good FE model are accomplished with great care, errors in the FE results still remain possible. For instance: the material description in my model can be inadequate. Consequently, performing a validation measurement is an essential part in establishing a model. This validation experiment needs to be a good mechanical representation of the loadings which one wants to investigate. In this dissertation, I present a loading at the upper beak to imitate the seed reaction

force (figure 2.12 and chapter 6). The small dimensions of the sample will result in additional experimental issues. In this section I describe some techniques which can be used and their advantages and drawbacks for measuring on beaks are discussed.

### **Strain gauges**

Strain gauges are widely used for validation in biomechanical research (for instance [122]). They are typically glued on the sample. The deformation is acquired by measuring the change of the gauge's resistance. There are some major drawbacks for biomechanical experiment. First, strain gauges are difficult and time consuming to install, especially on small and complex shaped samples. Second, only local and in plane deformations are obtained. Finally, attaching the gauges can influence the measurement.

### **Laser Doppler vibrometry**

Laser Doppler vibrometry is an optical method mainly used to measure velocities, but using phase detections it can also be used to measure displacements with very high accuracy. It is a non-contact technique and the typical problems associated with strain gauges are avoided. Out-of-plane displacement can be obtained precisely, but only for discrete points. This method is very useful for dynamic testing.

### **Digital speckle pattern interferometry**

Speckles appear when an optically rough surface is illuminated with coherent light. In digital speckle pattern interferometry (DSPI) a speckled object wave and a reference wave are combined to obtain interference. The full-field displacement is calculated by comparing the interference pattern before and after a deformation. Since it is an optical technique, measurements are done in a non-contact way. Numerous variations of different setups are possible, but in this dissertation an easy-to-use Michelson setup is used to obtain the out-of-plane displacement with high accuracy (up to 20nm). The major disadvantage of DSPI is its (nanoscale) sensitivity and its limited displacement measurements, which exclude *in vivo* experiments. More information can be found in chapter 4.

### **Digital image correlation**

In order to overcome stability issues inherent to interferometric techniques such as DSPI, one can use 3D digital image correlation (DIC). Pictures of a sample before and after deformation are compared and by using digital image correlation the in-plane displacement can be acquired. A speckled pattern is air brushed on the sample so a sub-pixel resolution can be obtained. As such, larger, but still realistic displacements are needed ( $\approx 200\mu m$  instead of  $\approx 10\mu m$  for DSPI). By using two cameras, one can obtain 3D topological information and 3D displacement information. Strains on the

complex sample can be calculated if one has results with sufficient signal-to-noise ratio. More information is given in chapter 6.

## **Part II**

# **Experimental methods**



---

### Double indentation technique

---

#### **Abstract**

*In this chapter, I introduce a novel method to determine the Young's modulus of thin (biological) samples. Such specimens cannot be examined with existing tests: compression and tensile tests need well-known geometry and boundary conditions while classic indentation tests need relatively thick pieces of material. In order to determine the elastic modulus I use the indentation theory as proposed by Sneddon and correct it with a finite element calculated  $\kappa$  factor to compensate for the small thickness. In order to avoid material deformations at the contact zone between the sample bottom and the sample stage, I replace the sample stage by a second indentation needle. In this way the sample can be clamped between two identical needles and a virtual mirror plane is introduced. The new method was used on four test-materials and results agreed well with the outcome of a standard compression method applied on large samples of the same materials. The technique was applied on thin biological samples, namely middle ear ossicles of rabbits and bone and keratin samples of the Java finch upper beak.*

This chapter is based on:

Soons Joris, de Baere Ives and Dirckx Joris. New double indentation technique for measurement of the elasticity modulus of thin objects. *Experimental mechanics*, 51(1),85-95, 2011.

Soons Joris, Aernouts Jef and Dirckx Joris. Elasticity modulus of rabbit middle ear ossicles determined by a novel micro-indentation technique. *Hearing research*, 263(1-2), 33-37, 2010

Soons Joris, Herrel Anthony, Aerts Peter and Dirckx Joris. Determination and validation of the elastic moduli of small and complex biological samples: bone and keratin in bird beaks. *J. R. Soc. Interface*, published online doi: 10.1098/rsif.2011.0667

### 3.1 Introduction

Finite element (FE) models are widely used to investigate (bio-)mechanical problems. However, to create accurate models, the exact geometry, the boundary conditions and the material properties of the components have to be known precisely [122]. A very important parameter for (linear elastic) materials is the Young's modulus ( $E$ ). For large material samples, standard tensile and compression methods for measuring Young's moduli are widely available (e.g. ASTM D695-02a 'Standard Test Method for Compressive Properties of Rigid Plastics' [5]). Those methods are very useful to determine the modulus of larger biomaterials, like the femur bone [43]. These tests require a precise description of the geometry of the specimen and usually a cylinder or a cuboid needs to be created. In order to avoid slipping or stretching, the boundary conditions at the contact zone have to be controlled very well. However, when applying this technique on small materials, these conditions are that difficult to realize that even a very fine preparation cannot avoid inaccuracies [118, 146].

Another way to obtain material parameters is through an inverse analysis: the material properties in the model are changed to get a best fit between simulation and experiment. Although good results on small specimens can be obtained (chapter 7), this technique needs unique experiments and time-consuming simulations [4, 80, 91, 106]. As an alternative, indentation testing can provide the material properties. Originally, these tests only give the hardness, an empirical number which represent the difficulty of cutting in the material. The hardness is not a real physical entity, so it is unusable for simulations. A method to obtain the elastic modulus, from those hardness indentation experiments, is based on classical Hertz contact mechanics and was proposed by Sneddon [116]. This technique is applied widely in material and biomechanical sciences, at micro-scale [10, 24, 44, 50, 74, 84, 100, 147] and nanoscale [53, 69, 108, 113]. Such tests use different punches (cylindrical, conical, Berkovich, Vickers) and different loading protocols [44, 95, 100]. Oliver and Pharr [95] found that the unloading-displacement relationships from the indentation experiment could be described by:

$$P = \alpha h^m \quad (3.1)$$

In this equation  $P$  is the indenter load,  $h$  is the elastic displacement of the indenter and  $\alpha$  and  $m$  are constants. The value of  $m$  depends on the punch geometries ( $m = 1$  for flat cylinders). According to Sneddon [116], the elastic modulus for a rigid body punch can be obtained by:

$$E = \frac{\sqrt{\pi}}{2} \cdot \frac{S \cdot (1 - \nu^2)}{\sqrt{A}} \quad (3.2)$$

In this equation,  $E$  represents the elastic modulus,  $A$  is the contact area,  $\nu$  is the Poisson's ratio of the material and  $S$  is the measured stiffness. The stiffness  $S$ , given by  $dP/dh$ , is obtained from the unloading curve which is, as seen in equation 3.1, linear for cylindrical punches ( $m = 1 \Rightarrow S = \alpha$ ). The Poisson's ratio  $\nu$  has to be known. Nevertheless, its exact value is not really important for values between 0.2 and 0.4 (see figure 3.6).

The method as described above was theoretically derived for a rigid punch which infinitesimally indents a half space elastic material. As a result, it is only valid for relatively thick materials (in comparison with the radius of the indenter), and not for thin samples. Decreasing the indenter size to measure such thinner specimens is not always a good solution, because it is important to use dimensions which represent the realistic loading (micro/nano versus macro effects), especially for biomaterials. A nano-indentation on bone for instance, gives information about the micro-mechanics (fibers and cells) and not about the macroscopic bulk properties [24]. For that reason, Hayes et al. [62] extended the solution of Sneddon [116] to measure the Young's modulus of a thin cartilage layer fixed on bone. They calculated a theoretical correction factor  $\kappa$  which compensates the mismatch for such a thin material fixed on a rigid body. The corrected formula for a cylindrical punch becomes:

$$E = \frac{\sqrt{\pi}}{2} \cdot \frac{S \cdot (1 - \nu^2)}{\sqrt{A}} \cdot \frac{1}{\kappa} \quad (3.3)$$

To apply this technique on freestanding thin materials, I have introduced two modifications to the existing theory. First I have calculated a new  $\kappa$  for thin materials laying on a rigid body without friction, instead of being fixed to it. For this purpose I have created a FE model of the indentation experiment. Secondly, when a force is applied, thin materials are easily deformed on large plane contacts, so the contact-dependent deformation is measured instead of the true indentation deformation. In order to avoid deformation on an extended and poorly controlled contact surface, a second indentation needle is introduced.

First, the new method will be validated on four test-materials with different thickness by comparing its results to a standard compression test (ASTM D695-02a). Finally, I will apply the validated technique on biological samples by determining the elasticity modulus of middle ear ossicle bone and beak bone and keratin of the Java finch (*Padda oryzivora*).

### 3.1.1 Middle ear ossicle bone

In current modeling of middle ear mechanics, the ossicles are treated as rigid bodies. Implicit in this treatment is the assumption that mechanical loads seen by the ossicles are insufficient to cause changes in their shape. Due to changes in altitude, meteorological changes etc., the ear is subject to pressure variations with frequencies far below the acoustic range, often referred to as quasi-static pressure changes. The amplitudes of these pressure variations can be hundreds and even thousands of Pascals, which is many times larger than the amplitude of the highest sound pressures. Due to these large pressures, it may be necessary to include the possibility of ossicle bending [35, 38]. Also in the high frequency acoustic range, it may be perfectly possible, even plausible, that thin parts of the ossicles may show bending. Especially in animal models such as gerbil or rabbit, the ossicles include extremely thin structures such as the wedge-shaped manubrium. Indeed, bending of the manubrium has been observed

in cat and gerbil [28, 31]. In those cases, rigid body modeling no longer suffices, and accurate elasticity parameters for the ossicles are needed [42]. Few material-elasticity parameters are available for ossicles [118]. Generally, values for larger bones, like the femur, which are obtained by tensile experiments are used [43]. Table 3.1 gives an overview of the available values.

**Table 3.1:** Overview of mechanical properties of bone. The values of Evans [43] were obtained on unembalmed wet cortical bone of the human femur, the values of Dempster [34] were obtained on wet adult human compact bone by a compression test and the values of Speirs et al. [118] were obtained on ME ossicles by an axial compression test.

Author	Young's modulus (GPa)
Evans [43]	$12 \pm 3$
Dempster [34]	$14 \pm 8$
Funnell et al. [48]	20
Speirs et al. [118]	$3.8 \pm 0.5$

### 3.1.2 Java finch beak

The beak of birds exists of a bony core and a keratin layer. The mechanical interaction between the multiple layers will change drastically depending on the material properties used. However, a large range of possible moduli can be found in literature with values for keratin varying from 0.2 to 4 GPa and for bone from 7 to 35 GPa for compact bone and down to 0.1 GPa for cancellous bone [92, 126]. Furthermore, the elastic modulus of keratin seems to depend on its humidity [126]. Given the wide range of bone moduli reported in the literature, the Young's modulus needs to be determined experimentally for the tissues of interest.

## 3.2 Material and methods

### 3.2.1 Experimental setup

Figure 3.1 and 3.2 illustrate the setup.

Two identical flattened cones were placed exactly opposite to one another so that a thin material could be clamped between them (1). The cones were custom-made from high speed steel (HSS) and had a top angle of  $25^\circ$  (angle to central axis). The point of the cones were polished to obtain a circular and flat contact zone. The exact radius of these surfaces was measured with a calibrated microscope (Zeiss LSM510 Meta laser scanning microscope) and was  $60.8 \pm 1.2 \mu\text{m}$ . The Young's modulus of HSS is 210 GPa which is significantly higher than the materials to be tested. The upper cone was attached to a piezo-transducer (PI P-841.60) (2) and a vertical translation stage (3). The piezo-transducer had an embedded strain gauge with an active feedback loop, so

the displacements were controlled to an accuracy better than  $50nm$ . Larger vertical translations, needed to bring the needle in position, were executed by a mechanical translation stage. The position of this translation stage could be read from the digital micrometer (4) and was used to measure the thickness of the sample. The bottom needle was attached to a loadcell (5) (Sensotec model 31, 50N range), which could be translated (6) in the horizontal plane in order to bring the two needles precisely into line, thus forming a virtual horizontal mirror plane in between the two needles. The whole process was observed with a stereo light microscope. In order to control the piezo displacements and to obtain displacement- and force-data, a Matlab program, interfacing with an A/D-D/A board in a personal computer (National Instruments Daqpad-6020E, 12bit multifunction I/O), was developed.

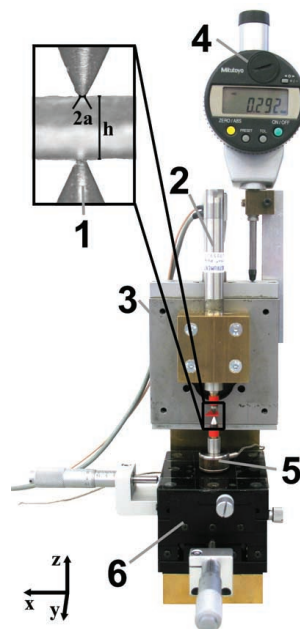


**Figure 3.1:** Picture of the experimental setup showing the flattened cone (1), piezo-transducer to apply displacement (2), vertical translation stage (3), micrometer(4), loadcell(5) and in plane translation stage(6)

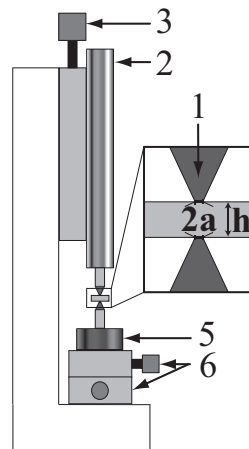


**Figure 3.2:** Schematic representation of the experimental setup showing the flattened cone (1), piezo-transducer to apply displacement (2), vertical translation stage (3), loadcell(5) and in plane translation stage(6)

### 3.2.2 Calibration and loading protocol

If the indentation test is performed with a perfect experimental setup and on a perfectly linear, isotropic and homogenous material, a typical relation between indentation depth and reaction force will be found. This curve, with slightly increasing stiffness for increasing indentation, can be found from FE-simulation, dealing with geometric nonlinearity, and is the same for loading and unloading [24, 147]. For real measurements, however, there will be some factors, such as nonlinear material behavior and inaccuracies of the experimental setup which will influence this ideal result. These factors are minimized by doing a calibration and using a proper loading protocol as follows.

First, the loadcell has a rather high compliance as compared to the materials under test, so the measured displacement distances were significantly larger than the actual indentation. The deformation of the loadcell is however solely dependent on the force which is applied to it, which means we could compensate this effect with a calibration. In order to perform the calibration the needles were pushed against each other without a sample in between. As there was no testing material between the needles the force measured on the loadcell purely corresponded to the deformation of the loadcell. Actually, not only the loadcell's compression was corrected, also all smaller deformations of the entire setup were taken into account.

Second, the indentation points themselves were no perfect rigid bodies, as assumed in equation 3.2, consequently, they also deformed slightly. This deformation is mainly determined by the indentation force, but also by the compliance of the material used under test. This brought me to choosing a very stiff material and a cone shape for the indentation points. In this way their deformation was much smaller than the deformation of the material under test and the bending of the needle itself was minimized. Next, the needle and the material surface were not perfectly flat, so the contact-surface

may not be constant as assumed in equation 3.1. I performed a FE simulation of this situation using the FE software package FEBio [88]. I found that the stiffness will not rise when the needle penetrated 1.2 times the variation on the contact-surface height. Figure 3.3 shows plots of the indentation force and the calculated material stiffness for simulations of an indentation using a slightly inclined flat punch, with offset angles between  $0$  and  $3.5^\circ$ . The values are given as a function of the ratio of the *non-flatness measure* of the indentation interface and the *indentation depth*. As one can see from these graphs, a steady value was obtained once this ratio equals 1.2.

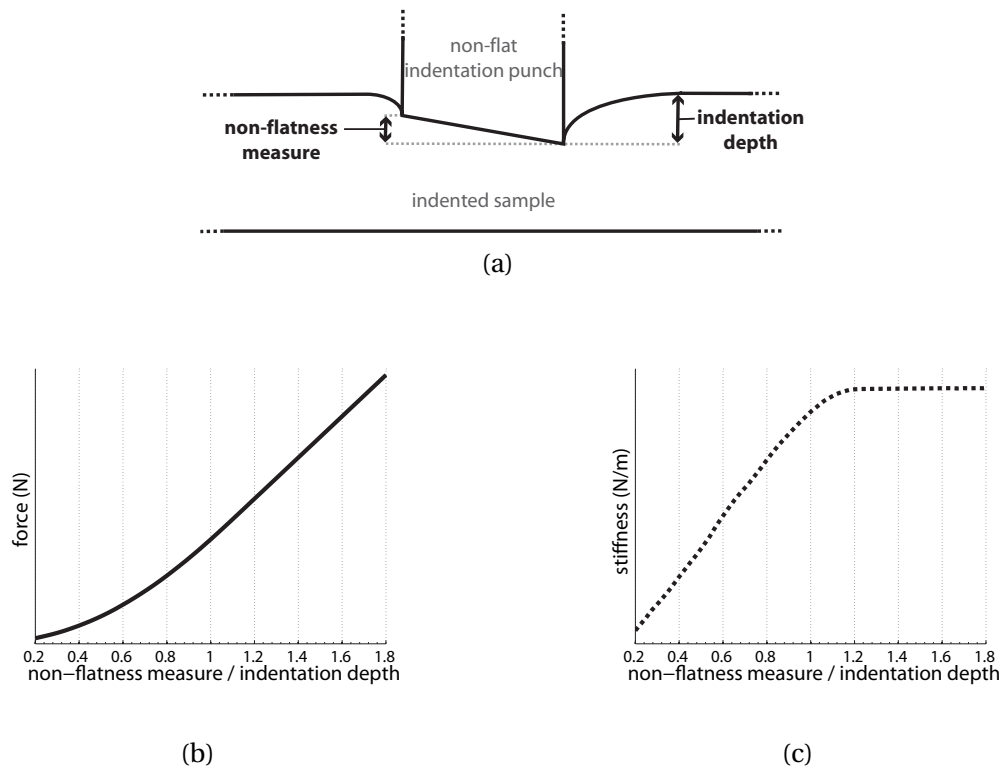


**Figure 3.3:** (a) Exaggerated cross-section of a situation where the interface between the indentation punch and the sample surface is not flat. The definition of *non-flatness measure* and *indentation depth* are indicated. A FE model of this situation was used to investigate the effect of the *non-flatness*. (b) indentation force found in this model as a function of the ratio of the *non-flatness measure* and the *indentation depth*. (c) Material stiffness obtained from the model as a function of this ratio.

Finally, real materials do not have a perfect linear elastic behavior and viscoelasticity induces creep and relaxation, so pre-conditioning is necessary. A testing protocol was developed and is presented in figure 3.4. A triangular wave function drove the piezo actuator to apply 50 preloading indentation cycles. The piezo-displacement and the loadcell reaction force were recorded. After using a median filter with a window of  $0.012s$ , a linear fit was made to the piezo-displacement and the reaction force

curve (to the middle part of this curve). Application of the calibration gave the effective indentation and so the stiffness could be calculated. The amplitude and period of the piezo-displacement were chosen in such a way that the effective indentation was approximately  $1\mu m$  and the effective unloading speed was  $1mm/min$ . Due to relaxation effects, material inertia and filtering, the resulting displacement and force curves were smoothed. This protocol was used repeatedly, with increasing indentation depth (offsets between 5 and  $10\mu m$ ), but with approximately the same loading/unloading speed and indentation amplitude. As such, the stiffness and the modulus were obtained (equation 3.2) with increasing indentation depth and the effect of stiffening and the effect of *non-flatness* of the needle contact was minimized.

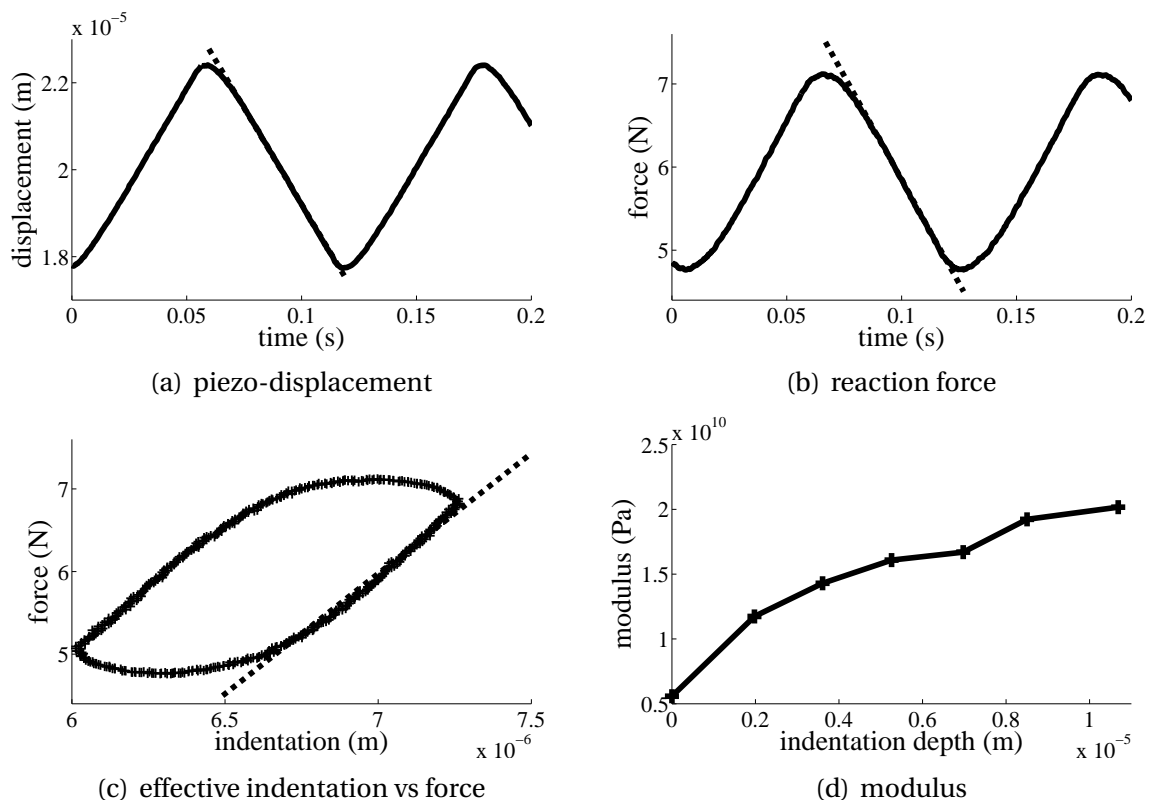


**Figure 3.4:** (a) and (b): piezo-displacement and loadcell reaction force as a function of time. The dotted line represents the linear fit used in the calculations. (c): the indentation force as a function of the effective indentation depth (both smoothed with median filter). The dotted line represent the stiffness ( $dF/d\omega$ ) calculated with the linear fit obtained from (a) and (b). (d): calculated moduli for different indentation depths.

### 3.2.3 FE calculations for correction factor ( $\kappa$ )

Equation 3.2 as proposed by Sneddon [116], gave the Young's modulus for an infinitesimally indented half-space linear elastic material, which is homogenous and isotropic. In order to investigate thin cartilage layers, fixed on bone, Hayes et al. [62] introduced a correction factor  $\kappa$  which compensates for thin materials:

$$E = \frac{E_{Sneddon}}{\kappa(a/h, \nu)} \quad (3.4)$$

where  $E$  is the corrected modulus,  $E_{Sneddon}$  is the modulus calculated with equation 3.2 and  $\kappa$  is the correction factor, which depends on the aspect ratio of the indenter radius ( $a$ ) and the material thickness ( $h$ ) and on the Poisson's ratio. The face opposite to the indented surface was fixed to a rigid body (bone). In this chapter, I wanted to obtain the Young's modulus for a material with a perfect sliding contact between the thin sample and a rigid body (sample stage). Consequently a new  $\kappa$  had to be calculated. This factor was obtained with finite element calculations performed in FEBio [88]. As seen on figure 3.5, the symmetry of the problem was used to reduce the amount of elements with a factor of 8. The maximum number of elements was approximately 50000 and a linear, tetrahedral element was used. The test was also done with less elements to test the sensitivity of the  $\kappa$ -value calculation to mesh density.

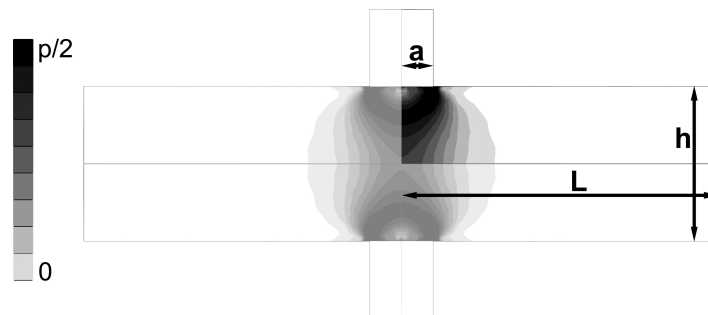


**Figure 3.5:** cross-section of the FE results: for the transparent parts the solution is not calculated but obtained from symmetry,  $a$  is the radius of the indenter,  $h$  the thickness of the material and  $L$  is the dimension/radius of the material surface. Darker colors represent higher von Mises stresses

The model had an adaptable indenter radius, material dimensions, Poisson's ratio and Young's modulus. A Young's modulus  $E$  was used in the model and compared to a calculated  $E_{Sneddon}$  (in the model) using equation 3.2. The ratio of  $E_{Sneddon}$  and  $E$  gave the value for  $\kappa$  (see equation 3.4). Repeating this simulation for different input-values indicated that  $\kappa$  depends on the Poisson's ratio ( $\nu$ ) and on the aspect ratio of the indenter radius and the material thickness ( $a/h$ ), which was the same as in the model from Hayes [62] et al.

Simulating and interpolating for a whole range of Poisson's ratios and aspect ratios (indenter radius versus material thickness) produced the curves shown in figure 3.6.

The difference between the two graphs is the boundary conditions for the needle. In the right figure the contact zone between the needle and material surface was fixed, while the left figure used a frictionless sliding contact.

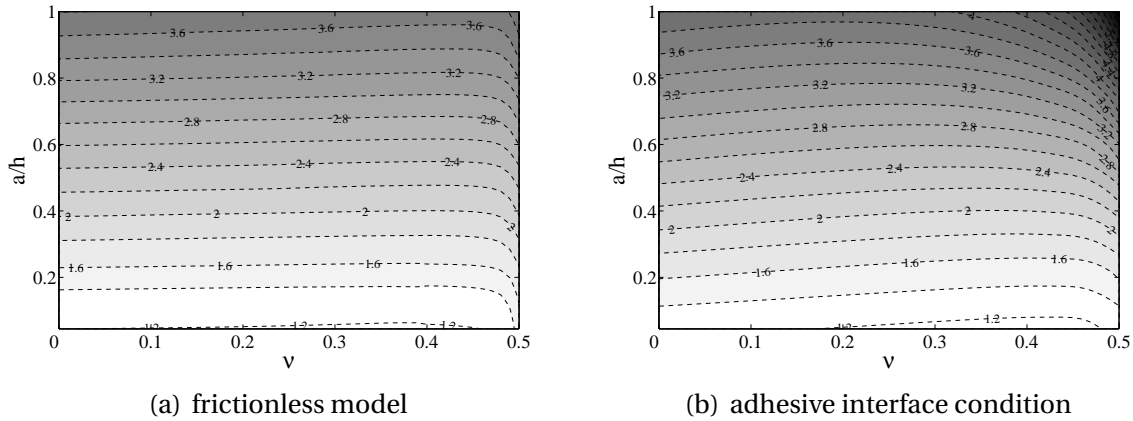


**Figure 3.6:**  $\kappa$  calculated for different Poisson's ratios ( $\nu$ ), and aspect ratio indenter radius and material thickness ( $a/h$ ). The contact zone between the indenter and the material surface is (a) a sliding contact, (b) fixed.

### 3.2.4 Validation materials and compression test

In order to validate the new test setup, we compared the material parameters obtained from experiments with my new indentation setup with those of a standardized test method. We performed indentation tests on thin samples of different materials of which large samples were also available. Four materials were selected, namely Aluminum (Al), Polyvinyl Chloride (PVC), Polymethyl methacrylate or acrylic glass (PMMA) and polycaprolactam or nylon 6 (PA6). These materials samples span a large range of Young's moduli ( $\pm 2$  GPa to  $\pm 60$  GPa). All experiments on the large samples were performed according to the ASTM D695-02a 'Standard Test Method for Compressive Properties of Rigid Plastics'. According to this standard, the specimens were milled to cylinders with a diameter of  $12.7\text{mm}$  and a height of  $25.4\text{mm}$  [5].

All experiments were done on an electromechanical Instron tensile testing machine with a FastTrack 8800 digital controller and a  $10\text{kN}$  or  $100\text{kN}$  loadcell, depending on the material. All tests were done in a displacement-controlled mode using a displacement speed of  $1\text{mm}/\text{min}$ , corresponding to the test speed in my indentation method. As such, time-dependent material effects did not differ between the two types of experiments. The cylindrically shaped specimen was placed in the centre of the two cylindrical pressure plates (see figure 3.7). In order to accurately measure the displacement of the discs, a linear variable differential transformer (LVDT) was used so the deformation of the tensile machine could be neglected.

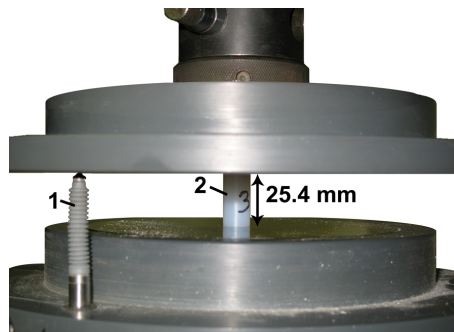


**Figure 3.7:** Compression method: linear variable differential transformer (LVDT) (1) and test material (2).

Since friction between the specimen and the pressure plate may have an important influence on the results, teflon spray was used between specimen and plate, so that the friction may be neglected for the lower load levels, used to calculate Young's modulus. Several experiments were conducted on different specimens of the same material and the stiffness and standard deviation were calculated according to the ASTM norm. The results of these experiments are given in section 3.3.1.

### 3.2.5 Middle ear ossicles

As a demonstration, I applied my method to measure the Young's modulus of auditory ossicles. Middle ear ossicles were harvested from young-adult, male New Zealand white rabbits immediately after sacrificing the animal by injection of 120 mg/kg natrium pentobarbital. The bulla was removed and opened and the ossicles were removed. Since a rabbit's malleus and incus are fused together, they had to be separated first. Afterwards, I performed the indentation tests on four positions as indicated in figure 3.8. A first set of measurements was performed within two hours post mortem, a second set 1.5 years post mortem without special preserving techniques. The results of these experiments are given in section 3.3.2. The study was performed according to the regulations of the local ethical committee.

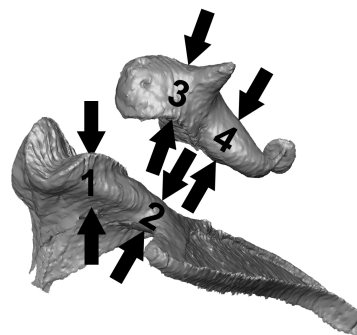


**Figure 3.8:** Micro-CT reconstruction of malleus and incudis with indentation positions indicated: 1.caput malleus, 2.collum malleus, 3.corpus incudis and 4.crus longum incudis

### 3.2.6 Java finch beak

I used the double indentation technique to obtain the Young's modulus of the keratin layer and the bony core of Java Finch's upper beak. In total seven Java Finches were examined. A first group of four finches was selected (Padda 1, 2, 3 and 4) for dry testing. After sacrificing the birds with CO<sub>2</sub> gas, bone and keratin of the upper beak were carefully dissected by use of a scalpel, resulting in square samples of a few millimeters wide and with a thickness ranging between 50 and 500  $\mu m$  (figure 3.9). The exact thickness was measured to calculate the FE correction factor for Sneddon's equation. Taking samples at the corner of the upper beak was avoided since they have a too large curvature. Keratin on top and at the bottom of the upper beak was harvested separately for Padda 2, 3 and 4.

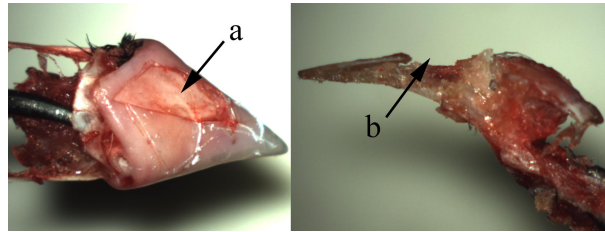


**Figure 3.9:** Harvesting of keratin (a) and bone (b) on top of Java finch upper beak

The samples were polished to obtain flatter surfaces for the indentation. Indentation tests were performed 2 hours post-mortem yielding the elastic modulus for dried samples. One expects a large variation for keratin depending on its humidity [126]. Therefore, the modulus of the keratin of a group of three Java Finches (Padda 5, 6 and 7) was measured during dehydration. The following exponential fit is used to model the evolution of the modulus as a function of time during the process of dehydration:

$$E(t) = (E_{fresh} - E_{dry}) \cdot \left(1 - \exp\left(\frac{-t}{\tau}\right)\right) + E_{dry} \quad (3.5)$$

$E(t)$  is the measured modulus during drying out at time  $t$ ,  $E_{fresh}$  is the modulus for fresh samples,  $E_{dry}$  is the modulus for dried samples and  $\tau$  is the time constant. The 'Matlab curve fitting toolbox' was used to calculate the best fit to the measured moduli. Keratin of Padda 5 was tested directly after harvesting. Bone and keratin samples of Padda 6 and 7 were studied moist before doing the actual exponential fit measurements. An ultrasonic humidifier was used to keep them moist during dissection and testing.

## 3.3 Results

### 3.3.1 Validation materials

#### ASTM compression test

In order to validate the new indentation setup, comparison needed to be made with standardized tests on large samples. Several experiments were performed for each material and the Young's modulus and its standard deviation were calculated. Since the results were very reproducible, only one example for each material is shown in figure 3.10. In order to have a clear graph, both stress and strain, which were negative in compression, are plotted as positive values. The compressive stiffness was calculated using the tangent line in the origin to the stress-strain curve.

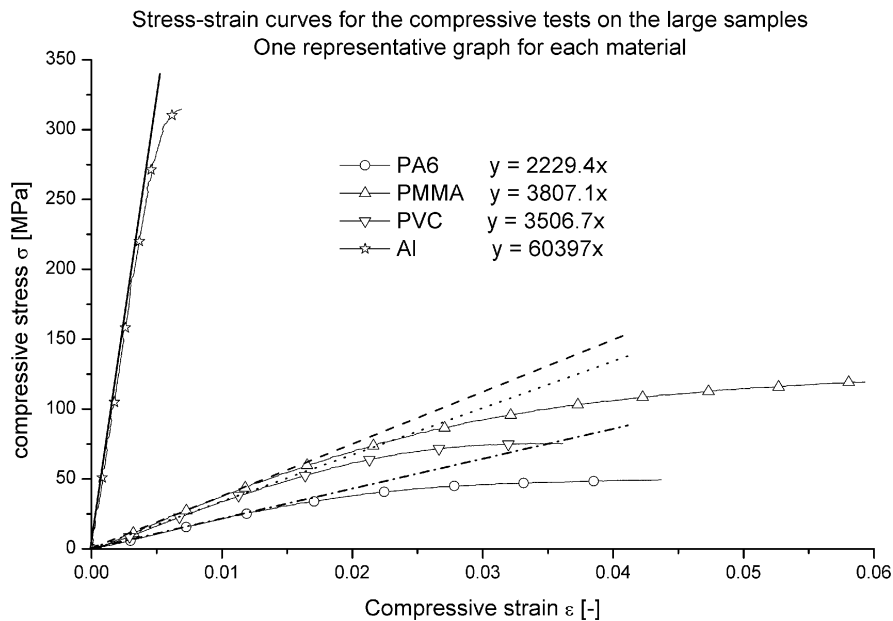


**Figure 3.10:** Normal stress as function of the longitudinal strain for the four selected materials.

As can be seen in figure 3.10, the calculated Young's modulus varied between 2.2 GPa and 61 GPa for the four different materials, so the validation runs over a selected range of stiffness moduli. Table 3.2 gives an overview of all calculated Young's moduli and the standard deviation for all four materials.

**Table 3.2:** Elasticity modulus (in GPa,  $\pm$  stdev) obtained from ASTM D695-02a test.

Material	N	$E_{ASTM}$
Al	3	$60.9 \pm 1.4$
PVC	5	$3.53 \pm 0.06$
PMMA	5	$3.80 \pm 0.04$
PA6	5	$2.26 \pm 0.09$

### Indentation test-material

After performing the compression test, I used the new indentation method to determine the Young's modulus of the four test-materials. I examined specimens with different thicknesses ranging from  $200\mu m$  to  $1000\mu m$ . For each test-case, three different samples were used and these were successively tested on three different indentation depths ( $5\mu m$ ,  $7.5\mu m$  and  $10\mu m$ ). These nine values enable me to calculate the average value and the standard deviation, which are shown in table 3.3 (in the column named  $E_{indentation}$ ).

$E_{Sneddon}$ , which is the Young's modulus calculated without the correction factor proposed in equation 3.4, is also given in table 3.3. Furthermore, the values of the sample thickness  $h$ , and the Poisson's ratio  $\nu$  are also shown in this table. Finally, the deviation between these two techniques, defined as  $deviation = \frac{E_{indentation} - E_{ASTM}}{E_{ASTM}}$ , is also shown in table 3.3.

### 3.3.2 Middle ear ossicles

After the validation on test-materials, the proposed technique was used on biological samples with properties within the same range as the test-materials ( $2GPa < E < 60GPa$  and  $200\mu m < h < 1000\mu m$ ).

After harvesting the malleus and the incus, four positions were carefully chosen (figure 3.8: 1.caput malleus, 2.collum malleus, 3.corpus incudis and 4.crus longum incudis). On these precise locations the ossicles had reasonably parallel surfaces which meant they could be clamped between the two needles with a minimal *non-flatness* of the contact (figure 3.3). The entire process is followed with a light microscope.

After positioning the ossicles, the thickness, which was inevitably different for all locations, is measured using the indentation cones and the digital micrometer. The indentation measurements were done at depths between  $5\mu m$  and  $10\mu m$  (in 3 or 4 steps) and on  $N$  different specimens. The average and standard deviation for the Young's modulus found at different locations are presented in table 3.4, together with the average thickness of the samples and results measured on middle ear ossicles 1.5 years post-mortem.

**Table 3.3:** Elasticity moduli for four test-materials with different thickness, with  $h$  the material thickness,  $\nu$  the Poisson's ratio,  $E_{ASTM}$  the elasticity modulus obtained with the standard compression test (table 3.2),  $E_{Sneddon}$  the elasticity modulus obtained with equation 3.2,  $E_{Indentation}$  the corrected elasticity modulus  $\pm$  stdev (equation 3.4) and  $deviation = \frac{E_{indentation} - E_{ASTM}}{E_{ASTM}}$ .

Material	$h$ ( $\mu m$ )	$\nu$	$E_{ASTM}$ (GPa)	$E_{Sneddon}$ (GPa)	$E_{indentation}$ (GPa)	$E_{indentation}$ (GPa)	deviation
Al	975	0.33	60.9	76.9	64.6 $\pm$ 5.5		+6.1%
Al	444	0.33	60.9	86.3	64.0 $\pm$ 4.8		+5.2%
Al	200	0.33	60.9	117	66.9 $\pm$ 6.7		+9.9%
PVC	988	0.35	3.526	3.87	3.27 $\pm$ 0.14		-7.2%
PVC	440	0.35	3.526	4.32	3.21 $\pm$ 0.17		-8.9%
PVC	300	0.35	3.526	4.77	3.21 $\pm$ 0.26		-9.0%
PMMA	1010	0.40	3.799	4.97	4.23 $\pm$ 0.22		+11.4%
PMMA	430	0.40	3.799	5.65	4.21 $\pm$ 0.20		+10.8%
PMMA	275	0.40	3.799	6.50	4.27 $\pm$ 0.22		+12.6%
PA6	1030	0.39	2.260	2.70	2.30 $\pm$ 0.14		+1.8%
PA6	450	0.39	2.260	2.72	2.05 $\pm$ 0.15		-9.1%

**Table 3.4:** The Young's moduli ( $\pm stdev$ ) for rabbit middle ear ossicles is obtained at different positions (caput malleus, collum malleus, corpus incudis and crus longum incudis) with different thickness ( $h$ ). N is the number of different specimens.

Position	$h(\mu m)$	Young's modulus (GPa)	N
caput malleus	540	$16.3 \pm 2.9$	5
collum malleus	480	$15.6 \pm 1.8$	5
corpus incudis	770	$16.8 \pm 3.1$	4
crus longum incudis	440	$17.1 \pm 3.8$	3
average		$16.4 \pm 2.8$	17
average (1.5 years post-mortem)		$18.2 \pm 2.5$	8

### 3.3.3 Java finch beak

Bone samples were between  $50\mu m$  and  $130\mu m$  thick, the keratin on the dorsal side of the upper beak was between  $40\mu m$  and  $200\mu m$  thick and the tested keratin on the ventral side of the upper beak had a thickness between  $250\mu m$  and  $500\mu m$ . One indentation cycle, including preconditioning and measurement on three depths ( $5\mu m$  to  $10\mu m$ ) took approximately one minute. The averages and standard deviations for the elastic modulus of bone and keratin of the dried upper beak (Padda 1, 2, 3 and 4) are shown in table 3.5. For Padda 2, 3 and 4, I obtained the modulus of the keratin on top and at the bottom of the upper beak separately.

**Table 3.5:** Mean values and standard deviations for the Young's modulus measured with the double indentation technique on dry samples. The first four Java Finches were tested when dried out, the following three were tested during drying out and the exponential fit of equation 3.5 was used to obtain  $E_{dry}$ . The results for the modulus of bone ( $E_{bone}$ ), keratin ( $E_{keratin}$ ), keratin on top of the upper beak ( $E_{topker}$ ) and at the bottom ( $E_{bottomker}$ ) are presented.

	$E_{bone}$ (GPa)	$E_{keratin}$ (GPa)	$E_{topker}$ (GPa)	$E_{bottomker}$ (GPa)
Padda 1	$7.3 \pm 2.0$	$2.85 \pm 0.69$		
Padda 2	$7.5 \pm 2.5$	$2.87 \pm 0.85$	$2.88 \pm 0.85$	$2.86 \pm 0.87$
Padda 3	$8.4 \pm 3.9$	$3.06 \pm 0.69$	$3.06 \pm 0.64$	$3.06 \pm 0.65$
Padda 4	$7.8 \pm 3.4$	$2.55 \pm 0.75$	$2.43 \pm 0.75$	$2.58 \pm 0.68$
Padda 5 (exp fit)		$3.31 \pm 0.69$	$3.59 \pm 0.51$	$2.90 \pm 0.83$
Padda 6 (exp fit)	$7.7 \pm 3.0$	$3.37 \pm 0.69$	$3.66 \pm 0.74$	$3.12 \pm 0.57$
Padda 7 (exp fit)	$6.5 \pm 3.5$	$3.34 \pm 0.80$	$3.39 \pm 0.85$	$3.22 \pm 0.74$
Weighted average	$7.5 \pm 1.2$	$3.1 \pm 0.3$	$3.2 \pm 0.3$	$3.0 \pm 0.3$

The obtained moduli for bone and keratin of moist samples and their standard deviations are presented in table 3.5. Figure 3.11 shows the data for the Young's modulus and the exponential fit for the keratin of Padda 5 during drying. For the three finches

an average value of 35 minutes with a standard deviation of 21 minutes was obtained for the time constant of the exponential which describes the change of the modulus as a function of time during dehydration (equation 3.5). The average time constant for keratin coming from the bottom of the beak was 38 minutes and for top keratin 32 minutes. The asymptotic values ( $E_{dry}$ ), which are the moduli of the dried samples, and the 68% confidence limits, are presented in table 3.5 (Padda 5, 6, 7). It should be noticed that the values of Padda 5 were measured directly after harvesting, Padda 6 and 7 were kept moist during a period of approximately two hours. The exponential fit also yields the values for the fresh samples ( $E_{fresh}$ ). These values are presented in table 3.7. Approximately 15 indentation cycles were taken to calculate the presented averages and exponential fits; outliers were removed.

**Table 3.6:** Elastic modulus of bone ( $E_{bone}$ ), keratin ( $E_{keratin}$ ), keratin on top of the upper beak ( $E_{topker}$ ) and at the bottom ( $E_{bottomker}$ ) for fresh samples, measured by keeping the samples moist during and after harvesting.

	$E_{bone}$ (GPa)	$E_{keratin}$ (GPa)	$E_{topker}$ (GPa)	$E_{bottomker}$ (GPa)
Padda 6	$7.6 \pm 3.5$	$1.59 \pm 0.47$	$1.45 \pm 0.46$	$1.74 \pm 0.55$
Padda 7	$6.6 \pm 3.0$	$1.78 \pm 0.68$	$1.90 \pm 0.74$	$1.62 \pm 0.55$
Weighted average	$7 \pm 2$	$1.7 \pm 0.4$	$1.6 \pm 0.4$	$1.7 \pm 0.3$

**Table 3.7:** Elastic modulus of keratin ( $E_{keratin}$ ), keratin on top of the upper beak ( $E_{topker}$ ) and at the bottom ( $E_{bottomker}$ ) for fresh samples, calculated with the exponential fit from equation 3.5

	$E_{keratin}$ (GPa)	$E_{topker}$ (GPa)	$E_{bottomker}$ (GPa)
Padda 5	$1.34 \pm 0.79$	$1.87 \pm 0.56$	$0.7 \pm 2.2$
Padda 6	$1.72 \pm 0.72$	$1.40 \pm 0.66$	$2.14 \pm 0.78$
Padda 7	$1.76 \pm 0.80$	$1.73 \pm 0.88$	$1.72 \pm 0.75$
Weighted average	$1.6 \pm 0.4$	$1.7 \pm 0.4$	$1.8 \pm 0.5$

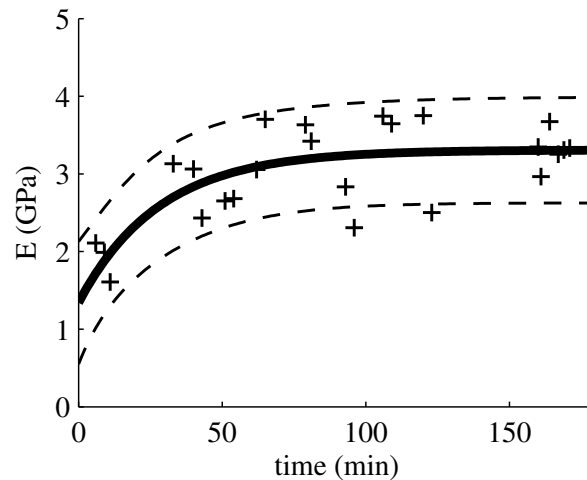


**Figure 3.11:** Elastic modulus of keratin from Padda 5 during drying out. The crosses indicates the average of three measurements on different depths ( $5\mu m$  to  $10\mu m$ ), the line is the exponential fit and the dashed lines indicate the 68% confidence bounds.

## 3.4 Discussion

### 3.4.1 FE corrected double indentation method

In order to obtain the elasticity modulus for a material standard tensile tests are easy and fast to perform on large objects. Sample preparation and controlling the boundary conditions in such tests are difficult for smaller objects [118, 147]. Dedicated experiments to determine the modulus give very good results but are difficult to perform and are time consuming [80, 91, 106] (and chapter 7).

Indentation tests, based on Sneddon's solution [116], do not need such complicated preparation and are easy to use on micro- and nanoscale. They are, however, designed for relatively thick materials which is an important drawback when applying the method to composite materials: decreasing the needle radius to measure thinner objects can change the results drastically because the bulk properties are not measured anymore. This behavior is even more important for biological materials which are often built up with cells and fibers [25]. Therefore I made two additions to Sneddon's solution.

First, I introduced a second needle to prevent surface deformations not caused by the indentation. By adding this second needle in such a way that a virtual mirror plane is introduced, the experimental setup becomes equivalent to a perfectly flat sample with half thickness which lays on a perfect sliding sample stage. Furthermore, the samples could be tested faster since they only had to be clamped between those two punches. It should be taken into account that it is necessary to suppose that a perfect mirror plane develops in the specimen between the two indenters. This condition will only

be met if the two indentation points are perfectly aligned. In order to acquire this condition, the loadcell is mounted on crossed translation tables with a translation precision of better than  $1\mu m$ . The indentation points are brought towards each other, and microscope observation from two perpendicular directions is used to align the indentation surfaces. The surfaces of the indentation points themselves are nearly perfectly perpendicular to the indentation direction. I achieved this by putting the cylindrical part of the points in a custom made holder which is placed perfectly perpendicular on a polishing disk, in order to polish the pointed end to a small plane which is perpendicular to the indentation axis. In addition the sample itself should be symmetrical on mechanical relevant places, which are the places with higher von Mises stress in figure 3.5. Furthermore, an offset indentation is necessary to assure full contact between material and indenter surface. Otherwise, the stiffness will be underestimated, as seen in equation 3.3. When the full contact requirements are not reached, in case of rough materials or inclined surfaces, sample preparation and polishing is needed. Observation with the light microscope allowed me to conclude that the investigated bone samples were smooth enough.

A second addition to Sneddon's solution was a new FE calculated correction factor  $\kappa$  for those thin, freestanding materials. I take geometric nonlinearities, in contrast with the infinitesimal results of Hayes et al. [62] into account, but the finite deformation effect which causes stiffening during larger indentations was left out [24, 147]. I obtain  $\kappa$  values for a frictionless sliding contact and a fixed sliding contact, shown in figure 3.6. The real values will be in between those two situations. In accordance with the conclusions by Zhang et al. [147], I could state that the value of  $\kappa$  is fairly constant for Poisson's ratios between 0 and 0.4, if the aspect ratio indenter radius and material thickness was smaller than 1. The new  $\kappa$ -values are higher when compared with the values of Hayes et al. [62] and Zhang et al. [147], which were obtained for an elastic layer bounded to a rigid half space. The correction factor depends on the aspect ratio of the indenter radius and the material thickness ( $a/h$ ), and on the Poisson's ratio ( $\nu$ ). Considering a fixed or a sliding contact at the needle-surface zone gives approximately the same solution for  $\kappa$  when the Poisson's ratio is smaller than 0.4 and aspect ratio is smaller than 1, which corresponds well with the conclusions by Zhang et al. [147].

By using a more sensitive loadcell, my technique can possibly also be extended towards much softer materials such as biological tissue. Because the indentation surfaces are very small, there will be little effect from local bending on the indentation surface itself. A very soft material should be supported in a holder to prevent the material from bending around the needle. In addition, an active vibration isolation will be necessary when smaller forces need to be measured. However, from my calibration measurements I did see that no significant noise was picked up due to acceleration effects caused by external vibrations. Therefore a regular rigid table was sufficient for this setup. Providing such technical problems can be solved, we think the double indentation method can have promising applications in soft tissue testing as well, but at the moment we are not equipped to demonstrate this.

Thinner objects could be measured by using a different indenter radius, but this

will also change the physical contact-properties as remarked earlier. In that case  $\kappa$  should be tested for thinner materials. The bulk properties of thicker materials can also be determined with this method. Furthermore, larger indentation punches are produced more easily. When the aspect ratio of the indenter radius and the material thickness ( $a/h$ ) is smaller than 0.025, the correction factor  $\kappa$  will be lower than 1.1. The double indentation will still be necessary to ensure no unwanted surface deformations. When the sample dimensions are larger than a few millimeters, tensile tests can easily be applied to determine material bulk properties. The materials examined with this indentation test, were considered to be homogenous, isotropic and linear (assumption in Sneddon's solution and in the FE calculations), just like in the ASTM test.

### 3.4.2 Loading protocol

Visco-elastic materials showed creep and relaxation and there were some plastic deformations and phase transformations due to local high stresses [50, 69]. Also, hysteresis caused the load and unload curves to be different. In order to minimize these effects, pre-loadings were used and the indentation-force curve was measured during unloading [95]. The force-indentation curves for most materials showed increasing stiffness for increasing indentation depth. This effect could be attributed to nonlinear phenomena, but it is also the result from geometric nonlinearity [24, 147]. The indentation depths should not be too deep to minimize this effect. Therefore, several offset indentations had to be tested empirically and the loading protocol as presented in figure 3.4 was introduced.

### 3.4.3 Validation

In order to test the proposed method, four test-materials with different material-properties (Al, PVC, PMMA and PA6) were selected and tested according to the ASTM D695-02a standard [5]. The standard deviation calculated from different samples was between 1 and 4%. A second part of the four test-materials were prepared with different thicknesses between  $200\mu m$  and  $1000\mu m$  and were used for the new double indentation method. As such, the FE calculated correction factor  $\kappa$  and the thickness independency of the measurement could be tested. A Young's modulus  $E_{indentation}$  and a standard deviation, which ranged between 5 and 10%, is obtained and presented in table 3.3. The Poisson's ratio, used in the calculations, were also presented. It should be possible to measure the Poisson's ratio by using two different sizes of indentation punches [72].

When comparing the results from the standard compression method ( $E_{ASTM}$ ) and from my double-needle indentation method ( $E_{indentation}$ ), the difference between the results obtained from the two techniques was always smaller than 13% (table 3.3). I also demonstrated the importance of the correction factor  $\kappa$  for thin materials by calculating  $E_{Sneddon}$ . The correction factor goes up to 1.75 for thin materials and the difference between the results of my method and Sneddon's solution goes up to 92%.

From the validation measurements we learn that my method allows to determine Young's moduli to an accuracy of better than 13% on small specimens in a large range of Young's moduli and material thickness ( $2GPa < E < 60GPa$  and  $200\mu m < h < 1000\mu m$ ).

### 3.4.4 Biological materials

In current mechanobiological research linear FE models are often used. Such models need information about the geometry, the boundary conditions and the material properties of all parts. The most important parameter for linear elastic models is the Young's modulus. Often general parameters are used: for instance for bone, the values of Evans [43] which were measured on the unembalmed wet cortical bone of the human femur are used even in papers dealing with other species or other types of bone [78]. In my method I only measure the bulk elasticity parameter of the material. Biological materials often consist of fine structures, which I do not take into account. However, the results from this method are intended to be used in FE modeling of biomechanical structures, where materials are often approximated as being homogeneous. Nevertheless, great care should always be taken, as in some cases the outer surface of a biological object can have significantly different properties from its inner structure. With the proposed method one can harvest thin samples out of such a structure, and thus obtain more detailed information on the distribution of the elasticity parameters, this is not possible in a classical compression test. It remains impossible to take into account inhomogeneities within the thin sample itself.

#### Middle ear ossicles

Rabbit middle ear ossicle bone is a good example of the usefulness of my method in mechanobiology, because the Young's modulus of bone is in the range of the test-materials [43] and because middle ear ossicle bone is too small for standard test methods [118]. In hearing science [30, 37, 78, 123], proper models with correct material-parameters are important to investigate the functioning of normal and pathologic ears [35, 138] by describing the correct ossicle bending and so their results for the middle ear transfer function [31, 38]. Bending of the auditory ossicles needs to be taken into account for large quasi-static pressure variations [36, 35, 38] or for high frequencies where inertia effects may be important [28, 31].

On incus and malleus, four locations are found with approximately parallel surfaces so the indentation test could be performed easily. The thickness cannot be chosen freely, but was measured and it was in the same range as the thickness of the samples used in the validation experiments. Young's moduli for all bones were found between 11 and 22 GPa, which is in the range of the test-materials. Standard deviations, which are obtained from indentation on different depths (between 5 and 10  $\mu m$ ) and on different specimens, ranged from 10 to 22 %. When comparing the elasticity modulus between different locations no significant difference was found and the Young's modulus from

rabbit middle ear ossicle bone could be determined as  $16 \pm 3$  GPa which is higher than the value given by Evans [43] ( $12 \pm 3$  GPa). When one compared this result to the nano-indentation results obtained by Rho et al. [99], my value is found to be between the highest and lowest Young's modulus of the micro-structural components of bone (13.4 GPa for trabecular and 25.8 GPa for cortical bone). These micro-structural properties are very useful for a better understanding of the building up and functional behavior of bone, but for modeling of complex biomechanical systems, such as the middle ear, a general bulk parameter will mostly suffice.

On dried auditory ossicles (1.5 years post-mortem), a Young's modulus of ( $18 \pm 3$  GPa) is found. This is a bit higher than the modulus found in the fresh specimens, as was also noticed by Evans [43], but the difference is not significant. I therefore conclude that dehydration (in a normal environment) of the ossicles does not influence their elasticity significantly, though the yielding point and ultimate strength may have changed.

### Java finch beak

The results of the elastic modulus obtained with the double indentation experiment on dry samples are presented in table 3.5. A weighted average for the modulus of all seven examined Java Finches (Padda 1-7) of 7.5 GPa for bone and 3.1 GPa for keratin is obtained. A small difference between the two sets of measurements is observed. A weighted average is obtained for the modulus of keratin of  $2.8 \pm 0.4$  GPa for Padda 1-4 and of  $3.3 \pm 0.4$  GPa for Padda 5-7. The small difference may be caused by the fact that the measurements were performed on not entirely dry samples for Padda 1-4. The relative error for the acquired moduli is however less than 16%. This precision is high for biological tissues which are subjected to inter- and intra-specimen variability and suggests that the proposed method provides consistent results. Moreover, the high precision of the keratin modulus suggests no significant difference in values for keratin on the top and at the bottom of the upper beak. Results correspond well with those obtained through an inverse analysis (chapter 7), suggesting that both techniques provide reliable and accurate results. Moreover, the obtained values lie within the range found in literature ( $0.2 \text{ GPa} < E_{\text{keratin}} < 4 \text{ GPa}$  [92, 126] and  $100 \text{ MPa} < E_{\text{bone}} < 35 \text{ GPa}$  [27, 49, 92]). Compared to other literature values of bone [29], the modulus I found is rather low. Literature values for keratin correspond well with my results [126]. The wide variety of bone and keratin samples in literature indicates the importance of measurements on the actual samples to be modeled.

Two strategies for the double indentation were used to obtain the elasticity modulus of fresh samples. A first strategy was to keep the samples moist during harvesting and double indentation testing. In practice this also enables the testing of bone samples which need a longer preparation time. Moreover, more tests can be performed, resulting in a better error analysis. The weighted averages for Padda 6 and 7 are given in table 3.6. A second strategy uses the exponential fit from equation 3.5 and the moduli obtained during drying, resulting in a modulus before and after drying out. A time constant ( $\tau$ ) of ( $35 \pm 21$ ) minutes was observed for the dehydration process of

keratin. The dehydration of keratin obtained from the top of the beak has a slightly lower time constant of  $(32 \pm 17)$  minutes, which can be explained by its thinness. The large variability in the measurements of the time constants can be explained by the impossibility to control air humidity and consequently the desiccation rate.

The time constant is clearly higher than the measurement time of one minute, which allows me to use the exponential fit for the presented data. No significant difference was found between a sample measurement directly after harvesting (Padda 5) and the measurement of samples which were kept moist (Padda 6, 7). No exponential fitting was done for bone, since there was no significant difference between the moist and dry elastic modulus. The weighted average for the Young's modulus of moist bone is  $(7 \pm 2)$  GPa (table 3.6). The weighted average for the modulus of moist keratin, obtained by the double indentation technique, is  $(1.7 \pm 0.4)$  GPa. No significant difference for keratin taken from the bottom and on top of the upper beak was found. My results also clearly show an effect of humidity on the stiffness of keratin, which is consistent with earlier reports [126]. The acquired linear elastic moduli for *in vivo* bone and keratin will be of high importance to build a realistic FE model (chapters 5 and 8).

### 3.5 Conclusions

Standard methods such as tensile tests are difficult to use on complex and small biological samples, such as middle ear ossicle bone and the upper beak of small birds. Nevertheless, the exact elastic modulus is very important in the corresponding FE models, especially for the multi-parts models, such as the upper beak of birds (chapter 5). Here I presented a custom-made, portable double indentation device which allows to measure the Young's modulus of thin samples. The material is clamped between two needles and symmetrically indented (figure 3.2). As such, the problem of creating a perfect smooth contact zone between sample and sample stage is avoided, as a virtual plane is created due to symmetry. A correction factor  $\kappa$ , which compensates for the small thickness, is calculated with FE modeling and added to Sneddon's solution. As such, the Young's modulus of the validation materials could easily be measured, independent from thickness, with an accuracy better than 13%. The Young's modulus of small middle ear ossicle bone of rabbits was found to be  $16 \pm 3$  GPa, which is much higher than the acquired elastic modulus of bone samples of the Java finch upper beak ( $7.3 \pm 0.6$  GPa), indicating the importance of measurements on the sample itself. Finally, the modulus of fresh keratin was found to be  $1.7 \pm 0.4$  GPa.



---

### Digital speckle pattern interferometry

---

#### **Abstract**

*A simple digital speckle pattern interferometry and shearography setup to measure the out-of-plane displacement and its derivative on small complex bony structures is developed. Both optical techniques are chosen because very small deformations on small specimens need to be measured. Furthermore full field and in situ measurements are preferred.*

*In this chapter, I start with a brief theoretical introduction of speckles and the general working principles of the proposed interferometric setups. Next, a description of the custom made experimental setups is given. Finally, a comparison and validation of the performance of both techniques on a simple deflection of a cantilever beam are presented, and some preliminary results on in situ loaded bird beaks are shown.*

This chapter is based on:

Soons Joris and Dirckx Joris. Full field displacement and strain measurement of small complex bony structures with digital speckle pattern interferometry and shearography. *Proceedings of SPIE: Speckle 2010*, p. 73870C, 1-73870C, 10, 2010.

## 4.1 Introduction

In the previous chapter, a new method to obtain the elastic moduli of thin, biological samples was proposed. Finite element (FE) models, with these values incorporated, can be used to simulate outcome from loading conditions or experiments. However, an essential part in a good FE analysis is the confirmation with a validation measurement (section 2.7), especially when the tested object is a complex biological structure (chapter 5). For this purpose, displacements or strains in the FE-model, of the Java finch (*Padra oryzivora*) for instance, have to be compared with *in situ* obtained displacements and/or strains. Strain gauges can be used to measure these small deformations, but they have some major drawbacks. Firstly, they are difficult and time consuming to install, especially on small samples such as a beak. In addition, a number of strain gauges have to be used because otherwise only local strain information is obtained. It is obvious that attaching the strain gauges can affect the measurement itself. Another disadvantage is that the complex shape of the beak makes it even more difficult to install the strain gauges in a proper way. Not only is the complex shape an issue, but also the complexity of the biological materials from which the beak is built up, namely: bone, keratin and other collagen tissue which are anisotropic and inhomogeneous [7, 71]. In order to measure the displacement of this complex and small sample, a full field and sensitive *in situ* measurement setup is needed. In this chapter, I will propose two interferometric techniques which can overcome the strain gauges' drawbacks: namely digital speckle pattern interferometry (DSPI) and shearography (Digital Speckle Pattern Shearing Interferometry, DSPSI) [73, 121].

Speckle pattern interferometry was first introduced in the 1970s to retain most of the measurement facilities of holography, but without the inconveniences arising from photographic recording. In this way, the full field in-plane and out-of-plane displacement could be obtained precisely (wavelength resolution) in a simple, direct and non contact measurement [18]. During last decades several improvements were added, such as phase shifting and the use of CCD (Charge-coupled device) cameras, which allow quantitative measurements with sub wavelength resolution. The obtained results are also increasingly used as a verification of FE models [61]. In spite of the very accurate displacement measuring, there are few DSPI applications outside the laboratory or for biomechanical research [14, 17, 33, 60, 96, 136, 144]. Most of the time strain gauges are used [79, 103]. DSPI offers full field displacement measurement, but it is very sensitive, susceptible to vibration and air turbulence and it is rather difficult to set up. Therefore, I will introduce an easy to use setup which could also be used by people who are not skilled in optics.

DSPI has two other disadvantages. First, only limited displacements can be measured due to phase unwrapping problems and speckle decorrelation. In addition, rigid body displacements, which are unimportant from a mechanical point of view, are also measured. Second, due to the induced speckle noise, additional filtering is needed to calculate derivatives (e.g. strains). Shearography was introduced to eliminate the

reference beam so that a much higher tolerance to environmental disturbances was achieved. By superimposing an image with its own sheared image instead of a reference beam, the variation of the displacement in the shearing direction can be obtained instead of the displacement itself. This variation equals to a good approximation the derivative of the displacement to the shearing direction. In this way the disadvantages of DSPI can be overcome and a more robust interferometric setup, which found his way outside the laboratory environment, is realized. This setup is often used for non-destructive qualitative testing in industry. However, in order to calculate the displacement precisely, a good calibration is needed and an integration has to be introduced [61, 83].

In this chapter both optical techniques, DSPI and shearography, will be introduced. After a description of the theory and the experimental setup, I will use a simple mechanical setup to test both techniques. The deflection of a clamped aluminum cantilever beam will be examined. First the out-of-plane displacement obtained with DSPI and shearography will be compared to the results obtained from a FE model and a single-point laser Doppler vibrometer (LDV). Next, the derivative of the out-of-plane displacement will be investigated and compared. This derivative will be shown to be a good (non-physical) parameter (also see chapter 6 and 7), since rigid bodies, which are uninteresting from a mechanical point of view, yield a constant for the derivative. Finally, the experimental setup and the results of an actual out-of-plane displacement of a complex biological sample, namely a finch's upper-beak during biting, is shown and discussed.

## 4.2 Theory

A schematic representation of the experimental setup is shown in figure 4.1. A Michelson digital speckle pattern interferometry (DSPI) setup is used to obtain the out-of-plane displacement. A He-Ne beam ( $\lambda = 632.8$  nm) is expanded by a telescopic lens. Next, the beam passes through a beam splitter and illuminates the object under test (a cantilever beam or the upper beak of the finch) and a reference plate. Both will show a speckle pattern resulting from their optical roughness and the use of coherent light. Both speckle patterns are subsequently back combined with the beam combiner, resulting in an interference pattern captured with a normal CCD camera. The captured speckle pattern of a beak before and after deformation are presented in figure 4.2 (two left images). The intensity distribution of this speckled interference pattern in a DSPI arrangement before loading ( $I(0)$ ) and in the final state ( $I(\Delta\phi)$ ) can be expressed as [73]:

$$I(0) = I_{obj} + I_{ref} + 2 \cdot \sqrt{I_{obj} \cdot I_{ref}} \cdot \cos(\Psi_{obj} - \Psi_{ref}) \quad (4.1)$$

$$I(\Delta\phi) = I_{obj} + I_{ref} + 2 \cdot \sqrt{I_{obj} \cdot I_{ref}} \cdot \cos(\Psi_{obj} - \Psi_{ref} + \Delta\phi) \quad (4.2)$$

$I_{obj}$  and  $I_{ref}$  are the intensities of the object and reference beam,  $\Psi_{obj}$  and  $\Psi_{ref}$  are the random speckle phases from the object and reference beam and  $\Delta\phi$  is the phase

difference resulting from the introduced deformation. We want to obtain  $\Delta\phi$ , since we can calculate the displacement  $\Delta z$  from it when we know the wavelength  $\lambda$ :

$$\Delta z(x, y) = \frac{\Delta\Phi(x, y)}{2\pi} \cdot \frac{\lambda}{2} \quad (4.3)$$

In order to obtain this phase difference ( $\Delta\phi$ ) between  $I(0)$  and  $I(\Delta\phi)$  different methods can be used, we shortly present two of them: the direct correlation and the subtraction method.

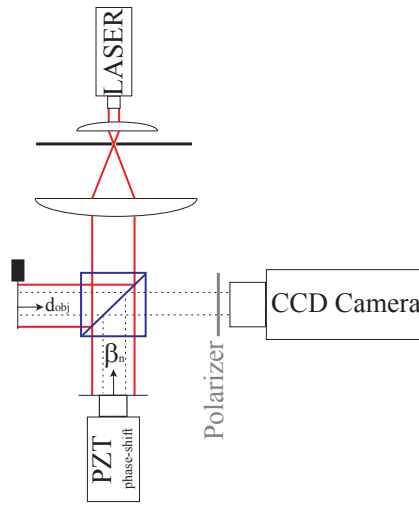


**Figure 4.1:** Experimental setup of DSPI

### 4.2.1 Direct correlation method

The Pearson correlation coefficient between a set of pixels in  $I(0)$  and a set of pixels in  $I(\Delta\phi)$  is defined as [73]:

$$\rho_{I(0), I(\Delta\phi)} = \frac{\langle I(0)I(\Delta\phi) \rangle - \langle I(0) \rangle \langle I(\Delta\phi) \rangle}{\sqrt{\langle I(0)^2 \rangle - \langle I(0) \rangle^2} \sqrt{\langle I(\Delta\phi)^2 \rangle - \langle I(\Delta\phi) \rangle^2}} \quad (4.4)$$

If we assume that  $I_{obj}$ ,  $I_{ref}$  and  $\phi$  are mutually independent variables, so they can be averaged separately,  $\langle \cos(\phi) \rangle = \langle \cos(\phi + \Delta\phi) \rangle = 0$ ,  $\langle I_{obj,ref}^2 \rangle = 2 \cdot \langle I_{obj,ref} \rangle^2$  and  $\langle I_{obj} \rangle = r \cdot \langle I_{ref} \rangle$ , then equation 4.4 can be written as:

$$\rho_{I(0), I(\Delta\phi)} = \frac{1 + r^2 + 2 \cdot r \cdot \cos \Delta\phi}{(1 + r)^2} \quad (4.5)$$

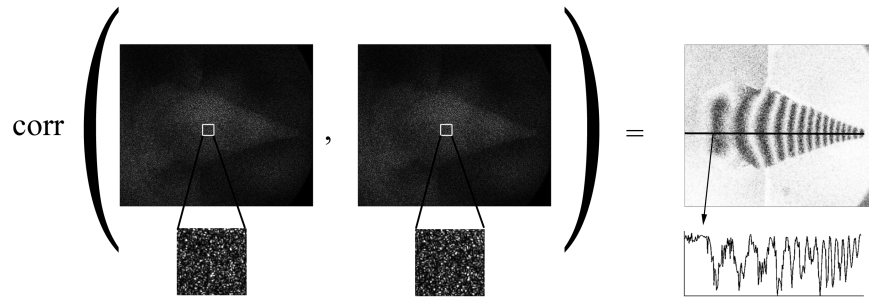


**Figure 4.2:** Correlation of two speckled interference pattern (before and after deformation). Results are between 0 and 1

When  $\Delta\phi$  equals to  $2n\pi$  (with  $n$  an integer), then  $I(0) = I(\Delta\phi)$  and the correlation will equals to 1 so bright fringes are formed. On the other hand, when  $\Delta\phi$  equals to  $(2n+1)\pi$ , the correlation will be minimal and dark fringes are obtained. In contrast with the subtraction method, described in the following part, the correlation method reduce the speckle noise and yields to clear interference fringes [75]. In figure 4.2 (right), one can count the amount of fringes to have an idea about the displacement. Indeed, one fringe represents a half wavelength displacement (equation 4.3). Nevertheless, the phase order of the fringes remains unknown and one can not obtain a sub-wavelength resolution. We want to calculate the phase difference  $\Delta\phi$ , for each pixel, in equation 4.5. Therefore phase-shifting is introduced: extra phases  $\beta_n$  are introduced in equation 4.2, so equation 4.5 becomes a set of  $N$  equations.

$$\rho_n = A + B \cdot \cos(\Delta\phi + \beta_n) \quad (4.6)$$

With  $A$  and  $B$  unimportant variables depending on  $r$  and noise and  $n = 1, 2, \dots, N$ . If we choose the  $\beta_n$ 's in equation 4.6, in a proper way, we can obtain  $\Delta\phi$  when  $n \geq 3$ . For  $N = 4$  and  $\beta_n = \{0, \pi/2, \pi, 3\pi/2\}$  we get [22]:

$$\Delta\phi = \arctan\left(\frac{\rho_2 - \rho_4}{\rho_3 - \rho_1}\right) \quad (4.7)$$

The result of the phase combining is presented in figure 4.3. On this figure, the phase difference  $\pi$  between  $\rho_2$  and  $\rho_4$  (two figures in numerator) can be clearly observed since light fringes become dark and vice versa. Different, more advanced phase combining algorithms are possible and they can be found in a paper by Buytaert and Dirckx [21].

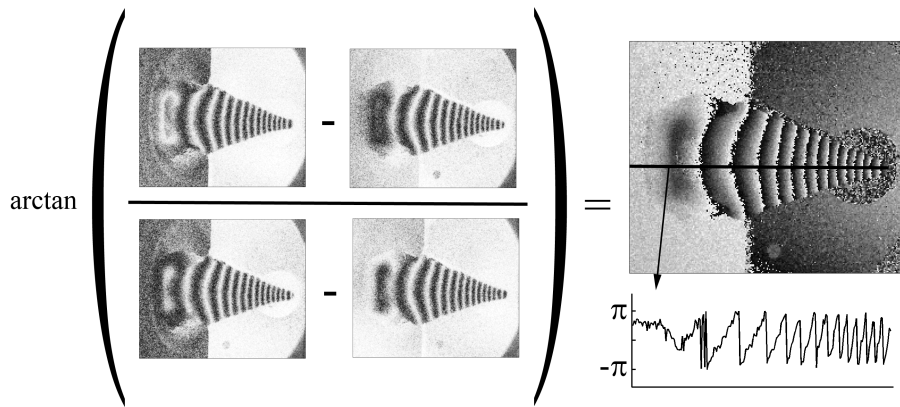


**Figure 4.3:** The wrapped phase map  $\Delta\phi$  can be obtained by introducing a phase shifts. Results are between  $-\pi$  and  $\pi$

### 4.2.2 Subtraction method

In the subtraction method, the difference between  $I(0)$  and  $I(\Delta\phi)$  is calculated:

$$I_{sub} = I(0) - I(\Delta\phi) \quad (4.8)$$

$$= 2\sqrt{I_{obj}I_{ref}} [\cos(\Psi_{obj} - \Psi_{ref}) - \cos(\Psi_{obj} - \Psi_{ref} + \Delta\phi)] \quad (4.9)$$

$$I_{sub}^2 = 16I_{obj}I_{ref} \left[ \sin^2\left(\frac{\Delta\phi}{2}\right) \cdot \sin^2\left(\frac{\Delta\phi}{2} + \Psi_{obj} - \Psi_{ref}\right) \right] \quad (4.10)$$

In equation 4.10, the first squared sine represent the fringes. When  $\Delta\phi$  equals to  $2n\pi$  (with  $n$  an integer), then  $I(0) - I(\Delta\phi) = 0$ , so dark fringes are formed (contrary to the bright fringes of the correlation method). Bright fringes, with speckle noise, will be obtained if  $\Delta\phi$  equals to  $(2n + 1)\pi$ . The second squared sine represent the speckle (noise) pattern  $(\Psi_{obj} - \Psi_{ref})$  and is random in nature across the whole area [75] so it will disappear when  $I_{sub}^2$  is averaged. This averaging can be obtained with a median filter. We get the next equation:

$$\langle I_{sub}^2 \rangle = 8I_{obj}I_{ref} [1 - \cos(\Delta\phi)] \quad (4.11)$$

This equation is similar to equation 4.6, so phase shifting can be applied and a value for  $\Delta\phi$  can be obtained.

The subtraction method is easy and fast to perform and could be done electronically. Therefore this method is practical in realtime, quality measurements. However, averaging is still needed to remove the speckle noise and to get  $\Delta\phi$ . The correlation method does not need averaging and reduces the noise, but is harder from a computational point of view[75]. So when computation time is not an issue, this correlation method is preferred.

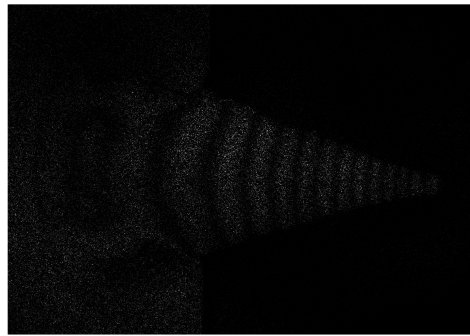


**Figure 4.4:** Result for subtraction method (for the same speckled interference patterns as in figure 4.2)

### 4.2.3 Phase unwrapping

The inherent phase uncertainty of  $2\pi$  in the  $\arctan$  function of equation 4.7 (figure 4.3) can be solved with a procedure called phase unwrapping. Let  $U$  be the unwrapping operator of  $\Delta\phi(x, y) \in [-\pi, \pi[$  and  $k$  an unknown integer [19]:

$$\Delta\Phi(x, y) = U \{ \Delta\phi(x, y) \} = \Delta\phi(x, y) + 2\pi k(x, y) \quad (4.12)$$

The integers  $k(x, y)$  are searched in such a way that  $\Delta\Phi(x, y)$  have no phase errors. Next this phase distance  $\Delta\Phi$  should be written in real distances  $\Delta l$ , therefore equation 4.3 is used. A smoothed result for an upper beak deformation of approximately  $3\mu m$  is shown in figure 4.5

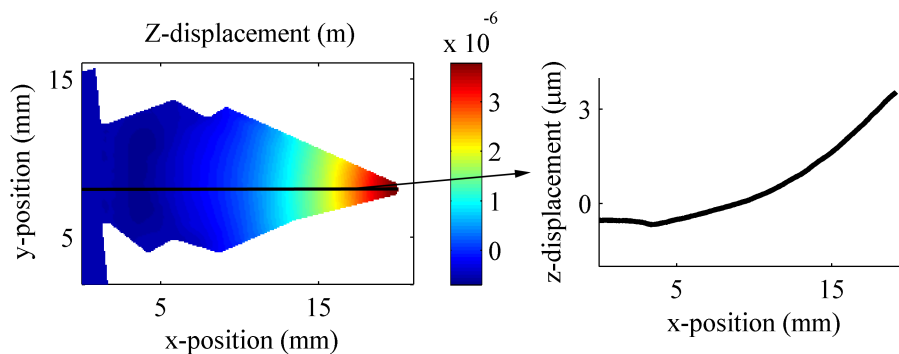


**Figure 4.5:** Final result of upper beak deformation of approximately  $3\mu m$ .

### 4.2.4 Angle corrections

In the previous part, the formulas were derived for objects which are illuminated and viewed in the same direction as the sensitivity vector. The illumination angle

( $\theta_{illumination}$ ) and the view angle ( $\theta_{view}$ ) are defined respectively as the angles between the sensitivity vector and the illumination direction and the sensitivity vector and viewing direction (figure 4.6). Taking these angles into account, equation 4.3 has to be rewritten as:

$$\Delta l(x, y) = \frac{\Delta\Phi(x, y)}{2\pi} \cdot \frac{\lambda}{\cos \theta_{illumination} + \cos \theta_{view}} \quad (4.13)$$

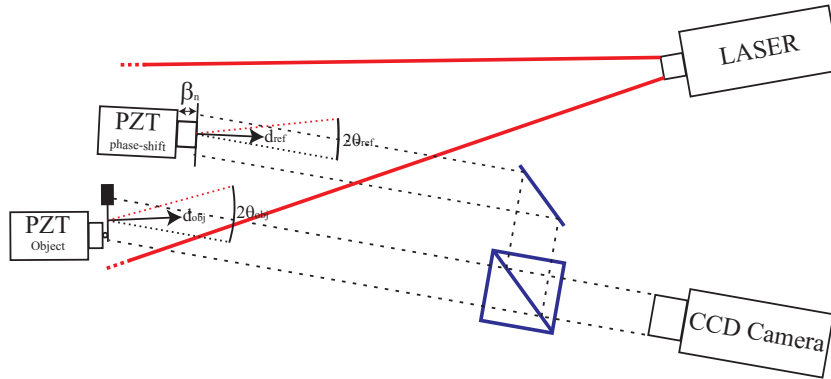


**Figure 4.6:** A DSPI setup with angle corrections.

Small values for  $\theta$  will give nearly the same solution as in the classical setup. The angle correction is important for both object as reference displacements.

Another effect of this setup is the use of a divergent beam instead of a collimating beam. Consequently, the illumination angle  $\theta_{illumination}$  will diver slightly over the object. For a flat object this can be solved by using a different  $\theta_{illumination}$  for each point:

$$\theta_{illumination} = \arctan \left( \frac{d \cdot \sin \theta_{center} - l}{d \cdot \cos \theta_{center}} \right) \quad (4.14)$$

where  $d$  is the distance from the center of the object to the focal point of the divergent beam,  $\theta_{center}$  is the illumination angle in the center of the object and  $l$  is the distance from the selected point to the center of the object. When the object has a random surface, the exact  $\theta_{illumination}$  is not known. This issue can be overcome by using a telecentric camera-lens.

### 4.2.5 Shearography

In digital shearography an image-shearing device is used to bring light scattered from two neighboring points on the object surface to interfere at one point on the image plane of a camera (figure 4.7 and 4.8). Actually, the sheared image will serve as the reference beam for the non-sheared imaged. In this way, the change of displacement is obtained instead of the displacement itself and equation 4.3 becomes:

$$d - d' = \frac{\Delta\phi}{4\pi} \cdot \lambda \quad (4.15)$$

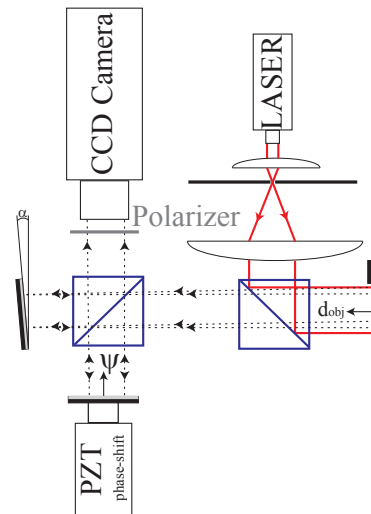


**Figure 4.7:** Experimental setup of shearography.



**Figure 4.8:** An example of a shearography image, obtained with with light illumination.

In equation 4.15,  $d$  and  $d'$  are the displacements of two points which are imaged on the same point of the CCD. We can write  $(d - d')$  as  $(\partial d / \partial x) \Delta x$ , when the shear  $\Delta x$  is infinitesimal small. In this way we can obtain the derivative of the displacement to the shearing direction. A major advantage of shearography is that the optical paths of the object image and the sheared object image are nearly the same. As a consequence, a more robust setup is achieved. A second advantage is that the derivative of the out-of-plane displacement in a chosen direction can be measured directly without a numerical derivation which can introduce large errors. A third advantage is that the derivative of the displacement is from a mechanical point of view (to calculate bending moments) a more important parameter than the displacement itself [83]. Indeed, for a rigid body movement, shearography will obtain a constant value in contrast to a linear change obtained by DSPI. If the derivative in two directions is known, the derivative in every other direction can be obtained by using the chain rule. Those measurements

can be obtained by using two different cameras with a different shear or by performing two measurements. The last solution requires that the deformation is repeatable. In addition, it is possible to calculate the actual displacement by integrating. A practical issue for the integration is that finite image-shears introduce image-doubling (as can be seen in figure 4.8). This image-doubling will result in a decrease of the spatial resolution. This problem is solved by using a summation which uses steps with the length of the shear [139], e.g. for a 1D displacement ( $\Delta\theta_{displ}$ ) and the summation over  $\theta_{shear}$  for pixels  $\xi$  with a pixel shear  $\Delta\xi$ :

$$\Delta\theta_{displ} = \sum \Delta\theta_{shear} \cdot (\xi - n\Delta\xi) \quad (4.16)$$

In this way one can obtain the out-of-plane displacement. However, a precise measurement and a well calibrated determination of the shear will be necessary because an error will propagate through the entire solution due to the summation. In addition, a priori knowledge is necessary to obtain the exact displacement. When the derivative of this displacement is calculated, one acquires a result with more noise but with a higher spatial resolution.

### 4.2.6 Speckle effect

When an optical/microscopic rough surface is illuminated with coherent light, from a laser for instance, a granular, speckle pattern appears. This speckle effect can be seen in figure 4.2. The effect can be considered as a severe drawback when using lasers to illuminate object. Several techniques are investigated to overcome them. Nevertheless, in this work, I will use the speckle pattern to obtain information about the object's deformation.

The physical principle of speckles is explained in figure 4.9. Light is diffusely reflected by every point of the (optical rough) surface (e.g.  $P_1$  and  $P_2$ ) so that every point acts as a point light source (cfr. Huygens-Fresnel principle). The complex amplitude and intensity at any point (e.g.  $Q_1$  and  $Q_2$ ) is given by the sum of amplitudes scattered from each point on the surface. The phases of these emitted complex amplitudes are random due to the roughness of the surface, yielding a random resultant amplitude (equivalent at random walk problem). Values vary between zero, which are dark speckles, and a maximal value, the white speckles, depending on the individual amplitudes. This type of speckles is called objective speckles, because they only depend on the surface and the position of observation, and not on the imaging system.

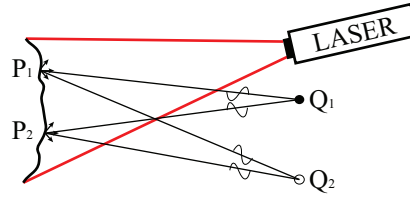


**Figure 4.9:** Objective speckles:  $P_1$  and  $P_2$  re-emit light and acting as a point light source (Huygens-Fresnel principle). Destructive interference (dark speckle) is obtained in  $Q_1$  and constructive interference (white speckle) is obtained in  $Q_2$ .

Subjective or image-plane speckles depends on the imaging system and its diffraction limit. A point  $P_1$  forms a diffraction pattern around  $Q_1$  in the image plane (see figure 4.10). This Airy pattern can be described with the next equation [73]:

$$I \sim \left[ \frac{2J_1(\pi b \sin(\theta/\lambda))}{\pi b \sin(\theta/\lambda)} \right]^2 \tag{4.17}$$

where  $I$  is the intensity measured on the image plane,  $J_1$  is the first order Bessel function,  $b$  is the diameter of the circular aperture,  $\theta$  is the angle with the optical axis and  $\lambda$  is wavelength. The maximum of  $J_1x/x$  is found for  $x = 0$ , the first minimum for  $x = 1.22\pi$ .

$P_2$  can be distinguished from  $P_1$  if the position of its image  $Q_2$  is on the first minimum of the  $Q_1$ -Besselfunction (cfr. Rayleigh criterion). The corresponding distance can be found as followed:

$$Q_1Q_2 = \frac{1.22\lambda l}{b} \tag{4.18}$$

with  $l$  the distance from the lens to the image plane.

This results in an observable speckle-size (or diameter) which is twice this quantity:

$$d_{speckle} = \frac{2.4\lambda l}{b} = 2.4\lambda(f/\#) \tag{4.19}$$

with  $(f/\#)$  is numerical aperture.

This equation show that the size of the speckles depends on the imaging system. Decreasing the numerical aperture (increasing diaphragm), results in smaller speckles. If the speckles are too small, they cannot be resolved by the detector. On the other hand, too large speckles reduce the spatial resolution.

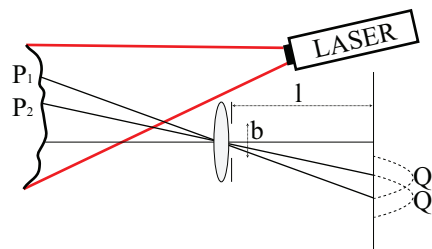


**Figure 4.10:** Subjective or image-plane speckles.

## 4.3 Experimental setup

### 4.3.1 Digital Speckle Pattern Interferometry

In Digital speckle pattern interferometry (DSPI) a speckled object wave and a reference wave are combined to obtain interference. Numerous variations of speckle pattern interferometry exist. In this thesis a speckled reference beam and the object beam are combined in a Michelson setup (figure 4.1). A parallel laser beam (He-Ne,  $\lambda = 632.8nm$ ), filtered with a pinhole spatial filter in order to improve the beam quality, illuminates the object and a reference plate through a Michelson setup. A graph paper with markers of  $1mm$  is glued on the reference plane so the pixel size can be easily obtained (figure 4.11). The reference plate is attached to a piezo-translator (PI S-303) so phase-shifting can be introduced during the initial undeformed step ( $\pi/2 \rightarrow \lambda/8$ ) and full field displacements with sub-wavelength resolution can be acquired ( $\pm 20nm$ ). The two speckled waves, namely the object wave and the reference wave, are back combined with the beam combiner and the interference pattern is directly captured with an ordinary CCD camera (AVT pike F-505) with telecentric lens. A polarizer is used in front of the camera to reduce specular reflections. Pearson's correlation between four images in the undeformed and the image in the deformed state are calculated (with a Gaussian weighted mask with a sigma of five pixels), resulting in the full field out-of-plane displacement.

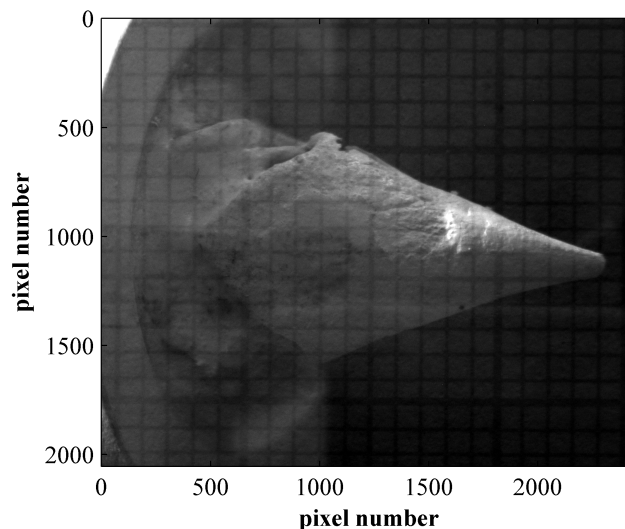


**Figure 4.11:** The object (upper beak) and reference plate (graph paper) with normal white light illumination.

The speckled reference beam and the Michelson setup yield two important advantages. First, in an interferometric setup with a plane reference wave front, the object and reference beam need to be combined after the imaging lens. Therefore

both beams have to be perfectly aligned. In this setup both beams are automatically aligned, as they pass through the same lens and aperture. So, an ordinary camera without any special modifications can be used, the presence of ambient light is not an issue and the setup is easy and fast. Indeed, both the object and the reference have to be brought in the camera field of view, and optimal exposure time ( $\approx 100 \mu s$ ) and numerical aperture ( $f/8$ ) are chosen. The second advantage is the perpendicular illumination and viewing direction. In this way, shadow artifacts on complex surfaces are avoided and the influence of in-plane displacement components is negligible. The entire setup is placed on an optical table (Newport, RS 3000) so vibration, which may induce length change in the separated interferometer arms, are minimized. A Matlab program controls the phase shifting, the image capturing, performs the correlation, the phase combining, the phase unwrapping and additional filtering. When the displacements are too big so phase unwrapping problems or speckle decorrelation effects occur, an iterative approach, taking new reference images at intermediate deformations, is used. Nevertheless, the intermediate displacements need to remain stable over time for applying this method.

### 4.3.2 Shearography

The shearing of the image is acquired using a Michelson setup with one tilted mirror with angle  $\alpha$  (figure 4.7 and 4.12). The other mirror is attached to a piezo transducer (PI S-303) so phase shifting can be introduced. Both optical paths have to be aligned as described in the DSPI setup. A beam expander with spatial filter is used to expand the laser beam (He-Ne laser,  $\lambda = 632.8nm$ ) and to illuminate the object. A beam splitter is used to acquire a perpendicular illumination and viewing direction so that shadow artifacts are avoided. Finally, a camera (AVT pike F-505) with a polarizer reducing specular reflections, is used.

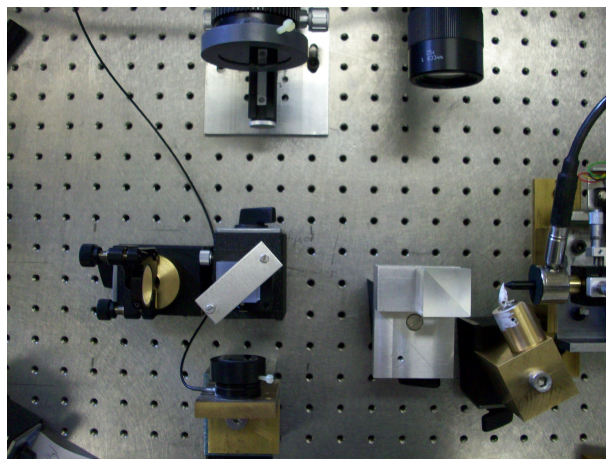


Figure 4.12: Picture of experimental setup of shearography

In order to determine the amount of image-shear, I will use digital image corre-

lation between the speckled image coming from the phase shifted mirror and the speckled image coming from the tilted mirror. A plane is fitted through the values of the x shear and the y shear in order to remove errors. In this way, the shear itself can be obtained fast and accurately. An accurate shear determination is preferable for calculating the displacement without an error accumulation. The same Matlab program as for DSPI is used to control the setup. The pixel size is obtained by either measuring a distance in the sample or by using a graph paper at the open space of the first beam splitter.

### 4.3.3 Deflection of a cantilever beam

In order to test both experimental setups, a fully clamped aluminum plate of  $1\text{mm}$  thickness was loaded with a polished point mounted on a loadcell (Sensotec 31, 5N range) (figure 4.13). The displacement of the point is controlled with a stepper motor (steps of  $1.25\mu\text{m}$ ). An indentation of  $1.25\mu\text{m}$  and  $10\mu\text{m}$  was applied. It should be noticed that the real indentation will be smaller due to the compliance of the loadcell. Two validations for both optical measurements were carried out. First a single-point laser Doppler vibrometer (LDV, Polytec OFV-353 sensor head with OFV-5000 Controller) was used to obtain the displacement on three marked positions. Second, a FE model of the test setup was created [88]. A simple linear material was used and the model was fitted to the LDV displacements. As a consequence, a full field displacement field and derivative of this field was obtained. The results were compared with measurements obtained by DSPI and shearography.

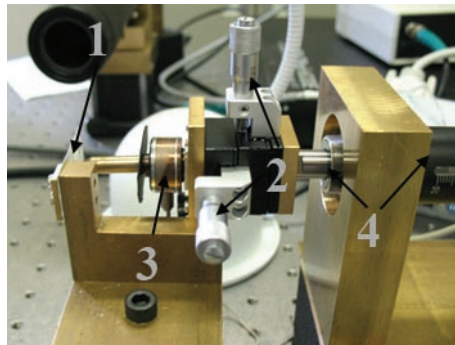


**Figure 4.13:** Sample setup deflection cantilever beam: (1) fully clamped aluminum plate (2) micrometer screws to position loading point (3) Loadcell (4) Stepper motor

### 4.3.4 Beak deformation

The upper-beak of a Java finch (*Padda oryzivora*) was used to test both experimental setups for measuring the displacement and the derivative of small complex bony structures. The head was harvested after scarifying the animal by using  $\text{CO}_2$  gas. Next the covering tissue of the head was removed manually and the other non-bony

parts were removed by using carnivorous beetles. The mechanical properties of the remaining bone and keratin are not affected by the use of these beetles, in contrast with for instance the use of chemical products. A first disadvantage of this technique is the long preparation time and the resulting drying effects. A second issue is the removal of some keratin on the top of the upper-beak. Finally, the lower beak was removed so a polished point, which is mounted on a loadcell (Sensotec 31, 5N range), can freely indent the bottom surface of the upper-beak. The displacement of the point was controlled with a stepper motor (steps of  $1.25 \mu m$ ).

The realistic loading during biting was imitated (figure 4.14) by constraining the jaw bones in a holder filled with polyester resin (VIAPAL 223BS/65) and by applying the biting reaction force with the polished point. This point can be precisely positioned by using a horizontal and a vertical micrometer screw. In this chapter I will impose a displacement at the tip of the beak. The displacements and its derivative on the topside of the upper-beak are recorded with DSPI and shearography and the results of these experiments are discussed. Additional information about the experimental setup of the Java Finch can be found in chapter 6.

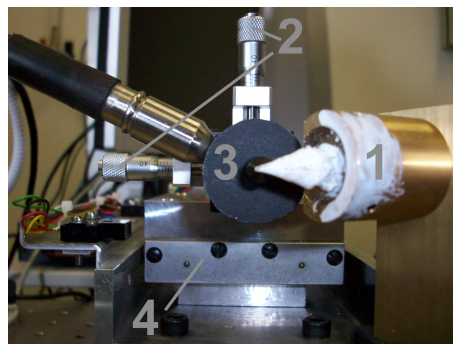


**Figure 4.14:** Sample setup (*Padda*): (1) *Padda* beak constrained in a holder filled with polyester resin (2) micrometer screws to position loading point (3) Loadcell (4) Stepper motor

## 4.4 Results

### 4.4.1 Deflection of a cantilever beam

The results of the displacements of the simple cantilever beam deflection for laser Doppler vibrometer (LDV), DSPI and shearography are shown in table 4.1. The results of the derivative of these displacements, for the FE model, DSPI and shearography are shown in table 4.2. The results are obtained for three different positions (point 1, 2 and 3) and for 2 different induced displacements ( $1.25 \mu m$  and  $10 \mu m$ ). The standard deviations are calculated from five measurements. In addition, the cross-sections of the out-of-plane displacement for DSPI, shearography and the optimized (to LDV) FE model are shown in figure 4.16. The discrete results of the LDV are also indicated. In

figure 4.17 the derivative of these displacements to the x-direction are given for the three techniques.

**Table 4.1:** Displacement of cantilever beam on 3 points with standard deviation for 5 measurements.

Displacement ( $\mu m$ )	pt	LDV ( $\mu m$ )	DSPI ( $\mu m$ )	Shearography ( $\mu m$ )
1.25	1	$0.19 \pm 0.02$	$0.189 \pm 0.003$	$0.18 \pm 0.02$
	2	$0.46 \pm 0.04$	$0.439 \pm 0.004$	$0.44 \pm 0.02$
	3	$0.70 \pm 0.03$	$0.677 \pm 0.002$	$0.70 \pm 0.03$
10	1	$2.41 \pm 0.07$	$2.30 \pm 0.04$	$1.8 \pm 0.2$
	2	$5.32 \pm 0.04$	$5.32 \pm 0.08$	$4.6 \pm 0.2$
	3	$8.07 \pm 0.02$	$8.18 \pm 0.14$	$7.6 \pm 0.2$

**Table 4.2:** Derivative of displacement for a cantilever beam on 3 points with standard deviation for 5 measurements.

Displacement ( $\mu m$ )	pt	FEM ( $10^{-3}$ )	DSPI ( $10^{-3}$ )	Shearography ( $10^{-3}$ )
1.25	1	0.05	$0.067 \pm 0.015$	$0.059 \pm 0.017$
	2	0.07	$0.061 \pm 0.015$	$0.06 \pm 0.02$
	3	0.07	$0.06 \pm 0.03$	$0.080 \pm 0.010$
10	1	0.66	$0.69 \pm 0.06$	$0.67 \pm 0.02$
	2	0.82	$0.82 \pm 0.04$	$0.83 \pm 0.05$
	3	0.85	$0.86 \pm 0.06$	$0.85 \pm 0.02$

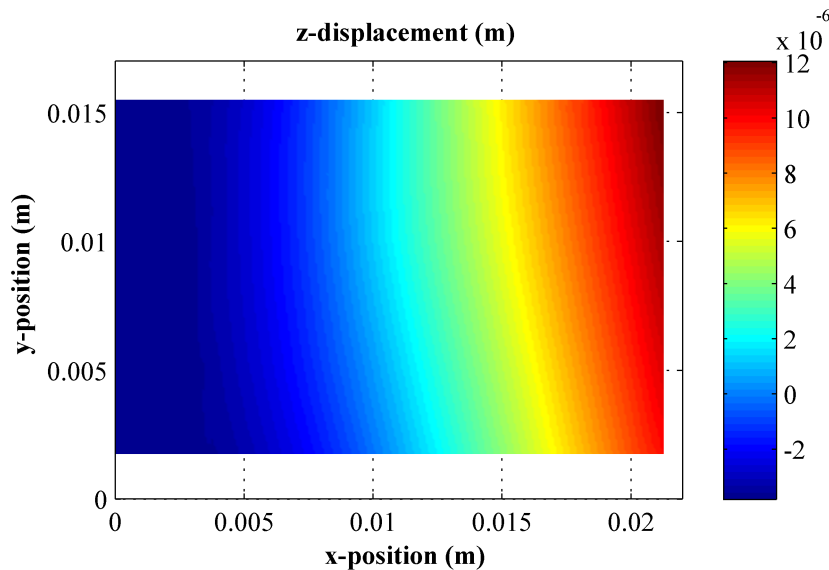


**Figure 4.15:** Out-of-plane displacement of a deflected beam obtained with DSPI.

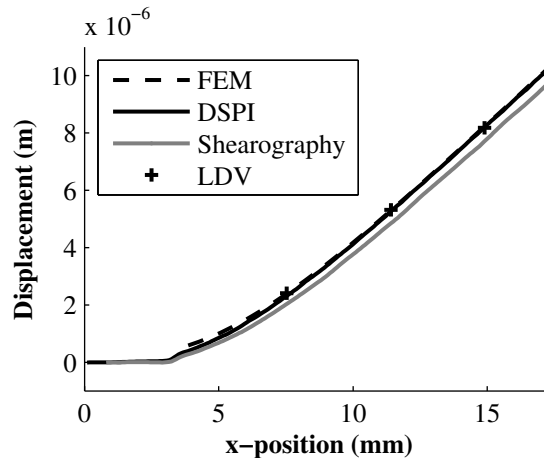


**Figure 4.16:** Out-of-plane displacement of a deflected beam obtained with FEM (optimized for LDV results), DSPI and shearography (for a  $10\mu\text{m}$  displacement).

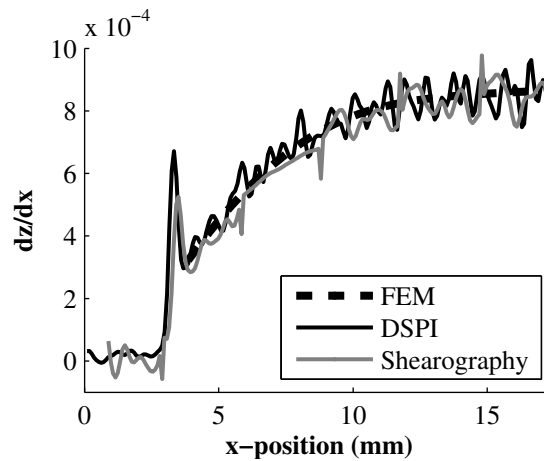


**Figure 4.17:** The derivative of the out-of-plane displacement along the x-direction of a deflected beam obtained by FEM, DSPI and shearography (for a  $10\mu\text{m}$  displacement).

#### 4.4.2 Beak deformation

Figure 4.18 shows the out-of-plane displacement of a Padda's beak for a tip loading of  $3.5\text{N}$ . The displacement is obtained by using DSPI with fifteen intermediate stages. The displacements along the dotted lines, in both longitudinal and transversal direction, are given in figure 4.19 and 4.20. In figure 4.21, the derivative of this longitudinal displacement in the longitudinal direction (x-direction) is plotted. Finally, figure 4.22 shows the displacement for different forces, which are obtained during the fifteen intermediate stages, for the tip of the beak and the cross points indicated in figure 4.18.

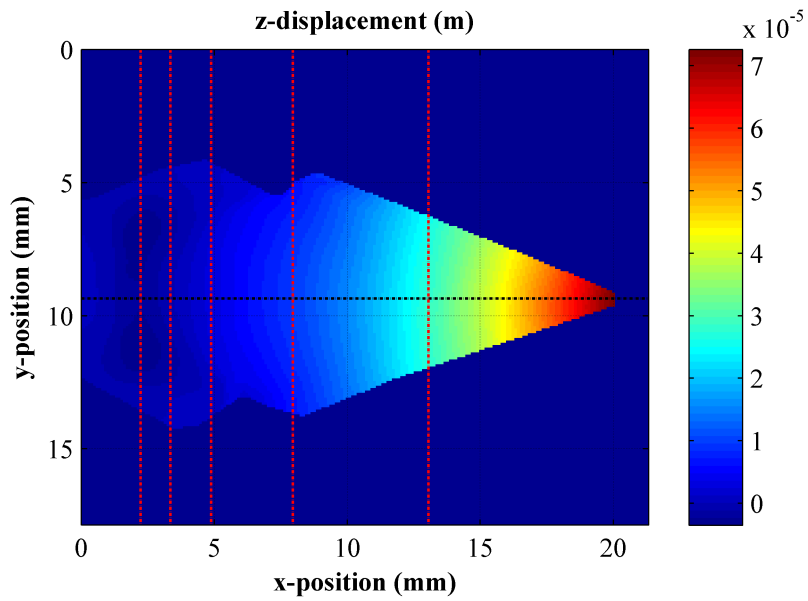


**Figure 4.18:** The obtained out-of-plane displacement for a  $3.5N$  tip loading (colorbar shows the displacements in  $10^{-5}m$ ).

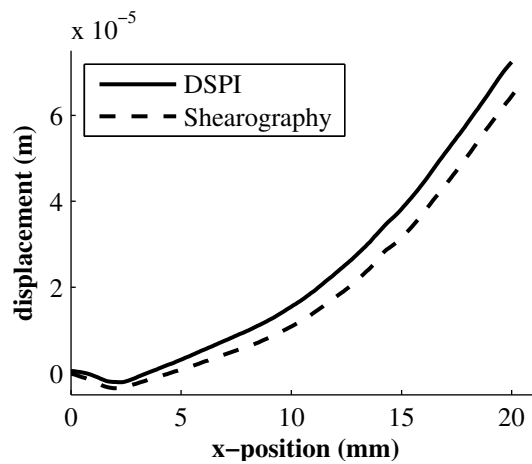


**Figure 4.19:** Displacements of the beak during tip-loading along the longitudinal axis as indicated in figure 4.18.

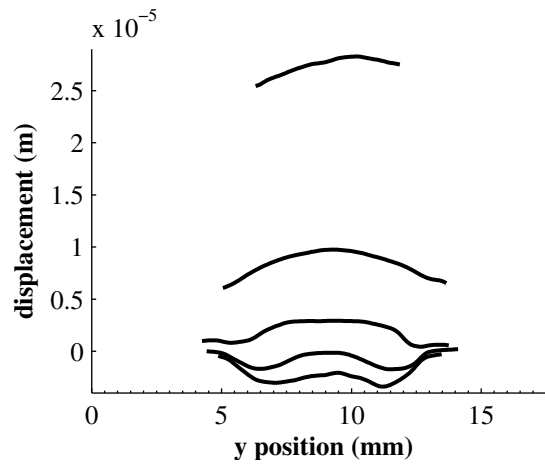


**Figure 4.20:** Displacements of the beak during tip-loading along the transversal axes as indicated in figure 4.18.

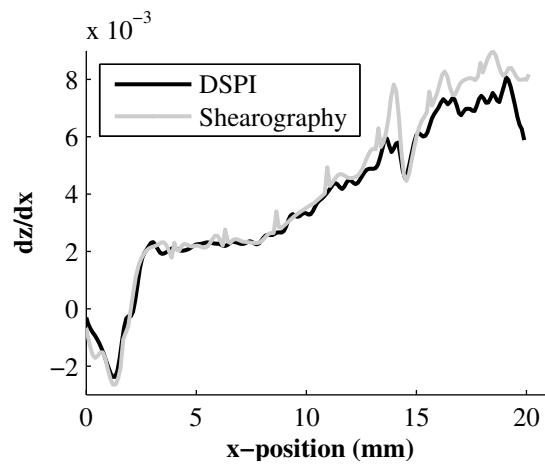


**Figure 4.21:** Derivative (increased with a constant) of the out-of-plane displacement (figure 4.19) along the longitudinal axis

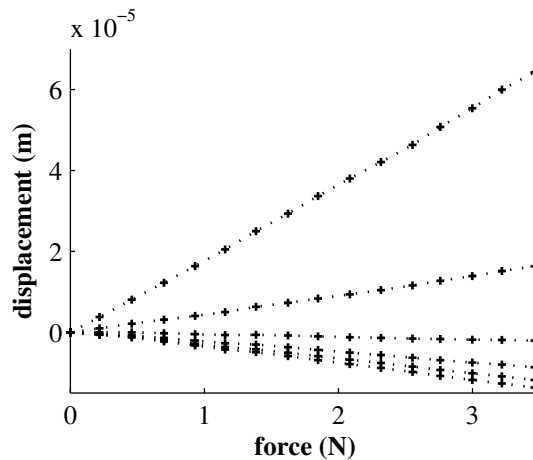


**Figure 4.22:** Displacements for different forces at the cross points indicated on figure 4.18 (the five lowest curves) and the tip of the beak (the highest curve).

## 4.5 Discussion

### 4.5.1 Deflection of a cantilever beam

The results for the displacement are given in table 4.1 and in figure 4.16. The standard deviation for the laser Doppler vibrometer (LDV) values is always smaller than  $0.1\mu m$ . The standard deviation for DSPI is smaller than 2%. The difference with the LDV is for all measurements better than 5%. The small differences between the two methods can be introduced by a positioning error of the LDV laser-point. Furthermore, the displacement of the FE-model, which is fitted to the LDV data, agree well with the experimental results. This FE model is used to calculate the derivative, which is interesting for understanding the mechanics, and to compare it with the experimental results. Table 4.2 and figure 4.17 show the results for the derivative of the out-of-plane displacements along the x-direction. For a small displacement ( $1.25\mu m$ ) the error on the obtained values is quite large (20%). Noise filtering has to be applied to reduce this error, but this will also reduce the spatial resolution. Nevertheless, the curve is smooth enough for larger displacements ( $10\mu m$ ) so the derivative can be calculated precisely (see figure 4.17). The figure indicates a bending between the indentation-point and the fixed constraint. On the other side of the indentation point, a rigid body movement is observed. The DSPI setup has the advantage of giving good results for the out-of-plane displacement by using a simple optical setup. Calculating the derivative is not an issue when smooth results are obtained. Limited displacements due to phase unwrapping problems can be overcome in the experiment because we have a quasi-static behavior. Since the setup is mounted on an optical table, sensitivity to vibrations is also not an issue. However, when one of the above conditions can not be reached, shearography can be a very good alternative.

The standard deviation and the difference with LDV for the displacement obtained with shearography is approximately 10%, which is larger than the results of DSPI. The results for the derivative of the displacement are similar to those obtained by DSPI. For this measurement, I only apply shears in the longitudinal direction. In order to obtain the displacement of a general object, one should perform a shear in two linear independent directions and apply a double integration. In addition, a priori knowledge is necessary to obtain the correct displacement. Indeed, a constant value which is added to the derivative obtained with shearography, will result in an additional unreal rigid body movement and a larger error on the displacement results. In contrast to the displacement results, the results of the derivative match very well with those acquired with FE-modeling. It should be noticed that by skipping equation 4.16, one could obtain a smoother result but with a worse spatial resolution.

This simple bending experiment shows that both DSPI and shearography are suitable for studying the deformations of small bony biomechanical structures. DSPI gives good results for the displacement. The results for the absolute displacement of shearography are less accurate. The derivative of the displacement obtained by both techniques gives very good results to compare with a FE-model.

### 4.5.2 Beak deformation

A beak will actually work as a cantilever: a large biting force has to be applied without damaging the beak and with minimizing the weight of this beak. As a result, one may expect that both imaging techniques, tested on the deflection of the cantilever beam will also work on the upper beak of the Java finch.

Figure 4.18 shows the full field out-of-plane displacement of a Padda's beak obtained with DSPI, during a  $3.5\text{N}$  tip-loading. This load is below the *in vivo* obtained maximum force of  $9 \pm 0.9\text{ N}$  (table 5.2). A maximal displacement of about  $70\mu\text{m}$  on the tip is obtained, and there are no excessive rigid body movements which indicate a good constraining of the sample. For shearography, a slightly different curve, with an additional rigid body movement, is obtained. This effect can be explained to the foreknowledge issue described in section 4.5.1 (figure 4.19). The displacement is too large to measure at once. Therefore, 15 intermediate stages are used. In this way, phase unwrapping problems and speckle decorrelation are avoided. In addition, the intermediate displacement and force, which yield linear force-displacement curves, are also obtained (figure 4.22). The quasi-static requirement is reached and the use of intermediate stages is acceptable since a stable linear response with steady forces is obtained.

On the longitudinal and transversal cross-sections of the out-of-plane displacement on top of the upper-beak, shown in figure 4.19 and 4.20, a negative displacement is observed for x-positions between  $1\text{mm}$  and  $3.5\text{mm}$ . On the transversal cross-section one sees a bending. When studying the derivative along the longitudinal direction (figure 4.21), a bending is observed at the tip of the beak while a rigid body movement is observed at the backside. A small difference between shearography and DSPI is

observed at the tip of the beak. This deviation may be a result of using a slightly different indentation position.

## 4.6 Conclusions

In this chapter, a simple Michelson DSPI and shearography setup to examine the deformation of small complex bony structures are introduced. The proposed Michelson setup is easy-to-use, but can only obtain out-of-plane displacements. The setup has a very high precision, but also needs high interferometric stability requirements. Both techniques are first executed on a simple beam deflection experiment, and validated with LDV. Both full field interferometric setups yield high quality results for the derivative of small displacements. Next, results for tip loading on the Java finch's upper beak are obtained. The results show that both techniques can be an important tool for *in situ* studying of complex and bony structures. Consequently, this technique will be used as validation measurement in chapter 6 and for an inverse analysis in chapter 7.

## **Part III**

## **Results**



---

### The role of keratin in stress dissipation

---

#### **Abstract**

*Bird beaks are layered structures, which contain a bony core and an outer keratin layer. The mechanical role and interaction of both materials in stress dissipation during seed crushing remains unknown. In this chapter, a multi-layered finite element (FE) model of the Java Finch's upper beak (*Padda oryzivora*) is established. Next, the Young's modulus of bone and keratin in this FE model was changed in order to obtain the smallest peak von Mises stress in the upper beak. These theoretically best values for both moduli in the Java Finch correspond well with experimentally obtained values, suggesting that material properties and morphology are tuned to the mechanical demands imposed during seed crushing.*

This chapter is based on:

Soons Joris, Herrel Anthony, Genbrugge Annelies, Adriaens Dominique, Aerts Peter and Dirckx Joris. Multi-layered bird beaks: a finite-element approach towards the role of keratin in stress dissipation. *Journal of the Royal Society Interface*, published online doi: 10.1098/rsif.2011.0910

## 5.1 Introduction

Finite element (FE) analysis is a popular and powerful modeling tool in engineering applications to explore the mechanical consequences of different possible designs. Recently, this technique has found its way to other applications including biomedical engineering and biology, where it is used to gain insight in the mechanical consequences of a given morphology [41, 97, 98, 103, 117]. One of the major advantages of finite element modeling is the possibility of performing *in silico* experiments allowing the theoretical exploration of a morphospace including morphologies of extinct species [97]. Moreover, computer models allow us to compare biological shapes under exactly the same boundary conditions and size, and as such separate pure shape effects from historical or developmental constraints. In chapter 8, the influence of the shape on the beak in Darwin's finches is compared using FE analysis. The use of a FE model will permit us to remove the effects of size, which enabled us to scale the beak virtually to the same dimensions and to apply the same loading and boundary conditions (chapter 8). Similarly, such an approach can be used to isolate the effects of the structural properties of different tissues in multi-layered structures, typical of biological objects.

Bird beaks are a good example of such a multi-layered, natural composite structure. They have to meet some high performance criteria. Indeed, some beaks need to resist large forces during biting or seed crushing, but over-engineering through addition of material may impede efficient flight capacity due to the constraints on mass. The beak not only consists of the beak bone, but also of a surrounding dermal layer with connective tissue and a cellular layer. The latter consists of living cells that keratinize towards the outer side of the beak, leaving a hard, cornified, dead keratin layer at the outer surface of the beak [135]. Epidermis, dermis and bone are anchored to each other with collagenous Sharpey's fibres (bone-dermis interaction) or numerous tissue interdigitations (dermis-epidermis interaction) (pers. obs. Annelies Genbrugge) (Figure 5.1A). Previous work on the composite structure and the mechanical behavior of a Toucan beak was done by Seki and co-workers [111, 112]. They found that the Toucan beak consists of a trabecular bony core, a cortical shell and a keratin shell. An FE model successfully described the deformation and failure of a beak's section under compression. Moreover, a synergy between the foam (trabecular bone) and shell was observed: the energy absorbed by the shell and foam together, is higher than the energy of both separately. In this chapter, we study a granivorous bird (the Java Finch), which uses its beak, in contrast to the Toucan, to crush seeds. In fact my principal interest resides in the mechanical stress exerted on the beak during seed-crushing, and how the beak morphology and constituent materials are tuned to optimizing bite performance.

Therefore I present a multi-layered FE model of the upper beak in the Java Finch (*Padda oryzivora*). The FE model contains the bony core of the upper beak and an outer 'keratin' layer, which is in fact an aggregation of the epidermal and dermal layer (figure 5.1, B, C and D). The keratin layer is attached to the beak bone and both

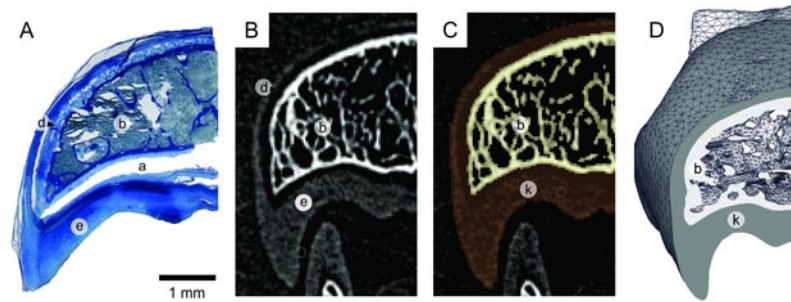


**Figure 5.1:** Transverse cross-section of the Java Finch upper beak. (A) Histological section, (B) CT reconstruction, (C) segmented CT reconstruction and (D) frontal view of transversal cut FE model (see figure 5.2). With (a) artifact, (b) bone, (d) dermis, (e) epidermis and (k) keratin layer in FE model.

bone and keratin FE-elements share nodes at the contact zone (section 2.7). This multi-layered FE model allows me to explore the effects of the material properties of both tissues on the mechanical behavior of the beak. The model geometry was based on CT data and muscle forces are obtained from dissections. An *in silico* experiment, where the elastic modulus of both bone and keratin are changed in order to minimize the maximal VM (von Mises) stress, is performed and allows me to (1) determine the theoretically ideal moduli for bone and keratin and (2) to explore the effects of the material properties of the multi-layered upper beak on the mechanical behavior of the bony core.

## 5.2 Material and methods

The skull of one adult Java Finch (*Padda oryzivora*) specimen was scanned at the European Synchrotron Radiation Facility (ESRF, Grenoble). 2000 x 2000 pixel images with a resolution of  $45\mu\text{m}$  were obtained. The distinction between keratin and bone was clearly visible on the reconstructed CT images (figure 2.8 and 5.1B) and both were segmented using semi-automatcal grayscale thresholding (Amira 4.1; 64-bit version, TGS systems). This means that an automatic segmentation of visually selected grayscale values was followed by a manual correction to reduce artifacts. Grayscale values were selected to incorporate as much material as needed (figure 2.8 and 5.1C). A surface model was obtained after smoothing. Although smoothing is necessary to build up a FE model, we need to take into account that it also removes small features of the model, such as the small trabeculae in the bony core (Figure 5.1D). Delaunay tetrahedralization was performed in the ‘Tetgen’ software package [114]. After conducting the convergence test (better than 5%) for the presented results (displacement, force, von Mises stress), a tetrahedral grid of approximately 1188k elements was generated. This convergence test is needed to find a FE mesh that is fine enough to produce accurate results. In our case a further refinement would have introduced a large computational cost, but would not change the results by more than 5%. Next, the mesh was imported

in FEBio, a FE program designed for the mechanical analysis of biological structures [88].

In the physiological FE model (figure 5.2), the elastic modulus was set at 7.3 GPa for fresh bone and 1.7 GPa for fresh keratin (average of inverse analysis in chapter 7 and double indentation technique in section 3.3.3). It should be noted that the anisotropy of bone is not considered in the model. Given the small size of these biological samples, it was impossible to measure the anisotropy experimentally. As a result, the Young's modulus along the loading direction, the longitudinal axis, might be underestimated. Nevertheless, the validation measurements (chapter 6) will show a good agreement, indicating that the chosen moduli are indeed appropriate. The Poisson's ratio for both materials was set at 0.4 [46, 141], although no experimentally determined values were available for avian bone and keratin. Both the beginning of the skull near the bending area and the bite point were constrained for both translation and rotation (figure 5.2). Constraining the bite point mimics a food reaction force. The bite point was based on *in vivo* observations of birds cracking seeds.

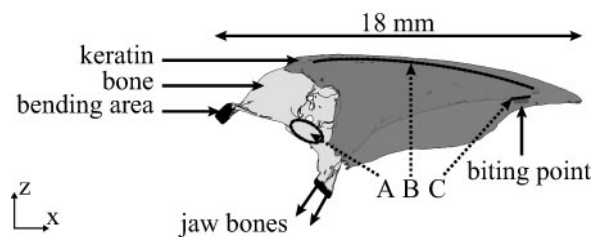


**Figure 5.2:** Schematic representation of the multi-layered physiological FE model of the Java Finch's upper beak. In the physiological FE model, the bending area and the biting point are constrained and muscle forces are applied on the jaw bones (in the direction of the arrows). The maximum stress at four locations is recorded: posterior right and left on the nasal bone (A), on top of the upper beak's bony part (B) and at the bottom of the bony core, above the bite point (C).

Muscle forces were obtained through dissection using a stereo-microscope (Olympus SZX7). For four Java Finches all jaw muscle bundles were removed individually during the dissections. Muscles were blotted dry and weighed using an OHAUS Adventurer microbalance ( $\pm 0.1mg$ ). Muscles were transferred to a 30% aqueous nitric acid solution for 24h to digest the connective tissue and transferred to a 50% aqueous glycerol solution [85]. Fibers were teased apart using blunt-tipped glass needles and were photographed with a Nikon d40x digital camera with macro lens. Based on the digital images, the fiber lengths were measured in the software program AnalySIS 5.0 (Soft Imaging System GmbH, Germany). Muscle physiological cross-sectional area (PCSA) of each muscle bundle was calculated by dividing muscle mass (g) multiplied by  $1.065g/cm^3$  (muscle density [89]) by fiber length (cm). The force generation capacity for each muscle was calculated by multiplying the PCSA ( $cm^2$ ) by  $25N/cm^2$  (muscle stress) [93]. The muscle mass, muscle fiber length, PCSA, and force generation capacity of each muscle bundles involved in jaw closing are listed in table 5.1. As the

external adductor and pseudotemporalis muscles act only indirectly on the upper beak [15, 52, 94, 132, 133], the component of the muscle force transferred to the upper beak was calculated taking into account the position of the muscles and their angles relative to the jugal bone. The pterygoid muscle bundles act directly on the upper beak [15, 52, 94, 132, 133], and muscle forces were assumed to be directly transmitted through the pterygoid/palatine complex.

In order to validate the model output, the bite force data of five Java Finches were measured using a piezoelectric force transducer (type 9203, Kistler Inc., Switzerland; 500 N) mounted in a custom-built holder, and connected to a portable charge amplifier (Kistler, type 5059A). A detailed description of this setup is available in Herrel et al. [63, 64, 66].

The FE model allows me to calculate the displacements of the nodes and the stresses on the elements. Stresses larger than the material strength will result in material failure. The maximum stress on the bone of the upper beak is biologically more interesting than the stress on keratin. Indeed, as the rhamphotheca can repair itself well [68], bone fracture is much more serious. The distortion energy theory, also known as the von Mises-Hencky theory, was chosen to estimate fracture loads because it is a reliable way to overcome difficulties in the interpretation of the complex stress-field [76] (eq. 2.36). The ratio of the strength of bone ( $\sigma_{ubone}$ ) to the peak VM stress ( $\sigma_{peakVM}$ ) is called the safety factor. Materials with a low safety factor ( $< 1$ ) are subjected to material failure, materials with too high safety factors are over-engineered and incur an extra cost in terms of material and/or energy. The Young's modulus of a bony material can be correlated with both its strength and its density [13, 49]. Fyhrie and Vashishth [49] obtained a linear relation between the Young's modulus of bone ( $E_{bone}$ ) and its ultimate strength ( $\sigma_{ubone}$ ), resulting in the following safety factor (SF):

$$SF = \frac{\sigma_{ubone}}{\sigma_{peakVM}} = 0.0061 \frac{E_{bone}}{\sigma_{peakVM}} \quad (5.1)$$

I want to explore how the elastic moduli for bone and keratin affect the peak stress in the entire upper beak. Moreover, I want to find which pair of moduli gives the lowest stress, and can thus be considered as 'the best'. Insights can be gained using a surrogate model. Such a surrogate model will yield a peak stress of the upper beak FE model for a given modulus of bone and keratin. Therefore, the FE model is calculated for several pairs of moduli and one obtains a surrogate model as presented in the results section (figure 5.3).

In the presented FE model, both the bony core and the keratin layer were modeled as linear elastic materials. The Young's modulus of both materials is the input variable for the model. The moduli can be changed and a corresponding output is obtained. As output, the peak VM stress in four different regions of the upper beak FE model was recorded: at the bottom of the bone close to the bite point (A, figure 5.2), on top of the bone (B) and posterior right and left on the nasal bone (C). Areas with high stresses close to areas that are constrained in the model, such as the bending area, were ignored. Four surrogate models were established to connect a set of elastic moduli of bone and keratin with the peak VM stresses for the four selected locations

**Table 5.1:** Summary of muscle mass, fiber length, physiological cross-sectional area (PCSA), and force generation capacity of the jaw adductor muscles in the Java Finch (N = 4). Muscles indicated in bold are assumed to be maximally active during the crushing of seeds (table entries are means  $\pm$  standard deviations).

	Muscle mass (mg)	Fiber length (mm)	PCSA (cm <sup>2</sup> )	F (N)
M. depressor mandibulae	12 $\pm$ 2	3.3 $\pm$ 0.3	0.033 $\pm$ 0.010	0.82 $\pm$ 0.13
<b>M. adductor mandibulae externus rostralis</b>	23 $\pm$ 3	1.46 $\pm$ 0.08	0.15 $\pm$ 0.02	3.7 $\pm$ 0.6
<b>M. adductor mandibulae externus ventralis</b>	3.9 $\pm$ 1.0	1.28 $\pm$ 0.14	0.029 $\pm$ 0.010	0.71 $\pm$ 0.18
<b>M. adductor mandibulae externus profundus</b>	8.9 $\pm$ 1.9	1.35 $\pm$ 0.13	0.062 $\pm$ 0.010	1.54 $\pm$ 0.26
<b>M. adductor mandibulae ossis quadrati</b>	2.9 $\pm$ 1.4	1.6 $\pm$ 0.3	0.016 $\pm$ 0.10	0.41 $\pm$ 0.19
<b>M. pseudotemporalis superficialis lateralis</b>	3.4 $\pm$ 1.9	1.4 $\pm$ 0.5	0.023 $\pm$ 0.010	0.6 $\pm$ 0.3
<b>M. pseudotemporalis superficialis medialis</b>	4.4 $\pm$ 1.6	1.4 $\pm$ 0.5	0.03 $\pm$ 0.02	0.8 $\pm$ 0.4
<b>M. pseudotemporalis profundus</b>	7.1 $\pm$ 1.3	2.6 $\pm$ 0.5	0.027 $\pm$ 0.010	0.67 $\pm$ 0.14
<b>M. pterygoideus ventralis lateralis</b>	10 $\pm$ 3	2.02 $\pm$ 0.12	0.048 $\pm$ 0.010	1.2 $\pm$ 0.3
<b>M. pterygoideus ventralis medialis</b>	5 $\pm$ 2	2.13 $\pm$ 0.11	0.021 $\pm$ 0.010	0.5 $\pm$ 0.3
<b>M. pterygoideus dorsalis lateralis</b>	18 $\pm$ 3	2.0 $\pm$ 0.3	0.083 $\pm$ 0.010	2.1 $\pm$ 0.3
<b>M. pterygoideus dorsalis medialis</b>	7.5 $\pm$ 1.8	1.7 $\pm$ 0.3	0.042 $\pm$ 0.010	1.1 $\pm$ 0.3
<b>M. retractor palatini</b>	6.4 $\pm$ 1.6	2.2 $\pm$ 0.4	0.028 $\pm$ 0.010	0.7 $\pm$ 0.2
<b>M. protractor pterygoidei et quadrati</b>	3.8 $\pm$ 1.0	2.06 $\pm$ 0.08	0.017 $\pm$ 0	0.43 $\pm$ 0.10

recorded at the level of the bone. Afterwards, an optimal set of moduli, which yields a minimal peak VM stress, is selected and the impact of the elastic moduli on stress is examined.

### 5.3 Results

The results for tip loading of five Java Finches and its average are presented in table 5.2. An average of  $9.0 \pm 0.9N$  for five Java Finches was measured. In the FE model, I obtained the vectorial components of the forces  $F_x, F_y, F_z = 2.2N, 0N, 6.5N$ , resulting in a total bite force of  $6.8N$ , which is somewhat lower, yet reasonably close to the observed *in vivo* bite forces (see discussion).

**Table 5.2:** Bite force at the tip of the beak measured *in vivo* (Padda 1-5), the average ( $\pm$ stdev) for the five specimens and the corresponding bite force derived from the FE model are also given. Table entries are in *N*.

	P1	P2	P3	P4	P5	Average	FE model
Tip bite force (N)	9.7	7.5	9.3	8.7	10	$9.0 \pm 0.9$	6.8

The surrogate model, relating the Young's modulus of bone and keratin with the maximal VM stress in bone is presented in figure 5.3. The maximal stress is obtained by calculating the maximum of the stress at the four selected locations (A, B and C in figure 5.2). The curves in figure 5.4 are the peak VM stress (y-axis) on those four selected locations for a constant bone modulus of 7.5 GPa and a changing keratin modulus (x-axis) and represent the results along the dotted line in figure 5.2. The peak VM stress, however, hardly changes for different moduli of bone. Nevertheless, it is known from eq. 5.1 that the strength and modulus of bone are linearly correlated, resulting in a strength of 45 MPa for a Young's modulus of 7.3 GPa. Consequently, a linear fit between the safety factor for bone and its modulus is also found (eq. 5.1). Therefore, the safety factor of bone is plotted as function of its modulus in figure 5.5.

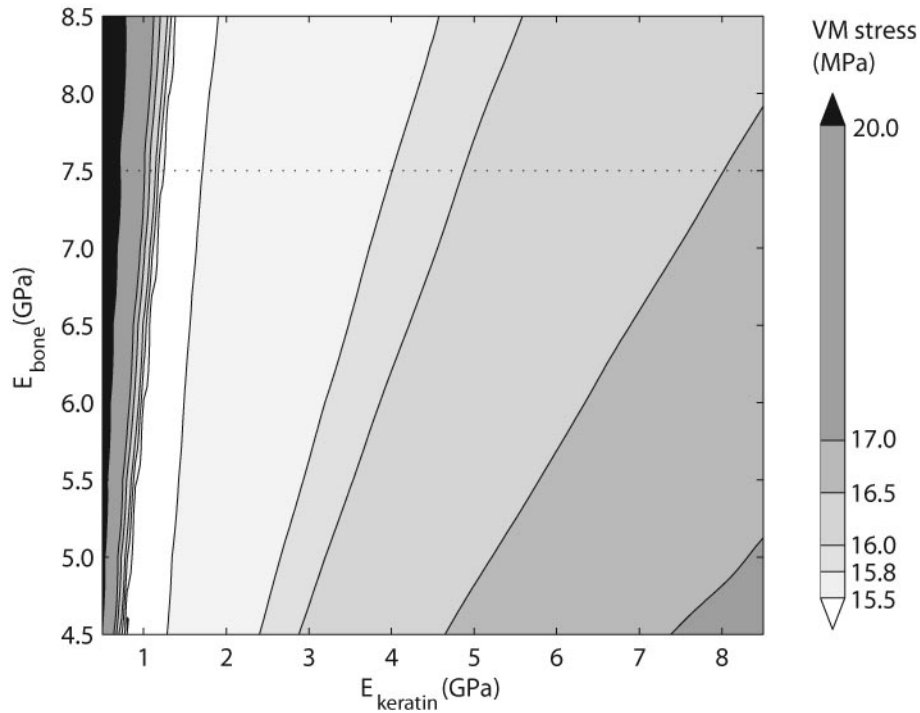


**Figure 5.3:** Peak von Mises stress (Pa) in bone for different moduli of the bony core ( $E_{bone}$ ) and the keratin layer ( $E_{keratin}$ ).

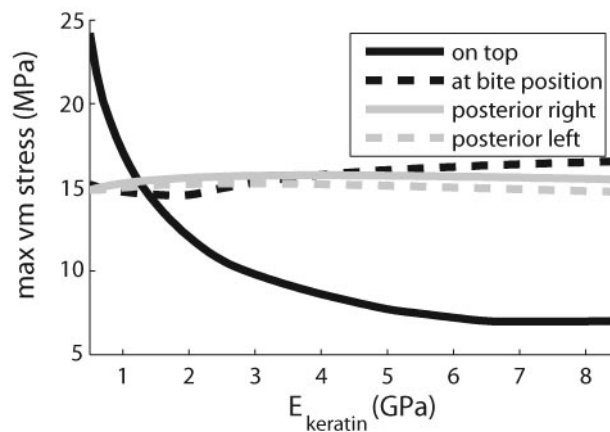


**Figure 5.4:** Peak von Mises stress results following the dotted line in figure 5.3 (as a function of the keratin modulus, for a fixed  $E_{bone} = 7.5$  GPa) at four different positions on the bone: on top, at bite position, posterior right and left (as indicated in figure 5.2).

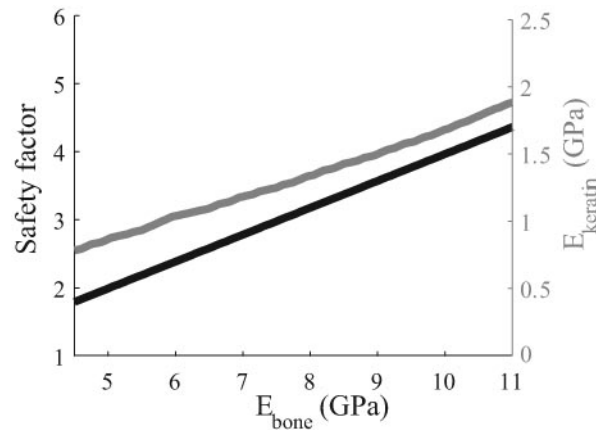


**Figure 5.5:** The relationship between the modulus of bone ( $E_{bone}$ ) and the corresponding modulus of keratin ( $E_{keratin}$ ) used to find the minimal peak VM stress in the model (gray line) and the safety factor of this corresponding minimum (black line) (see eq. 5.1).

The smallest peak VM stresses of approximately 15 MPa are found in an oblique valley in the surrogate model, with keratin moduli ranging from 0.8 GPa to 1.9 GPa (figure 5.3). When looking at different bone moduli, one will find slightly different keratin moduli to obtain the minimal peak VM stress ( $\pm 15$  MPa). For example, the minimal peak VM stress for a bone modulus of 5 GPa is found for a keratin modulus of 0.9 GPa. For a bone modulus of 11 GPa, a 1.8 GPa keratin modulus is found. This pair of optimal values for the modulus of bone and keratin is also shown as the gray line in figure 5.5.

As an example, three FE models of the Java Finch with natural loading conditions are presented in figure 5.6. The Young's modulus of bone in all these models is 7.5 GPa. Three different moduli for keratin are chosen:  $E_{keratin} = 0.5$  GPa, 1.6 GPa and 6.5 GPa. The color plot indicates the resulting VM stress on bone with warmer colors representing higher VM stresses. Finally, I also indicate the resulting force at the bite point. For softer keratin, this force is directed more towards the back of the beak. For  $E_{keratin} = 0.5$  GPa, 1.6 GPa and 6.5 GPa I found forces of 7.5N, 6.8N and 6.6N respectively with lower Young's moduli being associated with higher forces.

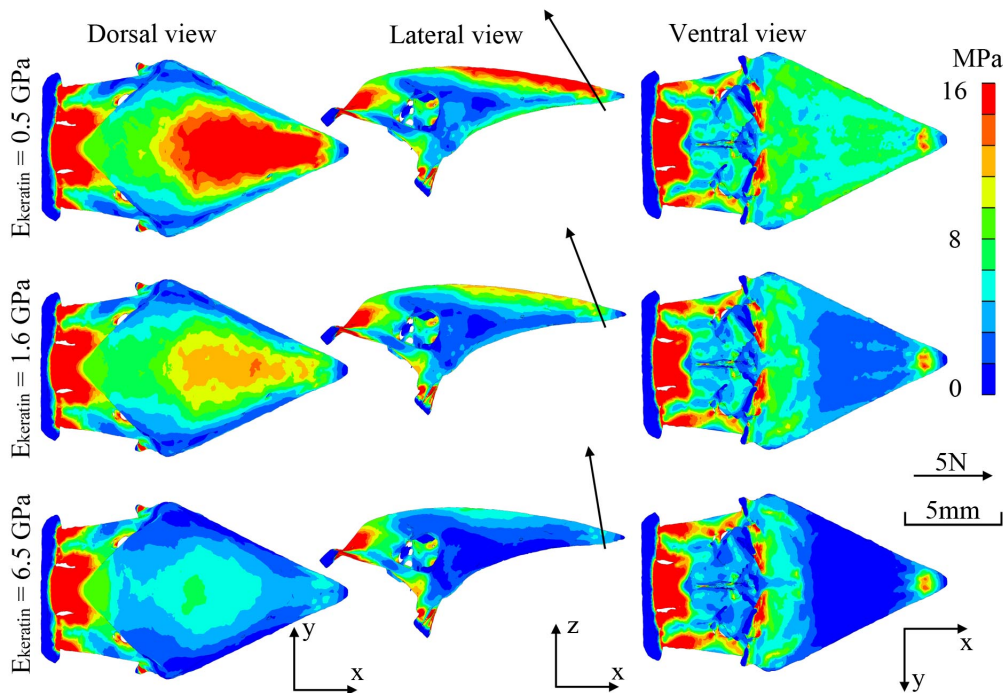


**Figure 5.6:** Dorsal, lateral and ventral view of the von Mises stress on the bony core of the upper beak of the Java Finch, for  $E_{bone} = 7.5$  GPa and  $E_{keratin} = 0.5$  GPa (1st row), 1.6 GPa (2nd row) and 6.5 GPa (3rd row). Note that the keratin layer is not shown. The resulting bite force is also presented.

## 5.4 Discussion

If we compare the resulting bite force calculated in the model with bite force measured *in vivo*, a lower bite force is obtained in the FE model, but the relative difference with the average value of five *in vivo* samples is smaller than 25% (note that the difference with Padda 2, for example, is less than 10%). This result seems acceptable, since the mean relative standard deviation of the model input forces (table 5.1) is almost 30% due to variation in muscle cross-sectional area in the individuals examined. In addition, results on Darwin's Finches (chapter 8: table 8.1) show that with this technique there is no systematic over- or underestimation of bite force. Hence, the model and the chosen boundary conditions appear realistic. However, several FE models, with different stress fields, will produce similar forces (figure 5.6) and thus ideally additional validation measurements are required. Such validation measurements are treated in chapter 6.

The surrogate model in figure 5.3 shows for every modulus of bone and keratin the highest peak VM stress on the four selected regions (figure 5.2). This peak VM stress is an important value to obtain the safety factor (eq.5.1). First the influence of the keratin modulus on this peak VM stress is explored. Therefore the bone modulus is

fixed at 7.5 GPa and the keratin modulus is changed. The peak VM stress is recorded at four different regions (indicated as A, B and C on figure 5.2) and are shown in figure 5.4. VM stress are not recorded at the bending area, because a much larger stress is expected due to the absence of the supporting bone of the skull in the model. As an example, the FE models for this bone modulus of 7.5 GPa and for keratin moduli of 0.5 GPa, 1.6 GPa and 6.5 GPa are presented in figure 5.6.

On the bottom view of figure 5.6, differences between the different models for the maximum VM stress close to the bite point (C in figure 5.2) are barely visible. This behavior can also be seen in figure 5.4, represented by an almost horizontal, black dashed line.

The peak VM stresses posterior right and left on the nasal bone (A in figure 5.2) also seem to be largely independent of variation in the keratin modulus (both gray lines in figure 5.4).

On the top view of figure 5.6, however, one can see a large variation in stress for the three models. A smaller elastic modulus for keratin will result in a higher peak stress on top of the upper beak and vice versa. This relationship is also visible upon inspection of the black line in figure 5.4). In addition, the FE models show a shift of the position of the peak stress region. Indeed, increasing the keratin modulus (e.g. from 1.6 GPa to 6.5 GPa) will shift the peak stress on top of the upper beak from the tip more to the center of the beak. In general, for all recorded locations, one can see a rapid increase in peak VM stress for keratin moduli smaller than 1 GPa (black line in figure 5.4) and an almost flat relation for moduli larger than 1.7 GPa (dotted and gray lines in figure 5.4). On the other hand, increasing the modulus of keratin probably has an effect on its density [13], which introduces a limiting factor for high keratin moduli. For a bone modulus of 7.5 GPa, a keratin modulus of approximately 1.3 GPa appears to be optimal if one assumes a requirement of a minimal peak VM. It is clear that the value of the keratin modulus has an impact on the VM stress detected at the level of the bony core, indicating the importance of selecting proper material properties in a multi-component FE model. The results also emphasize the biological role of keratin in complex multi-layered structures such as bird beaks. Indeed, the resulting bite force of the three FE case studies differs slightly in magnitude and orientation. A stiffer keratin modulus results in a smaller bite force. More interestingly, the direction of the bite force is more perpendicular to the biting surface for stiffer keratin. As a consequence, shear forces are kept minimal.

Finally, I examined the dependency of the VM stress upon the bone modulus. In the surrogate model (figure 5.3), a minimal VM stress of approximately 15 MPa is found for every bone modulus. This minimal VM stress has a slightly different keratin modulus for every bone modulus (see gray line in figure 5.5). Nevertheless, one can expect a change in the bone strength for the different bone moduli and thus a change in the safety factor. Indeed, the material strength is, besides the peak VM stress, also an important value to obtain the safety factor. Literature values for cortical bone strengths range from 106 to 244 MPa over a wide range of vertebrates [26, 137, 142]. On the other hand, a close correlation between Young's modulus, density and strength of

both cortical as well as cancellous bone has been proposed [49], resulting in a strength which linearly depends on the modulus (e.g. 45 MPa for a Young's modulus of 7.3 GPa). Consequently, the safety factor corresponding to a certain modulus of bone can be obtained using eq. 5.1. The results for the surrogate model are plotted as the black line in figure 5.5. Blob and Biewener [8] summarized safety factors for biological materials that ranged between 2 and 4 for tetrapod limb bones. Therefore, I supposed a safety factor of 3 for the upper beak bone, resulting in a bone modulus of 7.5 GPa and a corresponding keratin modulus of 1.3 GPa. The moduli show a good correspondence with those obtained experimentally with the double indentation technique in section 3.3.3, namely  $E_{bone} = 7 \pm 2$  GPa and  $E_{ker} = 1.7 \pm 0.4$  GPa.

The absolute results reported here should be treated with some care. First, the linear relation between bone strength and modulus, obtained by Fyhrie and Vashishth [49], has never been tested for avian bone. The linear relationship is acquired for standardized test on both cortical bone and cancellous bone samples. In this case, the cancellous and cortical bone are not separately loaded, but in parallel. As a consequence, this linear relation may not be met, but a similar correlation between modulus, strength and density can be expected. Moreover, a safety factor of three is presumed, but the exact value remains unknown. Nevertheless, even despite those assumptions, the relative outcome and the main conclusion remains valid.

## 5.5 Conclusions

It was shown that the constituent materials of multi-layered bird beaks are well tuned for biting. Indeed, the physiological elastic modulus of bone and keratin (chapter 7 and section 3.3.3) yields the lowest peak stress during bending. On the other hand, the presented model shows that higher moduli, probably increasing the beaks mass, have no effect on the maximal stress. As a result, the whole construction results in a high stiffness to weight ratio. In normal sandwich-structured composition for instance, this high stiffness to weight ratio is achieved by a high elastic modulus of the face-sheets. In the Java Finch's beak, a foam structured spongy bone in the center is also surrounded by stiffer compact bone. But, an extra, softer keratin layer surrounds the brittle bony core, potentially to protect it from impact loading for instance. This brittle behavior was observed by removing the keratin layer in the validation experiment. A similar loading as used before, resulted in the rupture of the bony core. For impact loadings, the time dependent properties of the material parameters will become important and thus the mechanical behavior may be significantly different compared to static loading cases. Dynamic and transient loading experiments are needed to investigate the behavior of the system when it is subjected to impact forces, and this will be subject for further research. Nevertheless, my results indicate that morphology and material parameters are well suited to support bending and therefore to perform tip biting in the Java Finch.

## CHAPTER 6

---

### Validation experiments

---

#### **Abstract**

*In this chapter two easy to build optical setups for the validation of biomechanical finite element models are presented. Digital speckle pattern interferometry (DSPI) is an interferometric technique with a very high sensitivity (20nm), but also high stability requirements, making it hard to use outside an optical laboratory and on living samples. Three-dimensional digital image correlation (DIC) is a less sensitive, highly scalable and robust photogrammetric technique. Here I apply both techniques to validate the finite element model of the Java finch (chapter 5). DSPI can measure very small deformations (5 $\mu$ m) with high signal-to-noise ratio, but it can only be applied for small displacements. DIC needs larger displacements (125 $\mu$ m), is much more flexible and can be easily used as a full field optical strain gauge.*

This chapter is based on:

Soons Joris, Herrel Anthony, Genbrugge Annelies, Adriaens Dominique, Aerts Peter and Dirckx Joris. Multi-layered bird beaks: a finite-element approach towards the role of keratin in stress dissipation. *Journal of the Royal Society Interface*, published online doi: 10.1098/rsif.2011.0910

Soons Joris, Lava Pascal, Debruyne Dimitri and Dirckx Joris. Full field optical deformation measurement in biomechanics: digital speckle pattern interferometry and 3D digital image correlation applied on bird beaks. *In preparation*

## 6.1 Introduction

Finite element modeling has proven to be an important tool in biomechanics (chapter 5 and 8) [17, 32, 41, 60, 79, 103]. It allows us to understand complex problems. In chapter 5 for instance, I used FE modeling to understand the stress dissipation in the complex multi-layered beak of the Java finch. An important step in a good FE analysis is a relevant validation measurement. Strain gauges are a well-known and straightforward validation experiment [79, 103], but they have some major disadvantages. They are attached to the sample, which may influence the measurement and its installment is also time consuming and difficult, especially on small and complex structures, such as the beak of finches. Moreover, only discrete information is obtained. These issues can be overcome by using optical techniques. In this chapter, I will show the results obtained with two easy to build full field methods: out-of-plane digital speckle pattern interferometry (DSPI) and digital image correlation (DIC). The results of bending of the Java finch's upper beak will be compared with FE model results and as such validating the FE modeling approach used in this thesis. The presented techniques are applicable in a wide range of biomechanical problems.

Both techniques rely on speckles. The nature of the used speckles is, however, completely different. In DSPI a speckled image is obtained by diffuse reflections of coherent light whereas in DIC a speckled pattern is physically applied to the object. DSPI is an interferometric setup. An object illuminated with coherent light will show a speckle pattern. These patterns are caused by interference due to the random variation of the surface. If this speckle pattern is combined with a reference beam, a complex interference pattern is obtained. After a deformation of the object, phase differences are introduced on this complex interference pattern. These phase differences can be linked to the displacement. If the displacements is measured in three different (linear independent) directions, and the surface shape is known, one can calculate the surface strains. The very high sensitivity (sub-wave length resolution) makes it a valuable tool for non-destructive testing. The sensitivity is independent of the pixel size. The pixel size determines the number of phases that can be resolved and as such the maximum permissible displacement. The high sensitivity requires sub-wavelength stability and makes it difficult to apply this technique outside the optical lab or *in vivo*. Recently, DSPI has been introduced in biomechanics. Some examples are found in literature, including the displacement of the tympanic membrane [33], the strains on the mouse femur [144] the ovine callus [14], the human mandible [60] and Zygomatic Arch of the pig [17].

DIC, on the other hand, is a photogrammetric setup. Coordinates of points, labeled by a randomly applied stochastic (speckled) pattern are captured with a camera and identified with a computing intensive image correlation. These points are followed when the object is deformed and displacements are acquired with sub-pixel resolution. Three-dimensional surface results can be acquired using a stereo camera system. The optical setup is straightforward and there are no interferometric stability requirements, making this technique easy to use, scalable, highly usable for applications outside the

lab and for measurements in biomechanics. Increasing computer power makes this technique more popular [107] and recently also results in biomechanical applications: including strains on bone and tendon [131], on mouse arteries [124] and on mouse bone [125].

## 6.2 Material and methods

### 6.2.1 Bending experiment

It is difficult to constrain the biting position and applying the (muscle) forces on the tiny jaw bones of the Java finch's upper beak, especially if interferometric stability is required. Hence I work the other way around and I propose a bending experiment to mimic tip biting (figure 6.1). In this experiment the jaw bones and the skull are constrained in a sample holder filled with cured polyester resin (VIAPAL 223BS/65). Feathers, muscles and brain were removed and the back of the skull was dried with ethanol to obtain a good bonding with the casting resin that is used to fixate the skull in a specimen holder (figure 6.2). The lower beak was removed, allowing me to position the polished point and introduce the seed reaction force (steps of 16 nm per motor step, range 2mm, PI M-235.2DG) at the tip of the beak. The reaction force was measured with a loadcell (Sensotec 31, 5N and 50N range). A curing time of minimal 48 hours was taken.

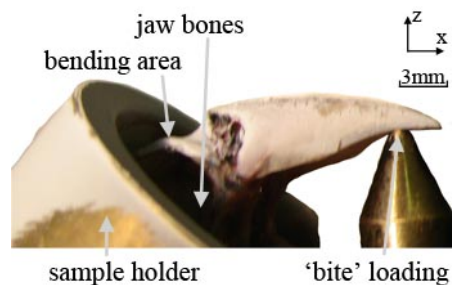


**Figure 6.1:** Experimental setup. The skull and jaw bones of a Java Finch are constrained in a sample holder, filled with polyester resin. The seed reaction force is mimicked by a indentation at the tip of the upper beak.



**Figure 6.2:** Preparation of sample for validation measurement.

### 6.2.2 Digital speckle pattern interferometry

DSPI was used to measure the displacements of the upper beak. This sensitive measurement technique precisely quantifies the out-of-plane displacement over the entire surface of this small object. The experimental setup is shown in figure 6.3 (more information can be found in chapter 4). Nevertheless, my custom-made DSPI does not allow me to measure the sample 3D topography and in-plane displacement components, such as the  $x$  and  $y$  (figure 6.4). As a consequence I was unable to calculate the strains *in vitro*. The sensitivity of the technique also causes some practical issues. First, *in vivo* experiments are not possible. In addition, the entire setup should be placed on a vibration-isolated optical table. Applying the muscle force on the jaw bones in an experiment is very difficult. Therefore, I presented the bending experiment in the previous section and introduced a force at three different positions: the center of the beak, the tip of the beak, and the rostral-most part of the keratinous upper beak, where there is no supporting bony core (locations are indicated on figure 6.4). Measurements on fresh keratin gave noisy results, indicating that the nanometer stability requirement for DSPI was not totally met, and these measurements could not be used (figure 6.5). This can be explained by the low light reflectance and the instability, probably due to creep, of the surface.

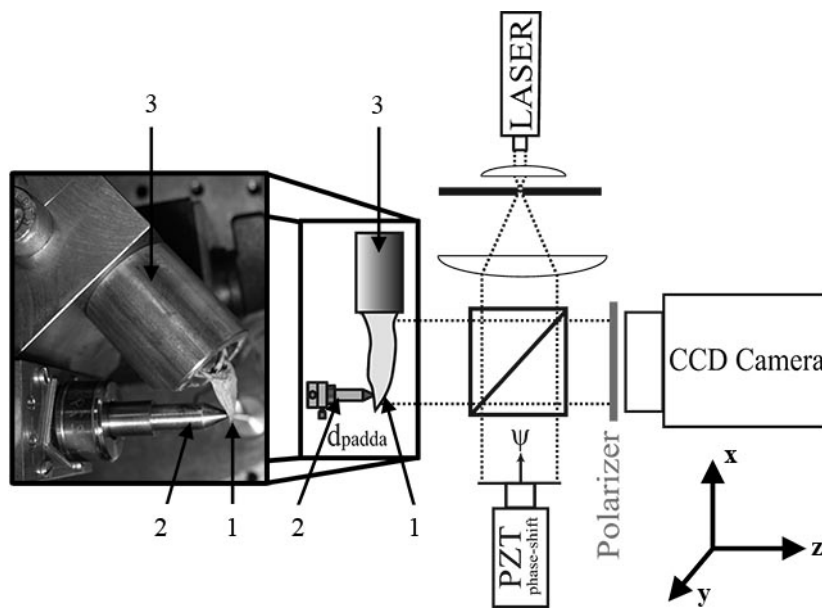


**Figure 6.3:** Bending experiment and DSPI setup: (1) upperbeak, (2) polished indentation point mounted on loadcell and (3) sample holder filled with polyester resin.

Consequently, the validation was performed on dry samples. The resulting reaction force was measured with a load cell (Sensotec 31, 5 N) and the resulting out-of-plane displacement, on top of the upper beak (on top of keratin) was acquired with a custom-made DSPI setup. Next, the derivative of this  $z$ -displacement (out-of-plane) along

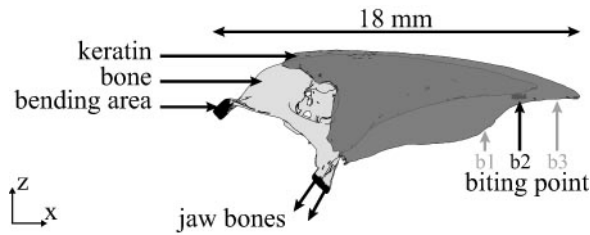


**Figure 6.4:** Schematic representation of the multi-layered FE model of the Java Finch's upper beak. For the three validation FE models, both the jaw bones as the bending area are constrained and a force is applied at three different positions: the center of the beak (b1), the tip of the beak (b2, natural loading position), and the rostral-most part of the keratinous upper beak (b3).

the x-direction was taken since it is a better parameter to describe bending experiments. Indeed, the derivative of a rigid body movement, which is not interesting from a mechanical point of view, will yield a constant [83] (see section 7.3.2). A high quality result is necessary to calculate this derivative, so the signal-to-noise ratio was improved by using a magnesium oxide coating to obtain a better light reflectivity and by performing each experiment 20 to 100 times. In order to combine these measurements, the displacements need to be divided by the imposed force. The upper beaks of three individuals were loaded on three different locations (b1, b2 and b3 in figure 6.4). Finally, the results for these three Java Finches were averaged. Since those beaks have approximately the same size, an average value could be calculated.

### 6.2.3 Validation finite element model

The geometry of the FE model was established as described in chapter 5 (section 5.2). The constraints, the applied forces and the material properties, however, are different for this validation FE model. The beginning of the skull, near the bending zone, and the jaw bones were both constrained for translation and rotation (the constrained elements are black in figure 6.4). A loading (the virtual reaction force) was introduced by applying a  $1N$  force on the corresponding elements at the bite position. In this way, I work around the experimental difficulties of applying the muscle forces on the jaw bones. The elastic modulus of dry bone and dry keratin is obtained in chapter 7 (inverse analysis) and section 3.3.3 (double indentation technique):  $E_{bone} = 7.3$  GPa and  $E_{keratin} = 3.1$  GPa. The Poisson's ratio for bone and keratin was chosen to be 0.4 [46, 141]. In order to check the quality of the FE results, a coefficient of determination between the derivative of the displacement from the FE models and from the DSPI measurements was calculated. The following formula was used, with  $Exp(q_i)$  being

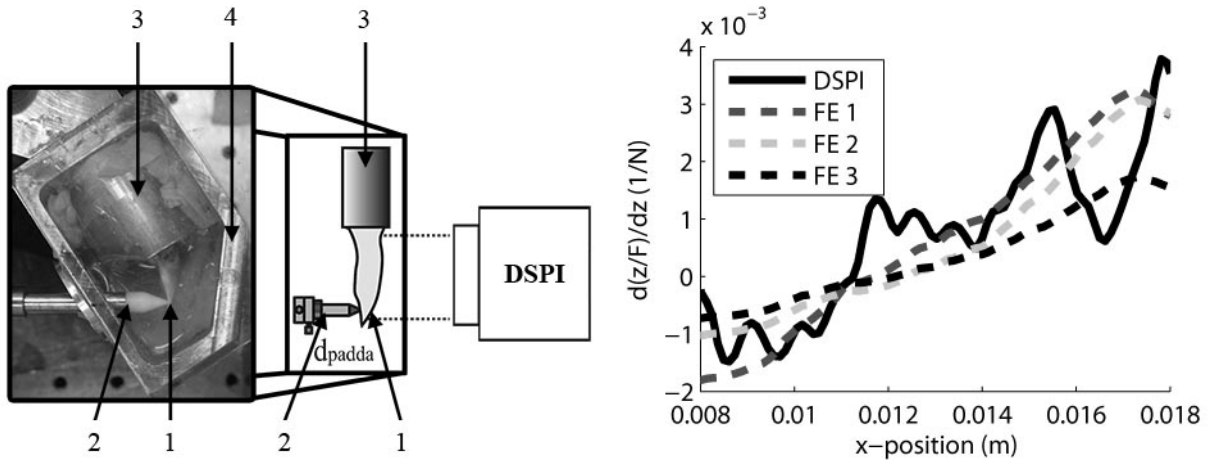


**Figure 6.5:** **Left figure:** DSPI setup for moist testing: (1) upperbeak, (2) polished indentation point, (3) sample holder filled with polyester resin and (4) airtight container with window. **Right figure:** Cross-sectional derivative result for moist tip loading: DSPI experiment (full black line) and several FE solutions (dashed lines) to show the large variation on DSPI results; FE1:  $E_{bone} = 1.7$  GPa,  $E_{keratin} = 1.2$  GPa (dark gray line); FE2:  $E_{bone} = 7.3$  GPa,  $E_{keratin} = 0.6$  GPa (light gray line) and FE3:  $E_{bone} = 7.3$  GPa,  $E_{keratin} = 1.4$  GPa (black line).

the experimental obtained values and  $FE(q_i)$  being the corresponding model output:

$$R^2 = 1 - \frac{SS_{err}}{SS_{tot}} \quad (6.1)$$

$$SS_{err} = \sum_{i=1}^N (Exp(q_i) - FE(q_i))^2 \quad (6.2)$$

$$SS_{tot} = \sum_{i=1}^N (Exp(q_i) - \overline{Exp})^2 \quad (6.3)$$

$$\overline{Exp} = \frac{1}{N} \sum_{i=1}^N Exp(q_i) \quad (6.4)$$

For non-linear regression, this coefficient of determination does not equal the square of the correlation coefficient. If the experimental values coincide with the model values ( $Exp(q_i) = FE(q_i)$ ),  $R^2$  will be 1.  $R^2$  smaller than 0 indicates that the model prediction is less accurate as the mean of the observed data.

In this full field calculation, the bending area and the resulting constant offset were ignored. Indeed, due to constraint errors near the bending area, an additional rigid body movement was introduced over the entire sample. This rigid body movement added an additional linear offset to the  $z$ -displacement, which became a constant offset after derivation. This constant offset was ignored so that rigid body movements, which are uninteresting from a mechanical point of view, were neglected (see section 7.3.2).

### 6.2.4 Digital image correlation

A stereo system (see appendix A) with two cameras (AVT pike F-505, 2048 x 2452 pixels, Smc Pentax bellows lens 1:4 100mm,  $f/32$ , resulting in a  $7\mu\text{m}$  pixelsize) with an opening angle of approximately 30 degrees was used (figure 6.6). Polarized light was used to illuminate the sample. As a consequence, polarizers in front of the camera could be used to reduce specular reflections. Automatic system calibration was conducted before and after the actual measurements using various images of a translated and rotated regular grid pattern within a bundle adjustment technique [129]. As a result, intrinsic (focal lengths, distortions and image plane center location) and extrinsic (rotation and translation) camera parameters were obtained.

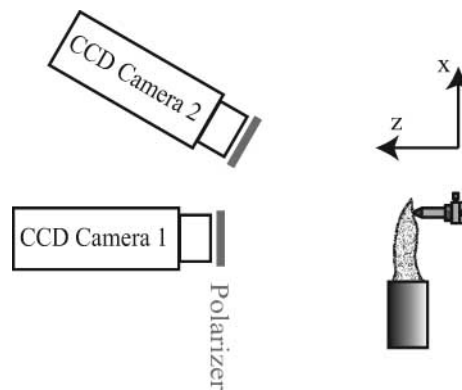


**Figure 6.6:** Schematic drawing of the digital image correlation (DIC) setup. Three dimensional displacements are acquired with sub-micron resolution (results are presented in figures 6.10).

Four stereo images were taken, two before and two after a  $200\mu\text{m}$  displacement of the indentation punch. In a first step, the initial undeformed shape was reconstructed by finding the corresponding speckles in the images captured by camera 1 and camera 2, respectively, and via a triangulation method invoking the determined stereo camera parameters [82]. Next, a similar procedure was applied to the images of the deformed state. Finally, a direct comparison of the deformed  $(x,y,z)$  and the undeformed  $(x_0, y_0, z_0)$  shape yields the 3D deformation coordinates  $(u,v,w)$ . These contain all the information needed to determine the in-plane normal and shear strain components  $(\epsilon_x, \epsilon_y, \epsilon_{xy})$ , and as such the principal strains  $(\epsilon_1, \epsilon_2)$ .

The following settings were used in the displacement determination: a subset size of 21, a step size of 10, Correlation Algorithm, bicubic interpolation and affine shape functions. Strains were calculated in the Green-Lagrange convention (chapter 2), a strain window of  $50 \times 50$  and bilinear interpolation. Results were transformed into the coordinate system of camera 1 (figure 6.6), which was aligned parallel to the direction of the punch force. Accordingly, the corresponding FE model can be easily transformed to the same coordinate system. DIC requires the presence of a random pattern on the specimen. This was applied by air brushing on top of the upper beak

(pattern can be seen in figure 6.10). The influence of this pattern is expected to be minimal due to the stiff keratin and bone. All calibration and correlation are executed in the MatchID software package [82]. Strain results were compared with FE outcome. In addition, the derivative of the out-of-plane displacement is compared with a single DSPI measurement.

## 6.3 Results

### 6.3.1 Digital speckle pattern interferometry

Results for tip loading of the derivative of the out-of-plane displacement ( $z$ ) along the  $x$ -direction are shown in figure 6.7.

In figure 6.8, the cross-sectional results for the bending experiments performed on

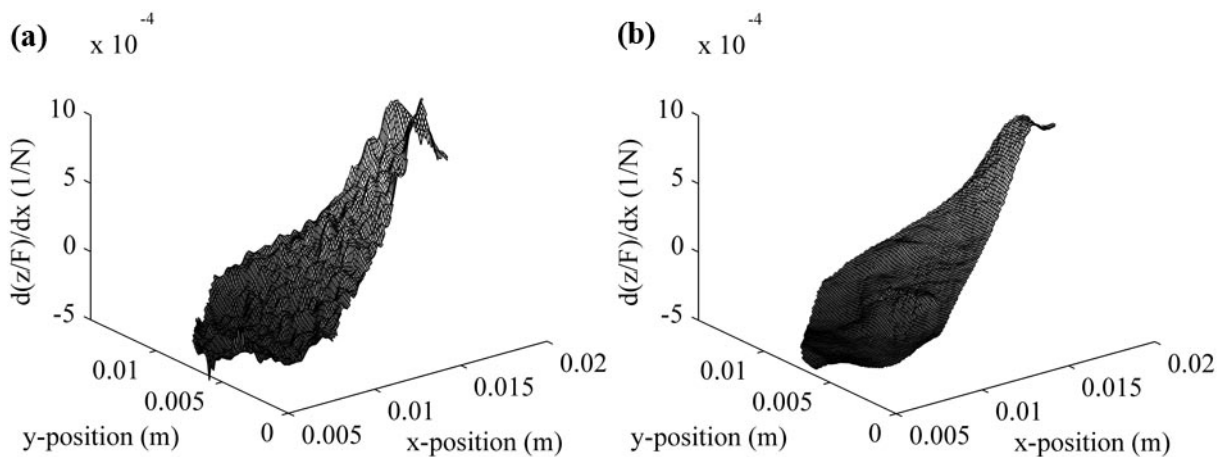


**Figure 6.7:** Full field upper beak results for a tip loading bending experiment of Padda (dry): the derivatives of the out-of-plane displacement along the  $x$ -direction are shown for the DSPI experiment (a) and the FE model (b).

three different locations of the beak are shown. Black lines indicate the derivative of the  $z$ -displacement along the  $x$ -direction of the validation FE models. Gray lines represent the average value of the corresponding DSPI measurements on three different Java Finches. Full lines represent the results for tip loading (b2 in figure 6.4), the dotted lines represent a loading at the center of the beak (b1 in figure 6.4) and the dashed lines are the results from a loading at the rostral-most part of the keratinous upper beak (b3 in figure 6.4). For tip loading an  $R^2$  of 0.97 is found and for center and total tip loading an  $R^2$  of 0.89 is obtained, suggesting that the FE model provides a good representation of the *in vitro* displacement of the actual biological sample.

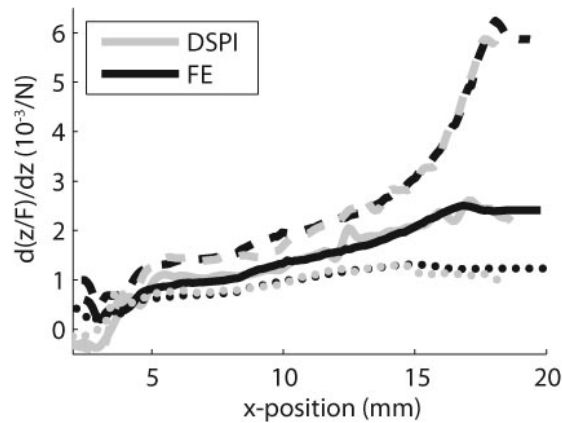


**Figure 6.8:** Results of the validation measurements: Black lines indicate the results of the validation FE model, gray lines the average (of 3 specimens) of the corresponding bending experiments. Dashed lines represent a loading at the rostral-most part of the keratinous upper beak ( $R^2 = 0.97$ ), full lines represent tip loading ( $R^2 = 0.89$ ) and dotted lines represent center loading ( $R^2 = 0.89$ ).

### 6.3.2 Digital image correlation

A longitudinal cross-section for the derivative of the out-of-plane displacement ( $w$ ) along the  $x$ -direction, obtained with DIC, is presented in figure 6.9 and compared with its corresponding FE model and a single DSPI measurement. The measured DIC displacement at the tip of beak was approximately  $125\mu m$  (25 times larger than DSPI,  $5\mu m$ ) and the reaction force was  $5.5N$  (DSPI:  $0.21N$ ). The results were noisier than for DSPI, so a larger window is used to calculate the derivatives and a worse  $R^2$  of 0.52 (instead of 0.89) is obtained.

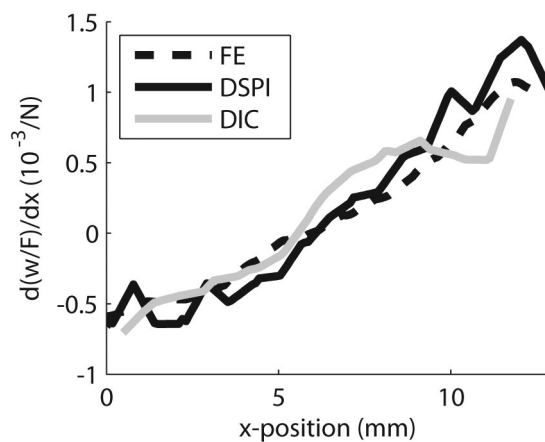


**Figure 6.9:** Derivative of the out-of-plane displacement( $w$ ) along  $x$ -direction, normalized to reaction force, for FE, DSPI and DIC.

Besides the displacement in the z-direction, DIC also yields the coordinates (x,y,z) of the surface and the displacement (u,v,w) at every (visible) point. As a result, we can obtain the strains ( $\epsilon_x, \epsilon_y, \epsilon_{xy}$ ) over this surface. The full field results of the strain, compared with their corresponding FE results, are presented in figure 6.10. A qualitative examination indicates a quite good correspondence between model and experiment. Quantitative results in the longitudinal and transversal directions are presented in figure 6.11 respectively. Maximal strains are approximately  $3000 \mu\text{m}/\text{m}$ .

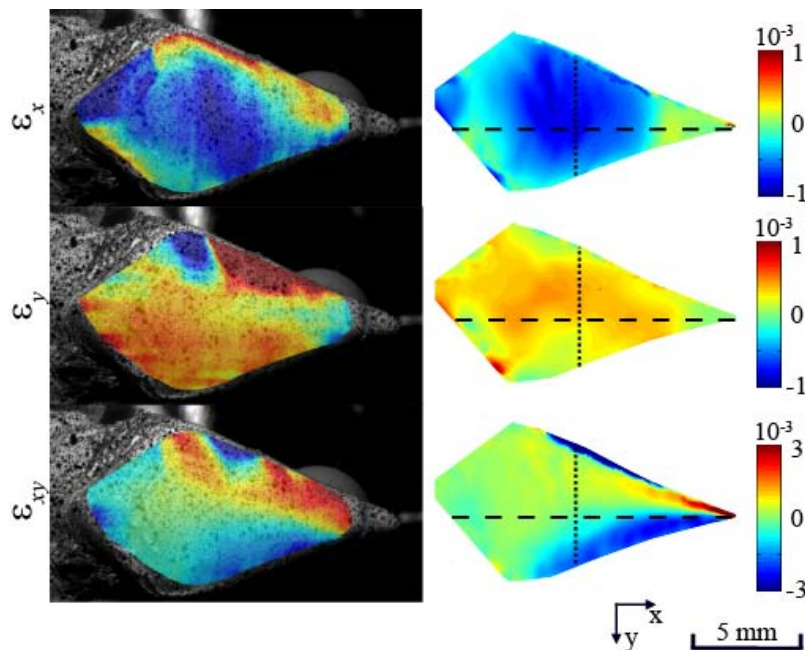


**Figure 6.10:** Surface strain components ( $\epsilon_x, \epsilon_y, \epsilon_{xy}$ ) for DIC (left) and calculated from FE modeling (right).

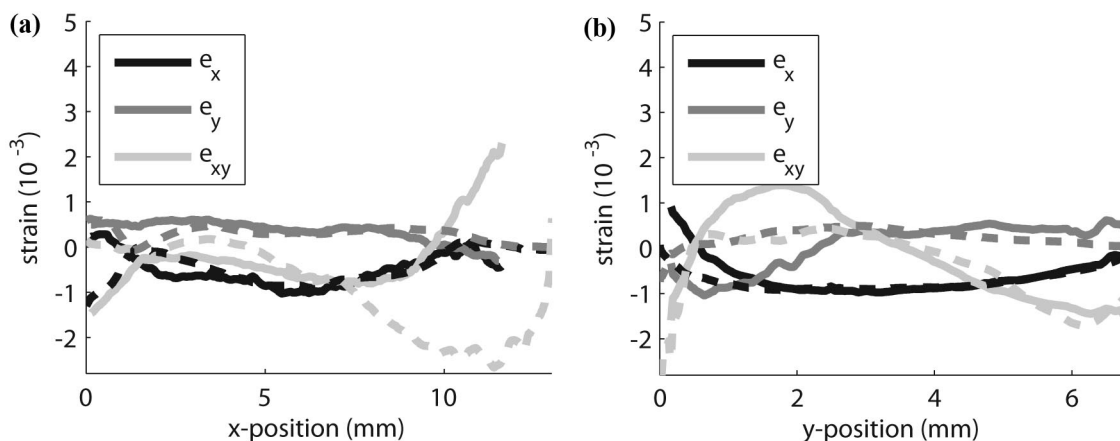


**Figure 6.11:** Longitudinal (a) and transversal (b) cross-section of strains ( $\epsilon_x, \epsilon_y, \epsilon_{xy}$ ) measured with DIC (full line) and calculated from FE model (dashed line) (along dashed line in figure 6.10).

## 6.4 Discussion

The beak is a complex, composite structure (figure 5.1) and some approximations are necessary to create a mechanical model of it (chapter 5). First the epidermal and dermal layers are modeled as one homogenous, isotropic and linear elastic keratin layer. Second, both the cortical and the cancellous bone are modeled as homogenous and isotropic. An elastic modulus of the cortical bone layer is obtained in chapter 7 and section 3.3.3. The cancellous bone does not appear to be homogenous at all. It forms struts at some regions and in other regions almost no bone is found. Moreover, such struts are too small for mechanical testing. Another inaccuracy is the overestimation of cortical and trabecular bone thickness (compare figure 5.1D with 5.1A,B), due to the semi-automatic segmentation. Additionally, after smoothing only the largest struts are left in the model. Finally, the connection between the keratin and bone is modeled as if they are fully attached at each other.

Those approximations can have an impact on the mechanical behavior of the model and therefore, a validation procedure is an important component of a good FE model. A first indication is the good correspondence between the measured force and the modeled force in chapter 5. However, several FE models, with different stress fields, will produce similar forces (chapter 5) and thus ideally additional validation measurements are required.

### 6.4.1 Digital Speckle Pattern interferometry

In this chapter, the derivative of the z-displacement (out-of-plane) along the x-direction, obtained with DSPI was compared with the outcome of a FE model. This interferometric technique offers some major advantages over conventional methods such as strain gauges. It is a non-contact method allowing us to quantify deformation of the small and complex upper beak. Furthermore, the method is full field, yielding a better validation. The major drawback of DSPI is its sensitivity, which makes *in vivo* experiments unfeasible and makes measurements on fresh samples difficult. This practical issue is overcome by introducing a bending experiment on a dry sample on three different locations. The signal-to-noise ratio of the experimental results is improved by using the average of multiple measurements. In addition, the measurements on three Java Finches are combined. The coefficient of determination ( $R^2$ ) for the three different locations is higher than 0.89, indicating a good fit of the model to the data points and thus validating the FE model. This goodness of fit for the three different loading conditions can also be observed in figure 6.8. It should be noticed that there is a discrepancy at the bending area, which is the zone with x values smaller than 5mm (in figure 6.8). This may be due to an approximation in the modeling. I believe that this bending area consists of less dense and less stiff bone. Therefore, the displacement at this position and the additional rigid body movement of the entire sample is ignored (also see section 7.3.2).

### 6.4.2 Digital image correlation

The derivative of the out-of-plane displacement along  $x$ , normalized to the reaction force ( $d(w/F)/dx$ ) was shown to be a good parameter to describe the bending [83]. Indeed, a rigid body movement will introduce a constant factor. This additional factor is neglected in our analysis because an offset is expected due an approximation near the bending zone. The normalization to the force allows us to compare the two experimental techniques. Indeed, the reaction force and the induced displacement of DSPI are 25 times smaller than DIC. The normalization requires a linear behavior of the sample. This assumption is reasonable, because the reaction forces of  $0.21N$  for DSPI and  $5.5N$  for DIC are below the natural maximum bite force of  $9.0N$  (chapter 5). A strong correlation is found between the FE model and the DSPI result for a single tip loading ( $R^2 = 0.89$ ). As a consequence, this measurement can be used in an inverse analysis to obtain values for the elastic modulus of bone and keratin (chapter 7). The lower coefficient of determination between DIC and FE modeling ( $R^2 = 0.52$ ) is caused by a noisier result, but, as can be seen in figure 6.9, a reasonable correspondence is obtained.

The major advantages of DIC is its stability and the possibility to acquire full 3D coordinates and displacements in one single measurement. Hence, surface strains ( $\epsilon_x, \epsilon_y, \epsilon_{xy}$ ) can be calculated. These strains are shown in figure 6.10. A qualitatively good agreement between DIC (left) and FE (right), except for a noisy part at the left side of the upper beak, can be observed. A quantitative comparison for the longitudinal and transversal (figure 6.11) cross-sections shows a good correspondence. More particular, a good correspondence is found for  $\epsilon_x$ . The negative, quite uniformly, values for  $\epsilon_x$  indicate an almost uniform compression at the top of the beak of approximately  $1000\mu m/m$ . For *in vivo* bite forces, which are expected to be approximately 2 times larger, strains about  $2000\mu m/m$  are expected. This compression is a result from the bending. More towards the edge of the beak, the bending becomes smaller and so do the  $\epsilon_x$  value (figure 6.11). For  $x$ -values smaller than 2, a larger deviation is observed. We believe that this deviation is a local error, caused by the modeling approach of the bending zone. The results for  $\epsilon_y$  show positive strains, thus an extension in the  $y$ -direction, on top of the upper beak. A deviation, probably due to noise, between experiment and model is observed for  $y$  smaller than  $3mm$ . The shear strain  $\epsilon_{xy}$  shows, except for the same noisy part, good correspondence in the transversal direction (figure 6.11b). The longitudinal results (figure 6.11a), however, show some offset towards the tip of the beak. This deviation is, in my opinion, due to the use of two different samples, resulting in a misalignment. Nevertheless, a good qualitative agreement is seen for all the strains and DIC can be a simple alternative for strain gauges.

## 6.5 Conclusions

In this chapter results of DSPI and DIC were presented. Both techniques rely on a completely different working principle. As a result, they both have a different measuring

---

range. DSPI is an interferometric resolutions in the nanometer range, resulting in high quality results (so they can be used in an inverse analysis: chapter 7), but having high stability requirements. DIC is a photogrammetric technique measuring coordinates on pixelsize dimensions ( $\mu m$ ). Both validation measurements indicate that the FE modeling approach provides reliable and biologically pertinent data. Hence, the *in silico* experiment performed in (chapter 5) is validated. The same modeling approach will be used in the modeling of Darwin's finches (chapter 8).



# CHAPTER 7

---

## Inverse analysis

---

### **Abstract**

*Material parameters are an essential part in a finite element modeling approach. In chapter 3, a novel double indentation technique was proposed and the elastic moduli of beak bone and keratin (dry and fresh) were obtained. Another way to obtain these values is through an inverse analysis: a finite element model is adapted to obtain a best fit with an experiment. It was shown that DSPI gives high quality results (chapter 4 and 6). Consequently, an inverse analysis for this DSPI results is proposed in this chapter and an in situ material characterization can be conducted. The results will be compared with the double indentation results from chapter 3.*

This chapter is based on:

Soons Joris, Herrel Anthony, Aerts Peter and Dirckx Joris. Determination and validation of the elastic moduli of small and complex biological samples: bone and keratin in bird beaks. *Journal of the Royal Society Interface*, published online doi: 10.1098/rsif.2011.0667.

Soons Joris and Dirckx Joris. Multi-Parts Geometry-Based Finite Element Modeling in Biomechanics: Elastic Modulus Determination of Bone and Keratin in the Java Finch's Beak by Double Indentation Technique and Inverse Analysis. In *Horizons in World Physics., Volume 278* and in *Advances in Mathematics Research, Volume 17*, Nova Science Publishers, Inc., 2011

Soons Joris and Dirckx Joris. Digital speckle pattern interferometry in biomechanics: *in situ* inverse analysis on birds beaks to obtain elastic modulus of the bony core and the keratin layer. *10th IMEKO symposium 2011, ISBN 978-3-18-092156-3* p. 73-80, 2011

Soons Joris and Dirckx Joris. Phase shifting digital speckle pattern interferometry and inverse analysis on bird beaks. *Photomechanics 2011, Brussel* p. 42-43, 2011

## 7.1 Introduction

The double indentation technique was introduced for samples too small for standard tests (chapter 3). A good agreement with measurements on test samples (PVC, PMMA, PA6, aluminum) was obtained. I was also able to measure the Young's modulus of bone and keratin on the upper beak of Java finches: a modulus of 7.3 GPa was found for bone, 3.1 GPa for dry keratin and 1.7 GPa for fresh keratin. Nevertheless, results should be treated with care. Therefore an inverse analysis is introduced in this chapter to obtain these values *in situ*: in a FE model the material properties are adjusted to obtain the best fit between the model and an experimental measurement quantifying actual beak deformation. In the previous chapter, it was shown that digital speckle pattern interferometry (DSPI) yields full field and accurate displacement measurements. Consequently, DSPI results are expected to be useful in an inverse analysis. First, the optimization is done with the derivative of this displacement. Next, the results of a failed inverse analysis using only the displacement is shown.

## 7.2 Material and methods

A group of three Java Finches was prepared according section 6.2.1. The out-of-plane displacement on the topside of the upper beak, introduced by the bending experiment, was quantified using a DSPI setup (section 6.2.2). FE models are similar to those in section 6.2.3. The upper beak in the FE model was scaled to the same dimension as used in the experiments. Pictures of the experimental setup were used for the scaling and estimation of the boundary conditions. The Young's moduli were changed in the inverse analysis as described below.

Inverse modeling is a technique where parameters of a model are explored by optimizing the fit between experimental and model data (figure 7.1). Here the best fit to the derivative of the z- displacement (out-of-plane) along the x-direction was determined. The major advantage of an inverse analysis is the *in situ* parameter determination. I used the measurement results of the bending experiment (described in section 6.2.1 and 6.2.2) and adapt the parameters in the corresponding FE model (described in section 6.2.3). The goodness of the fit will be described with a coefficient of determination  $R^2 = 1 - SS_{err}/SS_{tot}$  (eq. 6.1).

Since DSPI is a full field method, I calculated  $R^2$  for all  $N$  points on the upper beak surface, except for the noisiest parts and the bending area itself. Rigid body movements, which are not interesting from a mechanical point of view, were removed by subtracting the mean values and thus centering the results around zero. The closer the  $R^2$  values approach the value of 1, the better the fit.

Changing the Young's modulus of bone and keratin in the FE model will result in a different  $R^2$ . The goal is to obtain the highest  $R^2$ , because it indicates the best fit between the experiment and the FE model. The maximum in a selected domain of moduli can be obtained with surrogate modeling. In such a surrogate model, every Young's modulus for keratin and bone is linked with a corresponding  $R^2$  (e.g. figure

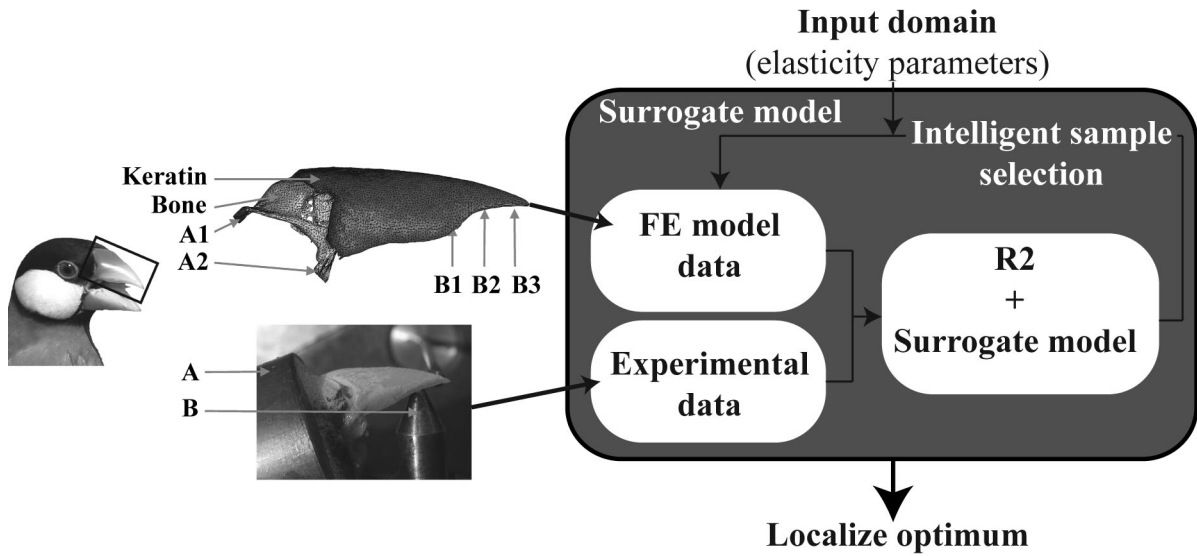


**Figure 7.1:** Left figure: Head of Java Finch (*Padda oryzivora*), upper beak is indicated. Center top figure: FE model of upper beak with keratin and bone indicated. Center bottom figure: Experimental setup for bending experiment. Right figure: schematic representation of the surrogate modeling approach. Legend: A) sample holder filled with polyester resin to constrain bending area (A1) and jaw bones (A2). B) seed reaction force imitated by an indentation at three different position: at the center of the upper beak (B1), at the tip near the limit of the bony core (B2) and at the rostral-most aspect of the keratinous upper beak (B3).

7.2). The 'Matlab SUMO toolbox' is used to create a good surrogate model with a low calculation cost [3]. Finally, I selected the highest  $R^2$  in the surrogate model and I obtained a keratin and bone modulus which describe the experiment in a best way. In practice,  $SS_{err}$  is minimized since  $SS_{tot}$  will not change with different model values (eq. 6.1).  $R^2$  from different loading positions can be obtained by:

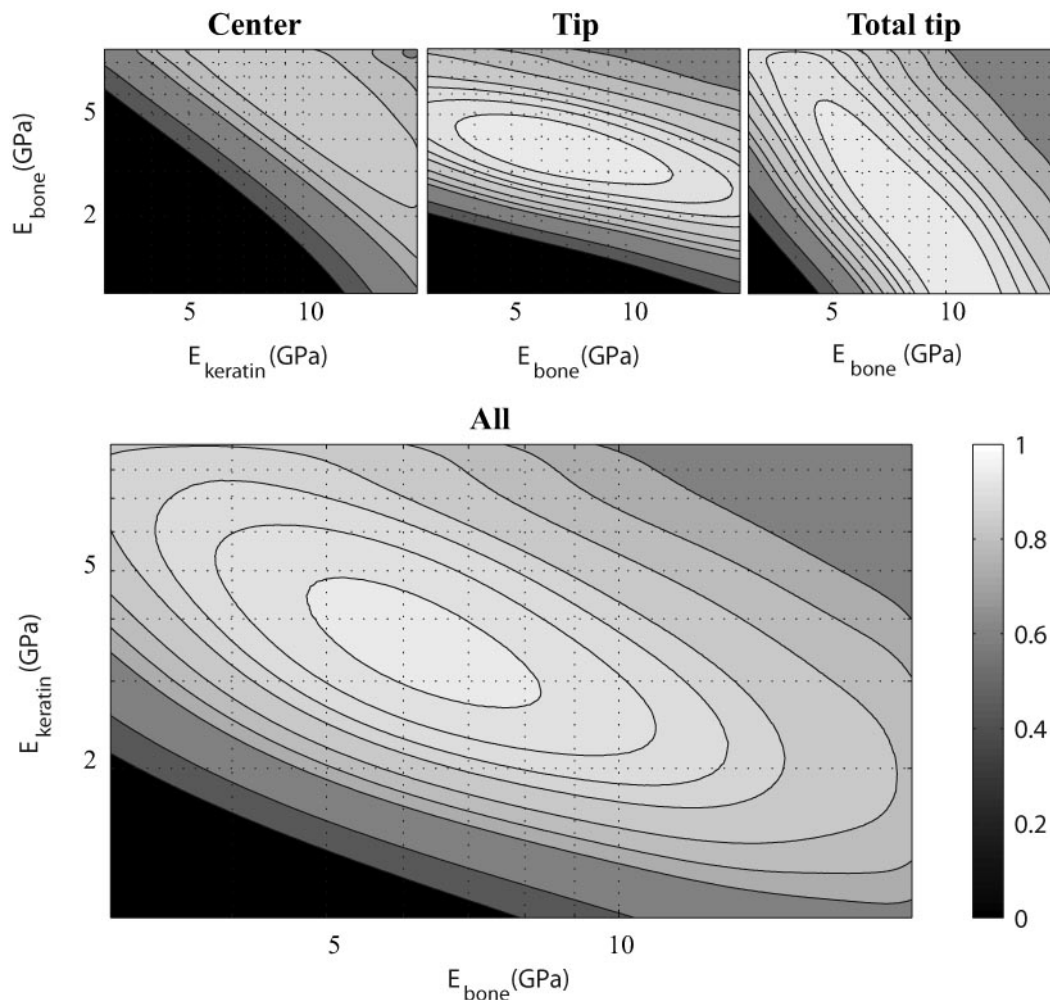
$$R^2_{combined} = 1 - \frac{\sum SS_{err}}{\sum SS_{tot}} \quad (7.1)$$

## 7.3 Results

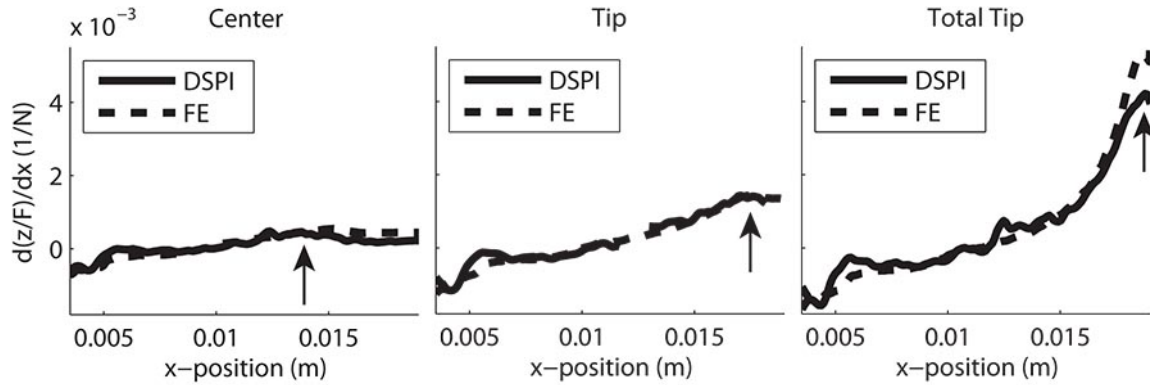
### 7.3.1 Inverse analysis with derivative of displacement

Figure 7.2 shows a surrogate model of Padda (1), linking the elastic modulus of bone and keratin to a corresponding  $R^2$  for the three bending experiments and for the three bending experiments combined (eq. 7.1). The maximum of the combined surrogate model indicates that for bone the optimal modulus is 7.0 GPa and for keratin 3.6 GPa (see table 7.1). The FE models with these optimal combined moduli (of Padda 1) are

shown in figure 7.3 and compared with the corresponding DSPI results. Results for three different species are given in table 7.1. An average ( $\pm stdev$ ) for the three samples of  $7.2 \pm 0.7$  GPa for bone and  $3.1 \pm 0.4$  GPa for keratin is obtained



**Figure 7.2:** Surrogate model for  $R^2$  of Padda 1 (dry). This model links the modulus of keratin and bone in the FE model to a corresponding  $R^2$  (for the bending experiments: tip, center, total tip loading and all combined). An optimal modulus of 7.0 GPa for bone and 3.6 GPa for keratin ( $R^2 = 0.94$ ) is found. Notice the logarithmic scale.



**Figure 7.3:** Cross-section results for the derivative of the out-of-plane displacement along the x-direction for padda 1. DSPI measurements (full line) and FE results (dashed line) are shown for the three bending experiments (center, tip and total tip loading). I used the results of the combined optimization for the FE model ( $E_{bone} = 7.0$  GPa,  $E_{keratin} = 3.6$  GPa, see table 7.1). The arrows indicate the indentation position.

**Table 7.1:** Elastic moduli of bone ( $E_b$ ) and keratin ( $E_k$ ) for three Java Finches (Padda 1, 2 and 3) which were dried before testing (values are in GPa). The values were obtained through an inverse analysis (corresponding  $R^2$  are given) for three bending experiments (center, tip and total tip loading). Combined values are calculated with eq. 7.1

	Center			Tip			Total Tip			Combined		
	$E_b$	$E_k$	$R^2$	$E_b$	$E_k$	$R^2$	$E_b$	$E_k$	$R^2$	$E_b$	$E_k$	$R^2$
Padda1	9.8	6.2	0.83	6.7	3.6	0.95	10	1.4	0.95	7.0	3.6	0.94
Padda2	20	9.0	0.62	3.0	4.5	0.96	8.0	2.8	0.97	8.0	2.8	0.90
Padda3	4.7	8.8	0.83	4.7	4.4	0.92	6.8	2.6	0.97	6.7	3.1	0.93

### 7.3.2 Inverse analysis with displacement

The model was also optimized to coincide with the measured (Padda 1) out-of-plane displacement of DSPI (without derivating). The model displacement map obtained with the optimization shows a good correspondence with the measured displacement map (figure 7.4). The next moduli are obtained:  $E_{bone} = 2$  GPa and  $E_{keratin} = 9$  GPa. These values are not really expected (see chapter 3). Indeed, a closer look to the derivative shows a roll-off (figure 7.5).

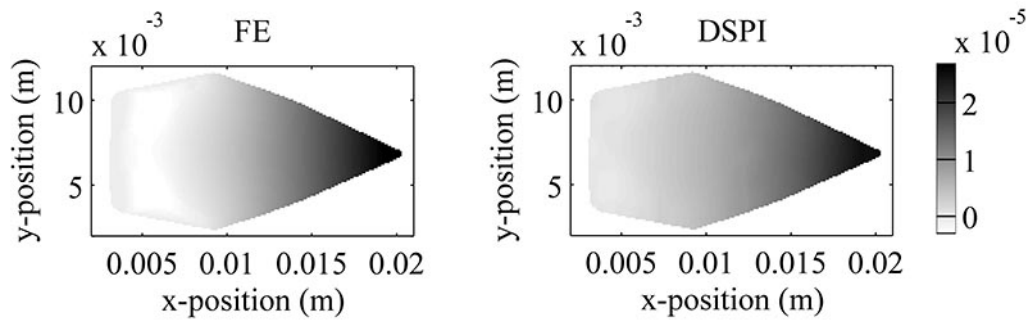


**Figure 7.4:** The out-of-plane displacement ( $m/N$ ) for the optimized FE model (1N load) and DSPI measurement ( $\pm 0.2$  N load).

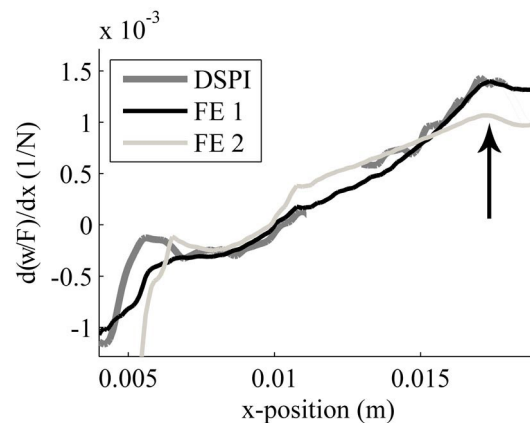


**Figure 7.5:** Cross-section results for the derivative of the out-of-plane displacement ( $w$ ) along the  $x$ -direction (averaged around zero) for DSPI and finite element model optimized for derivative (FE1) and for displacement (FE2).

The difference in displacement between DSPI and FE (constant factor in derivative) can be explained by a modeling approach near the bending zone. In CT images, a lower absorption is observed for the bending zone. As a result, a lower modulus is expected. This lower modulus will introduce an additional rigid body movement (and a constant factor for the derivative). This behavior was studied by using a bending area with a lower modulus (figure 7.6). The results are shown in figure 7.7. Adding the bending area will result in the expected additional rigid body movement. The difference behavior at the back of the beak ( $x < 0.005m$ ) is, in my opinion, caused by the absence of a supporting layer.

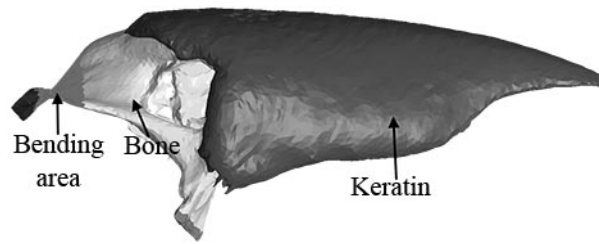


**Figure 7.6:** Finite element model with additional bending area

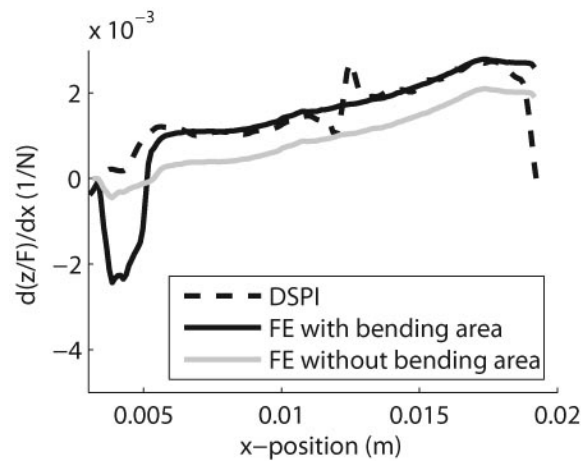


**Figure 7.7:** Cross-section results for the derivative of the out-of-plane displacement along the x-direction for DSPI and FE model with and without additional bending area (figure 7.6)

## 7.4 Discussion

The DSPI results for the bending experiment show a rather smooth derivative (figure 7.3), indicating low noise in the original displacement measurement (chapter 6). In addition, good results are obtained with the inverse analyses, based on the DSPI experiment (table 7.1). Indeed, all  $R^2$  values are above 0.90 (except for center loading), suggesting a very good fit of the model to the experimental data. Results for the optimization to the displacement were rather bad (figure 7.5). This roll-off (for the derivative) is induced by an attempt of the inverse analysis to incorporate the large rigid body movement, caused by an modeling approach of the bending area (figure 7.6 and 7.7). More specifically, I think it can also be caused by lower bone density and a supporting bony layer which are not present in my FE model (figure 7.6). The lower bone density will result in a lower elastic modulus and will thus introduce an extra rigid body movement (figure 7.7). This rigid body movement will result in an extra constant for the derivative. This offset will be ignored by averaging the results around zero.

The surrogate models (figure 7.2) return a  $R^2$  value for every elastic modulus of bone

and keratin in the selected domain. Very high  $R^2$  values are obtained, suggesting a high correspondence between the model and the DSPI measurements (except for center loading). It should be noticed that I ignored the noisiest parts, resulting in slightly higher  $R^2$  values. I also ignore the bending at the back of the beak which shows a divergence between the results obtained through DSPI and the FE model and the resulting rigid body displacement. The discrepancy at the bending area is caused by model constraints errors in this region (mentioned above).

The optimal Young's moduli are acquired through the inverse analysis. Interestingly, the surrogate model displays a ridge of high  $R^2$  values (figure 7.2). Indeed, less stiff bone can be compensated by stiffer keratin and vice versa. More noise in the experiment will result in a poorer selection of the optima and thus only a limited set of moduli can be selected on the ridge. The results presented in table 7.1, were obtained through optimization for the three different loading conditions (center, tip, total tip, see figure 7.1) and a combined optimization (eq. 7.1). This combined optimum (for the three different bending experiments) provide more stable results since experiments with a smaller  $R^2$  contributes less to the combined  $R^2$  (equation 7.1). In addition, a specific selectivity for some experiments can be seen (top row of figure 7.2).

A weighted averaging for the elastic moduli of the three tested finches resulted in an elastic modulus of 7.2 GPa for bone and 3.1 GPa for keratin, both with a relative error smaller than 13%. This small value suggests a rather high precision of this technique. In addition, the double indentation (section 3.3.3) as the inverse analysis yield similar values. This suggests that both techniques provide reliable and accurate results. Combining results from both approaches results in a weighted average of  $7.3 \pm 0.6$  GPa for the modulus of bone and  $3.1 \pm 0.2$  GPa for dry keratin. The obtained values lie within the literature range ( $0.2 \text{ GPa} < E_{\text{keratin}} < 4 \text{ GPa}$  [92, 126] and  $100 \text{ MPa} < E_{\text{bone}} < 35 \text{ GPa}$  [27, 49, 92]). Compared to the modulus of ossicle bone ( $16 \pm 3 \text{ GPa}$ , chapter 3) and other literature values of compact bone [43], the modulus I found is rather low. Literature values for keratin correspond well with my results [126]. The wide variety of bone and keratin samples in literature indicates the importance of measurements on the actual samples to be modeled.

## 7.5 Conclusions

The *in situ* elastic moduli of both bone and dry keratin were successfully obtained through an inverse analysis of a multi-layered FE model. Values correspond well with results obtained from double indentation (chapter 3), indicating that both techniques yield reliable results. Combining both techniques results in a bone modulus of  $7.3 \pm 0.6$  GPa and a dry keratin modulus of  $3.1 \pm 0.2$  GPa.

#### **Abstract**

*Darwin's finches are a text book example of adaptive radiation. From a single ancestor, fourteen species of Darwin's finches differing in beak size and shape and specializing in different food resources have radiated in the Galápagos archipelago. It has been shown that beak morphology in Darwin's finches evolves via natural selection as a response to variation in food type, food availability, and interspecific competition for food [15]. However, seed cracking ability is principally determined by bite force capacity which is, in turn, related to jaw closer muscle cross-sectional area [63]. Thus, beak morphology is predicted to evolve in concert with jaw adductor strength in order to avoid structural failure because of increased loading.*

*Here we present anatomical data on eight species, and finite element models of the bony beak with rhamphotheca for thirteen species of Darwin's finches. Our models offer two new insights. First, engineering safety factors are found to be relatively uniform, despite a broad range of shapes and sizes. Second, size-scaled FE models reveal precise tuning between inferred beak loading profiles and observed feeding strategies (edge-crushing versus tip-biting). Both lines of evidence suggest strong selection on beak shape as a response to fracture avoidance.*

This chapter is based on:

Soons Joris, Genbrugge Annelies, Podos Jeffrey, Adriaens Dominique, Aerts Peter, Dirckx Joris and Herrel Anthony. Precise tuning of beak morphology to loading demands in Darwin's finches. *In preparation*

Herrel Anthony, Soons Joris, Aerts Peter, Dirckx Joris, Boone Matthieu, Jacobs Patric, Adriaens Dominique and Podos Jeffrey. Adaptation and function of the bills of Darwin's finches: divergence by feeding type and sex. *Emu* 110(1) 39-47.

## 8.1 Tuning of beak morphology to loading demands

The often tight correspondence between bird beaks and plant morphology well-illustrates the power and precision of natural selection [128]. Within bird populations, subtle variations in beak morphology can indeed affect foraging efficiency [127], and in some cases tip the balance between survival and starvation [9]. For seed-crushing birds, however, analyses of feeding capacity require a broader view than just beak morphology per se. This is because birds' abilities to crush seeds are determined mainly by bite force capacity, which in turn depends primarily on jaw closer muscles and their cross-sectional area [63, 64, 132]. These muscles, situated at the back of the head, generate crushing forces that are transferred to food by means of the upper and lower beak [15, 94, 132]. Beak morphology, by contrast, likely evolves as a secondary response, to facilitate successful food manipulation yet also avoid structural failure during loading [63].

We here test, for Darwin's finches of the Galápagos Islands, the hypothesis that beak morphology has evolved as an adaptation for maintaining structural integrity. Beaks in Darwin's finches are known to vary broadly across and within species, and to evolve via natural selection as a response to variation in food type, food availability, and interspecific competition [9, 15, 45, 56, 57, 59, 81]. Our main approach was to develop and apply finite element (FE) models of the upper beak, to draw inferences about patterns of loading during biting. FE models enable exploration of the effect of complex shape variation on stress magnitude and distribution [101, 102]. Expanding on a prior study on Darwin's finch beak loading (see appendix B), we here incorporate into our models data not just from jaw bones and muscles, but also from the keratinous rhamphotheca that encapsulates the beak. We thus obtain a more realistic estimate of stresses incurred during biting. Stress regimes for multi-layered beaks, using experimentally-obtained elastic moduli of keratin and bone, have been modeled with success previously for another species, *Padda oryzivora*, and were validated using digital speckle pattern interferometry (see chapter 5 and 6).

We generated  $\mu$ CT scans of thirteen species of Darwin's finch, and constructed finite element models based on these scans. We constrained our models at the fronto-nasal hinge and either a unilateral bite point at the base of the beak, or a medial bite point at the tip of the beak, to simulate two bite positions favored by different finch species (figure 8.1). Models were loaded, using physiologically relevant force values, through the jugal and palatine jaw bones, in order to simulate the action of the jaw closing musculature. Physiologically relevant force values were derived from measures of muscle cross-sectional area and muscle geometry, obtained through dissection of eight Darwin's finch species. We applied a von Mises (VM) stress yield criterion, which provides a reliable means for interpreting complex stress fields [76]: VM stresses higher than a beak's material strength would result in failure and almost certain death, given the importance of the beak to feeding and foraging.

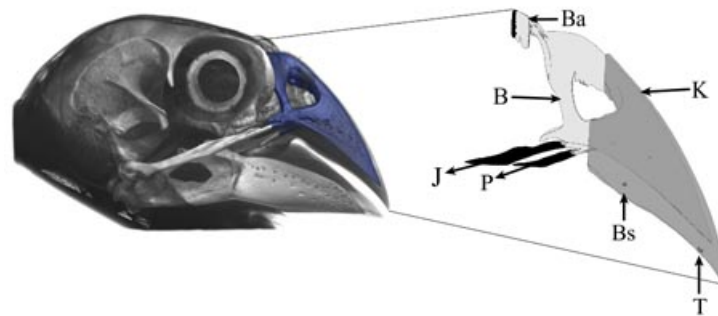


**Figure 8.1:** Schematic representation of our multi-layered (bone: B, keratin: K) finite element modeling approach, for the medium ground finch (*Geospiza fortis*). Bending area (Ba) and bite position (base: Bs, or tip: T) were constrained in our models for translation and rotation, and muscle forces were applied in our models via the jugal (J) and palatine (P) jaw bones. Schematic representations of the other Darwin's finches are given in 8.6 and 8.7.

## 8.2 Results and discussion

The output of our FE models, in which force vectors represent resulting bite forces (figure 8.2 and figure 8.8 and 8.9), corresponded closely to field-measured *in vivo* bite forces (table 8.1), thus validating our modeling approach. For all species, estimated maximum VM stresses, particularly near the nasal hinge, were lower in our present models, by 4–44%, compared to maximum VM stresses calculated in prior models that did not take into account the rhamphotheca (appendix B). The contrast in outcomes illuminates the role played by the rhamphotheca in stress dissipation, and thus in fracture avoidance.

To quantify birds' risk of beak fracture during biting, we calculated safety factors for each species' beak, by dividing bone strength by peak stress. Values for bone strength were obtained using the linear relationship of Fyhrie and Vashishth [49] (45 MPa for a experimentally obtained Young's modulus of 7.3 GPa for finch beak bone, chapter 5). We find that the beaks of different finch species operate within a narrow range of safety factors, between 0.7 and 2.5 (table 8.1 and figure 8.3). The realistic range of applicable safety factors is likely even narrower than this, given that the 0.7 value was calculated for tip-biting in the largest species, *G. magnirostris*, which in nature applies a base-biting strategy almost exclusively. Observed safety factors imply that beaks can withstand loading under normal conditions, although jaw muscle hypertrophy of the ground finches, particularly *G. magnirostris* (figure 8.10), introduces risk to the beak's structural integrity during tip biting. As a caveat, absolute values of the safety factor should be interpreted as provisional, since our measures for the Young's modulus were based on data for *P. oryzivora*. Indeed, a wide range of strengths for denser bone, ranging from 106 to 224 MPa [26, 137, 142], is available in literature, and Darwin's finches could potentially have denser bone with a higher strength. As a result, safety

**Table 8.1:** *in vivo* measured bite force (6 species) compared to the model bite force. Table entries are means  $\pm$  standard deviations.  $N$  = number of specimens. Model safety factors (SF) are also presented (for a strength of 45 MPa) (\* = juvenile).

	Measured force at base (N)	Measured (N) force at tip (N)	Model force at base (N)	Model force at tip (N)	Model base biting SF	Model tip biting SF
<i>G. fortis</i> (N=382)	23 $\pm$ 9	19 $\pm$ 7	30	22	1.6	1.0
<i>G. magnirostris</i> (N=29)	65 $\pm$ 17	44 $\pm$ 10	58	42	1.1	0.7
<i>G. fuliginosa</i> (N=115)	5.5 $\pm$ 1.9	4.6 $\pm$ 1.6	7.1	4.6	2.5	1.6
<i>G. conirostris</i> (*)			15	10	1.1	1.0
<i>G. scandens</i> (N=64)	10 $\pm$ 3	7 $\pm$ 3	8.9	6.1	2.0	1.3
<i>G. difficilis</i>			3.6	2.4	2.1	2.3
<i>C. olivacea</i> (N=18)	2.0 $\pm$ 0.5	1.2 $\pm$ 0.4	2.0	1.0	1.0	1.4
<i>C. parvulus</i> (N=29)	5.6 $\pm$ 1.3	4.2 $\pm$ 1.2	3.4	2.2	2.1	1.8

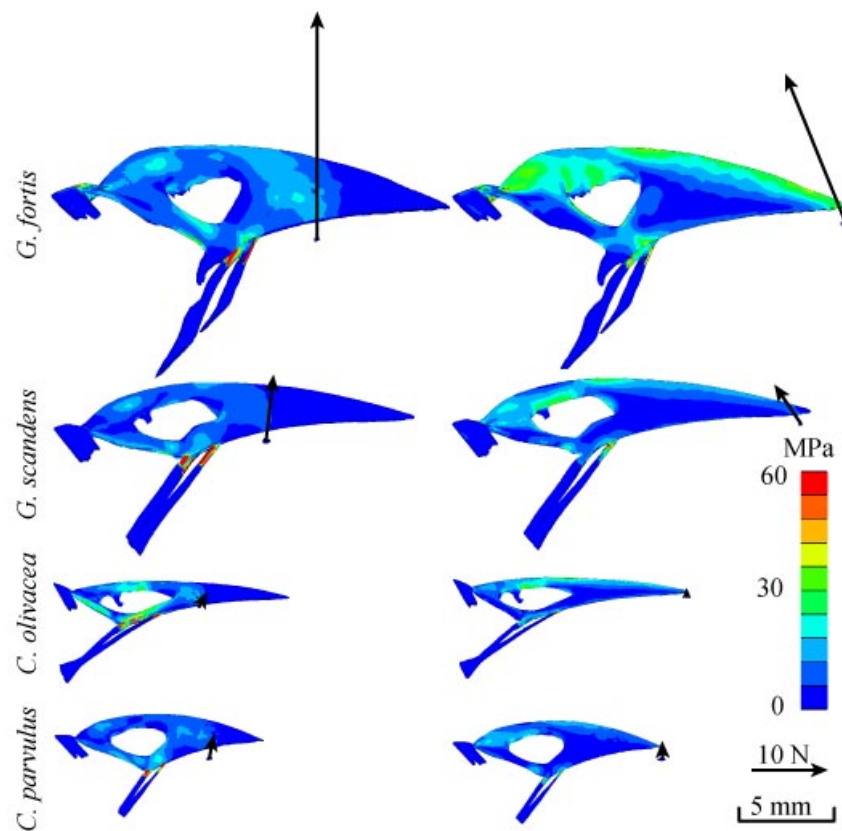


**Figure 8.2:** Finite Element Model results, lateral view, for 4 Darwin's finch species known to use their beaks in different ways while feeding [15, 58]: *G. fortis* (base crushing beak), *G. scandens* (probing and crushing beak), *C. olivacea* (probing beak) and *C. parvulus* (tip biting beak). Results are shown for both base (1st column) and tip (2nd column) biting constraints. Arrows indicate the location and magnitude of the calculated bite forces. Warmer colors represent higher von Mises stresses. Results for the eight Darwin's finches with available muscle data are presented in figure 8.8 and 8.9.

factors will be larger and closer to literature values (between 2 and 4 for tetrapods [8]). A unique advantage of FE models is that they can be size-scaled, which allows a unique, size-independent view on the structural merits of different beak shapes. Towards this end we calculated a second set of FE models, in which we scaled the beaks of all Darwin's finches to the same size (to that of *G. fortis*), and applied identical muscle forces (again, of *G. fortis*) to our models [40]. The VM stresses for base and tip loading of all 13 scaled models are shown in figures 8.3, 8.4 and 8.5 (and figure 8.11, 8.12, 8.13 and 8.14). A primary result to emerge is that the location of the maximum VM stress differs broadly across different species, in ways that align with the different species feeding strategies. The beaks of *C. olivacea* and *P. inornata* in our models show untenably high peak VM stresses, up to 100 MPa, under either base or tip loading conditions, suggesting that their beaks could not withstand large muscle forces under

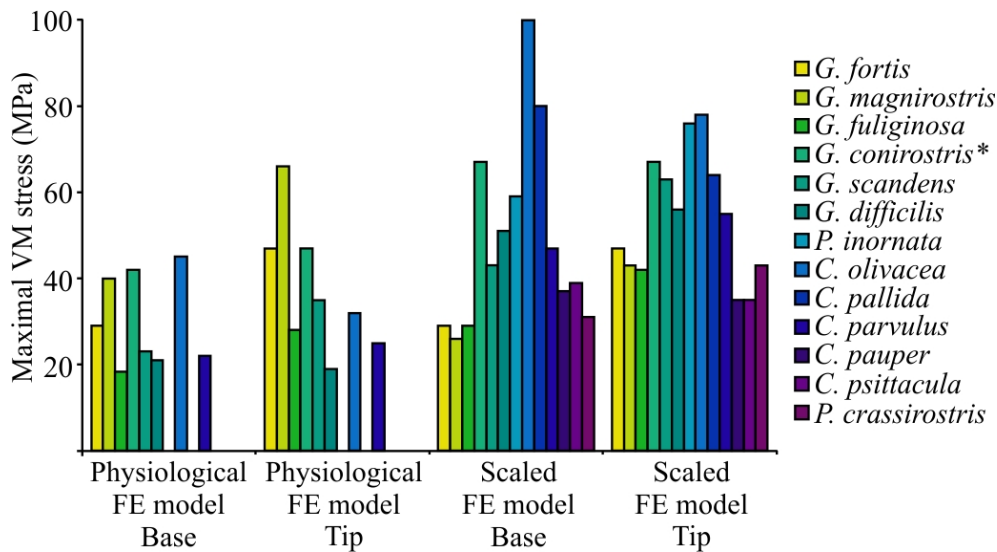


**Figure 8.3:** Peak VM stress for physiological FE models (tip and base loading, eight species with available muscle data) and for scaled FE models (tip and base loading, scaled to same size as *G. fortis* and with the same muscle forces) for thirteen species of Darwin's finch (\* = juvenile).

any loading condition. Indeed, these birds use their beaks almost exclusively to capture insects, rather than to crush or manipulate hard objects [58]. The deep and wide seed crushing beaks of *G. magnirostris*, *G. fortis* and *G. fuliginosa*, show lower stresses under base loading (below 30 MPa) than under tip loading, consistent with these birds' emphasis on base biting strategies in nature. Finally, comparatively low maximum stresses are found during tip loading for species that use the tips of their beak during foraging and have beaks with high curvature (e.g. *C. pauper* and *C. psittacula*, 35 MPa). The main exceptions to the otherwise precise tuning of beak strength and feeding mode concerns relatively high stresses observed for *G. conirostris* (67 MPa) and *Cactospiza pallida* (80 MPa) under different loading regimes. Whereas the results for *G. conirostris* might be explained by the fact that the specimen included in our study was a juvenile, results for *C. pallida* may be caused by the smaller mass of the constituent bone and keratin (volume in table 8.3).

In summary, our FE models show that beak size, shape and muscle force are tuned to yield similar safety factors across species, and help to demonstrate that beak shapes are well-suited for mitigating risk of fracture according to the feeding habitats the different species express. Understanding how beaks evolve to reduce risk of fracture may help to explain patterns of selection on beak size and shape in natural populations, and ultimately should be considered another central axis of adaptation and specialization in the Darwin's finch radiation.

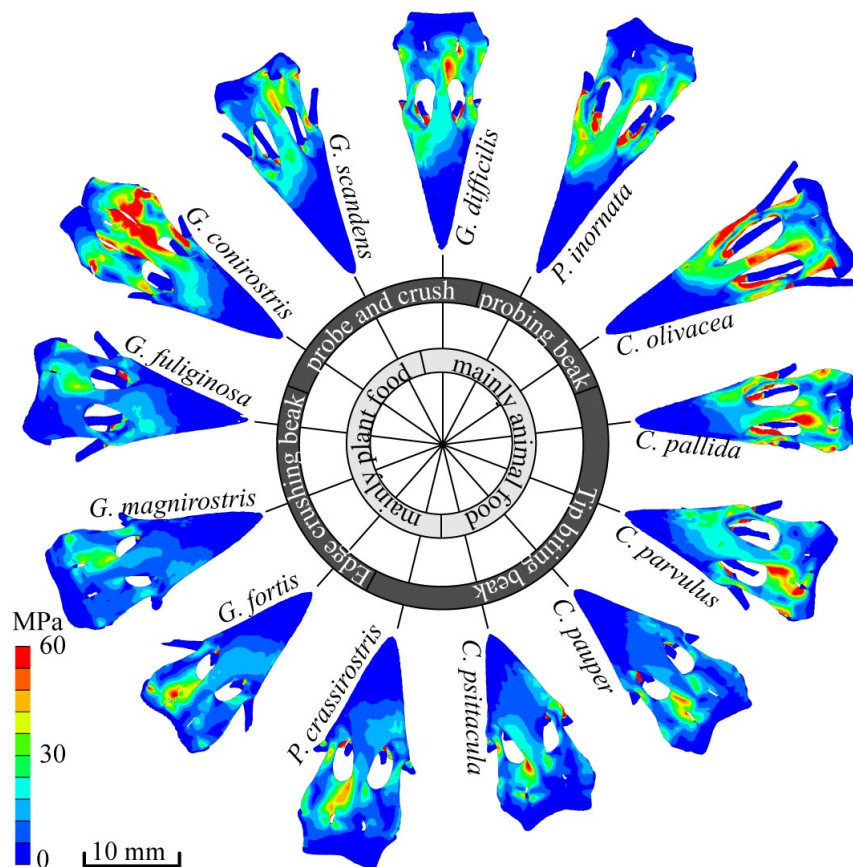


**Figure 8.4:** Dorsal view of scaled FE models of the upper beaks of 13 species of Darwin's finches. All beaks were scaled to same size and muscle force as *G. fortis*, and constrained to simulate base biting. Warmer colors represent higher VM stresses. Maximal stresses are given in figure 8.3. (Dorsal and lateral views of scaled FE models are presented in figure 8.11 and 8.12).

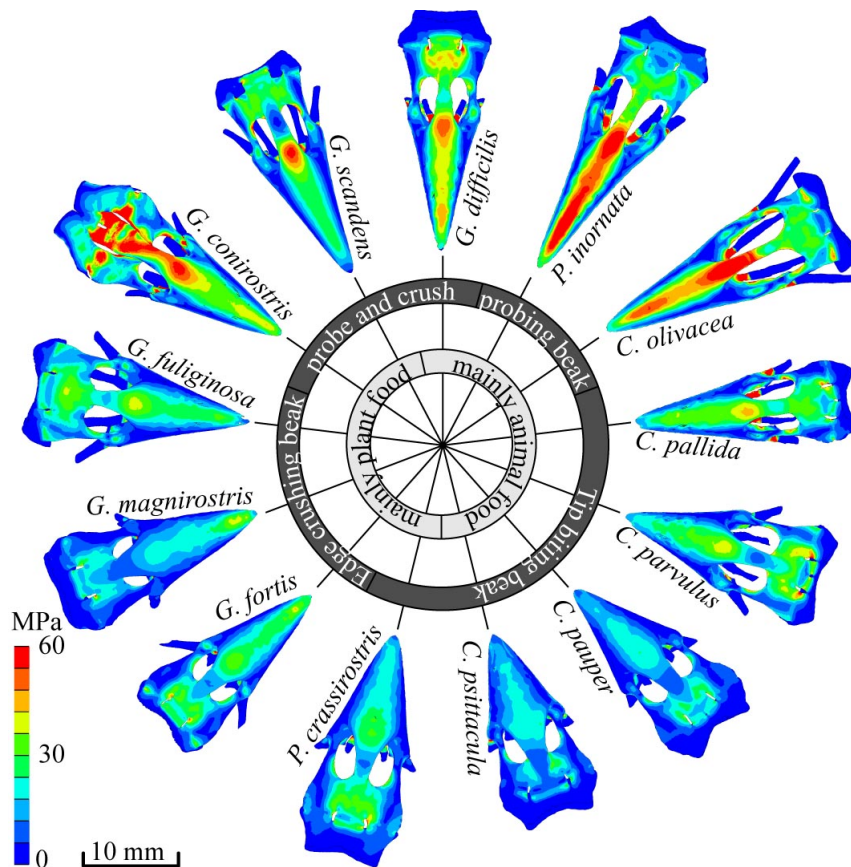


**Figure 8.5:** Dorsal view of scaled FE models of the upper beaks of 13 species of Darwin's finches. All beaks were scaled to same size and muscle force as *G. fortis*, and constrained to simulate tip biting. Warmer colors represent higher VM stresses. Maximal stresses are given in figure 8.3. (Dorsal and lateral view of scaled FE models are presented in figure 8.13 and 8.14).

## 8.3 Materials and Methods

### 8.3.1 Sample collection and CT scanning

Field work was conducted at coastal and upland sites on Santa Cruz Island during February and March of 2003, 2005 and 2006. Individuals of nine Darwin's finch species were captured in mist-nets, banded with unique color combinations, measured, tested for bite-force, and then released [65]. Bite-forces were measured using a Kistler force transducer set in a custom-built holder and attached to a handheld Kistler charge amplifier [63, 64]. Birds were induced to bite the force transducer at the back of the jaw where seeds are typically crushed [63, 64] as well as at the front of the jaw. At least three bites at each position were recorded for each individual, of which only the strongest was retained for analysis. Angle of the gape during bite-force measurement was kept consistent across birds by adjusting the distance between the bite plates according to the size of the bird.

Road-killed specimens were collected during February-March of 2005 and 2006 on Santa Cruz Island, under a salvage permit provided by the Galápagos National Park Service. Intact specimens were collected and preserved in a 10% aqueous formaldehyde solution for 24 h, rinsed and transferred to a 70% aqueous ethanol solution. Specimens were transported to Belgium where one individual of *G. fortis*, *G. fuliginosa*, *G. scandens*, *P. crassirostris*, *C. olivacea* and *C. parvulus* were scanned at the CT-scanning facility, Ghent University using a micro-focus directional type X-ray tube, set at a voltage of 80kV p and a spot size of 10 micrometer. Specimens were mounted on a controllable rotating table (MICOS, UPR160F-AIR). For each specimen a series of 1000 projections of 940x748 pixels was recorded covering 360 degrees. Specimens of *G. magnirostris*, *G. conirostris*, *G. difficilis*, *P. inornata*, *C. pallida*, *C. pauper* and *C. psittacula* were either from the museum of comparative zoology (Harvard) or from the California Academy of Sciences. An overview of the CT scans is given in table 8.2.

### 8.3.2 Muscle data

Muscle data was available for the following eight species: *G. fortis*, *G. magnirostris*, *G. fuliginosa*, *G. conirostris*, *G. scandens*, *G. difficilis*, *C. olivacea* and *C. parvulus*. These species were dissected and all muscle bundles of the jaw removed individually. Muscles were blotted dry and weighed on a Mettler microbalance ( $\pm 0.01\text{mg}$ ). Next, muscles were transferred individually to Petri dishes and submerged in a 30% aqueous nitric acid solution for 18 h to dissolve all connective tissue [85]. After removal of nitric acid, muscles were transferred to a 50% aqueous glycerol solution and fibers were teased apart using blunt-tipped glass needles. Thirty fibers were selected from each muscle bundle and drawn using a binocular scope with attached camera lucida. A background grid was also drawn in each image to provide an object for scaling. Drawings were scanned and fibre lengths determined using Scion Image (freely available at <http://www.scioncorp.com>, accessed January 2010).

**Table 8.2:** CT scans used in this chapter with their label, voxelsize and scaling factor to scale them to *G. fortis* size. (MCZ: Museum of comparative zoology, Harvard; DV: Darwin's finches scanned at Ghent University); CAS: California Academy of Sciences.

Species	label	voxelsize ( $\mu m$ )	scaling
<i>Geospiza fortis</i>	DV 09A01	29.44	1
<i>Geospiza magnirostris</i>	MCZ 112397	45.75	0.88
<i>Geospiza fuliginosa</i>	DV 10A03	22.00	1.68
<i>Geospiza conirostris</i>	CAS	26.60	1.14
<i>Geospiza scandens</i>	DV 12A01	43.78	1.28
<i>Geospiza difficilis</i>	MCZ 39828	25.26	1.57
<i>Pinaroloxias inornata</i>	MCZ 157930	47.00	1.00
<i>Certhidea olivacea</i>	DV 06A02	20.71	2.19
<i>Camarhynchus pallida</i>	MCZ 65744	27.55	1.60
<i>Camarhynchus parvulus</i>	DV 03A02	18.15	2.01
<i>Camarhynchus pauper</i>	CAS	30.79	1.28
<i>Camarhynchus psittacula</i>	MCZ 65738	30.74	1.46
<i>Platyspiza crassirostris</i>	DV 14A01	2.96	11.94

Based on muscle mass and fibre length, the physiological cross-sectional area of each muscle bundle was determined assuming a muscle density of  $1036 \text{ kg/m}^3$ . Since pennate muscles were separated into their individual bundles, no additional correction for pennation angle was included. Force-generation capacity for each muscle was calculated assuming a muscle stress of  $30 \text{ N/cm}^2$  [93]. As the external adductor and pseudotemporalis muscles act only indirectly on the upper mandible [15, 94, 132, 133], the component of the muscle force transferred to the upper mandible was calculated taking into account the position of the muscles and their angles relative to the jugal bone. The pterygoid muscle bundles act directly on the upper mandible [15, 94, 132, 133], and muscle forces were assumed to be directly transmitted through the pterygoid/palatine complex.

### 8.3.3 FE model

The segmentation of the bony core and the keratin layer in the CT images (Amira 4.1 64-bit version, TGS systems), the tetrahedral grid construction [114], the assigned material properties ( $E_{\text{keratin}} = 1.7 \text{ GPa}$ ,  $E_{\text{bone}} = 7.3 \text{ GPa}$ ) and the boundary conditions are similar to those reported elsewhere in this thesis (see section 5.2). Moreover, the output of these models of a different species of seed-cracking finch, *Padda oryzivora*, was validated using digital speckle pattern interferometry measurements (chapter 6). For every specimen, a FE model for base and tip loading is established. The available muscle forces obtained through dissection are applied to the jugal and pterygoid bones resulting in physiological FE models, for both base and tip loading, for eight

species. In addition we developed scaled FE models for all 13 species in such a way that their surface area and muscle forces are identical to those of *G. fortis*. As such, the effects of size are eliminated and the effect of shape variation on the mechanical behavior of the beak can be evaluated for the 13 species of Darwin's finches included here [41].

Bite force and maximum VM stress were obtained for all 40 FE models. Maximum VM stress was taken over four different locations of peak stress on the bony core, away from areas influenced by model constraints (figure 8.1). During base loading, VM stresses are not recorded at the contralateral side of the nasal bone. Other positions are chosen similar to those reported in chapter 5.

## 8.4 Supplementary data

Here, I present supplementary data and figures of the 40 FE models used in this chapter.

Results of stress distribution on Darwin's finch beaks without rhamphotheca are given in appendix B. This appendix also includes more information about the used methods. It should be noticed that differences in absolute values between chapter 8 and appendix B are caused by the inclusion or absence of the rhamphotheca and different recording positions.

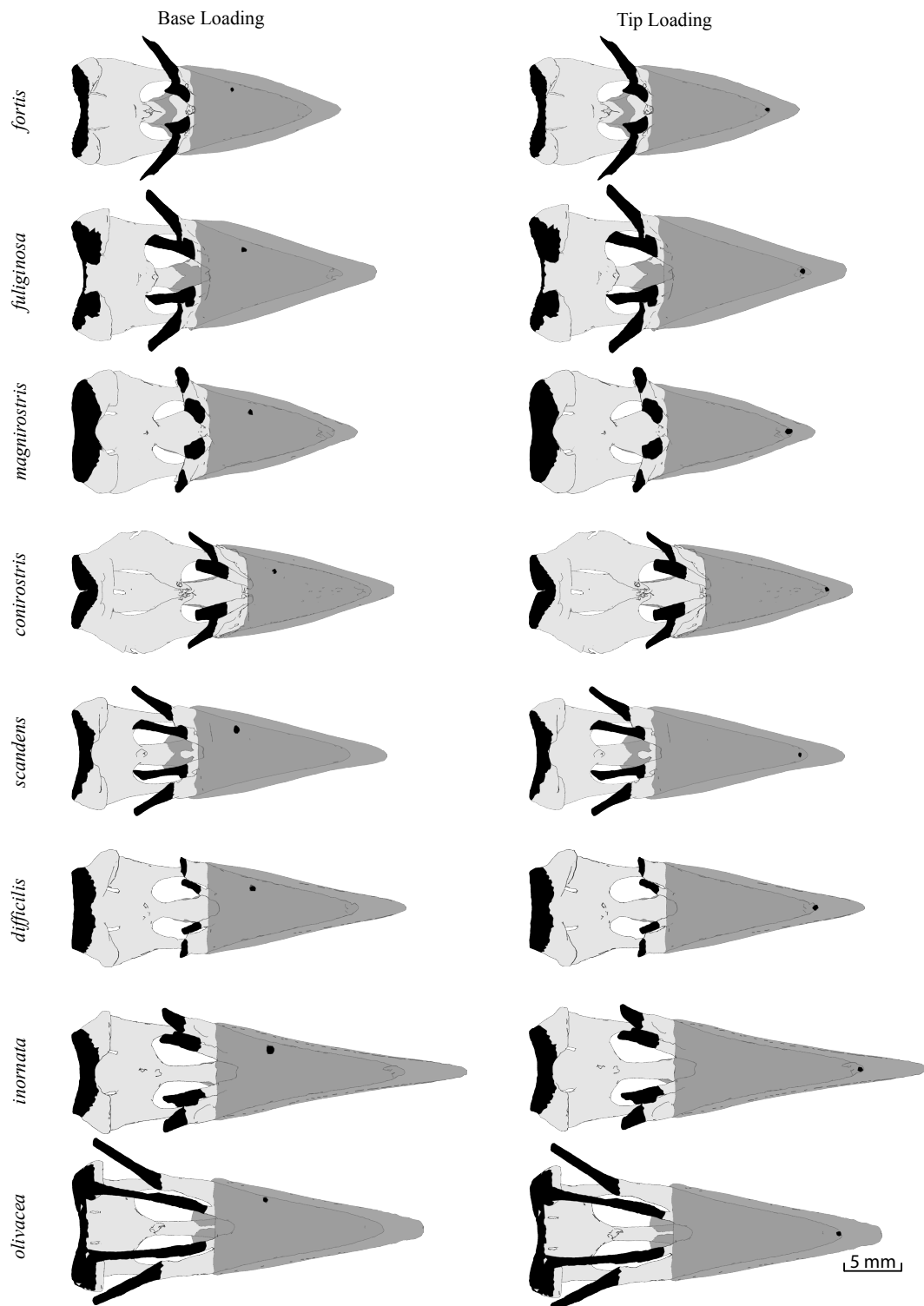


**Figure 8.6:** Ventral view of multi-layered finite element modeling approach for both base and tip loading (scaled models).

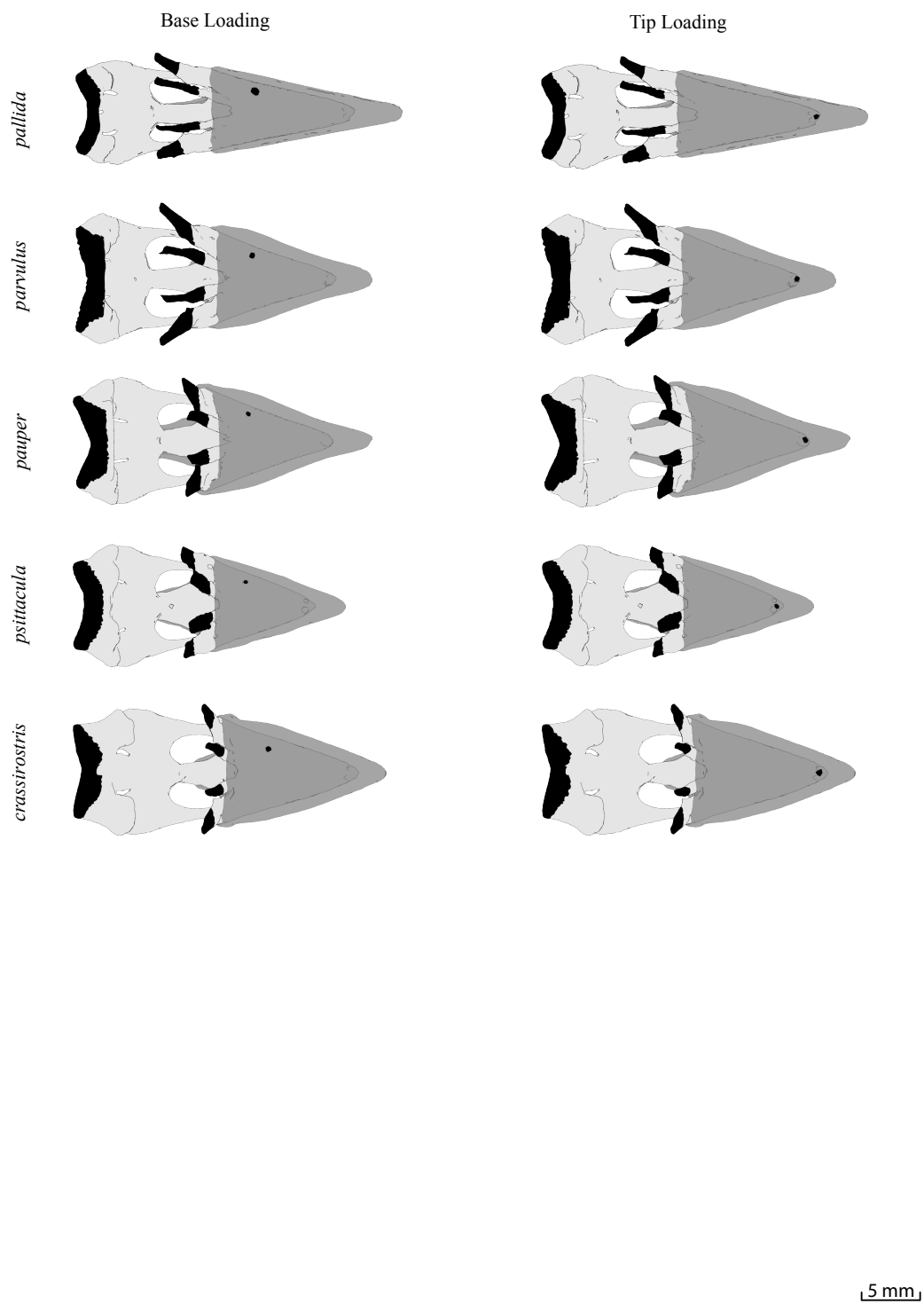


**Figure 8.7:** Ventral view of multi-layered finite element modeling approach for both base and tip loading (scaled models).

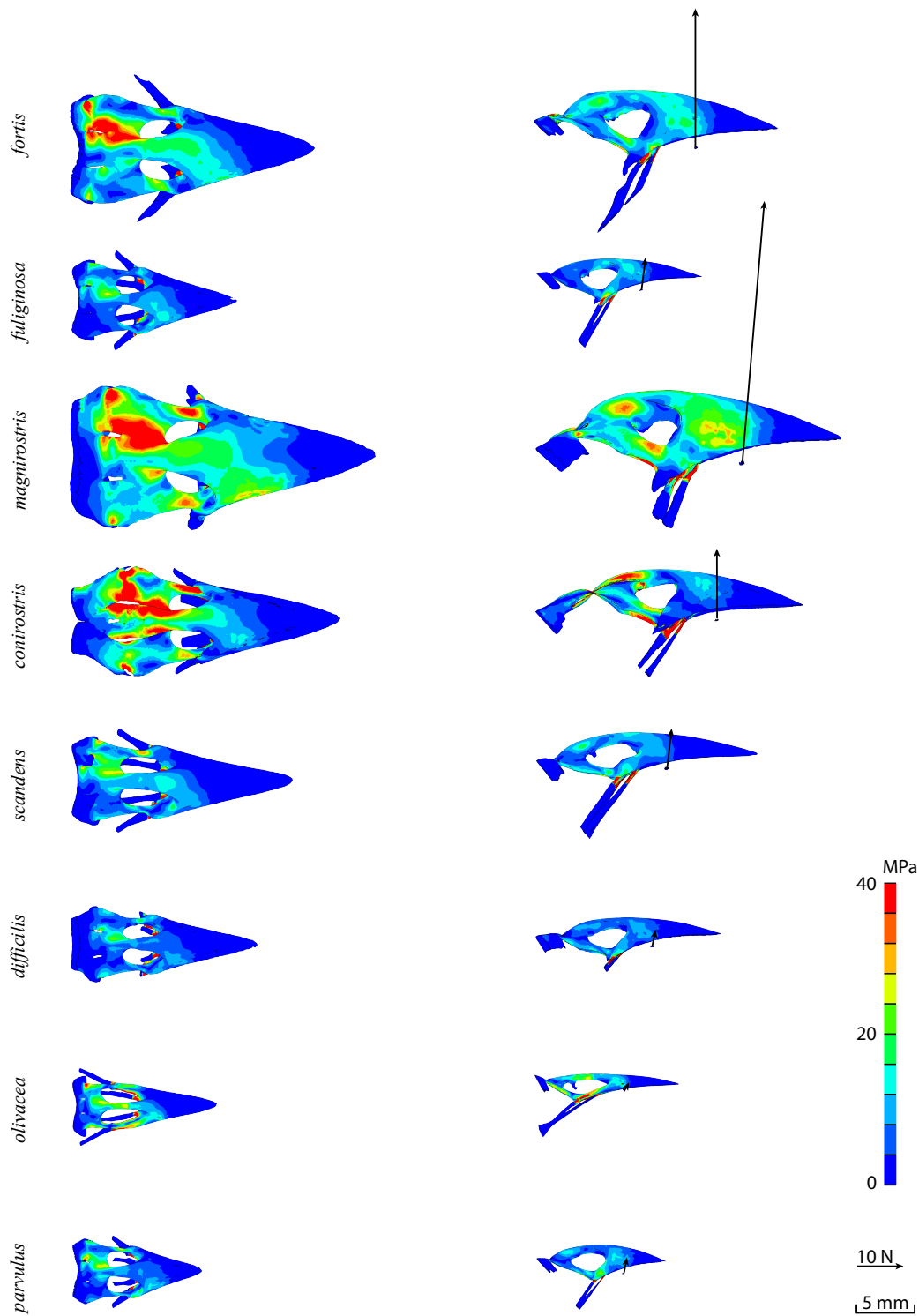


**Figure 8.8:** Dorsal (left) and lateral (right) view for finite element model results of base biting for 8 Darwin's finch species with available muscle data. Arrows indicate the location and magnitude of the calculated bite forces.

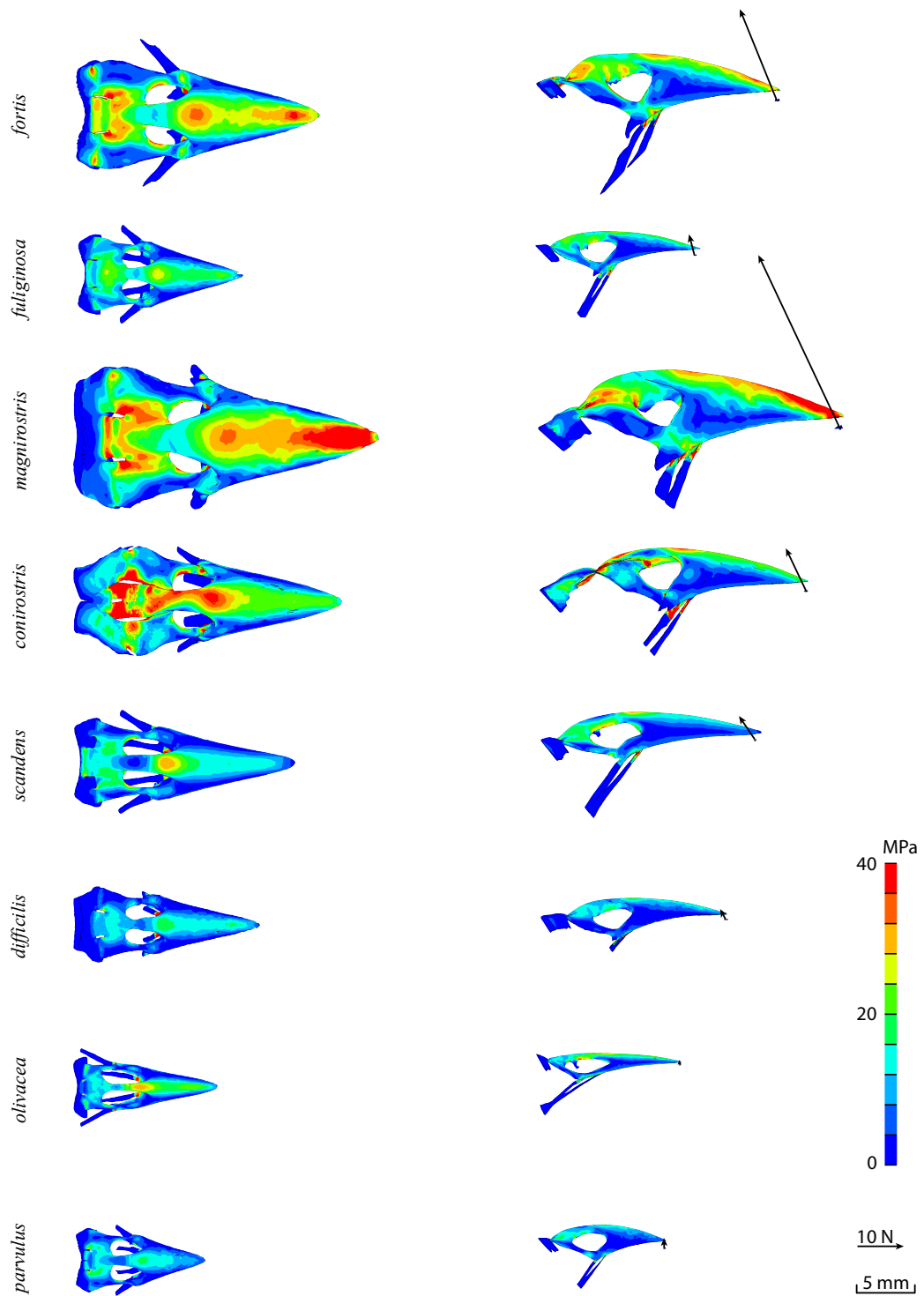


**Figure 8.9:** Dorsal (left) and lateral (right) view for finite element model results of tip biting for 8 Darwin's finch species with available muscle data. Arrows indicate the location and magnitude of the calculated bite forces.

**Table 8.3:** Von Mises stress for different loading conditions (LC) for 13 Darwin's finches (NB: natural base biting; NT: natural tip biting; FB: base biting scaled to *fortis*; FT: tip biting scaled to *fortis*). Results are given in MPa for five positions (Pos1: on top of bone, near bite position; Pos2: on top of the nasal hinge; Pos3: ipsilateral side of nasal bone; Pos4: on top of keratin; Pos5: at the bottom of the keratin). The resulting (model) force ( $F$ ) is given in N; the volume of keratin and bone ( $V_{ker}$  and  $V_{bone}$ ) are given in  $mm^3$ .

Species	LC	Pos1	Pos2	Pos3	Pos4	Pos5	F	$V_{bone}$	$V_{ker}$
<i>G. fortis</i>	NB	21	19	29	5	5	30.4	104	128
<i>G. fortis</i>	NT	47	36	41	13	11	21.5	104	128
<i>G. magnirostris</i>	NB	35	24	40	6	4	57.9	232	195
<i>G. magnirostris</i>	NT	66	35	46	18	18	41.6	232	195
<i>G. magnirostris</i>	FB	22	16	26	4	3	29.3	157	131
<i>G. magnirostris</i>	FT	43	23	30	12	12	20.9	157	131
<i>G. fuliginosa</i>	NB	18	15	18	4	3	7.1	24	35
<i>G. fuliginosa</i>	NT	24	28	27	8	7	4.6	24	35
<i>G. fuliginosa</i>	FB	29	23	28	6	4	29.2	115	164
<i>G. fuliginosa</i>	FT	35	41	42	12	10	19.0	115	164
<i>G. conirostris</i>	NB	16	25	42	19	4	15.3	76	82
<i>G. conirostris</i>	NT	25	40	47	12	7	10.4	76	82
<i>G. conirostris</i>	FB	25	33	67	29	7	32.3	112	121
<i>G. conirostris</i>	FT	45	63	67	18	16	18.8	112	121
<i>G. scandens</i>	NB	20	15	23	4	3	8.9	59	56
<i>G. scandens</i>	NT	17	33	35	9	6	6.1	59	56
<i>G. scandens</i>	FB	40	28	43	7	5	26.2	126	119
<i>G. scandens</i>	FT	30	60	63	16	10	17.9	126	119
<i>G. difficilis</i>	NB	14	12	21	3	3	3.6	22	30
<i>G. difficilis</i>	NT	18	19	18	6	6	2.4	22	30
<i>G. difficilis</i>	FB	38	24	51	8	8	26.1	86	116
<i>G. difficilis</i>	FT	50	56	53	18	17	16.7	86	116
<i>P. inornata</i>	FB	55	32	59	10	10	26.2	109	96
<i>P. inornata</i>	FT	76	67	61	26	37	13.8	109	96
<i>C. olivacea</i>	NB	23	31	45	7	3	2.0	9	9
<i>C. olivacea</i>	NT	23	32	22	9	12	1.0	9	9
<i>C. olivacea</i>	FB	58	66	100	17	9	24.4	99	100
<i>C. olivacea</i>	FT	58	78	59	21	33	12.3	99	100
<i>C. pallida</i>	FB	59	33	80	10	18	25.4	68	101
<i>C. pallida</i>	FT	38	46	64	14	16	15.1	68	101
<i>C. parvulus</i>	NB	22	12	20	4	2	3.3	11	18
<i>C. parvulus</i>	NT	13	19	25	6	4	2.2	11	18
<i>C. parvulus</i>	FB	47	26	43	8	6	29.6	88	143
<i>C. parvulus</i>	FT	29	41	55	14	9	19.5	88	143
<i>C. pauper</i>	FB	23	17	37	17	8	31.2	118	163
<i>C. pauper</i>	FT	19	25	35	8	8	19.4	118	163
<i>C. psittacula</i>	FB	39	24	33	6	6	30.5	93	127
<i>C. psittacula</i>	FT	25	28	35	7	7	21.9	93	127
<i>P. crassirostris</i>	FB	21	21	31	5	5	32.1	138	152
<i>P. crassirostris</i>	FT	25	32	43	9	6	21.7	138	152

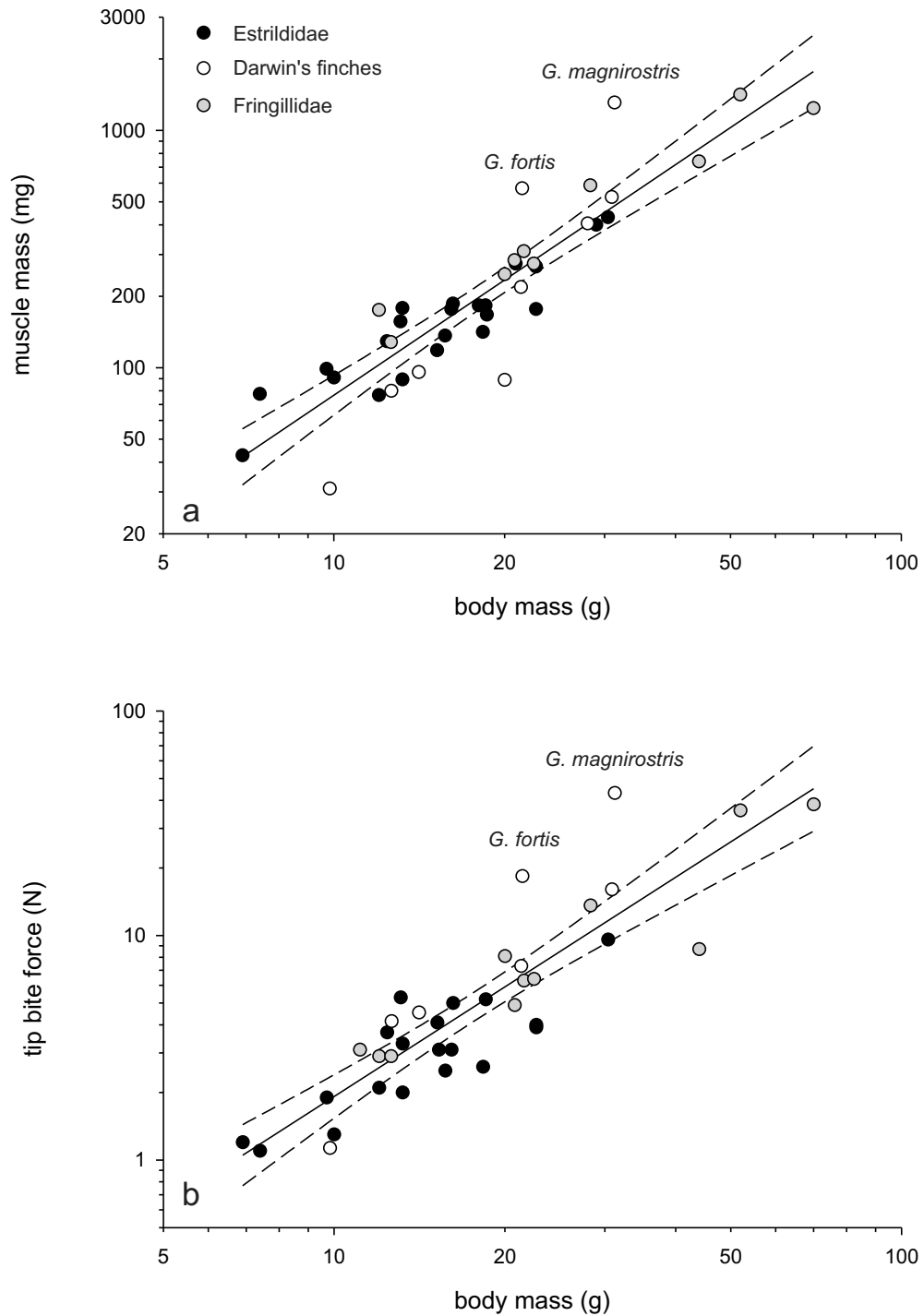


**Figure 8.10:** Muscle mass and tip bite force compared to the body mass of finches. Note how *G. magnirostris* and *G. fortis* have an exceptionally high muscle mass and bite force for their size.

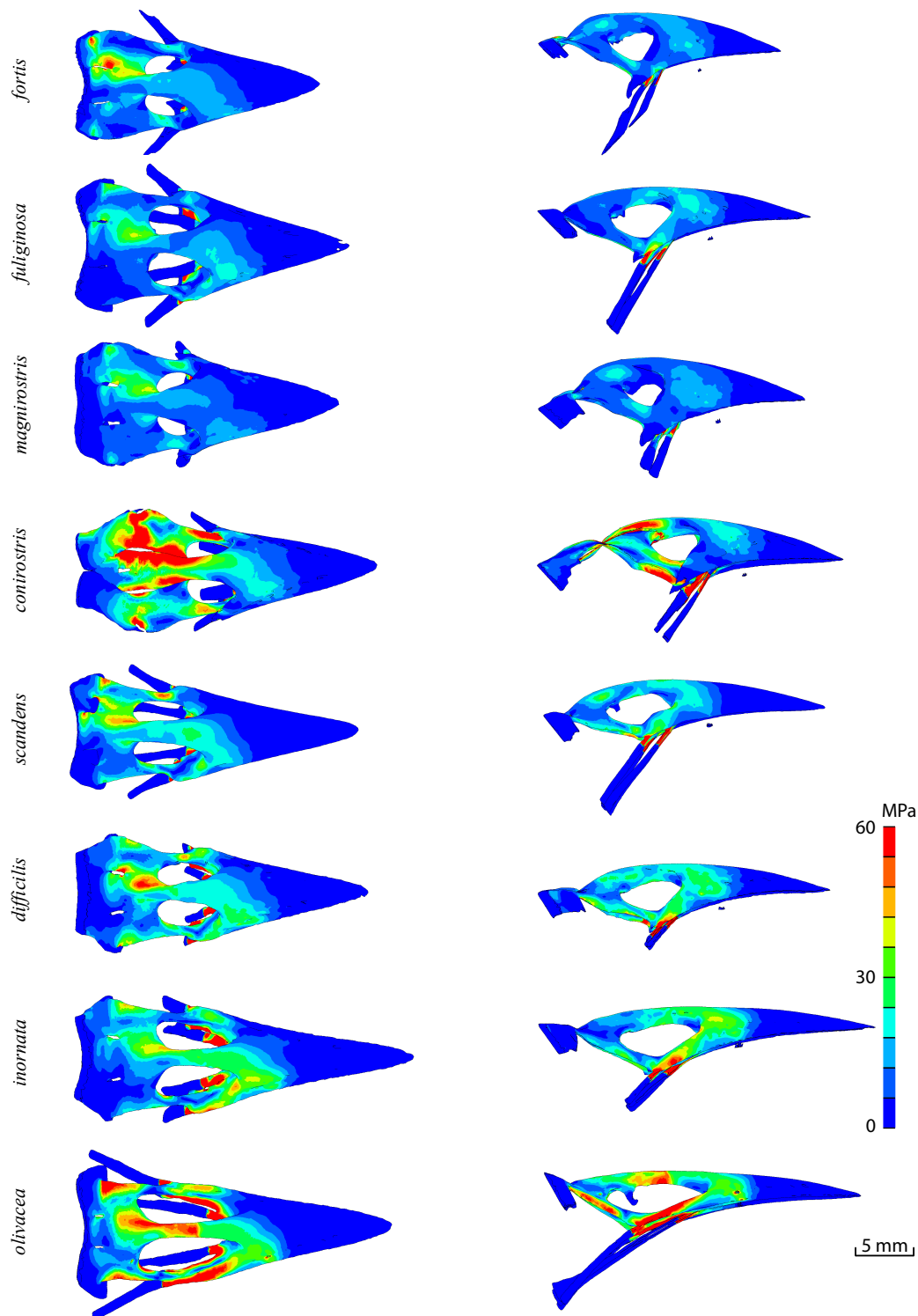


**Figure 8.11:** Dorsal (left) and lateral (right) view of scaled FE models of the upper beaks of Darwin's finches for base biting. All beaks were scaled to same size (*G. fortis*) and identical muscle forces (*G. fortis*) were applied.

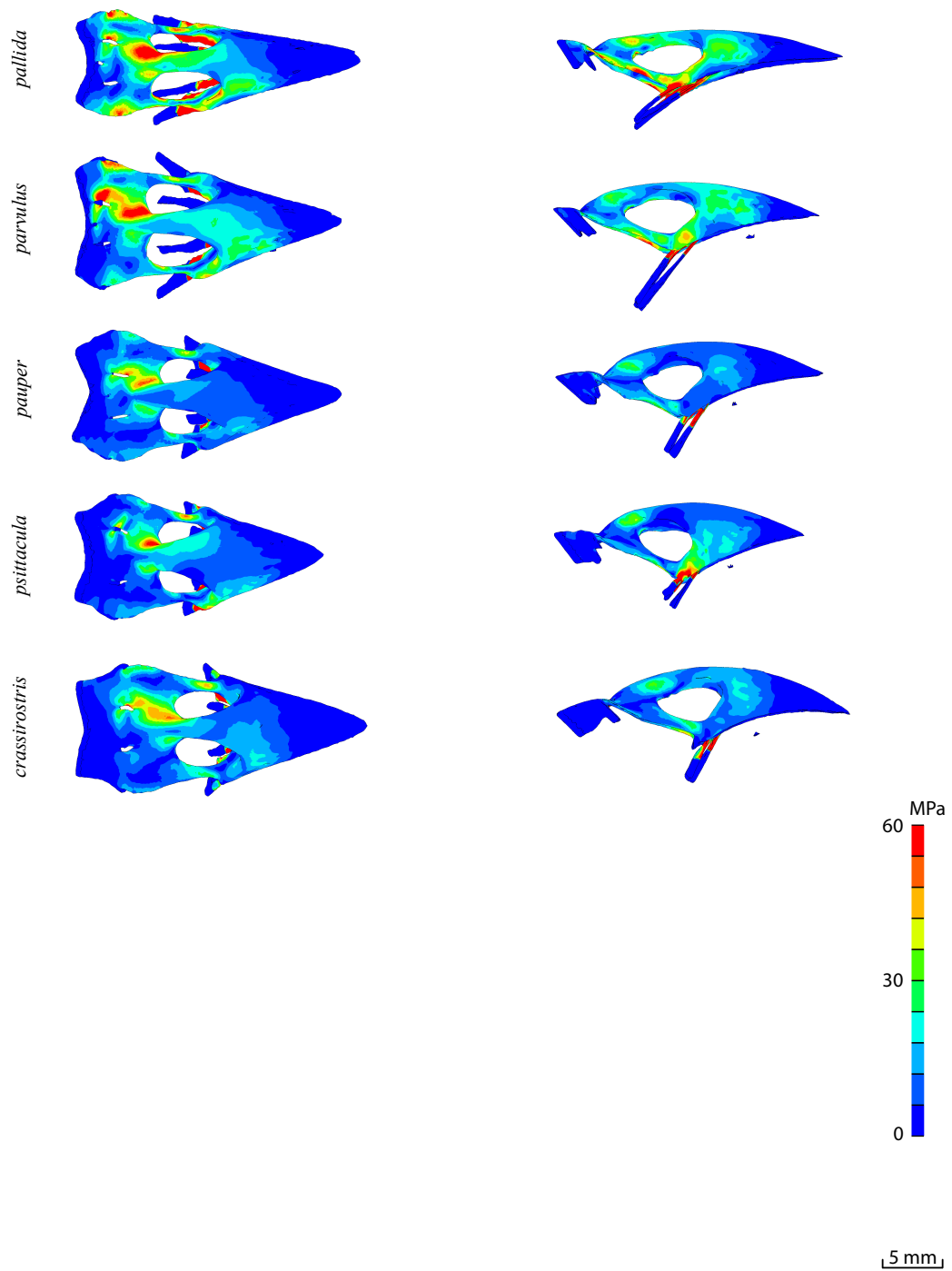


**Figure 8.12:** Dorsal (left) and lateral (right) view of scaled FE models of the upper beaks of Darwin's finches for base biting. All beaks were scaled to same size (*G. fortis*) and identical muscle forces (*G. fortis*) were applied.

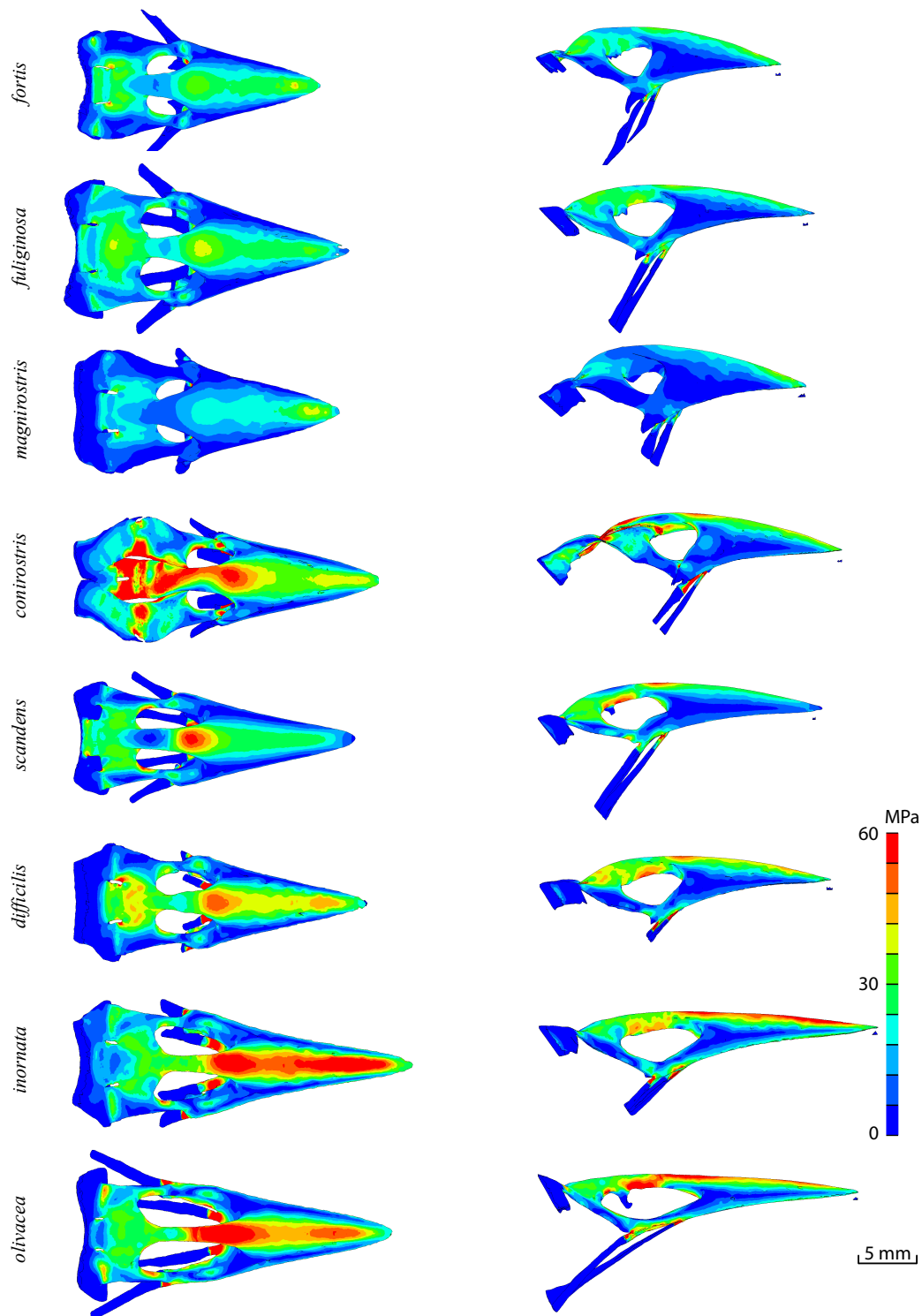


**Figure 8.13:** Dorsal (left) and lateral (right) view of scaled FE models of the upper beaks of Darwin's finches for tip biting. All beaks were scaled to same size (*G. fortis*) and identical muscle forces (*G. fortis*) were applied.

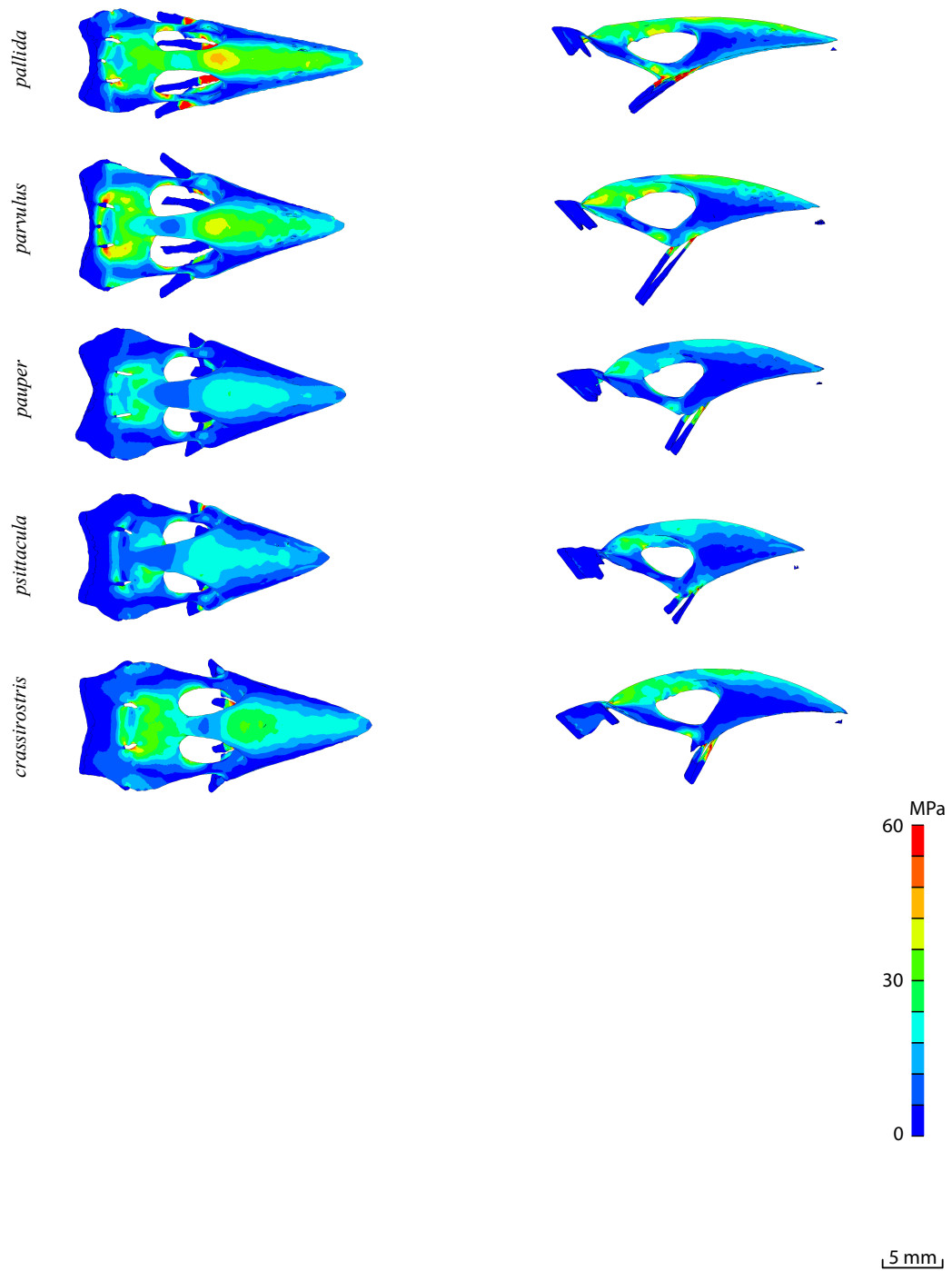


**Figure 8.14:** Dorsal (left) and lateral (right) view of scaled FE models of the upper beaks of Darwin's finches for tip biting. All beaks were scaled to same size (*G. fortis*) and identical muscle forces (*G. fortis*) were applied.



## CHAPTER 9

---

### General conclusions

---

The main goal of this dissertation was to prove the important role of beak size and shape in fracture avoidance. In order to conduct the study, I had access to a unique collection of 13 Darwin's finch specimens. From a single ancestor, these Galápagos finches have specialized in different food resources and have developed beaks of very different sizes and shapes. These beaks can be divided into 4 groups [15, 58]: edge crushing, probing and crushing, probing and tip biting beaks. Seed cracking ability is, however, principally determined by muscle force. In chapter 8, I made finite element (FE) models, starting from micro-CT images, to prove that beaks are indeed adapted to withstand their natural muscle loading (figure 8.2). Next, models were scaled to the same dimensions and the same input forces were applied (in total 40 FE models were created). As such, It was possible to study the influence of beak shape without scaling effects. I found physics-based evidence that beak shape is adapted to beak usage: edge crushing beak are superb for crushing hard seeds, while tip biting beaks for instance are better suited for loadings at their tip (figure 8.4 and 8.5).

Besides the main goal of this dissertation, I also needed to tackle some practical issues. A first practical issue was to build a finite element model based on morphological information. Geometrical input can be obtained by a process called segmentation (of micro-CT images), resulting in a surface model. Such surface models, however, need to meet specific criteria (described in chapter 2). Meeting these criteria is particularly challenging for the multi-layered structure of bird beaks (chapter 5). Hence, I first made a FE model of the Java finch beak. This bird is a model finch for the protected and difficult to obtain Darwin's finches [52]. I was able to successfully incorporate the rhamphotheca (keratin layer) in my model and I showed how this keratin layer is important for the strength of the lightweight beak.

A second important practical issue is the necessity of a good material description in my model. Therefore, I want to obtain the elastic moduli of bone and keratin. However,

material characterization on thin and small biological samples is difficult. Indeed, controlling the boundary conditions in standard tests is difficult for samples only a few  $100\mu\text{m}$ 's thick. To solve this problem, I introduced a novel double indentation technique (chapter 3). Compared to normal indentation testing, a second needle is introduced and samples can be easily clamped between the two needles. As a result, problems at the unknown sample - sample holder interface were avoided. Additionally, a FE-calculated correction factor was introduced since the standard indentation equation was only deduced for infinite thick samples. The new method was validated on well known test materials and by comparing the results with those obtained by an inverse analysis (chapter 7).

Although the material characterization and the finite element modeling were conducted with the greatest care, a lot of assumptions were made and model outcome should be compared with validation experiments. A first indication of the validity of the models is the good correspondence between measured and modeled bite force. However, one can obtain similar bite forces for different stress fields. Displacement or strain measurements are therefore better suited as validation. Measurements on small and complex shaped samples, such as the upper beak, are not straightforward. In chapter 6, model displacements and strains were compared to the results of two experimental techniques, namely digital speckle pattern interferometry (DSPI) and digital image correlation (DIC). A good correspondence was found, and as such, my modeling approach was validated.

In conclusion, I successfully introduced finite element models of bird beaks. In this way I gave mechanical evidence for the relation between beak shape and fracture avoidance in Darwin's finches. Therefore, I developed a novel double indentation technique for material characterization and an interferometric validation setup.

### Future directions

Bowman [15] suggested more than 50 years ago that the variation in beak shape is situated mainly along two axes: variation in width and depth, and variation in length. Interestingly, the two principal axes proposed by Bowman are also reflected in distinct developmental pathways [1, 2]. Recently, Campàs et al. [23] showed how affine transformations can be used to describe these underlying developmental processes and to link the different beak shapes. In future work, we can investigate the mechanical implications of these affine transformations and consequently of these developmental pathways. Other future work may include some further investigations and improvements regarding my modeling approach. First it would be interesting to know how the beak behaves under dynamic loading. E.g. how can the keratin layer protect the bony core for impact loading. Second, it would be interesting to have a closer look to the struts in the bony core. In my model, the largest struts are incorporated, but no examination of the influence of these struts have been done. Future improvements can also be expected by including a correct treatment of the bending area. In this way, stress levels close to this boundary condition can also be recorded correctly. Finally, we can include the lower beak and expand my model to the whole beak.

# APPENDIX A

---

## Stereoscopy

---

### **Abstract**

*A method for high-resolution measurement of 3D coordinates and translations of small objects, using single X-ray point source stereoscopy is presented in Salih et al. [105]. The method is implemented using a micro X-ray tomography setup with a single  $8\ \mu\text{m}$  point source. Stereo projections are obtained by rotating the object over  $90^\circ$  between subsequent recordings, and microscopic Tungsten beads are used as marker points. The accuracy of the method is tested on a spherical calibration object, and found to be better than  $10\ \mu\text{m}$ . Using a translation stage, the measurement uncertainty for translation measurements was found to be better than  $5\ \mu\text{m}$  along both axes parallel to the detector and at right angles to the detector. Due to the short measurement time and the high resolution, the method will be useful to study the biomechanics of small specimens, and the principle of the method is useful in any cone-beam based setup. In this appendix, I will show the theory for this X-ray stereo-system, which I developed and implemented in a 'matlab' program used in the above mentioned paper [105].*

This appendix is based on:

Salih Wasil, Soons Joris and Dirckx Joris. High-resolution 3D translation measurements using point source X-ray stereoscopy. *Measurement science and technology*, 22, 025502, 2011

## A.1 Theory

In classical X-ray stereoscopy, the object is placed relatively far away from the X-ray source, and close to the X-ray detector, so it is a good approximation to regard the rays as forming a parallel beam. In micro X-ray setups, the object is placed very close to a point source of X-rays and the detector is placed relatively far away. In this way, the conical X-ray beam is used to provide a magnified shadow projection of the object. In order to combine the micro X-ray technique with stereoscopy, a simple treatment based on a parallel beam can no longer be applied. In this case, the X-rays fan out over a certain angle, starting out from a nearly point-like source.

For photographic stereogrammetry, the pinhole model was developed to calculate object coordinates from two projections through two small aperture lenses. We will now use this approach for X-rays emerging from a point source. The setup is somewhat different because in an optical setup the light coming from the object is imaged onto a camera target through a small aperture. In our case, it works somewhat the other way round: the rays start from the point source, go through the object, and then fall upon the detector. We will derive the equations for the calculation of the object coordinates from the two stereograms in this case.

Instead of using two pinhole cameras, our method makes use of two point-like sources of X-rays. In practice, only one source is used, and the object will be rotated between the recordings of the two stereograms. Like in a pinhole stereo camera setup, an object point  $Q$  is imaged onto image point  $Q_1$  and  $Q_2$  on the respective detectors. The positions of  $Q_1$  and  $Q_2$  lie at the intersection of the detector plane  $\sigma_1$  and  $\sigma_2$  with the line which connects pinhole  $O_1$  or  $O_2$  (in our case: the point sources) with the object point  $Q$ . (figure A.1). Under specific circumstances, it is possible to provide the back-projection from the two images and to calculate the coordinates of the point  $Q$  [120, 130]. By changing the position of the object between the source and the detector, a different magnification is obtained. In contrast to tomography, it is not necessary for the entire object to remain within the X-ray cone, but coordinates can of course only be measured on points which cast a shadow on both detectors.

In figure A.1 the world coordinate system ( $WCS$ ) and the camera coordinate systems for two cameras ( $CCS_1$  and  $CCS_2$ ) are shown. The Y-axes are out of plane, pointing to the reader. A set of points  $Q$  in the  $CCS_1$  or  $CCS_2$  can be transformed to  $WCS$  by multiplying the coordinates with a rotation matrix  $R_1$  or  $R_2$  and adding a translation  $T_1$  or  $T_2$ . Those parameters defining the rigid body transformation are called the extrinsic parameters of the camera, which are necessary to determine the position of camera respectively to world. So

$$Q_{WCS} = R \cdot Q_{CCS} + T \quad (\text{A.1})$$

In photographic stereoscopy,  $O_1$  and  $O_2$  represent the pinholes and  $\sigma_1$  and  $\sigma_2$  represent the photographic plates. Here,  $O_1$  and  $O_2$  are the X-ray point sources and  $\sigma_1$  and  $\sigma_2$  are now the corresponding image planes on the X-ray detectors. Whereas the standard pinhole setup has a  $\sigma_1 - O_1 - Q$  sequence, the X-ray setup has a  $O_1 - Q - \sigma_1$  sequence. The distance between  $O_1$  and  $\sigma_1$  is called the principal distance ( $f_1$ ) (idem for  $f_2$ ).

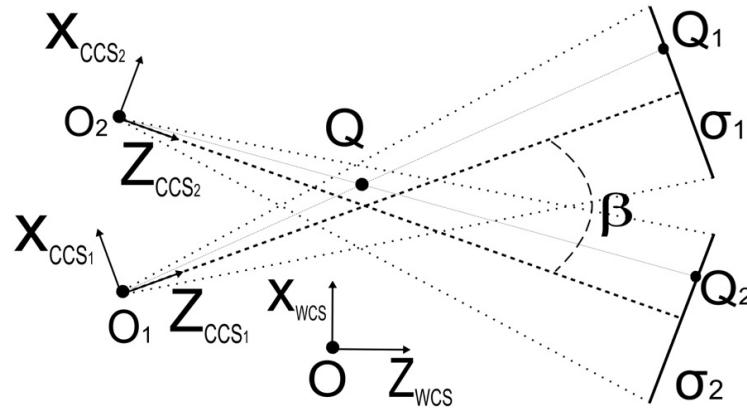


Figure A.1: A simple stereo system.

The image of point  $Q$  on detector 1 can easily be transformed to  $Q_1$  in  $WCS$ . First, the pixel representing  $Q_1$  is written in the image coordinates. This is done by defining the origin in the image, giving the pixel number the same direction as the X-axis and Y-axis of  $CCS_1$  and by multiplying with the pixel size. Secondly, a transformation to  $CCS_1$  is applied by making the Z-coordinate equal to  $f_1$ . The principal distance  $f$ , the centre of the image and the pixel size are called the intrinsic parameters of the camera which are necessary to link the pixel coordinates of an image point with the corresponding coordinates in the camera reference frame. Next, those coordinates are transformed with  $R_1$  and  $T_1$  to the  $WCS$ . To transform  $Q_2$  to the  $WCS$  the same method is used. Finally,  $Q$  will be found in  $WCS$  as the intersection of  $O_1Q_1$  and  $O_2Q_2$ . There will often be no intersection point due to the limited precision of the X-ray detection and small misalignments of the setup. In this case, the midpoint on the line perpendicular to  $O_1Q_1$  and to  $O_2Q_2$  is been taken as  $Q$ .

In our setup, we will have a simple case (see figure A.1). We consider the rotation  $\beta$  around the y-axis and a translation along x and z axes. Therefore, the rotation matrix  $R$  for both images is given as:

$$R_1 = \begin{bmatrix} \cos \frac{\beta}{2} & 0 & -\sin \frac{\beta}{2} \\ 0 & 1 & 0 \\ \sin \frac{\beta}{2} & 0 & \cos \frac{\beta}{2} \end{bmatrix} \quad (\text{A.2})$$

$$R_2 = \begin{bmatrix} \cos \frac{\beta}{2} & 0 & \sin \frac{\beta}{2} \\ 0 & 1 & 0 \\ -\sin \frac{\beta}{2} & 0 & \cos \frac{\beta}{2} \end{bmatrix} \quad (\text{A.3})$$

and the translation  $T$  is

$$T_1 = (-t_{X_{CCS}}, 0, -t_{Z_{CCS}})^T \quad (\text{A.4})$$

$$T_2 = (t_{X_{CCS}}, 0, t_{Z_{CCS}})^T \quad (\text{A.5})$$

From these equations, we can obtain the three coordinates as follows:

$$X_{WCS} = \frac{X_{CCS_1} + X_{CCS_2}}{2 \cos \frac{\beta}{2}} \quad (\text{A.6})$$

$$Y_{WCS} = \frac{Y_{CCS_1} + Y_{CCS_2}}{2} \quad (\text{A.7})$$

$$Z_{WCS} = \frac{X_{CCS_1} - X_{CCS_2}}{4 \sin \frac{\beta}{2}} \quad (\text{A.8})$$

Where  $X_{CCS_1} - X_{CCS_2}$  is known as disparity ( $d$ ) which measures the difference in retinal position between the corresponding points in the two stereo images. The disparity is an important parameter to determine the  $Z_{WCS}$ -axis value [120]. From the previous equations, we are now able to determine the  $X_{WCS}$ ,  $Y_{WCS}$  and  $Z_{WCS}$  coordinates of point  $Q$  and thus the exact 3D position.

## A.2 Matlab code

The matlab function 'backprojection.m' calculates  $Q_{WCS}$  for  $Q_{CCS_1}$  and  $Q_{CCS_2}$ . The function also needs the intrinsic and extrinsic parameters of the camera:

```

1 function Marker_WCS = backprojection(Marker_image_left , Marker_image_right
  , pos_cam_l , pos_cam_r , angle_cam_l , angle_cam_r , f , kappa , imageon)
2
3 %#####
4 %#          (c) Joris Soons (c)          #
5 %#          mailto: joris.soons@ua.ac.be  #
6 %#####
7 %
8 %
9 %Marker_WCS = backprojection(Marker_image_left , Marker_image_right ,
10 %   pos_cam_l , pos_cam_r , angle_cam_l , angle_cam_r , kappa , imageon)
11 %
12 % - Marker_Wcs: set of calculated 3D points in world coord system
13 % - Marker_image_lef and _right: image on pinhole camera (remark: negative)
14 % - pos_cam_l and _r: respective 3D position of pinhole of camera
15 % - angle_cam_l and _r: respective direction of camera given in 3 angles [a
  , b , c] , a is around
16 % x-as , b around y-as , c around z-as
17 % - f: principal distance (distance between pinhole and projection-plane
18 % - kappa: lens distortion
19 % - imageon: image output on (1) or off (0)
20
21
22 %% de-distort the images
23 %kappa distortion
24 de_distortion=1./(1+kappa*(Marker_image_left(:,1).^2+Marker_image_left(:,2)
  .^2));

```

```

25 Marker_image_left(:,1)=de_distortion.*Marker_image_left(:,1);
26 Marker_image_left(:,2)=de_distortion.*Marker_image_left(:,2);
27
28 de_distortion=1./(1+kappa*(Marker_image_right(:,1).^2+Marker_image_right
    (:,2).^2));
29 Marker_image_right(:,1)=de_distortion.*Marker_image_right(:,1);
30 Marker_image_right(:,2)=de_distortion.*Marker_image_right(:,2);
31
32 %% give position cameras in World coord system
33 T_l=pos_cam_l';
34 T_r=pos_cam_r';
35
36
37 %% changeAxes is to: z->x, x->y,y->x
38 changeAxes=eye(3);[0,0,1;1,0,0;0,1,0];
39 % Remark: This is for the negative
40
41 %% create rotation matrix for transformation camera coord system to world
42 %% coord system
43 angle_cam=angle_cam_l;%rotx, roty, rotz
44 Rx=[1 0 0; 0 cos(angle_cam(1)) -sin(angle_cam(1)); 0 sin(angle_cam(1)) cos(
    angle_cam(1))];
45 Ry=[cos(angle_cam(2)) 0 sin(angle_cam(2)); 0 1 0;-sin(angle_cam(2)) 0 cos(
    angle_cam(2))];
46 Rz=[cos(angle_cam(3)) -sin(angle_cam(3)) 0; sin(angle_cam(3)), cos(
    angle_cam(3)), 0; 0 0 1];
47 R_l=Rx*Ry*Rz*changeAxes;
48
49 angle_cam=angle_cam_r;%rotx, roty, rotz
50 Rx=[1 0 0; 0 cos(angle_cam(1)) -sin(angle_cam(1)); 0 sin(angle_cam(1)) cos(
    angle_cam(1))];
51 Ry=[cos(angle_cam(2)) 0 sin(angle_cam(2)); 0 1 0;-sin(angle_cam(2)) 0 cos(
    angle_cam(2))];
52 Rz=[cos(angle_cam(3)) -sin(angle_cam(3)) 0; sin(angle_cam(3)), cos(
    angle_cam(3)), 0; 0 0 1];
53 R_r=Rx*Ry*Rz*changeAxes;
54
55
56 %%
57 %% R=R_r*R_l';
58 %% % T=pos_cam_l'-R'*pos_cam_r';
59 %% % T=pos_cam_r'-pos_cam_l'; %remark: different from book pages 163
60
61 %% calculate coord in World coord system
62
63 clear point
64 for herh=1:length(Marker_image_left(:,1))
65     p_l=R_l*[Marker_image_left(herh,:),f]';
66     p_r=R_r*[Marker_image_right(herh,:),f]';
67     %image_vector from camera coord system to world coord system
68
69     w=cross(p_l,p_r);

```

```

70     %perpendicular on p_l and p_r (shortest distance)
71
72     Temp=[p_l,-p_r,w];
73     coeff=Temp^-1*(T_r-T_l);
74     a=coeff(1);
75     b=coeff(2);
76     c=coeff(3);
77     % find cross-section T_r+b*p_r and T_l+a*p_l+c*w
78
79     Marker_WCS(:,herh)=T_r+b*p_r;
80
81 end
82
83 %% plot in world coord system
84 if imageon==1
85     figure
86     plot3(Marker_WCS(1,:),Marker_WCS(2,:),Marker_WCS(3,:),'+')
87     grid on
88     view(2)
89     axis vis3d
90 end

```

The matlab function 'stereoscopyPlanar.m' calculates  $Q_{WCS}$  for the simple case presented in figure A.1. Markers can be indicated in the left and right image stereo image. The function 'backprojection.m' is used for the actual calculation:

```

1 function markers_WCS_new=stereoscopyPlanar(fileName_imageL,fileName_imageR,
2     theta,dist_imageplane_rotation,imageon)
3
4 %
5 %
6 %     #####
7 %     #           (c) Joris Soons (c)           #
8 %     #           mailto: joris.soons@ua.ac.be           #
9 %     #####
10 % markers_WCS_new=stereoscopyPlanar(fileName_imageL,fileName_imageR,theta,
11 %     dist_imageplane_rotation,imageon)
12 %
13 %
14 %     This program calculate the 3D coords from a point given in 2
15 %     stereopictures. Those pictures are obtained by rotating the camera
16 %     around a rotation point with an angle theta.
17 %
18 %
19 %     Don't forget to change the camera parameters!
20 %
21 %
22 %
23 %- markers_WCS_new: the calculated 3D coordinates from the stereoscopy
24 %- fileName_imageL and fileName_imageR: the path from the left and the
25 %     right image

```

```

26 %- theta: angle between left and right stereo pictures
27 %- dist_imageplane_rotation: distance between imageplane (center) and
28 %rotation point
29 %- imageon: image output on (1) or off (0)
30 %
31
32
33 %% Camera parameters (fill in!)
34 pixelsize=0.03e-3;
35 kappa=0.0;
36 scaleFactor=0.98; %h2/h1 with h2 dimension in image, h1 in object
37
38 %% calculated camera parameters
39 f=dist_imageplane_rotation/(1/scaleFactor+1); %principal distance
40 dist_cam=dist_imageplane_rotation-f;
41 pos_cam_r=[dist_cam*sin(theta/2),0,dist_cam*cos(theta/2)];
42 pos_cam_l=[-dist_cam*sin(theta/2),0,dist_cam*cos(theta/2)];
43 angle_cam_r=[0,theta/2,0];
44 angle_cam_l=[0,-theta/2,0];
45
46
47
48 %% plot images
49 figure
50 imageL=imread(fileName_imageL);
51 subplot(2,1,1)
52 imshow(imageL)
53 title('Left Image')
54 axis image
55
56 imageR=imread(fileName_imageR);
57 subplot(2,1,2)
58 imshow(imageR)
59 title('Right Image')
60 axis image
61
62 %calculate center pixel
63 centerL=(size(imageL)+1)/2;
64 centerR=(size(imageR)+1)/2;
65
66 zoom
67 input('zooming (press enter if ok)');
68
69 %% choose pixels to calculate 3D Coord (first left and then corresponding
70 %% right)
71
72 disp('Stop by using right mouse button')
73 count_markers=1;
74 while 1
75     disp('choose pixel on left image')
76     [p_l(count_markers,1),p_l(count_markers,2),button]=ginput(1);
77     if button == 3

```

```

78     p_l=p_l(1:(count_markers-1),:); %to remove last right button click
79     break %right click to stop
80 end
81 disp('choose corresponding pixel on right image')
82 [p_r(count_markers,1),p_r(count_markers,2),button]=ginput(1);
83 if button == 3
84     p_l=p_l(1:(count_markers-1),:);%to remove last right button click
85     p_r=p_r(1:(count_markers-1),:);
86     break %right click to stop
87 end
88 count_markers=count_markers+1;
89 end
90 %% calculate image coordinates
91
92 Marker_image_left= (p_l-ones(length(p_l),1)*[centerL(2),centerL(1)]) *
    pixelsize;
93 Marker_image_left(:,2)=-Marker_image_left(:,2);
94
95 if imageon==1
96     figure
97     plot(Marker_image_left(:,1),Marker_image_left(:,2),'+')
98 end
99
100
101
102 Marker_image_right= (p_r-ones(length(p_r),1)*[centerR(2),centerR(1)]) *
    pixelsize;
103 Marker_image_right(:,2)=-Marker_image_right(:,2);
104
105 if imageon==1
106     figure
107     plot(Marker_image_right(:,1),Marker_image_right(:,2),'+')
108 end
109
110 %% de the backprojection and compare with real solution
111
112 %the negative Marker_image_* is because the backprojection is written for
113 %negatives.
114 markers_WCS_new=backprojection(-Marker_image_left,-Marker_image_right,
    pos_cam_l, pos_cam_r, angle_cam_l, angle_cam_r, f, kappa, imageon);
115 if imageon==1
116     hold on
117     plot3(Marker_WCS_new(:,1),Marker_WCS_new(:,2),Marker_WCS_new(:,3),'r+')
    %real solution
118 end

```

## APPENDIX B

---

### Mechanical stress, fracture risk, and beak evolution in Darwin's ground finches (*Geospiza*)

---

#### **Abstract**

*Darwin's finches have radiated from a common ancestor into fourteen descendent species, each specializing on distinct food resources and evolving divergent beak forms. Beak morphology in the ground finches (*Geospiza*) has been shown to evolve via natural selection in response to variation in food type, food availability, and interspecific competition for food. From a mechanical perspective, however, beak size and shape are only indirectly related to birds' abilities to crack seeds, and beak form is hypothesized to evolve mainly under selection for fracture-avoidance. Here we test the fracture-avoidance hypothesis using finite element modeling (without inclusion of the rhamphotheca). We find that across species, mechanical loading is similar and approaches reported values of bone strength, thus suggesting pervasive selection on fracture-avoidance. Additionally, deep and wide beaks are better suited for dissipating stress than are more elongate beaks when scaled to common sizes and loadings. Our results illustrate that deep and wide beaks in ground finches enable reduction of areas with high stress and peak stress magnitudes, allowing birds to crack hard seeds while limiting the risk of beak failure. These results may explain strong selection on beak depth and width in natural populations of Darwin's finches.*

This appendix is based on:

Soons Joris, Herrel Anthony, Genbrugge Annelies, Aerts Peter, Podos Jeffrey, Adriaens Dominique, de Witte Yoni, Jacobs Patric and Dirckx Joris. Mechanical stress, fracture risk and beak evolution in Darwin's ground finches (*Geospiza*). *Philosophical transactions of the Royal Society: B: biological sciences*, 365, 1093-1098, 2010

## B.1 Introduction

Beak morphology in Darwin's finches has been shown to evolve via natural selection in response to variation in food type, food availability, and interspecific competition for food [56, 57, 81]. Consequently, divergent beak sizes and shapes evolved in Darwin's finches specializing on different food items [15, 45, 56, 81]. Variation in beak shape in the ground finches of the genus *Geospiza* is situated mainly along two axes: variation in width and depth, and variation in length (Bowman, 1961). Species that crush hard seeds at the base of their beaks, such as *G. fortis* and *G. magnirostris* tend to have relatively short but wide and deep beaks [56]. Other species, such as *G. scandens* and *G. difficilis* tend to have longer yet narrower and shallower beaks, a design that has been suggested to be a compromise between base-crushing and probing [15]. Interestingly, the two principal axes of variation observed within the ground finch clade are also reflected in distinct developmental pathways [1, 2].

While much research has focused on beak size and shape, the seed cracking ability of a bird is determined more directly by bite force capacity which is, in turn, closely dependent on jaw closer muscle cross-sectional area [15, 63, 64, 132]. The jaw closer muscles, situated at the back of the head, generate crushing forces that are transferred to food by means of the upper and lower beak [63, 64]. Beak morphology is thus expected to evolve in concert with jaw adductor force generation capacity, through selection for the capacity to avoid structural failure under conditions of increased muscle and food reaction forces [15]. Indeed, more than 50 years ago Bowman (1961) [15] suggested that the shape of the beak was adapted for fracture resistance, with beaks with more or less straightened culmen or gonys (resp. upper and lower beak) tending to reduce fracture risk. Modifications towards increased beak depth, on the other hand, were interpreted as adaptations towards more powerful crushing bites. To test these hypotheses, I developed finite element (FE) models of the upper beak in 13 Darwin's finches. As finite element models quantify the effect of complex shape variation on stress magnitude and distribution [97, 101, 102], they are ideally suited to address the hypothesis that beak shape has evolved in response to fracture avoidance, and may also offer insights into observed patterns of selection on beak shape (depth, width and curvature) in species that crack hard seeds.

## B.2 Material and methods

Sample collection, CT scanning and muscle data collection are described in section 8.3.

### B.2.1 Finite element modeling

CT image sequences were segmented semi-automatically based on grayscale thresholding and smoothed using Amira 5.0 (64-bit version, Computer Systems Mercury), to

obtain a triangular surface mesh of the upper beak figure B.1. Next, a Delaunay tetrahedral volume mesh with a minimum radius-edge ratio of 1.4 was generated in tetgen [114] and imported in the finite element program FEBio [88]. A left unilateral load with all muscles 100% and bilaterally active was applied at a posterior bite point, the position of which was determined based on recordings of birds cracking seeds in the field. For each modeled specimen, the bite point was simulated through a translation constraint of the corresponding elements. The fronto-nasal hinge was modeled as two rotating but fixed elements. The forces on palatine and jugal bones were applied along the long axis of these bones as determined on the CT-data, and with a magnitude derived from calculated muscle forces. Bone was modeled as a linear elastic, isotropic and homogeneous material with a Young's modulus from 18 GPa, and a Poisson's ratio of 0.3 [26, 43, 137, 142]. Linear elements were used in the models, which were solved with an iterative Newton-based Broyden-Fletcher-Goldfarb-Shanno (BFGS) solver. The convergence and the stability of the results were tested by an iterative refinement of the mesh up to 500000 elements and terminated at an accuracy of 5% or better.

As stress is a complex three-dimensional phenomenon, inherently difficult to interpret, we chose to combine the stresses using the von Mises yielding criterion. Three areas with high stress were noted in our base loading simulations: posterior on the maxilla in front of the nasal apertures, and on the ipsi- and contra-lateral processi maxillari of the nasal bone. A high stress area posterior on the beak was not considered as high stresses in this region may be due to constraints imposed at the fronto-nasal hinge. Maximal von Mises stresses were calculated and compared across loading conditions for the different species (table B.1). Additionally, the external force needed to satisfy the constraint at the bite point, perpendicular to the surface area was calculated and the magnitude thereof was calculated and compared to the bite forces measured *in vivo* (table B.1). Finally, FE-models for *G. difficilis*, *G. fuliginosa*, *G. magnirostris*, and *G. scandens* were scaled by area [40] to the same size as the *G. fortis* model, and simulations were run with input forces based on *G. fortis* in order to evaluate how beak shape affects loading of the beak.

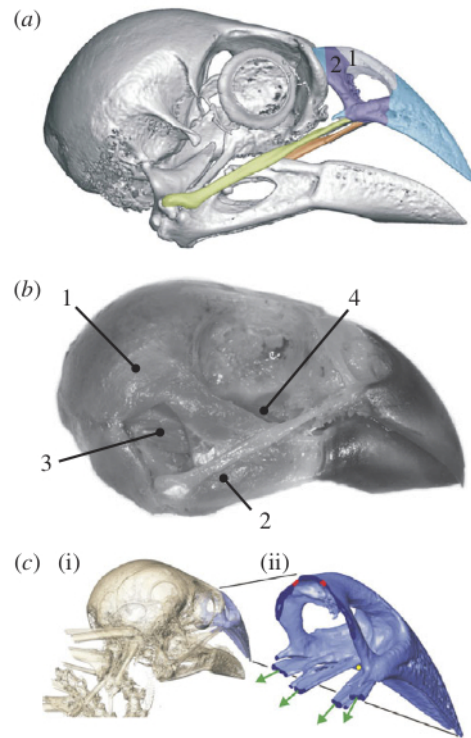


**Figure B.1:** Schematic overview of the model derivation. (a) Lateral view on a three-dimensional reconstruction of the skull of a medium ground finch (*G. fortis*) based on micro CT scans. When birds bite, forces are transmitted by the jaw muscles to the upper beak (blue) via the jugal bones (green) and the pterygoid-palatine complex (orange). The colored zone labeled 1 represents the dorsal nasal region, and the zone labeled 2 represents the maxillary process of the nasal bone. (b) photograph of the head of a *G. fortis* specimen, skin removed, illustrating the major jaw closing muscles. The external adductor muscles (1, 2) and the *m. pseudotemporalis* (3) transmit force to the upper beak through the jugal bone. The pterygoideus muscles (4) directly pull the upper beak downward through the pterygoid-palatine complex. (c) posterior oblique view of (i) the head and (ii) upper beak (right) of a *G. fortis*, illustrating loadings and constraints used in the finite element models. Red zones indicate the dorsal constraints on the rotating fixed elements, (i) the yellow circle indicates the bite point and green arrows indicate the orientation of the load acting on the jugals and palatines.



### B.3 Results

The three species of Darwin's finch featured in our analysis showed a nearly three-fold absolute difference in the cross-sectional area of the jaw adductor muscles ( $0.28\text{mm}^2$  in *G. fuliginosa* versus  $0.72\text{mm}^2$  in *G. fortis*), and thus also in the maximal potential loading of the beak. A first set of FE simulations was performed using actual beak size and shape as determined from CT scans, and applied input forces based on information derived from muscle dissections for the three species for which specimens were available for dissection. Results from these simulations show that beaks in all species show stress concentrations in similar regions, specifically in the region of the nasal bone posterior to the nasal aperture, and in the processi maxillari of the nasal bone (figure B.2). Stresses were typically highest at the dorsal and posterior aspect of the nasal bone and at the processus maxillaris contra lateral to the bite side (figure B.2, table B.1).

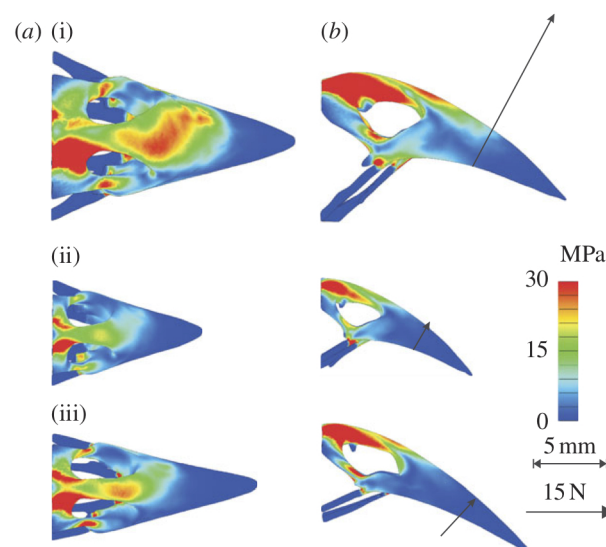


**Figure B.2:** Output of finite-element analyses performed for three different species of ground finches (*Geospiza*) for which specimens were available for dissection. Input forces were calculated from muscle mass and fibre length measurements. Colors indicate calculated resultant von Mises stresses on the beak in (a) dorsal and (b) lateral views: (i) *G. fortis*, (ii) *G. fuliginosa*, and (iii) *G. scandens*. Warmer colors depict higher stresses. For all species, maximum stress concentration occurs at the posterior part of the nasal bone, posterior to the nasal aperture (zone 1 in figure B.1a), and within the maxillary processes of the nasal bone (zone 2 in figure B.1a). Arrows depict calculated bite forces.

A second set of FE simulations was performed in which beaks were scaled to the area of the *G. fortis* specimen, and then loaded using the input forces calculated for this species (figure B.3). This was done to characterize the potential effects of beak shape

variation on force dissipation. If interspecific variation in beak shape does not impact force dissipation, all simulations would show comparable stress distributions and stress magnitudes. In contrast, the results identify marked differences among species in stress distributions, thus demonstrating the importance of beak shape in force dissipation. Species with elongate beaks such as *G. scandens* and *G. difficilis* show notable increases in the surface area subjected to high stress, spreading forward to the dorsal aspect, anterior of the nasal aperture. Moreover, the peak stresses calculated for the species with the longer and narrower beaks (*G. scandens* and *G. difficilis*; table B.1) were substantially higher (max. of 72 MPa). In contrast, the tall and wide beaks as seen in *G. fortis*, *G. fuliginosa*, and *G. magnirostris* are seen to distribute the load applied to the beak with lower peak stress values (max. of 44 MPa across the three species), largely confined to the posterior aspect of the nasal bone. Note, however, how an additional area of high stress in the *G. magnirostris* model is present at the level of the bite point.

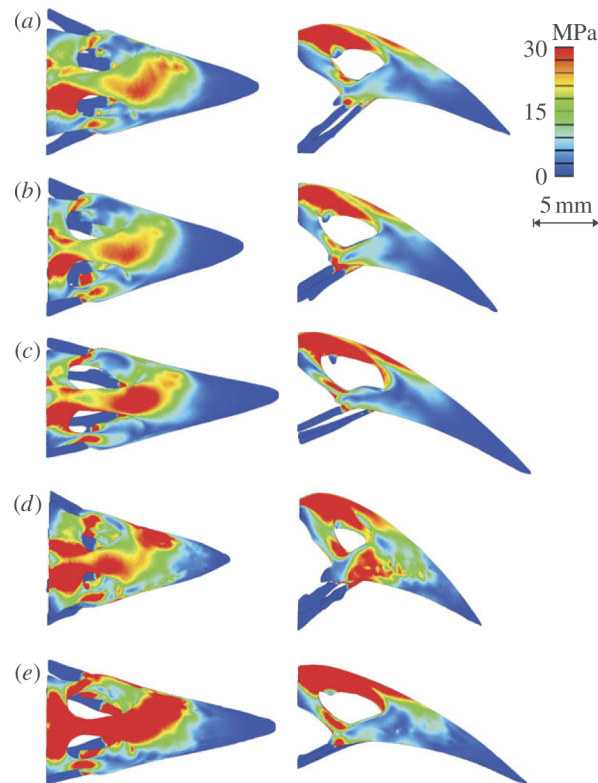


**Figure B.3:** Output of finite element simulations, in which beak surface area of the five species of ground finch was scaled to a common surface area (that of *G. fortis*) prior to calculations, and in which the input force calculated for *G. fortis* was applied to all species. This simulation enables the evaluation of the effects of beak shape on stress distribution. The relatively long and slender beaked *G. scandens* and *G. difficilis* showed disproportional increases in the magnitude of the von Mises stress and the distribution of areas with high stress (table B.1). (a) *G. fortis*, (b) *G. fuliginosa*, (c) *G. scandens*, (d) *G. magnirostris*, and (e) *G. difficilis*.

## B.4 Discussion

A comparison of the bite forces calculated in our FE model with actual bite forces measured *in vivo* (table B.1) shows that calculated values fall within the *in vivo* range, thus confirming that our models provide realistic estimates of beak loadings. Interestingly, our results provide one of the few cases where the output of FE models is validated against *in vivo* data and suggest that FE models can provide realistic output if based on realistic inputs (see also Rayfield (2007) [97] for an overview). However, our models must be considered as only a first step, and planned future models including the keratinous rhamphotheca and material properties for the beaks of Darwin's finches are needed to test whether a refinement of our models affects the output of our FE

models in terms of stress distributions and magnitudes (chapter 8).

A comparison of peak stresses reported here in the different species of Darwin's finch with values reported for the compressive strength of bone suggests that Darwin's finch beaks operate with safety factors between 3 and 5 in most species, assuming an average compressive bone strength of 165 MPa (note that bone strength ranges from 106-224 MPa across a wide range of vertebrates [26, 137, 142]). Previously it was suggested that beak morphology should evolve in concert with the force generating capacity of the jaw adductors through selection for the capacity to avoid structural failure under conditions of increased muscle and food reaction forces [15]. Our data support this assertion and suggest that beaks are indeed optimized to withstand their natural loading regimes.

More than five decades ago Bowman (1961) [15] suggested that the shape of the beak in Darwin's finches was related to fracture resistance, such that beaks with a more or less straightened culmen and gonys (the upper and lower beak respectively) tend to reduce fracture risk. Modifications towards increased beak depth, on the other hand, were interpreted as adaptations towards a more powerful crushing bite. Our data provide only partial support for these hypotheses. Whereas deeper and wider beaks indeed appear better suited to withstand reaction forces from biting and may thus allow for higher bite forces, the straighter beaks of *G. scandens* and *G. difficilis* clearly induce greater stresses, thus presumably increasing fracture risk. The difference between *G. difficilis* and *G. fuliginosa* is especially notable, with the highest peak von Mises stress in *G. difficilis* being almost twice that of *G. fuliginosa* when scaled to the same surface area. Interestingly, however, the beak with the greatest curvature in *G. magnirostris* is seen to perform somewhat poorer than that of *G. fuliginosa* when scaled to the same surface area, suggesting that too much curvature may negatively affect stress magnitudes as predicted by Bowman (1961) [15]. Alternatively, the relatively high stress may be due to the relatively low volume (and thus bone present) of the upper beak of the *G. magnirostris* specimen used in our models (see table B.1). As this specimen and the *G. difficilis* used are dried historical specimens, this may represent a preservation artifact and thus results for both *G. difficilis* and *G. magnirostris* should be interpreted with caution. Testing for potential preservation artifacts will require freshly preserved specimens, which may prove to be difficult to obtain.

In summary, our results illustrate that deep and wide beaks in Darwin's finches, long associated with an ability to crack hard seeds, more specifically limit beak areas that experience high stress and peak stress magnitudes. Consequently, deep and wide beaks may allow birds to crack hard seeds while limiting the risk of beak failure. Deeper beaks are indicative of deeper dorsal nasal regions, and wider beaks indicative of a broader maxillary process of the nasal bone, the two areas typically showing high stress concentrations in our model. Thus, our simulations may help explain the low survival of birds with smaller beaks in times of food scarcity when seeds of intermediate size are rapidly depleted from the environment [9]. Given the often large within-population variation in beak size and shape [56, 57, 59], birds with relatively smaller (more narrow or shallow) beaks for a given jaw adductor size may be subject to mechanical failure

more rapidly under the repeated loading needed to crack hard seeds such as *Tribulus* [55] which are relatively abundant during dry years [56]. Finally, our data show how the jaw musculature and beak shape have co-evolved in Darwin's finches that specialize on different food resources. We suggest that finch jaw musculature and its relationship to beak safety factors is as critical in finch evolution and adaptive radiation as is the evolution of the beak morphology itself.

The FE models presented in chapter 8 include the rhamphotheca and 13 species of Darwin's finches. Moreover, both base and tip biting are investigated. As a consequence, the results which are presented in that chapter are more general.

In this appendix the results on the upper beak of the bull finch (*Loxigilla noctis*) are shown and compared to these of the medium groundfinch (*Geospiza fortis*). The methods are the same as described in chapter 8, but no rhamphotheca was included in these models. The bull finch model was scaled to same size as the *fortis* model and *fortis* muscles forces were applied in both models. As a result, only the beak shape differs. The VM stress is shown in figure C.1

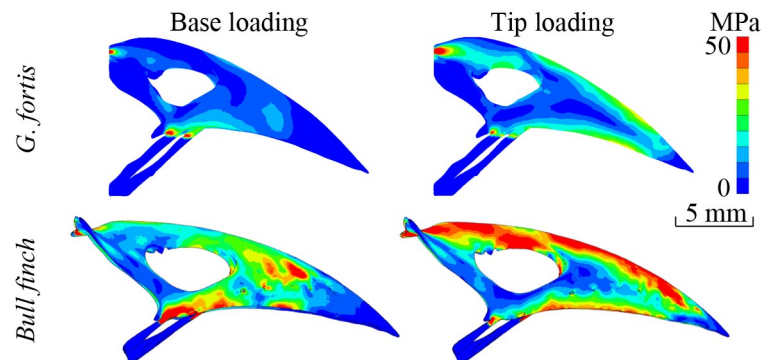


**Figure C.1:** Lateral view of the VM stress for *G. fortis* and *L. noctis* for both base and tip loading conditions. The *L. noctis* model is scaled to the size of *G. fortis* and the *G. fortis* muscle forces are used as input force for both models.

It is clear that *L. noctis* has high stresses during base (48 MPa) and tip (62 MPa) loading, if it is compared to the results of *G. fortis* (16 MPa for base and 39 MPa for tip loading). It should be noticed that differences in absolute values with appendix B are caused by different input forces and different recording positions.



---

## Bibliography

---

- [1] A. Abzhanov, W. P. Kuo, C. Hartmann, B. R. Grant, P. R. Grant, and C. J. Tabin. The calmodulin pathway and evolution of elongated beak morphology in Darwin's finches. *Nature*, 442(7102):563–7, Aug. 2006.
- [2] A. Abzhanov, M. Protas, B. R. Grant, P. R. Grant, and C. J. Tabin. Bmp4 and morphological variation of beaks in Darwin's finches. *Science (New York, N.Y.)*, 305(5689):1462–5, Sept. 2004.
- [3] J. Aernouts, I. Couckuyt, K. Crombecq, and J. J. Dirckx. Elastic characterization of membranes with a complex shape using point indentation measurements and inverse modelling. *International Journal of Engineering Science*, 48(6):599–611, June 2010.
- [4] J. Aernouts, J. a. M. Soons, and J. J. J. Dirckx. Quantification of tympanic membrane elasticity parameters from in situ point indentation measurements: validation and preliminary study. *Hearing research*, 263(1-2):177–82, May 2010.
- [5] ASTM. ASTM D695-02a: Standard Test Method for Compressive Properties of Rigid Plastics. *Annual Book of ASTM Standards*, 2008.
- [6] R. Bade, J. Haase, and B. Preim. Comparison of Fundamental Mesh Smoothing Algorithms for Medical Surface Models. In *Simulation und Visualisierung*, volume 1, pages 289–304, 2006.
- [7] M. M. Barak, A. Sharir, and R. Shahar. Optical metrology methods for mechanical testing of whole bones. *Veterinary journal (London, England : 1997)*, 180(1):7–14, Apr. 2009.
- [8] R. Blob and A. Biewener. In vivo locomotor strain in the hindlimb bones of alligator mississippiensis and iguana iguana: implications for the evolution of limb bone safety factor and non-sprawling limb posture. *The Journal of experimental biology*, 202 (Pt 9):1023–46, May 1999.
- [9] P. T. Boag and P. R. Grant. Intense Natural Selection in a Population of Darwin's Finches (Geospizinae) in the Galapagos. *Science (New York, N.Y.)*, 214(4516):82–5, Oct. 1981.

- [10] J.-E. Bolduc, L. J. Lewis, C.-E. Aubin, and A. Geitmann. Finite-element analysis of geometrical factors in micro-indentation of pollen tubes. *Biomechanics and modeling in mechanobiology*, 5(4):227–236, Nov. 2006.
- [11] J. Bonet and R. D. Wood. *Nonlinear continuum mechanics for finite element analysis*. Cambridge university press, New York, USA, 1997.
- [12] R. H. C. Bonser. The Young's modulus of ostrich claw keratin. *Journal of materials science letters*, 19:1039–1040, 2000.
- [13] R. H. C. Bonser. The mechanical performance of medullary foam from feathers. *Journal of materials science letters*, 10:941 – 942, 2001.
- [14] M. Bottlang, M. Mohr, U. Simon, and L. Claes. Acquisition of full-field strain distributions on ovine fracture callus cross-sections with electronic speckle pattern interferometry. *Journal of biomechanics*, 41(3):701–5, Jan. 2008.
- [15] R. I. Bowman. *Morphological differentiation and adaptation in the galapagos finches*. University of california press, Berkeley and Los Angeles, 1961.
- [16] A. Bowyer. Computing Dirichlet tessellations. *The Computer Journal*, 24(2):162–166, 1981.
- [17] J. a. Bright and F. Gröning. Strain accommodation in the zygomatic arch of the pig: A validation study using digital speckle pattern interferometry and finite element analysis. *Journal of morphology*, 272:1388–1398, July 2011.
- [18] J. N. Butters and J. A. Leendertz. Holographic and video techniques applied to engineering measurement. *Transactions of the institute of measurement and control*, 4:349–354, 1971.
- [19] J. A. Buytaert and J. J. Dirckx. Phase-shifting Moiré topography using optical demodulation on liquid crystal matrices. *Optics and Lasers in Engineering*, 48(2):172–181, Feb. 2010.
- [20] J. A. N. Buytaert and J. J. J. Dirckx. Design and quantitative resolution measurements of an optical virtual sectioning three-dimensional imaging technique for biomedical specimens, featuring two-micrometer slicing resolution. *Journal of biomedical optics*, 12(1):014039, 2007.
- [21] J. A. N. Buytaert and J. J. J. Dirckx. Study of the performance of 84 phase- shifting algorithms for interferometry. *Journal of Optics*, 40(3):114–131, 2011.
- [22] J. A. N. Buytaert and J. J. J. Dirckx. *Structured light projection techniques tutorial*. Wiley-VCH, Berlin, 2012.
- [23] O. Campàs, R. Mallarino, a. Herrel, a. Abzhanov, and M. P. Brenner. Scaling and shear transformations capture beak shape variation in Darwin's finches. *Proceedings of the National Academy of Sciences of the United States of America*, 107(8):3356–60, Feb. 2010.

- [24] A. P. C. Choi and Y. P. Zheng. Estimation of Young's modulus and Poisson's ratio of soft tissue from indentation using two different-sized indentors: Finite element analysis of the finite deformation effect. *Medical & Biological Engineering & Computing*, 43(2):258–264, Apr. 2005.
- [25] K. Choi, J. L. Kuhn, M. J. Ciarelli, and S. A. Goldstein. The elastic moduli of human subchondral, trabecular, and cortical bone tissue and the size-dependency of cortical bone modulus. *J Biomech*, 23(11):1103–1113, 1990.
- [26] J. Currey. *Bones: structure and mechanics*. Princeton University Press, Princeton, 2006.
- [27] J. D. Currey. Physical characteristics affecting the tensile failure properties of compact bone. *Journal of biomechanics*, 23(8):837–44, Jan. 1990.
- [28] O. de La Rochefoucauld and E. S. Olson. A sum of simple and complex motions on the eardrum and manubrium in gerbil. *Hearing research*, 263(1-2):9–15, May 2010.
- [29] P. C. Dechow, G. a. Nail, C. L. Schwartz-Dabney, and R. B. Ashman. Elastic properties of human supraorbital and mandibular bone. *American journal of physical anthropology*, 90(3):291–306, Mar. 1993.
- [30] W. F. Decraemer, J. J. J. Dirckx, and W. R. J. Funnell. Three-dimensional modelling of the middle-ear ossicular chain using a commercial high-resolution X-ray CT scanner. *Journal of the Association for Research in Otolaryngology : JARO*, 4(2):250–63, June 2003.
- [31] W. F. Decraemer, S. M. Khanna, and W. J. Funnell. Malleus vibration mode changes with frequency. *Hearing Research*, 54(2):305–318, Aug. 1991.
- [32] F. J. Degrange, C. P. Tambussi, K. Moreno, L. M. Witmer, and S. Wroe. Mechanical analysis of feeding behavior in the extinct "terror bird" *Andalgalornis steulleti* (Gruiformes: Phorusrhacidae). *PloS one*, 5(8):e11856, Jan. 2010.
- [33] M. Del Socorro Hernández-Montes, C. Furlong, J. J. Rosowski, N. Hulli, E. Harrington, J. T. Cheng, M. E. Ravicz, and F. M. Santoyo. Optoelectronic holographic otoscope for measurement of nano-displacements in tympanic membranes. *Journal of biomedical optics*, 14(3):034023, 2009.
- [34] W. T. Dempster and R. T. Liddicoat. Compact bone as a non-isotropic material. *The American journal of anatomy*, 91(3):331–62, Nov. 1952.
- [35] J. Dirckx and W. Decraemer. Effect of middle ear components on eardrum quasi-static deformation. *Hearing Research*, 157(1-2):124–137, July 2001.
- [36] J. J. Dirckx and W. F. Decraemer. Area change and volume displacement of the human tympanic membrane under static pressure. *Hearing Research*, 62(1):99–104, Sept. 1992.
- [37] J. J. Dirckx, W. F. Decraemer, M. von Unge, and C. Larsson. Measurement and modeling of boundary shape and surface deformation of the Mongolian gerbil pars flaccida. *Hearing research*, 111(1-2):153–64, Sept. 1997.

- [38] J. J. J. Dirckx, J. A. N. Buytaert, and W. F. Decraemer. Quasi-static transfer function of the rabbit middle ear' measured with a heterodyne interferometer with high-resolution position decoder. *Journal of the Association for Research in Otolaryngology : JARO*, 7(4):339–51, Dec. 2006.
- [39] E. R. Dumont. Bone density and the lightweight skeletons of birds. *Proceedings. Biological sciences / The Royal Society*, 277(1691):2193–8, July 2010.
- [40] E. R. Dumont, I. R. Grosse, and G. J. Slater. Requirements for comparing the performance of finite element models of biological structures. *Journal of theoretical biology*, 256(1):96–103, Jan. 2009.
- [41] E. R. Dumont, J. Piccirillo, and I. R. Grosse. Finite-element analysis of biting behavior and bone stress in the facial skeletons of bats. *The anatomical record. Part A, Discoveries in molecular, cellular, and evolutionary biology*, 283(2):319–30, Apr. 2005.
- [42] N. Elkhouri, H. Liu, and W. R. J. Funnell. Low-frequency finite-element modeling of the gerbil middle ear. *Journal of the Association for Research in Otolaryngology : JARO*, 7(4):399–411, Dec. 2006.
- [43] F. G. Evans. *Mechanical properties of bone*. Thomas Springfield, IL, 1973.
- [44] C. Feng, J. M. Tannenbaum, B. S. Kang, and M. A. Alvin. A Load-Based Multiple-Partial Unloading Micro-Indentation Technique for Mechanical Property Evaluation. *Experimental Mechanics*, 50(6):737–743, July 2009.
- [45] D. J. Foster, J. Podos, and A. P. Hendry. A geometric morphometric appraisal of beak shape in Darwin's finches. *Journal of evolutionary biology*, 21(1):263–75, Jan. 2008.
- [46] A. Franck, G. Cocquyt, P. Simoens, and N. De Belie. Biomechanical Properties of Bovine Claw Horn. *Biosystems Engineering*, 93(4):459–467, Apr. 2006.
- [47] R. D. Fraser and T. P. Macrae. Molecular structure and mechanical properties of keratins. *Symposia of the Society for Experimental Biology*, 34:211–46, Jan. 1980.
- [48] W. R. J. Funnell, S. M. Khanna, and W. F. Decraemer. On the degree of rigidity of the manubrium in a finite-element model of the cat eardrum. *The Journal of the Acoustical Society of America*, 91(4):2082, 1992.
- [49] D. P. Fyhrie and D. Vashishth. Bone stiffness predicts strength similarly for human vertebral cancellous bone in compression and for cortical bone in tension. *Bone*, 26(2):169–73, Feb. 2000.
- [50] B. A. Galanov, V. Domnich, and Y. Gogotsi. Elastic-plastic contact mechanics of indentations accounting for phase transformations. *Experimental Mechanics*, 43(3):303–308, Sept. 2003.
- [51] A. Genbrugge. *Evolutionary morphology of the feeding apparatus in darwins finches: a case study of adaptive evolution of complex musculoskeletal systems*. Phd thesis, University of Antwerp, 2011.

- [52] A. Genbrugge, A. Herrel, M. Boone, L. Van Hoorebeke, J. Podos, J. Dirckx, P. Aerts, and A. Dominique. The head of the finch: the anatomy of the feeding system in two species of finches (*Geospiza fortis* and *Padda oryzivora*). *Journal of anatomy*, Oct. 2011.
- [53] J. Gong, H. Miao, and Z. Peng. Simple method for determining the initial unloading slope for ceramics nanoindentation tests. *Journal of materials science letters*, 22(4):267–268, 2003.
- [54] D. Gorissen, L. Tommasi, K. Crombecq, and T. Dhaene. Sequential modeling of a low noise amplifier with neural networks and active learning. *Neural Computing and Applications*, 18(5):485–494, Dec. 2008.
- [55] P. Grant. The feeding of darwin’s finches on *Tribulus cistoides* (L.) seeds. *Animal Behaviour*, 29(3):785–793, Aug. 1981.
- [56] P. Grant. *Ecology and evolution of Darwin’s finches*. Press, Princeton Univ, Princeton, 1999.
- [57] P. Grant and B. Grant. Evolution of character displacement in Darwin’s finches. *Science*, 313:224–226, 2006.
- [58] P. P. R. Grant and B. R. Grant. *How and Why Species Multiply: The Radiation of Darwin’s Finches*. Princeton University Press, Princeton & Oxford, 2008.
- [59] P. R. Grant. Inheritance of Size and Shape in a Population of Darwin’s Finches, *Geospiza conirostris*. *Proceedings of the Royal Society B: Biological Sciences*, 220(1219):219–236, Dec. 1983.
- [60] F. Gröning, J. Liu, M. J. Fagan, and P. O’Higgins. Validating a voxel-based finite element model of a human mandible using digital speckle pattern interferometry. *Journal of biomechanics*, 42(9):1224–9, June 2009.
- [61] E. Hack and A. Schumacher. DSPI strain measurement on an externally reinforced bending beam: A comparison of step-by-step addition and pixel shift correlation. *Optics and Lasers in Engineering*, 45:589–595, 2007.
- [62] W. Hayes, L. Keer, G. Herrmann, and L. Mockros. A mathematical analysis for indentation tests of articular cartilage. *Journal of Biomechanics*, 5(5):541–551, Sept. 1972.
- [63] A. Herrel, J. Podos, S. K. Huber, and A. P. Hendry. Bite performance and morphology in a population of Darwin’s finches: implications for the evolution of beak shape. *Functional Ecology*, 19:43–48, 2005.
- [64] A. Herrel, J. Podos, S. K. Huber, and A. P. Hendry. Evolution of bite force in Darwin’s finches: a key role for head width. *Journal of evolutionary biology*, 18(3):669–75, May 2005.
- [65] A. Herrel, J. Soons, P. Aerts, J. Dirckx, M. Boone, P. Jacobs, D. Adriaens, and J. Podos. Adaptation and function of the bills of Darwin’s finches: divergence by feeding type and sex. *Emu*, 110(1):39, 2010.

- [66] A. Herrel, L. Spithoven, R. Van Damme, and F. De Vree. Sexual dimorphism of head size in *Gallotia galloti*: testing the niche divergence hypothesis by functional analyses. *Functional Ecology*, 13(3):289–297, June 1999.
- [67] G. A. Holzapfel. *Nonlinear solid mechanics*. John Wiley & Sons, New York, 2001.
- [68] D. G. Homberger and A. H. Brush. Functional-morphological and biochemical correlations of the keratinized structures in the African Grey Parrot, *Psittacus erithacus* (Aves). *Zoomorphology*, 106(2):103–114, May 1986.
- [69] G. Huang and H. Lu. Measurements of Two Independent Viscoelastic Functions by Nanoindentation. *Experimental Mechanics*, 47(1):87–98, May 2006.
- [70] S. K. Huber, L. F. De León, A. P. Hendry, E. Bermingham, and J. Podos. Reproductive isolation of sympatric morphs in a population of Darwin's finches. *Proceedings. Biological sciences / The Royal Society*, 274(1619):1709–14, July 2007.
- [71] Y. Hung and H. Ho. Shearography: An optical measurement technique and applications. *Materials Science and Engineering: R: Reports*, 49(3):61–87, Apr. 2005.
- [72] H. Jin and J. L. Lewis. Determination of poisson's ratio of articular cartilage in indentation test using different sized indenters. In *Summer bioengineering conference, Florida*, 2003.
- [73] R. Jones and C. Wykes. *Holographic and speckle interferometry: a discussion of the theory, practice and applications of the techniques*. Cambridge university press, 1983.
- [74] B.-F. Ju and Y. Ju. Video enhanced depth-sensing indentation technique for characterizing mechanical behaviour of biomaterials. *Measurement Science and Technology*, 17(7):1776–1784, July 2006.
- [75] C.-C. Kao, G.-B. Yeh, S.-S. Lee, C.-K. Lee, C.-S. Yang, and K.-C. Wu. Phase-Shifting Algorithms for Electronic Speckle Pattern Interferometry. *Applied Optics*, 41(1):46, Jan. 2002.
- [76] J. H. Keyak and S. A. Rossi. Prediction of femoral fracture load using finite element models: an examination of stress- and strain-based failure theories. *Journal of Biomechanics*, 33(2):209–214, Feb. 2000.
- [77] A. Kitchener and J. F. V. Vincent. Composite theory and the effect of water on the stiffness of horn keratin. *Journal of Materials Science*, 22(4):1385–1389, Apr. 1987.
- [78] T. Koike, H. Wada, and T. Kobayashi. Modeling of the human middle ear using the finite-element method. *The Journal of the Acoustical Society of America*, 111(3):1306, 2002.
- [79] K. Kupczik, C. a. Dobson, M. J. Fagan, R. H. Crompton, C. E. Oxnard, and P. O'Higgins. Assessing mechanical function of the zygomatic region in macaques: validation and sensitivity testing of finite element models. *Journal of anatomy*, 210(1):41–53, Jan. 2007.
- [80] Y. A. Kvistedal and P. M. F. Nielsen. Estimating material parameters of human skin in vivo. *Biomechanics and modeling in mechanobiology*, 8(1):1–8, Feb. 2009.

- [81] D. Lack. *Darwin's Finches*. Cambridge Univ Press, Cambridge, 1947.
- [82] P. Lava, S. Coppieters, Y. Wang, P. Van Houtte, and D. Debruyne. Error estimation in measuring strain fields with DIC on planar sheet metal specimens with a non-perpendicular camera alignment. *Optics and Lasers in Engineering*, 49(1):57–65, Jan. 2011.
- [83] J. Leendertz and J. N. Butters. An image-shearing speckle-pattern interferometer for measuring bending moments. *Journal of Physics E: Scientific Instruments*, 6:1107–1110, 1973.
- [84] D. C. Lin, D. I. Shreiber, E. K. Dimitriadis, and F. Horkay. Spherical indentation of soft matter beyond the Hertzian regime: numerical and experimental validation of hyperelastic models. *Biomechanics and modeling in mechanobiology*, 8(5):345–58, Oct. 2009.
- [85] G. E. Loeb and C. Gans. *Electromyography for experimentalists*. University of Chicago Press, Chicago, 1986.
- [86] R. Lohner. Automatic unstructured grid generators. *Finite Elements in Analysis and Design*, 25(1-2):111–134, Mar. 1997.
- [87] W. E. Lorensen and H. E. Cline. Marching cubes: a high resolution 3D surface construction algorithm. *Computer Graphics*, 21(4):163–169, 1987.
- [88] S. Maas and J. A. Weiss. FEBio: Finite Elements for Biomechanics. User's Manual, Version 1.0. *Online publication*, 2008.
- [89] J. Méndez and A. Keys. Density and composition of mammalian muscle. *Metabolism*, 9:184–188, 1960.
- [90] Mercury Computer Systems. *Amira 4.1: amira User's Guide*. 2005.
- [91] L. Meunier, G. Chagnon, D. Favier, L. Orgéas, and P. Vacher. Mechanical experimental characterisation and numerical modelling of an unfilled silicone rubber. *Polymer Testing*, 27(6):765–777, Sept. 2008.
- [92] M. Meyers, P. Chen, A. Lin, and Y. Seki. Biological materials: Structure and mechanical properties. *Progress in Materials Science*, 53(1):1–206, Jan. 2008.
- [93] B. Nigg and W. Herzog. *Biomechanics of the Musculo-skeletal System*. John Wiley & Sons Ltd, University of Calgary, 3th edition, 2007.
- [94] F. W. Nuijens and G. A. Zweers. Characters discriminating two seed husking mechanisms in finches (Fringillidae: Carduelinae) and estrildids (Passeridae: Estrildinae). *Journal of Morphology*, 232(1):1–33, Apr. 1997.
- [95] W. C. Oliver and G. M. Pharr. An improved technique for determining hardness and elastic modulus using load and displacement sensing indentation experiments. *Journal of material research*, 7:1564–1583, 1992.
- [96] J. Orr and J. Shelton. *Optical measurement methods in biomechanics*. Chapman & Hall, London, 1997.

- [97] E. J. Rayfield. Finite Element Analysis and Understanding the Biomechanics and Evolution of Living and Fossil Organisms. *Annual Review of Earth and Planetary Sciences*, 35(1):541–576, May 2007.
- [98] D. a. Reed, L. B. Porro, J. Iriarte-Diaz, J. B. Lemberg, C. M. Holliday, F. Anapol, and C. F. Ross. The impact of bone and suture material properties on mandibular function in Alligator mississippiensis: testing theoretical phenotypes with finite element analysis. *Journal of anatomy*, 218(1):59–74, Jan. 2011.
- [99] J. Y. Rho, T. Y. Tsui, and G. M. Pharr. Elastic properties of human cortical and trabecular lamellar bone measured by nanoindentation. *Biomaterials*, 18(20):1325–1330, Oct. 1997.
- [100] B. RICCARDI. Indentation of metals by a flat-ended cylindrical punch. *Materials Science and Engineering A*, 381(1-2):281–291, Sept. 2004.
- [101] B. G. Richmond, B. W. Wright, I. Grosse, P. C. Dechow, C. F. Ross, M. A. Spencer, and D. S. Strait. Finite element analysis in functional morphology. *The anatomical record. Part A, Discoveries in molecular, cellular, and evolutionary biology*, 283(2):259–74, Apr. 2005.
- [102] C. F. Ross. Finite element analysis in vertebrate biomechanics. *The anatomical record. Part A, Discoveries in molecular, cellular, and evolutionary biology*, 283(2):253–8, May 2005.
- [103] C. F. Ross, M. a. Berthaume, P. C. Dechow, J. Iriarte-Diaz, L. B. Porro, B. G. Richmond, M. Spencer, and D. Strait. In vivo bone strain and finite-element modeling of the craniofacial haft in catarrhine primates. *Journal of anatomy*, 218(1):112–41, Jan. 2011.
- [104] M. H. Sadd. *Elasticity: Theory, Applications and Numerics*. Elsevier, Oxford, UK, 2009.
- [105] W. H. M. Salih, J. A. M. Soons, and J. J. J. Dirckx. High-resolution 3D translation measurements using point source x-ray stereoscopy. *Measurement Science and Technology*, 22(2):025502, Feb. 2011.
- [106] A. Samani and D. Plewes. A method to measure the hyperelastic parameters of ex vivo breast tissue samples. *Physics in Medicine and Biology*, 49(18):4395–4405, Sept. 2004.
- [107] T. Schmidt, J. Tyson, and K. Galanulis. Full-field dynamic displacement and strain measurement using advanced 3d image correlation photogrammetry: part 1. *Experimental Techniques*, 27(3):47–50, May 2003.
- [108] I. Scholz, W. Baumgartner, and W. Federle. Micromechanics of smooth adhesive organs in stick insects: pads are mechanically anisotropic and softer towards the adhesive surface. *Journal of comparative physiology. A, Neuroethology, sensory, neural, and behavioral physiology*, 194(4):373–84, Apr. 2008.
- [109] W. J. Schroeder, J. A. Zarge, and W. E. Lorensen. Decimation of triangle meshes. In *Computer Graphics (SIGGRAPH '92 Proceedings)*, Jan. 1992.
- [110] Y. Seki, B. Kad, D. Benson, and M. Meyers. The toucan beak: Structure and mechanical response. *Materials Science and Engineering: C*, 26(8):1412–1420, Sept. 2006.

- [111] Y. Seki, M. Mackey, and M. A. Meyers. Structure and micro-computed tomography-based finite element modeling of Toucan beak. *Journal of the Mechanical Behavior of Biomedical Materials*, 9:1–8, May 2012.
- [112] Y. Seki, M. S. Schneider, and M. A. Meyers. Structure and mechanical behavior of a toucan beak. *Acta Materialia*, 53(20):5281–5296, Dec. 2005.
- [113] D. J. Shuman, A. L. M. Costa, and M. S. Andrade. Calculating the elastic modulus from nanoindentation and microindentation reload curves. *Materials Characterization*, 58(4):380–389, Apr. 2007.
- [114] H. Si. TetGen: A Quality Tetrahedral Mesh Generator and three-dimensional Delaunay Triangulator v1.4, 2006.
- [115] H. Si and K. Gärtner. Meshing Piecewise Linear Complexes by Constrained Delaunay Tetrahedralizations. In *Proceedings of the 14th international meshing roundtable*, pages 147–163, 2005.
- [116] I. Sneddon. The relation between load and penetration in the axisymmetric boussinesq problem for a punch of arbitrary profile. *International Journal of Engineering Science*, 3(1):47–57, May 1965.
- [117] J. A. M. Soons, J. Aernouts, and J. J. J. Dirckx. Elasticity modulus of rabbit middle ear ossicles determined by a novel micro-indentation technique. *Hearing research*, 263(1-2):33–7, May 2010.
- [118] A. Speirs, M. Hotz, T. Oxland, R. Häusler, and L.-P. Nolte. Biomechanical properties of sterilized human auditory ossicles. *Journal of Biomechanics*, 32(5):485–491, May 1999.
- [119] A. J. M. Spencer. *Continuum mechanics*. Courier Dover Publications, Mineola (NY), 2004.
- [120] C. Steger, M. Ulrich, and C. Wiederman. *Machine vision algorithms and applications*. Wiley-VCH, Berlin, 2008.
- [121] W. Steinchem and L. Yang. *Digital shearography*. SPIE, Bellingham, 2003.
- [122] D. S. Strait, Q. Wang, P. C. Dechow, C. F. Ross, B. G. Richmond, M. A. Spencer, and B. A. Patel. Modeling elastic properties in finite-element analysis: how much precision is needed to produce an accurate model? *The anatomical record. Part A, Discoveries in molecular, cellular, and evolutionary biology*, 283(2):275–87, Apr. 2005.
- [123] Q. Sun, R. Z. Gan, K.-H. Chang, and K. J. Dormer. Computer-integrated finite element modeling of human middle ear. *Biomechanics and modeling in mechanobiology*, 1(2):109–22, Oct. 2002.
- [124] M. A. Sutton, X. Ke, S. M. Lessner, M. Goldbach, M. Yost, F. Zhao, and H. W. Schreier. Strain field measurements on mouse carotid arteries using microscopic three-dimensional digital image correlation. *Journal of biomedical materials research. Part A*, 84(1):178–90, Jan. 2008.

- [125] P. Sztetek, M. Vanleene, R. Olsson, R. Collinson, A. a. Pitsillides, and S. Shefelbine. Using digital image correlation to determine bone surface strains during loading and after adaptation of the mouse tibia. *Journal of biomechanics*, 43(4):599–605, Mar. 2010.
- [126] A. M. Taylor, R. H. C. Bonser, and J. W. Farrent. The influence of hydration on the tensile and compressive properties of avian keratinous tissues. *Journal of Materials Science*, 39(3):939–942, Feb. 2004.
- [127] E. J. Temeles, C. R. Koulouris, S. E. Sander, and W. J. Kress. Effect of flower shape and size on foraging performance and trade-offs in a tropical hummingbird. *Ecology*, 90(5):1147–1161, May 2009.
- [128] E. J. Temeles and W. J. Kress. Adaptation in a plant-hummingbird association. *Science (New York, N.Y.)*, 300(5619):630–3, Apr. 2003.
- [129] B. Triggs, P. F. McLauchlan, R. I. Hartley, and A. W. Fitzgibbon. Bundle Adjustment - A Modern Synthesis. *vision algorithms: theory and practice*, 1883:153–177, 2000.
- [130] E. Trucco and A. Verri. *Introductory techniques for 3-D computer vision*. Prentice Hall, New Jersey, 1998.
- [131] J. Tyson, T. Schmidt, and K. Galanulis. Biomechanics deformation and strain measurements with 3d image correlation photogrammetry. *Experimental Techniques*, 26(5):39–42, Sept. 2002.
- [132] M. van der Meij and R. Bout. Scaling of jaw muscle size and maximal bite force in finches. *Journal of Experimental Biology*, 207:2745–2753, 2004.
- [133] M. van der Meij and R. Bout. The relationship between shape of the skull and bite force in finches. *The Journal of experimental biology*, 211:1668–1680, 2008.
- [134] M. a. a. van der Meij and R. G. Bout. Seed husking time and maximal bite force in finches. *The Journal of experimental biology*, 209(Pt 17):3329–35, Sept. 2006.
- [135] C. Van Hemert, C. M. Handel, J. E. Blake, R. M. Swor, and T. M. O’Hara. Microanatomy of passerine hard-cornified tissues: Beak and claw structure of the black-capped chickadee (*Poecile atricapillus*). *Journal of morphology*, 000, Oct. 2011.
- [136] M. R. Viotti, A. G. J. Albertazzi, and W. Kapp. Experimental comparison between a portable DSPI device with diffractive optical element and a hole drilling strain gage combined system. *Optics and Lasers in Engineering*, 45:589–595, 2007.
- [137] S. Vogel. *Comparative biomechanics: lifes physical world*. Princeton University Press, Princeton, 2003.
- [138] M. von Unge, W. F. Decraemer, J. J. Dirckx, and D. Bagger-Sjöbäck. Tympanic membrane displacement patterns in experimental cholesteatoma. *Hearing research*, 128(1-2):1–15, Feb. 1999.
- [139] S. Waldner. Removing the image-doubling in shearography by reconstruction of the displacement field. *Optics Communications*, 162:205–210, 1999.

- [140] L. Wang, J. T.-M. Cheung, F. Pu, D. Li, M. Zhang, and Y. Fan. Why Do Woodpeckers Resist Head Impact Injury: A Biomechanical Investigation. *PLoS ONE*, 6(10):e26490, Oct. 2011.
- [141] S. Wroe. Cranial mechanics compared in extinct marsupial and extant African lions using a finite-element approach. *Journal of Zoology*, 274(4):332–339, Apr. 2008.
- [142] H. Yamada. *Strength of biological materials*. Williams & Wilkins, Baltimore, 1970.
- [143] G. M. Yanega and M. A. Rubega. Feeding mechanisms: Hummingbird jaw bends to aid insect capture. *Nature*, 428(6983):615, Apr. 2004.
- [144] L. Yang, P. Zhang, S. Liu, P. R. Samala, M. Su, and H. Yokota. Measurement of Strain Distributions in Mouse Femora with 3D-Digital Speckle Pattern Interferometry. *Optics and lasers in engineering*, 45(8):843–851, Aug. 2007.
- [145] P. G. Young, T. B. H. Beresford-West, S. R. L. Coward, B. Notarberardino, B. Walker, and a. Abdul-Aziz. An efficient approach to converting three-dimensional image data into highly accurate computational models. *Philosophical transactions. Series A, Mathematical, physical, and engineering sciences*, 366(1878):3155–73, Sept. 2008.
- [146] H. Zhang, B. E. Schuster, Q. Wei, K. Ramesh, H. Zang, and R. K. T. The design of accurate micro-compression experiments. *Scripta Materialia*, 54(2):181–186, Jan. 2006.
- [147] M. Zhang, Y. Zheng, and A. F. Mak. Estimating the effective Young's modulus of soft tissues from indentation tests nonlinear finite element analysis of effects of friction and large deformation. *Medical Engineering & Physics*, 19(6):512–517, Sept. 1997.
- [148] O. C. Zienkiewicz and R. Taylor. *The Finite Element Method*. Butterworth-Heinemann, Oxford, UK, 2000.



---

## Nomenclature

---

$\nu$	Poisson's ratio
$E$	Young's modulus
CAD	Computer-aided design
CCD	Charge-coupled device
CT	Computer tomography
DIC	Digital image correlation
DSPI	Digital speckle pattern interferometry
FE	Finite element
LDV	Laser Doppler vibrometer
MRI	Magnetic resonance imaging
PCSA	Physiological cross-sectional area
VM	Von Mises
VOI	Volume of interest



De bekken van Darwinvinken zijn een tekstboekvoorbeeld voor evolutie. Deze veertien vinken soorten leven op de Galápagos eilanden en hebben één enkele gemeenschappelijke voorouder. De vorm en grootte van hun bek verschilt sterk en hangt af van het beschikbare voedsel. De spierkracht is echter de bepalende factor of zaden al dan niet gekraakt kunnen worden. De hypothese van deze thesis luidt dan ook als volgt: 'Is de vorm en de grootte van de bek zodanig geëvolueerd dat hij deze spierkrachten kan weerstaan?' Om een fysisch gebaseerd antwoord op deze vraag te vinden heb ik gebruik gemaakt van eindige elementen modelering.

Dit werk is opgedeeld in drie delen. Het eerste deel is een literatuurstudie. In **hoofdstuk 1** geef ik een inleiding over enkele basisconcepten in de biologie, morfologie en evolutie van vogels en Darwinvinken in het bijzonder. Zo kunnen lezers die niet vertrouwd zijn met deze concepten, de resultaten uit de latere hoofdstukken toch plaatsen. Verder wordt het belang van de bek en zijn anatomische opbouw besproken. **Hoofdstuk 2** start met een korte inleiding waar enkele basisconcepten uit de mechanica van de vervormbare lichamen worden toegelicht. Vervolgens worden deze concepten op een striktere wijze afgeleid en toon ik hoe eindige elementen modelering gebruikt kan worden in de mechanica. Eindige elementen modelering is een techniek die veel gebruikt wordt in ingenieurs toepassingen. Ze toepassen in biologie levert echter enkele praktische problemen op. Deze worden behandeld in de laatste sectie uit dit hoofdstuk.

In het tweede deel van dit werk worden twee op maat gemaakte opstellingen besproken. Ten eerste zijn materiaal parameters nodig om een correcte modellering te bekomen. Voor dunne biologische specimens zijn deze parameters moeilijk te bekomen. Standaard technieken vereisen namelijk goed gedefinieerde randvoorwaarden. Daarom stel ik in **hoofdstuk 3** een nieuwe dubbele indentatie techniek voor om de elastische modulus te bepalen. Door de specimenhouder te vervangen door een tweede naald, worden problemen aan de interface tussen specimen en specimenhouder vermeden. Daarenboven is de klassieke indentatie formule afgeleid voor oneindig dikke specimens. In mijn opstelling worden echter specimens van enkele  $100\mu m$ 's dun

gebruikt. Een correctiefactor is daarom noodzakelijk. De resultaten worden vergeleken met testmaterialen en de moduli voor gehoorbeentjes en voor bot en keratine van vogelbekken worden gemeten. In **hoofdstuk 4** stel ik een interferometrische opstelling ('digital speckle pattern intererometry', DSPI) voor om de resultaten van het eindige elementen model te valideren. De theorie en experimentele opstelling worden besproken en de eerste testresultaten tonen een hoge precisie.

In het derde en laatste deel worden de resultaten op vogelbekken gepresenteerd. De bek van vogels bestaat uit een benig kern met errond de rhamphotheca (keratine laag). In **hoofdstuk 5** stel ik een eindige elementen model op om de mechanica van deze ge-laagde structuur, tijdens het bijten, te simuleren. Op deze manier kan ik onderzoeken wat de rol van keratine in het verzwakken van de stresspieken is en hoe dat de bek zijn sterk maar toch licht karakter bekommt. Concreet pas ik de moduli van bot en keratine in het model aan zodat de maximale stress geminimaliseerd wordt. De parameters die ik met deze theoretische benadering vind, komen overeen met experimenteel bekomen waarden. Deze wijze van modelleren levert mooie resultaten op, maar validatie metingen zijn noodzakelijk. Een eerste validatie is de goede overeenkomst van de gemodelleerde en de gemeten bijtkrachten. Meerdere stressverdelingen leveren echter gelijkaardige bijtkrachten op. Daarom is het beter om naar de vervormingen te kijken. In **hoofdstuk 6** wordt een goede overeenkomst gevonden tussen de model resultaten en resultaten bekomen met DSPI en 'digital image correlation' (DIC). DSPI levert zeer goede resultaten. Daarom kan deze methode ook gebruikt worden voor een inverse analyse (**hoofdstuk 7**). De moduli van bot en keratine worden gezocht door deze waarden aan te passen en een beste fit te zoeken met het experiment. De resultaten die op deze manier bekomen worden, komen zeer goed overeen met de dubbel indentatie techniek uit hoofdstuk 3. Tenslotte worden de inzichten uit deze thesis toegepast op de Darwinvinken (**hoofdstuk 8**). Eerst gebruik ik eindige elementen modellen met realistische randvoorwaarden. De berekende stressniveaus zijn gelijkaardig voor bekken van verschillende Darwinvinken. Spierkracht, bek vorm en grootte zijn dus aangepast om gelijkaardige belasting te krijgen. Vervolgens worden de modellen geschaald zodat enkel de bekvorm verschillend is. Hierdoor kan ik aantonen dat deze bekvorm aangepast is aan zijn gebruik. In het laatste hoofdstuk (**hoofdstuk 9**) worden de algemene conclusies herhaald.

# Joris Soons

Oosterveldlaan 95 b3  
2610 Wilrijk, Belgium  
<http://www.ua.ac.be/joris.soons>

Phone: (+32)472/97.70.97  
Email: [jorissoons@hotmail.com](mailto:jorissoons@hotmail.com)  
Email work: [joris.soons@ua.ac.be](mailto:joris.soons@ua.ac.be)

## Personal information

Gender: Male  
Date of Birth: 2 January 1985  
Place of Birth: Borgerhout, Belgium  
Citizenship: Belgian



## Education

M.Sc. in physics, 2007  
University of Antwerp (Belgium)  
*summa cum laude*  
Master thesis: *Electro-anatomical FE model of the cochlea* (Supervisor: Prof. S. Peeters, Med-elec, University of Antwerp)

B.Sc. in physics, 2005  
University of Antwerp (Belgium)  
*cum laude*

Master in didactics, 2008  
University of Antwerp (Belgium)

Secondary school degree: Science-mathematics (8h), 2003  
Sint-Lievenscollege Antwerpen (Belgium)

## **Research Interest**

In my PhD research, I have studied the influence of beak morphology of the famous Darwin finches on the stress distribution during biting. My research interests include both numerical as experimental techniques:

- Optical measurement techniques: speckle and holographic techniques such as digital speckle pattern interferometry (DSPI) and shearography, digital image correlation (DIC)
- Finite element analysis
- (micro-)biomechanics, imaging, scientific programming

The main results of this research are presented in this PhD dissertation.

---

## List of publications

---

### A. Journal publications with peer review

1. **Soons Joris**, Herrel Anthony, Genbrugge Annelies, Aerts Peter, Podos Jeffrey, Adriaens Dominique, de Witte Yoni, Jacobs Patric and Dirckx Joris “Mechanical stress, fracture risk and beak evolution in Darwin’s ground finches (\*\*Geospiza\*\*)” *Philosophical transactions of the Royal Society: B: biological sciences*, 2010, 365 (1543), 1093-98 (IF: 6.053) (<http://dx.doi.org/doi:10.1098/rstb.2009.0280>)
2. **Soons Joris**, Aernouts Jef and Dirckx Joris “Elasticity modulus of rabbit middle ear ossicles determined by a novel micro-indentation technique” *Hearing research*, 2010, 263 (1-2), 33-37 (IF: 2.428) (<http://dx.doi.org/doi:10.1016/j.heares.2009.10.001>)
3. **Soons Joris**, de Baere Ives and Dirckx Joris “New double indentation technique for measurement of the elasticity modulus of thin objects” *Experimental mechanics*, 2011, 51(1),85-95 (IF: 1.854) (<http://dx.doi.org/doi:10.1007/s11340-010-9340-8>)
4. **Soons Joris**, Herrel Anthony, Aerts Peter and Dirckx Joris “Determination and validation of the elastic moduli of small and complex biological samples: bone and keratin in bird beak” *the Journal of the Royal Society Interface* (published online: doi: 10.1098/rsif.2011.0667) (IF: 4.259)
5. **Soons Joris**, Herrel Anthony, Genbrugge Annelies, Adriaens Dominique, Aerts Peter and Dirckx Joris “Multi-layered bird beaks: the role of keratin in stress dissipation, a finite element model approach” *the Journal of the Royal Society Interface* (published online: doi: 10.1098/rsif.2011.0910) (IF: 4.259)
6. Herrel Anthony, **Soons Joris**, Aerts Peter, Dirckx Joris, Boone Matthieu, Jacobs Patric, Adriaens Dominique and Podos Jeffrey “Adaptation and function of the bills of Darwin’s finches: divergence by feeding type and sex” *EMU*, 2010, 110 (1), 39-47 (IF: 1.191) (<http://dx.doi.org/doi:10.1071/MU09034>)

7. Aernouts Jef, **Soons Joris** and Dirckx Joris “Quantification of tympanic membrane elasticity parameters from in situ point indentation measurements: Validation and preliminary study” *Hearing research*, 2010, 263 (1-2), 177-82 (IF: 2.428)  
(<http://dx.doi.org/doi:10.1016/j.heares.2009.09.007>)
8. Dirckx Joris, Aernouts Jef, Aerts Johan, Buytaert Jan A.N. and **Soons Joris** “Towards high-realism physics based models of middle ear mechanics: High definition morphology, precise materials parameters and introduction of non-linearity” *Hearing research*, 2010, 263 (1-2), 241-2 (IF: 2.428)  
(<http://dx.doi.org/10.1016/j.heares.2010.03.038>)
9. Salih Wasil, **Soons Joris** and Dirckx Joris “High-resolution 3D translation measurements using point source x-ray stereoscopy” *Measurement science and technology*, 2011, 22 (2), 025502 (IF: 1.35)  
(<http://dx.doi.org/doi:10.1088/0957-0233/22/2/025502>)

#### **A(bis). Papers in preparation**

1. **Soons Joris**, Genbrugge Annelies, Podos Jeffrey, Adriaens Dominique, Aerts Peter, Dirckx Joris and Herrel Anthony “Precise tuning of beak morphology to loading demands in Darwin’s finches.”
2. **Soons Joris**, Lava Pascal, Debruyne Dimitri and Dirckx Joris “Full field optical deformation measurement in biomechanics: digital speckle pattern interferometry and 3D digital image correlation applied on bird beaks.”
3. **Soons Joris** and Dirckx Joris “Digital speckle pattern interferometry on a multi-layered biological structure: the role of top keratin in bird beaks.” *Optimes 2012* (Conference proceeding)
4. **Soons Joris**, Aerts Peter, Herrel Anthony and Dirckx Joris “The influence of scaling transformations on the stress dissipation in Darwin’s finch beaks.”

#### **B. Book chapters with peer review**

1. **Soons Joris** and Dirckx Joris “Multi-Parts Geometry-Based Finite Element Modeling in Biomechanics: Elastic Modulus Determination of Bone and Keratin in the Java Finch’s Beak by Double Indentation Technique and Inverse Analysis” in *Horizons in World Physics*. Volume 278 - Nova science Publishers  
ISBN: 978-1-61942-537-8  
and in *Advances in Mathematics Research*. Volume 17 - Nova science Publishers  
ISBN: 978-1-62100-882-8

#### **C. Conference proceedings**

1. **Soons Joris** and Dirckx Joris “Full field displacement and strain measurement of small complex bony structures with digital speckle pattern interferometry and shearography” *Proc. SPIE 7387, 73870C*, 2010  
(<http://dx.doi.org/doi:10.1117/12.870678>)

2. **Soons Joris** and Dirckx Joris “Phase shifting digital speckle pattern interferometry and inverse analysis on bird beaks” *Photomechanics 2011*, p. 42-43, 2011
3. **Soons Joris** and Dirckx Joris “Digital speckle pattern interferometry in biomechanics: in situ inverse analysis on birds beaks to obtain elastic modulus of the bony core and the keratin layer” *10th IMEKO symposium 2011*, ISBN 978-3-18-092156-3 - S.l., VDI, p. 73-80, 2011

#### D. Conference contributions

1. **Soons Joris** and Aernouts Jef, Dirckx Joris “Micro-indentation to determine middle ear ossicles elasticity parameters” *Memro 2009*, Stanford University, CA, USA, 24-28 June 2009 (Poster presentation)
2. **Soons Joris** and Dirckx Joris “Full field displacement and strain measurement of small complex bony structures with digital speckle pattern interferometry and shearography” *SPIE speckle 2010*, Florianopolis, SC, Brazil, 13-15 September 2010 (Oral presentation)
3. **Soons Joris** and Dirckx Joris “Phase shifting digital speckle pattern interferometry and inverse analysis on bird beaks” *Photomechanics 2011*, Brussels, Belgium, 7-9 February 2011 (Oral presentation)
4. **Soons Joris** and Dirckx Joris “Digital speckle pattern interferometry in biomechanics: in situ inverse analysis on birds beaks to obtain elastic modulus of the bony core and the keratin layer” *10th IMEKO symposium 2011*, Braunschweig, Germany, 12-13 September 2011 (Oral presentation)
5. **Soons Joris** and Dirckx Joris “Deformation of a multi-layered biological structure: digital speckle pattern interferometry on bird beaks” *Optimes 2012*, Antwerp, Belgium, 4-5 April 2012 (Oral presentation)
6. **Soons Joris**, Lava Pascal, Debruyne Dimitri and Dirckx Joris “Bendy beaks: 3D digital image correlation” *Optimes 2012*, Antwerp, Belgium, 4-5 April 2012 (Poster presentation)
7. Herrel Anthony, **Soons Joris**, Dirckx Joris, Vanhooydonck Bieke, Aerts Peter and Podos Jeff “Biting, mechanical constraints, and trade-offs in Darwin’s finch beaks: a recipe for ecological speciation?” *Deakin symposium*, Melbourne, 8-13 Feb. 2009
8. Dirckx Joris, Aernouts Jef, Aerts Johan, Buytaert Jan and **Soons Joris** “Towards high-realism physics based models of middle ear mechanics: high definition morphology, precise materials parameters and introduction of non-linearity” *Memro 2009*, Stanford University, CA, USA, 24-28 June 2009
9. Aernouts Jef, **Soons Joris** and Dirckx Joris “Quantification of tympanic membrane elasticity parameters from in situ measurements” *Memro 2009*, Stanford University, CA, USA, 24-28 June 2009
10. Genbrugge Annelies, **Soons Joris**, Herrel Anthony, Dirckx Joris, Aerts Peter and Adriaens Dominique “Comparative cranial osteology of Darwin’s finches in relation to feeding mechanics: preliminary results” *16th Benelux Congress of Zoology*, Wageningen, the Netherlands, 29-30 October 2009

11. Adriaens D., Praet T., Genbrugge A., Leysen H., **Soons Joris**, Van Loo D., Van Cauter D., Dierick M., Boistel R., De Beule M., Herrel A., Verheghe B., Dirckx J. and Van Hoorebeke L. "Micro-CT-scanning as a valuable source of data for musculoskeletal studies in biology" *Symposium on X-ray tomography as a multidisciplinary research tool*, Ghent, Belgium, 8 December 2010
12. Salih Wasil, **Soons Joris**, Buytaert Jan and Dirckx Joris. "High-resolution 3D ossicle displacements measured with point source x-ray stereoscopy" *The Society for Experimental Biology (SEB) annual meeting*, Glasgow, UK, July 2011

### **E. Other publications**

1. Vernimmen Tim in collaboration with: Dirckx Joris, Genbrugge Annelies, Herrel Anthony, Raeymaekers Joost, **Soons Joris** en Vanhooydonck Bieke "Bekende bekken" *EOS-magazine*, december 2011
2. Salleh Anna in collaboration with: **Soons Joris** "Perfect blend behind bird beak strength" *ABC news in science*, 16 February 2012

### **F. Academic honors**

Aspirant fellowship Research Foundation - Flanders (october 2008)

Winner engineering category poster competition at MEMRO conference (June 24-28, 2009 at Stanford University)

---

## Acknowledgements - Dankwoord

---

Na een stevige eindsprint ben ik beland bij het schrijven van dit dankwoord. Hoewel dit het laatste is dat ik schrijf, is dit waarschijnlijk hetgeen u als eerste opzoekt. Uiteraard hoop ik dat dit niet het enigste is dat u zal lezen.

Ik zou graag enkele mensen willen bedanken die mij tijdens deze vier en een half jaar onderzoek, met de bijhorende *ups* en *downs*, bijgestaan hebben. Mijn eerste woorden van dank gaan naar mijn beide promotoren, Prof. Joris Dirckx en Prof. Peter Aerts. Zij bedachten dit interessante onderwerp, gaven mij de kans om te doctoreren en bleven mij stimuleren tijdens dit project.

Met Prof. Joris Dirckx werkte ik de voorbije jaren zeer nauw samen. Ondanks de steeds groeiend administratieve 'rompslomp' voor hem, stond hij steeds klaar met 'raad en daad'. Met zijn praktische kennis in de fysica en zijn creativiteit hielp hij mij meermaals verder bij verschillende experimenten. Zo maakte hij van mij zonder twijfel een betere onderzoeker. Dankzij zijn kwaliteiten als uitmuntend onderzoeker, twijfel ik er niet aan dat het labo voor biomedische fysica (BIMEF) in de komende jaren nog verder zal uitbreiden. Bedankt Joris voor de vruchtbare en zeer fijne samenwerking de voorbije jaren!

Met Prof. Peter Aerts had ik minder direct contact. Desondanks gaf hij mij, niettegenstaande zijn drukke agenda, meermaals zeer waardevolle raad in verband met de biologische aspecten. Ik had ook het geluk om te kunnen samenwerken met Dr. Anthony Herrel. Tussen zijn veldwerkstudies en internationale congressen was hij zeer goed bereikbaar voor allerhande vragen. Zijn enthousiasme en internationale contacten verbeterden zonder twijfel mijn onderzoek. Onze samenwerking en zijn expertise in biologie leverden dan ook enkele zeer mooie publicaties op.

Ik zou ook de leden van mijn doctoraatsjury willen bedanken, Prof. Bart Partoens en Prof. Dirk Lamoen van het departement fysica van de Universiteit Antwerpen. Ik ben hen dankbaar voor hun commentaren en de beoordeling van mijn werk.

It was also a great honor to have Prof. Michael Fagan from the department of engineering from the University of Hull (UK) as external member. I am also thankful for his insightful comments and for reviewing this dissertation.

Een doctoraat is niet mogelijk zonder financiële steun. Hiervoor zou ik de volgende organisaties willen bedanken. Dankzij een aspirantenmandaat van het Fonds voor Wetenschappelijke Onderzoek - Vlaanderen (FWO) kon ik gedurende vier jaar mijn onderzoek uitvoeren en bekostigen. Verder verworf ik een FWO reiskrediet om deel te nemen aan de 'SPIE speckle 2010' conferentie te Florianopolis (Brazilië). Mijn eerste onderzoekjaar werd betaald door een interdisciplinaire beurs van de Universiteit Antwerpen.

Verder gaat mijn dank ook naar mijn collega's van BIMEF. Bij hen kon ik steeds terecht met vragen. In het bijzonder zou ik Jef, Jan en Johan willen bedanken voor hun deskundige hulp. Bovendien waren de middagpauzes, de congressen, de sport en 'overige' activiteiten vaak dolle pret. Daarvoor ook dank aan de andere leden van 'den buro' (Stef, Adriaan en Wasil) en aan 'de jeugd' (Sam, Daniël, John en Jana). Graag zou ik ook Prof. Wim Decraemer willen bedanken voor de interessante gesprekken. Uiteraard ook een woord van dank voor de vele desserts verzorgd door mijn recente bureaugenote, *cake-vrouw* Greet. Daarnaast zou ik de medewerkers van het secretariaat fysica (Hilde, Gert en Nathalie) willen bedanken voor hun logistieke hulp en de labomedewerkers voor hun hulp tijdens mijn zeldzame studentenlabo's (Ilse en Luc). Een bijzonder woord van dank en bewondering gaat naar de mensen van het elektronisch en mechanisch atelier: Fred, William en Jan. Zij hielpen mijn theoretische hersenspinsels naar concrete experimentele opstellingen te vertalen.

Verder zou ik mijn appreciatie willen uitspreken voor de samenwerking met de volgende mensen:

Steve Maas (MRL Lab, University of Utah) voor het ter beschikking stellen van de FEBio software en de technische en theoretische hulp in verband met eindige elementen modellering.

Prof. Dominique Adriaens en Annelies Genbrugge (Evolutionary Morphology of Vertebrates, Universiteit Gent) voor de vruchtbare samenwerking en hun hulp in verband met de biologische aspecten van mijn onderzoek en het CT scannen.

Pascal Lava (Katholieke Hogeschool Sint-Lieven) voor het ter beschikking stellen van de matchID software en de technische hulp in verband met digital image correlation (DIC).

Prof. Jeff Podos (Biology department of the University of Massachusetts) for the insightful discussions and his assistance to improve our paper.

Ives de Baere (Mechanics of Materials and Structures, Universiteit Gent) voor het uitvoeren van de compressie testen.

Prof. Marleen Verhoye (Bio-Imaging Lab, Universiteit Antwerpen) voor het testen van MRI op vogelbekken.

Prof. Nora de Clerck en Dr. Andrei Postnov (Micro CT Research group, Universiteit Antwerpen) voor het ter beschikking stellen van de CT scanner en hun deskundige hulp.

Prof. Hugo Sol (Faculty of Engineering, Vrije Universiteit Brussel) voor de interessante discussie over digital image correlation (DIC).

Jan van Daele (Laboratory of Cell Biology and Histology, Universiteit Antwerpen) voor de hulp bij confocale microscopie.

Prof. Callum Ross (Department of Organismal Biology and Anatomy, University of Chicago) for the insightful discussions.

Michael Ravicz (Massachusetts Eye and Ear Infirmary) for his assistance to improve the english grammar of my first paper.

Tenslotte zou ik ook vrienden en familie willen bedanken om mij tijdens deze doctoraatsjaren bij te staan. Eerst zou ik mijn ouders willen bedanken voor alle kansen die ze mij gegeven hebben. Ook zou ik mijn drie broers willen bedanken omdat ze altijd voor mij klaar staan. Ook bedankt aan al mijn vrienden: kameraden van op het studentenhome en aanverwante vrienden, leden van der Antwerper Kreis, sportraad-mensen, de CMT fysici, mannen van de voetbal, ... en één ieder die ik hier vergeet.

Bedankt iedereen,  
Joris

Graag zou ik dit dankwoord willen afsluiten met een korte paragraaf voor iemand héél speciaal. Deze persoon staat altijd voor mij klaar en zij steunt mij in alles wat ik doe. Bedankt Sarah!